2019-01-01

Study Of Multielectron Redox Chemistry In Bimetallic Complexes And Metal-Free Macrocycles

Nancy Rodriguez Lopez

University of Texas at El Paso

Recommended Citation

Rodriguez Lopez, Nancy, "Study Of Multielectron Redox Chemistry In Bimetallic Complexes And Metal-Free Macrocycles" (2019). *Open Access Theses & Dissertations*. 2896. https://digitalcommons.utep.edu/open_etd/2896

STUDY OF MULTIELECTRON REDOX CHEMISTRY
IN BIMETALLIC COMPLEXES AND METAL-FREE MACROCYCLES

NANCY RODRIGUEZ LOPEZ

Doctoral Program in Chemistry

APPROVED:

Dino Villagrán, Ph.D., Chair

Katja Michael, Ph.D.

Skye Fortier, Ph.D.

Chunqiang Li, Ph.D.

Stephen L. Crites, Jr., Ph.D.
Dean of the Graduate School

Dedication

To my family. Thank you for all your love and support.

STUDY OF MULTIELECTRON REDOX CHEMISTRY IN BIMETALLIC COMPLEXES AND METAL-FREE MACROCYCLES

by

NANCY RODRIGUEZ LOPEZ, B.S.

DISSERTATION

Presented to the Faculty of the Graduate School of
The University of Texas at El Paso
in Partial Fulfillment
of the Requirements
for the Degree of

DOCTOR OF PHILOSOPHY

Department of Chemistry and Biochemistry
THE UNIVERSITY OF TEXAS AT EL PASO
December 2019

Acknowledgements

I want to thank my advisor, Dr. Villagrán for all his guidance, patience, and support throughout my undergraduate thesis and doctoral studies. Thank you for giving me the opportunity to work in your laboratory, but most importantly for shaping the scientist I became. In addition, I would like to thank the members of my committee, Dr. Michael, Dr. Fortier, and Dr. Li for their constructive criticism, and valuable research and life advice.

I thank all former and current lab members of the Villagrán lab (Maripaz, Iván, Mariana, Yanyu, Yulu, Nathalie, Jose, and Karen) for all the chemistry and non-chemistry related discussions, but specially for making this a gratifying experience. I would like to recognize the great effort and dedication of all the undergraduate students I had the honor to train and work with (Marisol, Macy, Eileen, Jin, and David). Special thanks to Maripaz, Iván, and Marisol for all the talks, for listening to me, but mainly for being my friends. Special

I want to thank my parents and my sister that, although far away, have always being there for me. I am lucky to have such a supportive family that has always encouraged me to follow my dreams. I will always appreciate all the sacrifices you have made to get me where I am.

Finally, I would like to thank the most amazing person in my life, Ale. Thank you for always being by my side in both the good and not-so-good times. Thanks for all the laughs, the fun, the love and support, for always picking me back up or pulling me back to earth, but most importantly for always believing in me.

Abstract

Multielectron redox chemistry is fundamental for the activation of small molecules (e.g. H_2O, CO_2, CO, N_2). Although these processes are of great importance, they are not well understood. Unravelling the mechanisms of electron transfer and its principles is essential for the design and development of efficient catalysts. Our approach towards the understanding of multielectron redox chemistry includes theoretical study of mechanistic pathways in the hydrogen evolution reaction (HER) by metal-free porphyrinoids, the study of electronic communication in non-symmetric multimetallic two-state models (D–B–A) and the tuning of the electronic properties of bimetallic systems (Mo, and Au) by ligand control.

In Chapter 2, the free-base *meso*-tetra(pentafluorophenyl)porphyrin was found to be electrocatalytically active for hydrogen gas generation in the presence of *p*-toluenesulfonic acid. The electrochemical potential of hydrogen evolution (–1.31 vs Fc/Fc^+ in THF and –0.69 V vs Ag/Ag^+ MeCN) is comparable to metal containing electrocatalysts such as metallated porphyrins or other metallated macrocycles. In combination of spectroscopic and spectroelectrochemical observations along with DFT computations, we proposed the most thermodynamically favorable hydrogen generation mechanism to be a (1) reduction, (2) protonation, (3) reduction, (4) protonation (*E*-*P*-*E*-*P*) pathway in THF, and a (1) protonation, (2) protonation, (3) reduction, (4) reduction (*P*-*P*-*E*-*E*) pathway in MeCN.

In Chapter 3, the free-base 5, 10, 15-tris(pentafluorophenyl)corrole showed to be active towards hydrogen evolution in acetonitrile under acidic conditions. The electrochemical potential of HER using *p*-toluenesulfonic acid (–1.22 V vs Fc/Fc^+ in acetonitrile) is comparable to other metalated and metal-free macrocycles. In combination of experimental observations and Density Functional Theory calculations a mechanistic pathway was obtained when a strong was used as

proton source (*p*-toluenesulfonic acid). The most favourable hydrogen gas generation mechanism is a (1) protonation, (2) reduction, (3) reduction, (4) protonation (*PEEP*) pathway when *p*-toluenesulfonic acid is used. On the other hand, when a weaker acid (benzoic acid) was used, the metal-free corrole cannot catalyse the proton reduction reaction.

Chapter 4 depicts the synthesis and characterization of three non-symmetric multimetallic systems of the D–B–A type for the study of Inner-Sphere electron transfer. In the first part of this chapter, two *dimers-of-dimers* ($[Mo_2(DAniF)_3]_2(C_{12}O_3NH_7)$ and $[Mo_2(DAniF)_3]_2(C_{18}O_2N_2H_{12})$) were prepared and studied. Cyclic voltammetry on these compounds displayed multielectron redox processes with two one-electron and three one-electron oxidations for $[Mo_2(DAniF)_3]_2(C_{12}O_3NH_7)$ and $[Mo_2(DAniF)_3]_2(C_{18}O_2N_2H_{12})$, respectively. Calculation of their comproportionation constants based on the obtained data ($K_c = 6.36 \times 10^3$ and $K_c = 9.7 \times 10^{10}$) regarded $[Mo_2(DAniF)_3]_2(C_{12}O_3NH_7)$ and $[Mo_2(DAniF)_3]_2(C_{18}O_2N_2H_{12})$ as Class II and Class III on the Robin–Day classification. The HOMO and HOMO-1 energy gap, which is directly related to the interaction between the Mo_2 centers, suggests the electronic coupling of the dimolybdenum units in $[Mo_2(DAniF)_3]_2(C_{18}O_2N_2H_{12})$ are stronger than that on $[Mo_2(DAniF)_3]_2(C_{12}O_3NH_7)$. This result is consistent with the larger separation between the redox potentials waves.

In the second part, the effect of a non-metallic redox active unit in the electronics of the D–B–A system, where a C_{60} fullerene cage was used as the second active site, was studied. We describe the synthesis and characterization of $Mo_2(DAniF)_3(C_{69}O_2NH_8)$. The UV-Vis spectra showed a strong band in the UV region corresponding to a MLCT transition from the interaction of the δ orbitals of the Mo_2 core with the π^* orbitals of the bridging ligand. This electronic transition was assigned based on the nature of the HOMO and LUMO and supported by TDDFT calculations. Electrochemical studies showed a one-electron oxidation at 0.543 V vs Ag/Ag^+

related to the $Mo_2^{4+/5+}$ process, as well as reduction events associated to reductions of the fullerene cage. The change on the reduction events suggests the presence of communication between the donor and acceptor sites in the form of $Mo_2^{5+} \rightarrow C_{60}$ charge transfer.

The last part of this chapter explores the study of charge transfer in a D–B–A system where both the donor and acceptor are organic units, while the bridging ligand is a dimolybdenum center. We synthesized and characterized $Mo_2(DAniF)_3(C_{18}O_2N_2H_{12})$ and *trans*-$Mo_2(DAniF)_3[C_{18}O_2N_2H_{12}]_2$ by means of ^1H NMR, mass spectrometry and single crystal X-Ray diffraction. Cyclic voltammetry showed a one-electron oxidation at –0.03 and –0.017 V vs Fc/Fc^+ for $Mo_2(DAniF)_3(C_{18}O_2N_2H_{12})$ and *trans*-$Mo_2(DAniF)_3[C_{18}O_2N_2H_{12}]_2$ corresponding to the $Mo_2^{4+/5+}$ process. The presence of a second redox event assigned to oxidation of the organic ligands was observed at 0.465 and 0.148 V vs Fc/Fc^+ to the mono and trans complex, respectively. Integration of the redox waves showed a one-electron and two-electron oxidation for $Mo_2(DAniF)_3(C_{18}O_2N_2H_{12})$ and *trans*-$Mo_2(DAniF)_3[C_{18}O_2N_2H_{12}]_2$. The presence of only one wave for the second event in the trans complex suggested the ligands are not considerably coupled.

Chapter 5 reports the synthesis and characterization of a series of dimolybdenum paddlewheel complexes of the type $Mo_2(DAniF)_{4-n}(hpp)_n$ ($n = 1 - 3$) where DAniF is the anion of N,N’-di-p-anisyl-formamidine and hpp is the anion of 1,3,4,6,7,8-Hexahydro-2H-pyrimido[1,2-a]pyrimidine. The effect on the electronic structure of these tetragonal paddlewheel dimolybdenum was studied upon systematic substitution of formamidinate ligands by the more basic guanidinates. Mo—Mo distances in the paddlewheel structures decreased upon guanidinate ligand substitution, and were found to be 2.0844(6), and 2.0784(6), for $Mo_2(DAniF)_3(hpp)$ and trans-$Mo_2(DAniF)_2(hpp)_2$, respectively. Electrochemical studies show that the half wave potential of the Mo_2^{5+}/Mo_2^{4+} couple shifts cathodically upon ancillary ligand substitution ranging from –0.286 V for the tetraformamidinate complex to –1.795 V for the tetraguanidinate analogue, and with redox potentials of –0.75, –1.07 and –1.14 V for $Mo_2(DAniF)_3(hpp)$, $Mo_2(DAniF)_2(hpp)_2$, and $Mo_2(DAniF)(hpp)_3$, respectively. The presence of a second redox event assigned to the Mo_2^{6+}/Mo_2^{5+} couple was not observed until two guanidinate ligands were introduced. Raman spectroscopy shows that the *v*(M-M) stretch gets systematically strengthen upon formamidinate ligand substitution by the guanidinate ligand hpp. The destabilization of the delta bond by the basic hpp ligand was measured using DFT calculations by tracking the energy of the frontier orbitals. The decrease in the HOMO-LUMO gap was supported by the red-shift in the UV-Vis spectra of the compounds, 412, 442, and 450 nm for $Mo_2(DAniF)_3(hpp)$, $Mo_2(DAniF)_2(hpp)_2$, and $Mo_2(DAniF)(hpp)_3$, respectively.

In the first part of Chapter 6 we report the synthesis and characterization of a series of digold complexes of the type $Au_2(DippF)_2Cl_n$ (n = 0, 2) were DippF is the anion of N,N'-di-isopropyl-formamidine. The formation of the gold (I) and (II) species was studied under different solvents, namely THF and DCM. Au···Au distances in the structures decreased upon oxidative addition of Cl_2, and were found to be 2.7385(7) and 2.5303(3) Å, for $Au_2(DippF)_2$ and $Au_2(DippF)_2Cl_2$, respectively. Electrochemical studies show a one-electron reversible oxidation for $Au_2(DippF)_2$ at 0.843 V vs Fc/Fc^+, and a non-reversible one-electron oxidation at 0.15 V vs Fc/Fc^+ for $Au_2(DippF)_2Cl_2$, assigned as oxidations of the Au_2 center and ligand. The decrease in the HOMO-LUMO gap due to oxidative addition was supported by the red-shift in the UV-Vis spectra of the compounds, 350, and 470 nm for $Au_2(DippF)_2$ and $Au_2(DippF)_2Cl_2$.In addition, the high energy bands observed were assigned to MLCT and LMCT electronic transitions as supported by TDDFT calculations.

Finally, we report the synthesis and characterization of a series of digold (I) complexes of the type $Au_2(ArNCHNAr')_2$. The effect on the electronic structure of these open coordination digold compounds was studied upon variation of the substituents in the aryl groups of the formamidinate ligands (Ar = RC_6H_5, Ar = $R'C_6H_5$) $Au_2(^{m}DippAF)_2$ (R = 2,6-$CHMe_2$, R' = *m*-OMe), $Au_2(ClDippF)_2$ (R = 2,6-$CHMe_2$, R' = *p*-Cl), and $Au_2(^{m,p}DAniF)_2$ (R = *p*-OMe, R' = *m*-OMe). The Au···Au distances in the dinuclear structures were found to be 2.7281(3) and 2.7431(11) Å, for $Au_2(^{m}DippAF)_2$ and $Au_2(ClDippF)_2$ respectively. Electrochemical studies show that the half wave potential of the $Au_2^{2+/3+}$ couple can be tuned due to inductive effects, displaying a one-electron oxidation for $Au_2(^{m}DippAF)_2$, $Au_2(ClDippF)_2$, and $Au_2(^{m,p}DAniF)_2$ at 0.602, 0.806, and 0.328 V vs Fc/Fc^+ in DCM. The degree of electronic tuning was quantified by the linear correlation of the redox potential ($E_{1/2}$) with the Hammett constant of their ligand substituents. An anodic-shift in $E_{1/2}$ was observed as the electron-withdrawing ability of the ligand increased. The stabilization of the δ* bond (HOMO) was measured using DFT calculations by tracking the energy of the frontier orbitals. The addition of electron-withdrawing substituents stabilized this metal-based orbital.

Table of Contents

List of Tables

List of Figures

List of Illustrations

Chapter 1: Introduction

According to the U.S. Energy Information Administration (EIA) the global energy consumption in 2015 was 600 quadrillion Btu (~20 TW).[1] The total energy consumption is projected to reach 30 TW by 2050, and 46 TW by the end of the century.[2] In 2016, about 80% of the consumed energy was based upon non-renewable energy sources, namely oil, coal, and natural gas (Figure 1.1).[2–4] Our dependence on fossil fuels, due to fast economic development, population growth, and expanding industrialization has created a rising concern on the use of these energy sources.[5,6] These type of non-renewable fuels is characterized by their high energy densities, however their extraction and combustion have environmental, economic, and safety repercussions.[7]

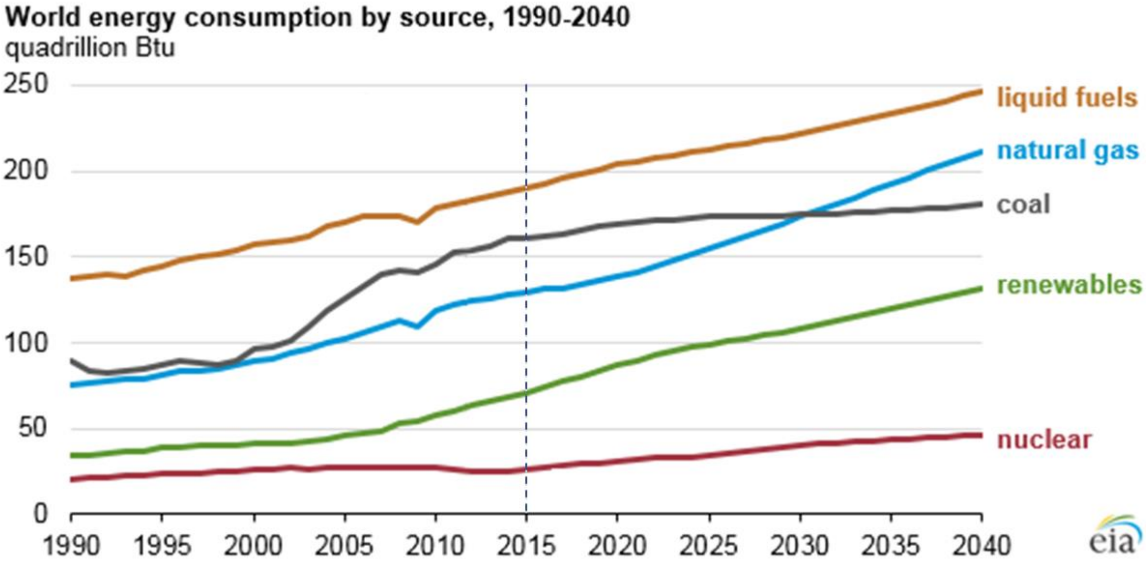

Figure 1.1. Reported and estimated global energy consumption by fuel source, from 1990 to 2040, according to the U.S. Energy Information Administration (EIA).

The increased energy demand can be associated with an increase on greenhouse gas emissions. According to the EIA, the United States alone was responsible for about 18% of CO_2 global emissions in 2017.[8] The concentration of this compound in the atmosphere is naturally regulated by processes involved in the carbon cycle.[9] Although these processes can absorb some of the annually produced carbon dioxide, both the capacity of this cycle to process carbon and the amount of CO_2 in the atmosphere has been perturbed by human activity. This imbalance has resulted in an increased concentration of atmospheric CO_2, from pre-industrial levels of 280 ppm[10] by volume to 410 ppm[11] in 2019. In addition, an increase in the concentration of carbon dioxide and other greenhouse gases has been related to the rising average global temperature.[9,12]

In order to decrease our dependence on fossil fuels, efforts have been made to increase the production of fuels from abundant, clean, and sustainable renewable sources. Among these sources, solar energy is the most abundant and reliable one providing enough power in one hour to fulfill a year's consumption of energy.[13,14] It is estimated that only 1.5% of the total amount of solar energy reaching earth's surface is effectively used.[15] Therefore, some of the major challenges solar energy faces reside on sunlight conversion and storage.

$$2\ H_2O \xrightarrow[\Delta E = +\ 1.23\ \text{eV}]{h\nu} 2\ H_2 + O_2$$

$$\begin{array}{lrcl}
\text{HER} & 4\ H^+ + 4\ e^- & \longrightarrow & 2\ H_2 \\
\text{OER} & 2\ H_2O & \longrightarrow & O_2 + 4\ H^+ + 4\ e^-
\end{array}$$

Scheme 1.1. Overall water splitting reaction, hydrogen evolution reaction (HER) and oxygen evolution reaction (OER).

One alternative is using solar energy to activate small molecules, thus storing energy into chemical bonds. For this purpose, the water splitting process provides an attractive model. Plants have been converting and storing light for millennia via photosynthesis.[16] During this process water reacts with carbon dioxide to produce oxygen and carbohydrates, which requires the transfer of multiple electrons.[17] Although simple, efficient generation of hydrogen and oxygen gas in this reaction is not well understood. Moreover, the effective production of hydrogen (and other small molecules) is significant when we analyze and compare the energy density obtained from different types of batteries. Hydrogen has one of the highest energy density values per mass, between 120 and 142 MJ/kg (33 and 39 KWh/kg).[18] In contrast, lithium ion batteries (up to 1000 Wh/kg)[19,20], solid state batteries (around 8 Wh/in)[21], and flow batteries (330.5 Wh/L)[22,23], have energy densities that are orders of magnitude smaller.

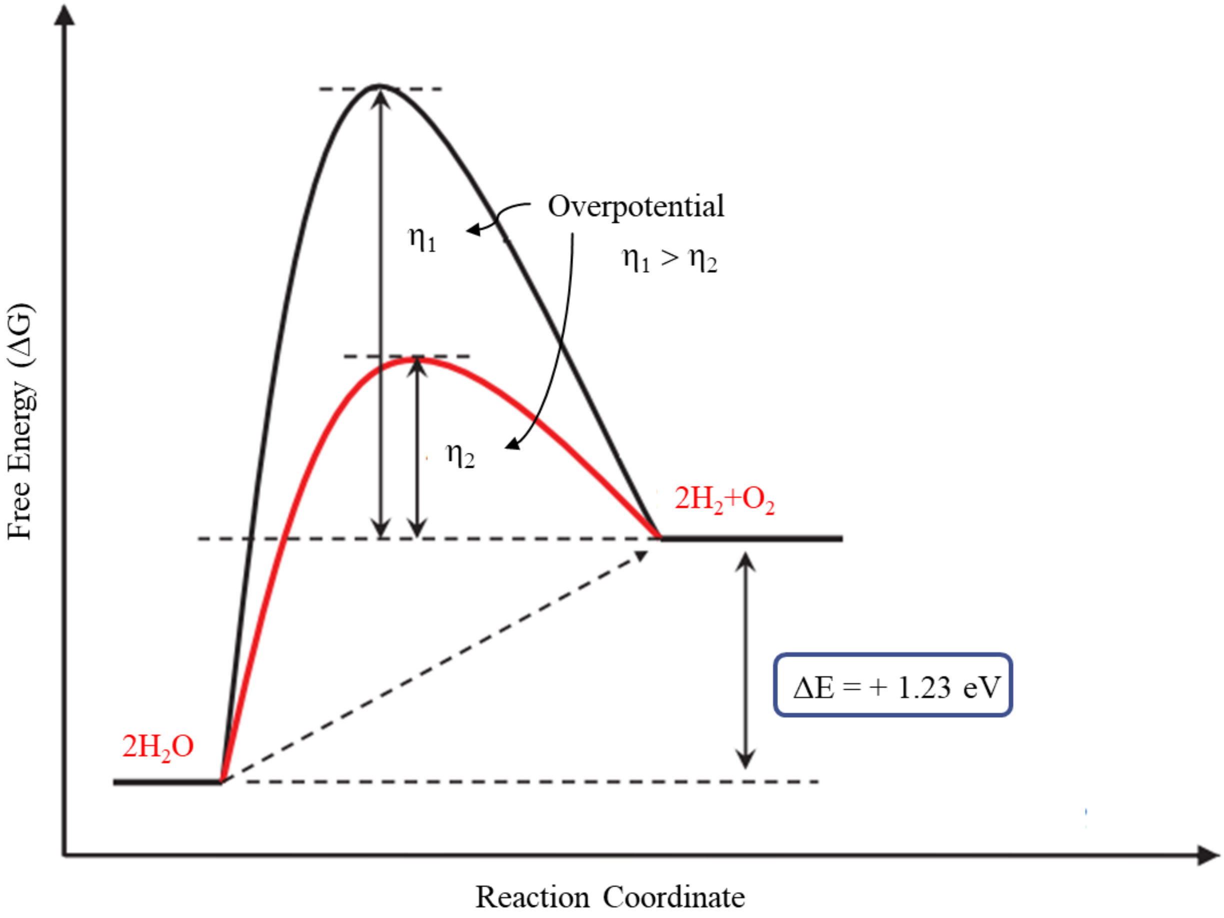

Figure 1.2. Free energy required for splitting water, (red) catalyzed vs (black) uncatalyzed process.

The splitting of water into hydrogen and oxygen is a four electron process which transforms external energy (solar, thermal, electrochemical, etc.) into chemical energy in the form of covalent bonds. The electrolysis of water consists of two half reaction: the hydrogen evolution reaction

(HER) and the oxygen evolution reaction (OER), as shown in Scheme 1.1. This process is thermodynamically and kinetically demanding, requiring a minimum Gibbs free energy change of +237 kJ mol^{-1} (+1.23 eV) to proceed.[24,25] The water oxidation reaction involves large overpotentials due to the formation of highly energetic intermediates, as depicted in Figure 1.2.[26–28] This multielectron redox process is challenging since the chemical transformations are energetically demanding as well as mechanistically complex. The study of electron transfer from a donor to an acceptor site is a crucial concept in understanding the fundamental chemistry of energy conversion. Therefore, the study of multielectron redox chemistry represents a promising pathway to render water splitting and other multielectron redox reactions more feasible.

Electrocatalysts have been implemented for water electrolysis to lower the kinetic barrier and overpotential associated to this process.[29] The design of new and efficient catalyst for HER and OER has become an active field of research.[30–32] Heterogeneous catalysts typically demonstrate better catalytic activity when compared to homogeneous catalysts.[33,34] However, homogeneous catalysts give fundamental knowledge on the mechanism involved in the catalytic process,[35,36] which has led to the study of these systems through both experimental and theoretical methods.[37–43] Metallated porphyrinoids have shown to be catalytic towards hydrogen generation working as electron reservoirs stabilizing the electron rich metal in their core.[44] Nonetheless, little work has been done on understanding electrocatalytic HER by metal-free porphyrinoids.[45,46] In Chapter 2 and Chapter 3 of this dissertation, we evaluate the ability of a metal-free organic macrocycle such as porphyrins and corroles (Scheme 1.2) to generate hydrogen gas under acidic conditions. In addition, we employed theoretical calculations to assign the mechanistic pathway HER follows when free-base organic macrocycles are used as catalysts.

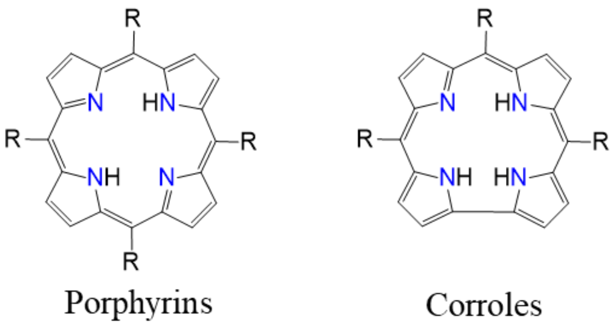

Scheme 1.2. General structure of metal-free porphyrins and corroles.

As previously stated, the study of multielectron redox chemistry is of essential for the understanding of the chemistry behind energy conversion. Several important multielectron redox reactions (hydrogen generation[47], nitrogen fixation[48], carbon dioxide reduction[49], etc.) require the use of heterogeneous catalysts containing transition metals. The catalytic activity in these systems can be enhanced by increasing the number of active sites, and as a result inducing cooperative behavior among the metal centers.[50] Obtaining mechanistic information from heterogeneous catalysis is difficult, nevertheless their understanding is essential for the design of more efficient catalysts. Therefore, we can utilize molecular systems as platforms to study the basics of small molecule activation by reducing the catalytic process from metal surfaces to the molecular level.

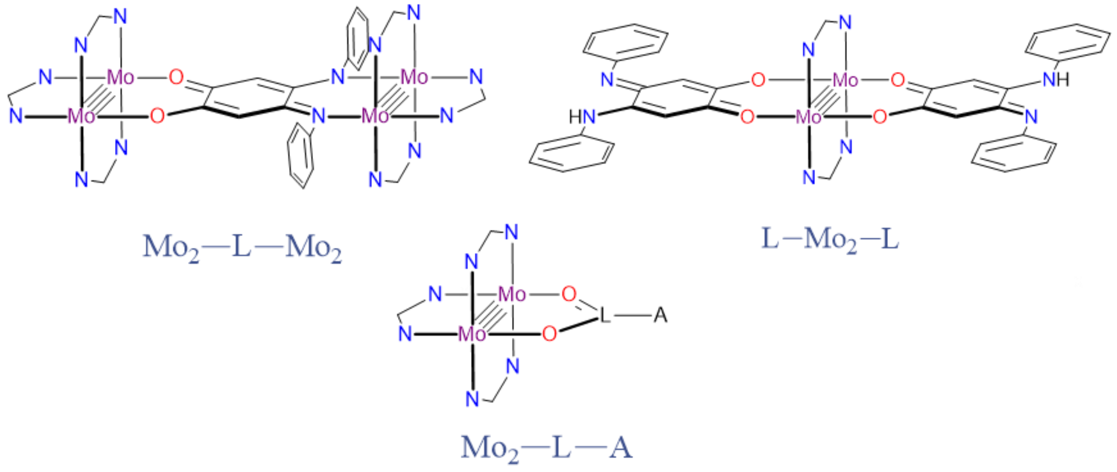

Scheme 1.3. D-B-A systems that will be explored for the understanding of Inner-Sphere electron transfer.

Depending on the nature of the connectivity between the donor and acceptor sites, electron transfer can occur via outer- or inner-sphere electron transfer. Chapter 4, will explore the study of electron transfer through inner-sphere configuration using mixed-valent systems where the donor and acceptor are connected by a bridging ligand (D–B–A) as depicted in Scheme 1.3. Finally, Chapter 5 and Chapter 6 present fundamental studies of ligand effect on the electronic properties and the reactivity of dinuclear gold and molybdenum systems (Scheme 1.4) used as platforms for the understanding of multielectron redox chemistry.

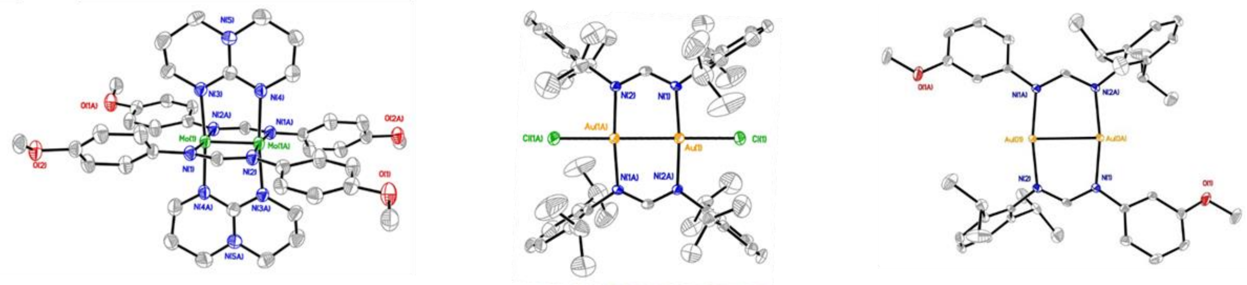

$Mo_2(hpp)_n(DAniF)_{4-n}$ $Au_2L_2Cl_n$ (n = 0, 2) $Au_2(ArNCHNAr')_2$

Scheme 1.4. Dinuclear gold and molybdenum systems studied in Chapters 5 and 6. The ligand effect on the electronic properties of these complexes was analyzed.

Chapter 2: Hydrogen Gas Generation by a Metal-Free Fluorinated Porphyrin[1]

2.1 INTRODUCTION

In this chapter electrocatalytic generation of hydrogen gas from acidic organic solutions using a free-base perfluorinated porphyrin and the mechanistic studies through both spectroscopic and computational approaches are described. Metalloporphyrins have been well investigated for their ability to generate H_2 both electrochemically and photochemically.[35,37,51–54] In metallated HER electrocatalysts, the metal center is the active site in the hydrogen production process by participating in the formation of metal-hydrogen bonds and as the redox center in the multi-electron reduction process.[41,52,55,56] In comparison, free-base porphyrins are known to exhibit rich multi-electron redox chemistry.[57,58] The two basic imine nitrogen atoms in the porphyrin core can produce a diprotonated porphyrin species.[59,60] Thus, free-base porphyrins have the ability to form covalent nitrogen-hydrogen bonds and can also be electrochemically active. In addition, the four-nitrogen porphyrin core is perfectly suited for bringing protons in close proximity to lower the activation energy of dihydrogen production by prearranging the transition state of hydrogen-hydrogen bond formation. However, whether a molecular metal-free porphyrin has the ability to perform similar and comparable electrocatalytic HER activity to the existing well-studied metallated macrocyclic complexes has not yet been studied or reported. Organic-based hydrogen generation catalysts may provide superior synthetic flexibility, lower manufacturing costs, and greater chemical stability.

In this work we show that free-base meso-tetra(pentafluorophenyl)porphyrin, **1**, is a HER electrocatalyst in the presence of p-toluenesulfonic (tosic) acid as the proton source with THF as

---

[1] This chapter is excerpted with permission from a published article: Yanyu Wu, Nancy Rodríguez-López, Dino Villagrán; Hydrogen Gas Generation by a Metal-Free Fluorinated Porphyrin. *Chemical Science*, **2018**, 9, 4689-4695.

the solvent. The electrocatalytic activity of **1** was estimated by electrochemical studies and H_2 gas analysis in acidic solutions. Spectroscopic measurements including UV-Vis spectra and spectroelectrochemical studies reveal the spectral signatures of the intermediates during the catalysis giving insight into the mechanism of hydrogen generation. In addition, density functional theory (DFT) calculations were performed to provide further support to the mechanistic HER behavior of **1**.

2.2 EXPERIMENTAL SECTION

2.2.1 Materials.

All reagents used for synthesis were purchased from Sigma Aldrich. Pyrrole was freshly distilled prior to use. Solvent used for electrochemical studies were dried and degassed through a Pure Process Technology solvent purification system. Tetrabutylammonium hexafluorophosphate ($TBAPF_6$) and tosic acid were purchased from Acros Organic. Meso-tetra(pentafluorophenyl)porphyrin and meso-tetraphenylporphyrin were synthesized according to Lindsey's method.[61]

2.2.2 Synthesis of meso-tetra(pentafluorophenyl)porphyrin, 1.

Pentafluorobenzaldehyde (3.00 g, 0.0153 mol) was dissolved in 500 mL of DCM, followed by addition of pyrrole (1.04 g, 0.0153 mol) dropwise. The mixture was stirred and bubbled with N_2 for 15 minutes. Next, 0.500 mL of $BF_3{\cdot}Et_2O$ was added with a glass syringe without exposing to air. After 2 h, the resulting porphyrinogen was oxidized by adding 2,3-dichloro-5,6-dicyanobenzoquinone (DDQ) (5.00 g, 0.0220 mol) and letting it react for 30 minutes. Compound **1** (1.80 g, 24.3% yield) was obtained after recrystallization and column chromatography purification on silica gel eluted with a mixture of hexane and dichloromethane (2:1). ^1H NMR

(C_6D_6): 8.71 ppm (s, 8H), –2.10 ppm (s, 2H); ^{19}F NMR (C_6D_6): –161.3 ppm (t, 2F), –150.5 ppm (t, 1F), –137.2 ppm (d, 2F); ESI-MS: m/z: 975.5; UV-Vis (THF): λ max 408, 503, 543, 584, 634 nm.

2.2.3 Cyclic voltammetry.

All electrochemical measurements were obtained by using a CHI760D potentiostat, with 0.1 M $TBAPF_6$ as supporting electrolyte. The electrolyte was recrystallized three times in ethanol prior to use. Tosic acid was placed under vacuum and oven dried prior to use. All cyclic voltammograms were obtained in a dry N_2-filled glovebox, using a 4 mm diameter glassy carbon working electrode, Pt mesh auxiliary counter electrode and an Ag/Ag^+ reference electrode. Ferrocene (Fc) was added after each measurement as an internal standard.

2.2.4 Controlled-potential electrolysis and H_2 detection.

Controlled-potential electrolysis was done in a custom-built two-compartment gas-tight electrochemical cell under argon atmosphere. One part of the cell contains: (I) a carbon rod working electrode (3 mm diameter, 0.95 mm length); (II) Ag/Ag^+ reference electrode; (III) gas inlet and gas outlet. The other part of the cell contains a Pt auxiliary wire counter electrode and gas outlet. The working and counter electrodes are separated through a glass frit. Electrolysis was carried out at –1.7 V vs Fc/Fc^+ in THF, containing 0.1 M $TBAPF_6$, 10 mM tosic acid with and without adding the catalyst.

2.2.5 Spectroelectrochemistry.

Spectroelectrochemistry was performed using an optical transparent 1 mm thin-layer spectroelectrochemical cell containing an Au gauze working electrode, non-aqueous Ag/Ag^+ reference electrode and Pt wire counter electrode. The absorption spectra were recorded in a UV-

Vis spectrophotometer while the bulk electrolysis was performed by the CHI760D potentiostat. Solutions of **1** containing 0.1 M $TBAPF_6$ with and without acid were prepared and degassed with N_2 before each measurement. The changes of the UV-Vis spectra were recorded at one second interval for 10 minutes at different applied potentials.

2.2.6 Overpotential Calculation.

The overpotential is calculated through $|E_{H+} - E_{cat/2}|$, where E_{H+} is the equilibrium potential of H^+/H_2 of tosic acid in THF and $E_{cat/2}$ is the potential at $i_{cat/2}$. E_{H+} is equal to the open circuit potential of tosic acid in THF solution using a platinum electrode at 1 atm hydrogen gas atmosphere.

2.2.7 Other physical methods.

^1H NMR and ^{19}F NMR spectra were recorded on a JEOL 600 MHz NMR spectrometer. Proton NMR spectrum was referenced to the residual deuterated solvent signal as an internal calibration (C_6D_6 = 7.16 ppm). The UV-Vis spectra were recorded on a SEC2000 spectra system equipped with a VISUAL SPECTRA 2.1 software.

2.3 COMPUTATION DETAILS

The molecular geometries of the free base porphyrin and porphyrin derivatives (Figure 2.1) were optimized using density functional theory (DFT). The DFT method employed was Becke's[62] three parameter hybrid exchange functional, coupled with the Lee-Yang-Parr[63] nonlocal correlational functional (B3LYP) for all calculations. The 6-31+G[64,65] Pople basis set, as implemented in Gaussian 09, was used for all atoms.[66] Zero point energies and thermodynamic data were calculated at 298.15 K and 1 atm by performing frequency calculations. Calculations were performed on the optimized gas-phase geometries using the solvation model based on density (SMD) as implemented in the Gaussian 09 suite.[67–69]

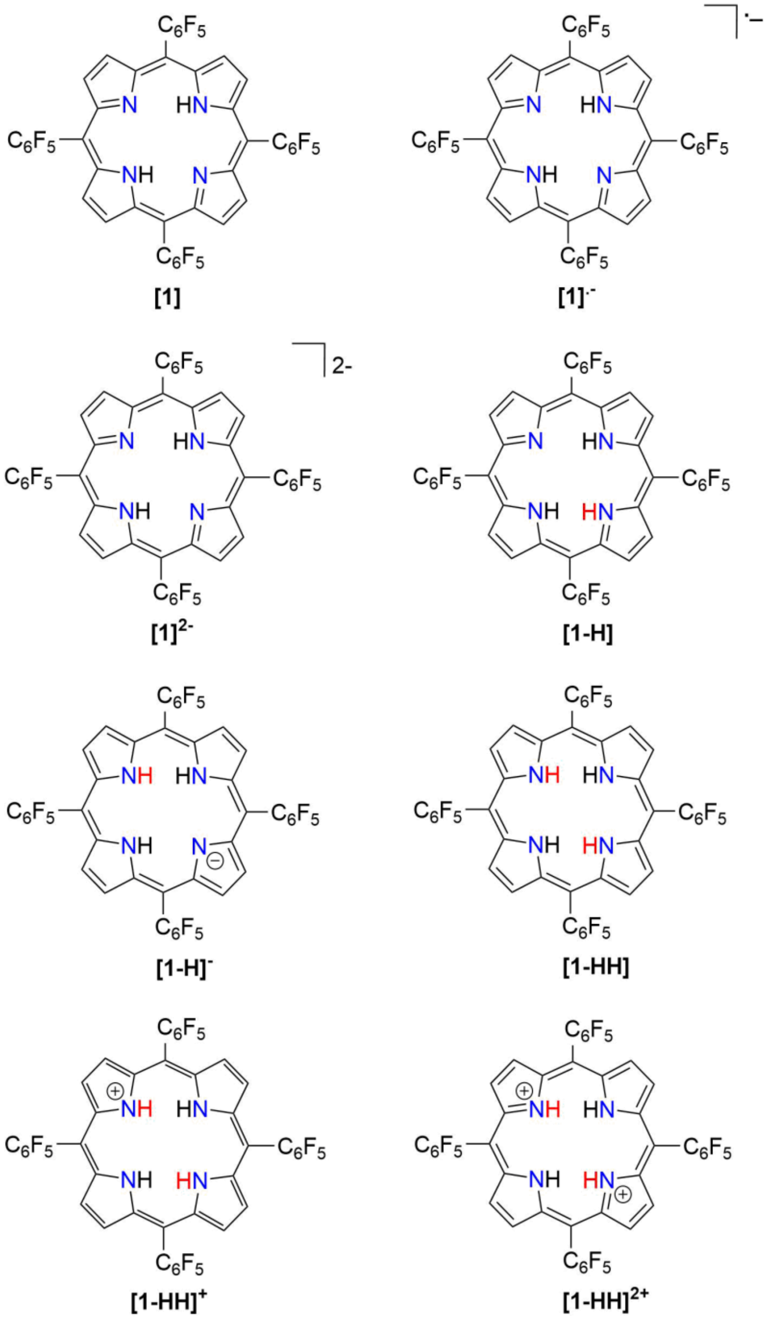

[1] **$[1]^{\bullet -}$**

$[1]^{2-}$ **[1-H]**

$[1\text{-H}]^{-}$ **[1-HH]**

$[1\text{-HH}]^{+}$ **$[1\text{-HH}]^{2+}$**

Figure 2.1. Porphyrin derivatives involved in the proposed mechanistic pathways for hydrogen generation.

In order to ease the computational expense a model in which the pentafluorophenyl groups are replaced with chlorine atoms was employed. This substitution is reasonable due to the similar electron-withdrawing ability of Cl compared to -C_6F_5 as supported by their Hammett substitution constants (Table 2.1). We followed several theoretical models[35,36,38,54,70–75] for the determination of thermodynamic quantities such as reduction potentials and p*K*a's so as to give insight on the hydrogen evolution mechanism.

Table 2.1. Hammett constants for substituents.[76]

Substituent	σ_m	σ_p
C_6F_5	0.26	0.27
Cl	0.37	0.23
F	0.34	0.06

2.3.1 Calculation of reduction free energies.

From a Born-Haber thermodynamic cycle (Figure 2.2**Figure**), we can associate the reaction free energies with the gas-phase and solvation energies using equation 2.7:

$$\Delta G^\circ_{(sol)} = \Delta G^\circ_{(g)} + \Delta G^\circ_{solv}(Red) - \Delta G^\circ_{solv}(Ox) - \Delta G^\circ_{solv}(e^-) \qquad \text{Eq 2.7}$$

where $\Delta G^\circ_{solv}(Red)$ and $\Delta G^\circ_{solv}(Ox)$ represent the free energies upon solvation for both the reduced and oxidized species, $\Delta G^\circ_{solv}(e^-)$ the contribution of the electron to the solvation free energy, and $\Delta G^\circ_{(g)}$ the free energy of the reaction in the gas phase. We can calculate the last value with the expression $\Delta G^\circ_{(g)} = \Delta H^\circ_{(g)} - T\Delta S^\circ_{(g)}$. Calculation of $\Delta G^\circ_{(sol)}$, allows the determination of redox potentials using equation 2.8:

$$E^\circ = (-\Delta G^\circ_{sol} / nF) + E^\circ_{ref} \qquad \text{Eq 2.8}$$

where E° is the standard reduction potential, F is the Faraday constant and n is the number of electrons involved is the redox reaction. In order to allow a direct comparison of calculated vs experimental data, the redox potentials are reported referenced to the Ferrocene/Ferrocenium (Fc/Fc^{+}) couple.

$$\begin{tikzcd}
\mathrm{Ox}\ (g) \arrow[d, "\Delta G^{o}_{solv}\ (ox)"] & + & e^{-}\ (g) \arrow[d, "\Delta G^{o}_{solv}\ (e^{-})"] \arrow[r, "\Delta G^{o}\ (g)"] & \mathrm{Red}\ (g) \arrow[d, "\Delta G^{o}_{solv}\ (Red)"] \\
\mathrm{Ox}\ (sol) & + & e^{-}\ (sol) \arrow[r, "\Delta G^{o}\ (sol)"'] & \mathrm{Red}\ (sol)
\end{tikzcd}$$

Figure 2.2. Born-Haber thermodynamic cycle for the calculation of the free energy of reduction.

2.3.2 Calculation of proton dissociation free energies.

The direct calculation of reaction free energies in solution cannot be performed because the free energy of the solvated proton is difficult to calculate with accuracy. In order to calculate the thermodynamic value, we need to consider a proton-exchange reaction between a reference compound (AH) and the free base porphyrin (1):

$$A^{-} + 1\text{-}H^{+} \rightarrow AH + 1 \qquad \text{Eq 2.9}$$

Herein, we define the free energy change of reaction (2.9) as $\Delta G°_{(sol)}$. To calculate $\Delta G°_{(sol)}$, we must relate it to the free energy in the gas phase using the thermodynamic cycle depicted in Figure 2.3, obtaining the following equation:

$$\Delta G°_{(sol)} = \Delta G°_{(g)} + \Delta G°_{solv}(AH) + \Delta G°_{solv}(1) - \Delta G°_{solv}(A^{-}) - \Delta G°_{solv}(1\text{-}H^{+}) \qquad \text{Eq 2.10}$$

where $\Delta G°_{solv}(A^{-})$, $\Delta G°_{solv}(1\text{-}H^{+})$, $\Delta G°_{solv}(AH)$ and $\Delta G°_{solv}(1)$ are the free energies upon solvation of the referenced conjugated base, the protonated porphyrin, the referenced acid and the porphyrin, respectively. We can calculate $\Delta G°_{(g)}$ by the expression $\Delta G°_{(g)} = \Delta H°_{(g)} - T\Delta S°_{(g)}$. The pK_a can be calculated from $\Delta G°_{(sol)}$ by:

$$pK_a = (\Delta G^{\circ}_{sol} / 2.303\ RT) + pK_{a(ref)} \qquad \text{Eq 2.11}$$

where R is the gas constant, T is the temperature (298.15 K), and $pK_{a(ref)}$ is the experimentally reported pK_a of the reference reaction. Since the deprotonation of acetic acid has been studied in THF and the pK_a value is available, we chose this reaction as our reference.[77]

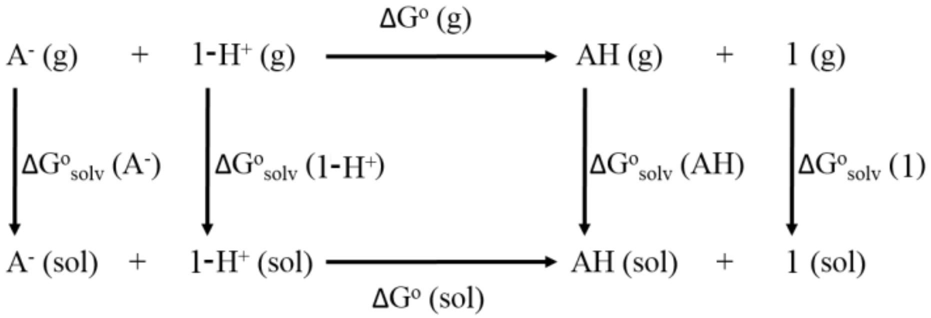

Figure 2.3. Born-Haber thermodynamic cycle for the calculation of the free energy of proton transfer.

2.4 RESULTS AND DISCUSSIONS

Cyclic voltammetry experiments were conducted in THF in order to assess the electrocatalytic activity of **1**. In the absence of acid, 1 features two reversible one-electron reductions at $E_{1/2} = -1.14$ V and $E_{1/2} = -1.54$ V vs Fc/Fc$^+$ that yield the porphyrin radical anion $[\mathbf{1}]^{\cdot-}$ and the dianion species $[\mathbf{1}]^{2-}$, respectively (Figure 2.4). Upon successive addition of tosic acid, the first reduction wave of **1** remains unchanged while a catalytic wave appears at a potential near –1.31 V vs Fc/Fc$^+$, which occurs before the second reduction wave of 1 at –1.54 V. This indicates that protonation of this porphyrin is not possible under these conditions prior to the one-electron reduction. The reduction potential of H^+/H_2 (E_{H+}) with tosic acid in THF is –0.605 V vs Fc/Fc$^+$, which corresponds to an overpotential of 1.02 V.[77,78] Notably, addition of acid without the presence of **1** shows negligible current increase.

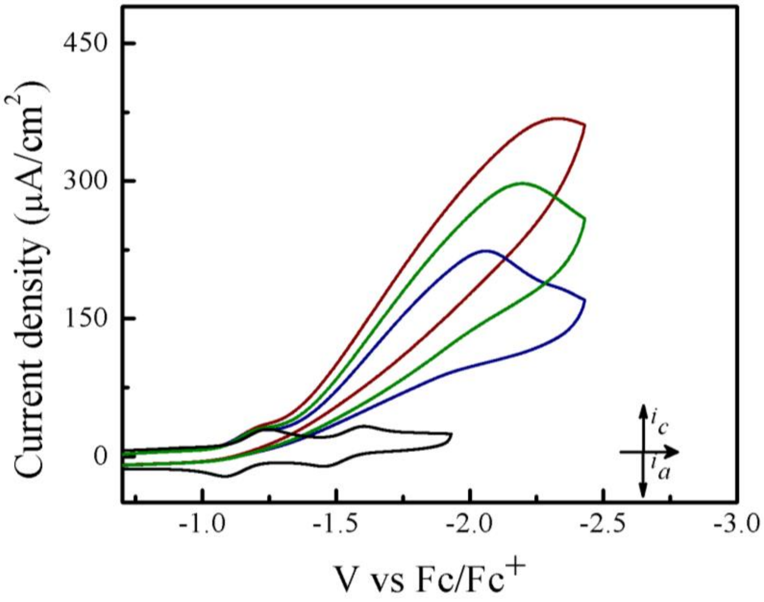

Figure 2.4. Cyclic voltammograms of 0.1 mM **1** in a solution containing 0.1 M $TBAPF_6$ with and without tosic acid: (from bottom to top): 0 equiv acid, 4 equiv acid, 9 equiv acid, and 12 equiv acid. Scan rate: 100 mV/s; glassy carbon working electrode.

As a control, a second metal-free porphyrin, meso-tetraphenylporphyrin was also evaluated as HER electrocatalyst using tosic acid as the proton source. The electrocatalytic current achieved by this porphyrin was very low (Onset potential: –1.89 V vs. Fc/Fc^+; Peak current: 18 μA. See Figure 2.5). Hydrogen gas production was confirmed by Gas Chromatography through the evaluation of the gas product obtained from controlled potential electrolysis.

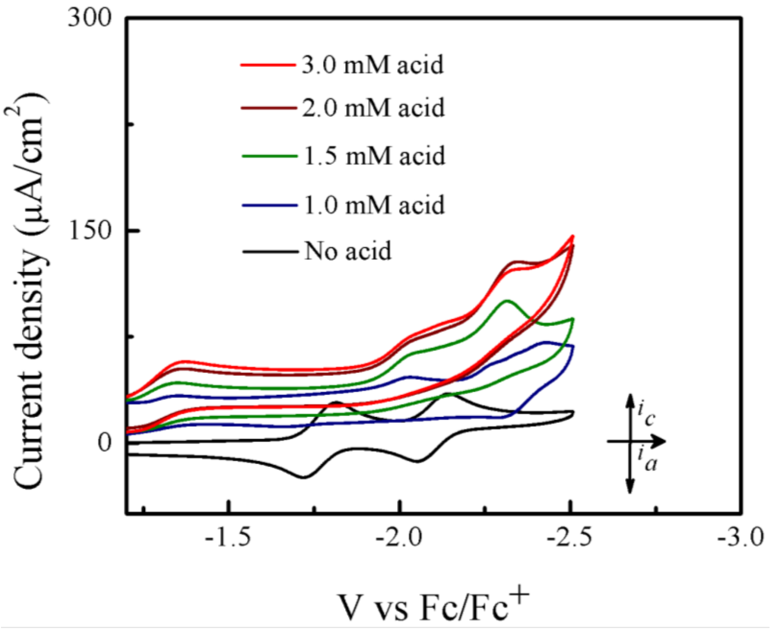

Figure 2.5. Cyclic voltammograms of meso-tetraphenylporphyrin with 0.1 M $TBAPF_6$ in THF and titrating with tosic acid: 100 mV/s; glassy carbon working electrode.

In order to investigate whether there is a formation of a heterogeneous metal-free porphyrin thin film on the working electrode, which can be responsible for HER activity, cyclic voltammograms were obtained using a glassy carbon electrode after performing controlled-potential electrolysis. Two glassy carbon electrodes were subjected to 1 h of electrolysis in the presence of **1** with and without tosic acid, respectively. After the experiment, the electrodes were rinsed with THF and dried in air. Then they were exposed to fresh acidic solutions (1.5 mM) without the addition of **1**. In neither case the working electrode shows any increase of catalytic current (Figures 2.6 and Figure 2.7), implying that **1** does not adsorb on the working electrode surface during our electrochemical studies.

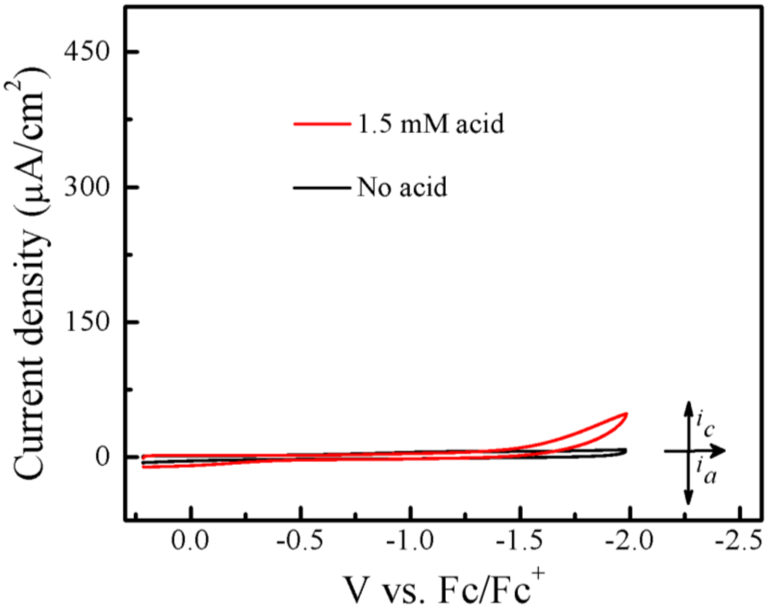

Figure 2.6. Cyclic voltammograms recorded using the rinsed glassy carbon electrode after performing bulk electrolysis in the presence of 0.1 mM **1** at –1.7 V vs. Fc/Fc$^+$ for an hour. Scan rate: 100 mV/s; glassy carbon working electrode.

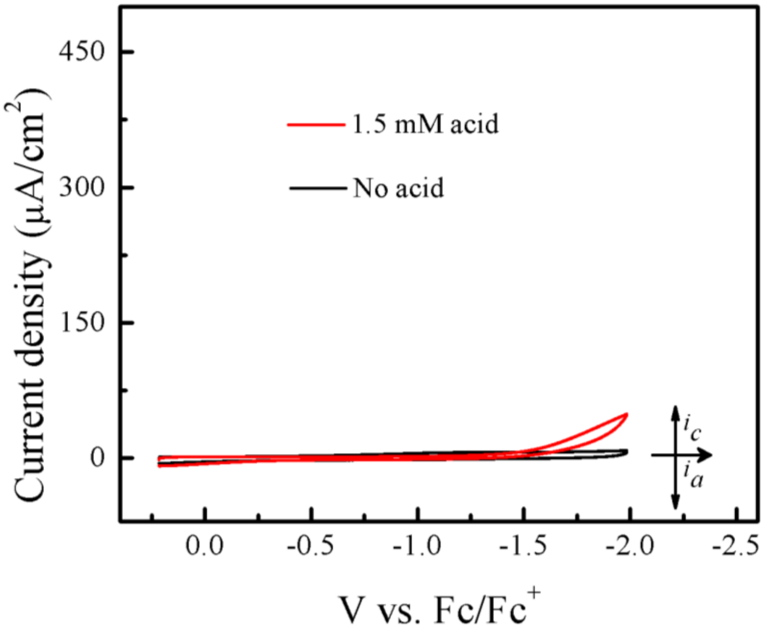

Figure 2.7. Cyclic voltammograms recorded using the rinsed glassy carbon electrode after performing bulk electrolysis in the presence of 0.1 mM **1** and 10 equiv tosic acid at –1.7 V vs. Fc/Fc$^+$ for 1 h. Scan rate: 100 mV/s; glassy carbon working electrode.

The HER mechanism of **1** was probed through spectroscopic techniques. When two protons and two electrons are involved, several different pathways can be followed in order to generate hydrogen. The following possible sequential mechanistic steps were considered: *E-E-P-P*, *E-P-E-P*, *E-P-P-E*, *P-E-E-P*, *P-E-P-E*, and *P-P-E-E*, where *E* stands for reduction and *P* stands for protonation. In THF, **1** exhibits a narrow and intense absorbance in the typical Soret (375-425 nm) region and four small Q-bands between 470 and 650 nm. Upon titration of tosic acid, the electronic spectrum remains constant (Figure 2.8). This indicates that in THF, tosic acid is not strong enough to protonate **1**, suggesting that the first step of hydrogen generation is a reduction.

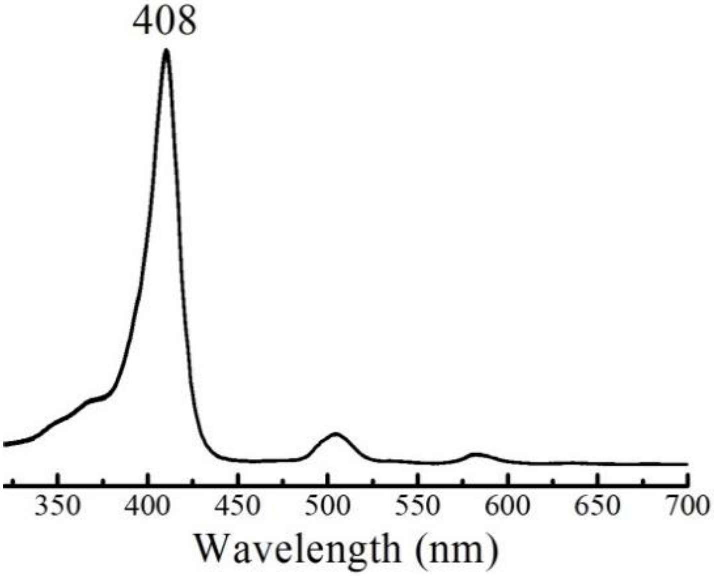

Figure 2.8. UV-Vis spectrum of **1** in THF containing 0.1 M $TBAPF_6$ before and after titrating with tosic acid.

The UV-vis spectrum of **1** upon controlled-potential bulk electrolysis at the potential of the first one-electron reduction of the porphyrin (–1.35 V vs Fc/Fc^+), shows a decrease of the Soret (408 nm) and Q-bands (503, 530, 584, 634 nm); and the appearance of an absorption band at 436 nm along with an isosbestic point at 428 nm. This new band can be attributed to the generation of the radical anion $[\mathbf{1}]^{\bullet-}$ (Figure 2.9a). Under the same controlled potential of –1.35 V vs Fc/Fc^+ but in the presence of tosic acid, the band at 436 nm corresponding to the radical anion $[\mathbf{1}]^{\cdot-}$ is also seen but the isosbestic point at 428 nm disappears as a function of time (Figure 2.9b). This implies that in addition to the generation of the radical anion $[\mathbf{1}]^{\cdot-}$, other chemical species are also produced. Since the only condition changed between Figure 2.9a and Figure 2.9b is the addition of acid, the second step of the catalytic cycle should be assigned to a protonation after the one-electron reduction.

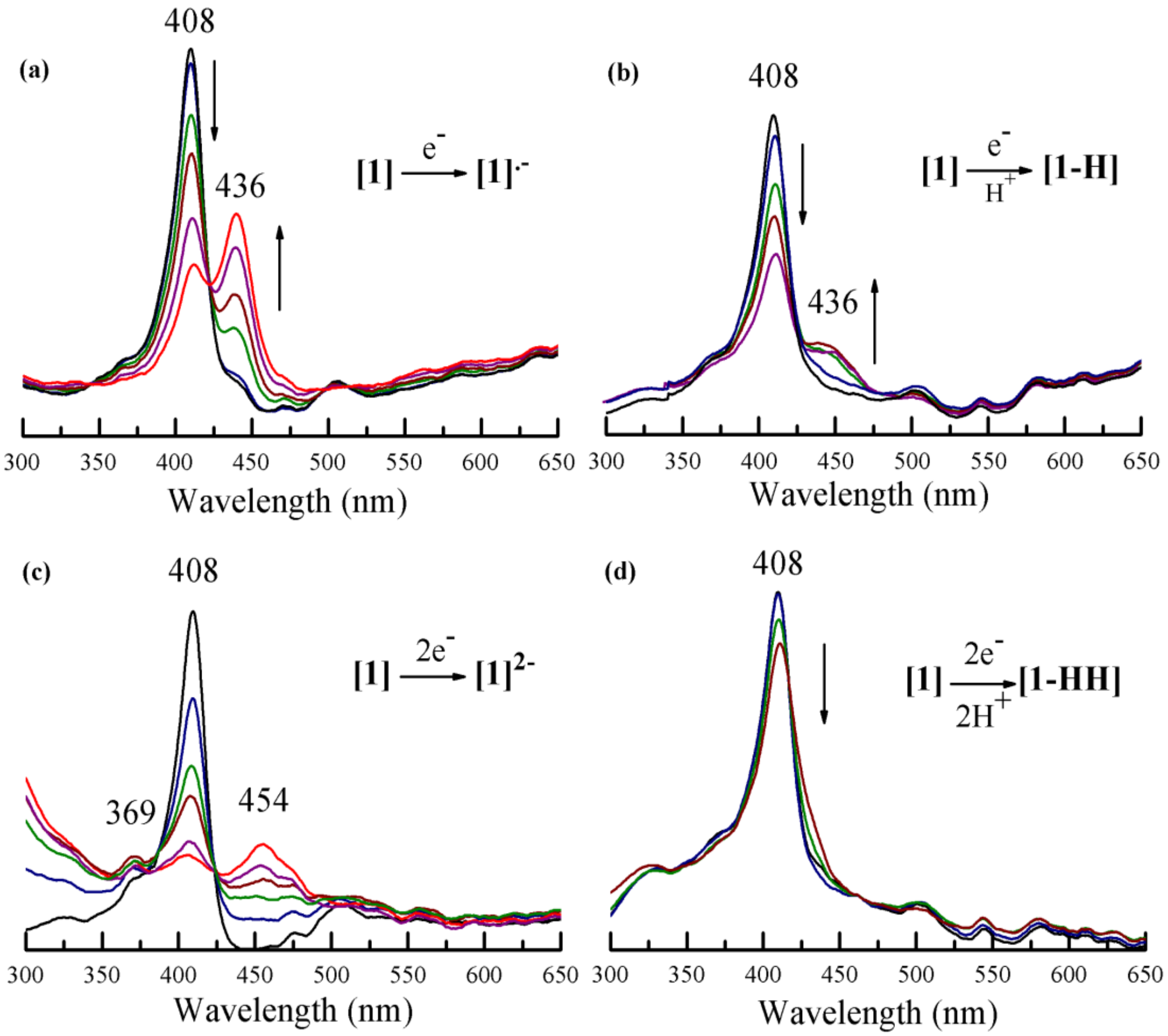

Figure 2.9. UV-Vis spectroelectrochemistry of **1** in the absence and in the presence of tosic acid containing 0.1 M $TBAPF_6$ in THF: (a) **1** at –1.35 V; (b) **1** containing tosic acid at –1.35 V; (c) **1** at –1.7 V; (d) **1** containing tosic acid at –1.7 V. (Potentials are referred vs Fc/Fc$^+$ couple)

When performing bulk electrolysis at the potential above the second electron reduction wave (–1.7 V vs Fc/Fc$^+$) without the presence of acid, the recorded spectrum (Figure 2.9c) shows an immediate decay of the Soret absorbance coupled to an increase of a broad absorbance at 454 nm, a new band at 369 nm and another new band in the ultraviolet region (300 nm), along with an isosbestic point at 425 nm. This features the transformation from the free-base porphyrin [**1**] to the dianion species [**1**]$^{2-}$. When bulk electrolysis was conducted at the same potential (–1.7 V vs Fc/Fc$^+$) in the presence of tosic acid, the absorbance belonging to the dianion [**1**]$^{2-}$ is not observed and only a decrease of the Soret absorbance occurs (Figure 2.9d). However, the rate of decay of the Soret band in the presence of acid is slower compared to that without acid (Figure 2.10). This suggests that **1** is regenerated upon H_2 production. Overall these spectroscopy studies show that the first and second events of the mechanism of hydrogen generation with **1** in the presence of tosic acid are reduction and protonation, respectively.

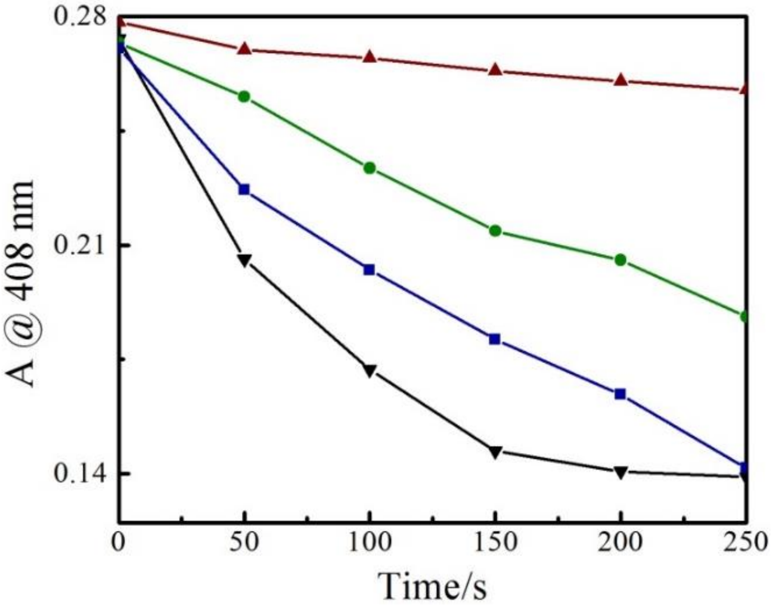

Figure 2.10. Change of absorption of **1** at 408 nm over time during electrolysis containing 1 M $TBAPF_6$ in THF. (From bottom to top) (▼) –1.7 V without acid; (■) –1.35V without acid; (●) –1.35 V with tosic acid); (▲) –1.7 V with tosic acid (Potentials referred to Fc/Fc$^+$).

Thermodynamic theoretical calculations were also performed to provide further insight of the next steps of hydrogen generation. Scheme 2.1 shows the three different pathways for hydrogen generation in THF after the first reduction, and Figure 2.11 shows the calculated relative free energies corresponding to each of these pathways. The calculated relative free energies are plotted relative to the tosic acid/dihydrogen (TsOH/H_2) couple.

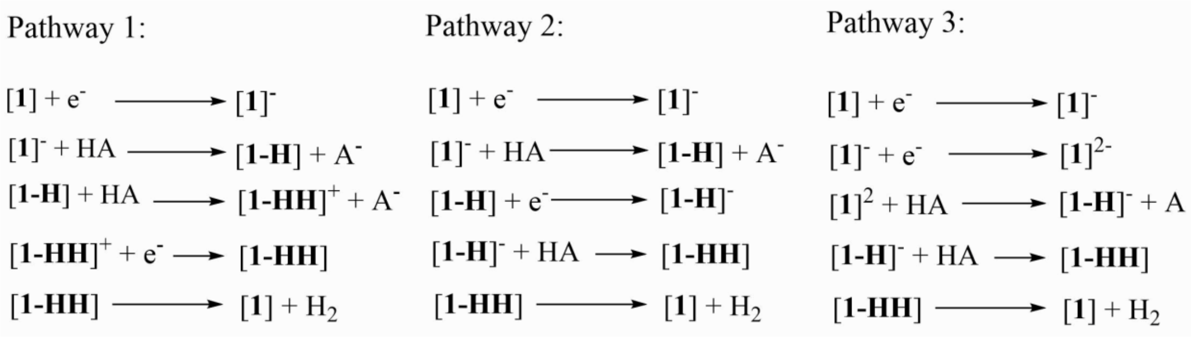

Pathway 1:

$[\mathbf{1}] + e^- \longrightarrow [\mathbf{1}]^-$

$[\mathbf{1}]^- + HA \longrightarrow [\mathbf{1\text{-}H}] + A^-$

$[\mathbf{1\text{-}H}] + HA \longrightarrow [\mathbf{1\text{-}HH}]^+ + A^-$

$[\mathbf{1\text{-}HH}]^+ + e^- \longrightarrow [\mathbf{1\text{-}HH}]$

$[\mathbf{1\text{-}HH}] \longrightarrow [\mathbf{1}] + H_2$

Pathway 2:

$[\mathbf{1}] + e^- \longrightarrow [\mathbf{1}]^-$

$[\mathbf{1}]^- + HA \longrightarrow [\mathbf{1\text{-}H}] + A^-$

$[\mathbf{1\text{-}H}] + e^- \longrightarrow [\mathbf{1\text{-}H}]^-$

$[\mathbf{1\text{-}H}]^- + HA \longrightarrow [\mathbf{1\text{-}HH}]$

$[\mathbf{1\text{-}HH}] \longrightarrow [\mathbf{1}] + H_2$

Pathway 3:

$[\mathbf{1}] + e^- \longrightarrow [\mathbf{1}]^-$

$[\mathbf{1}]^- + e^- \longrightarrow [\mathbf{1}]^{2-}$

$[\mathbf{1}]^2 + HA \longrightarrow [\mathbf{1\text{-}H}]^- + A$

$[\mathbf{1\text{-}H}]^- + HA \longrightarrow [\mathbf{1\text{-}HH}]$

$[\mathbf{1\text{-}HH}] \longrightarrow [\mathbf{1}] + H_2$

Scheme 2.1. Mechanistic pathways proposed for hydrogen generation in THF, with tosic acid as proton source.

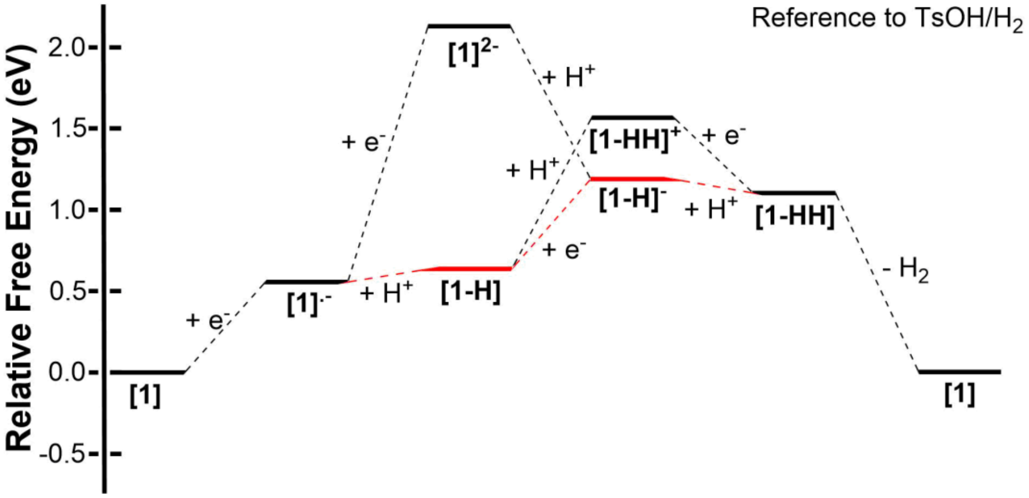

Figure 2.11. Free energy diagram of H_2 evolution catalyzed by **1** in THF with tosic acid, as calculated by the Born-Haber cycles shown in Figure 2.2 and Figure 2.3. The free energies are plotted relative to the tosic acid/dihydrogen (TsOH/H_2) couple.

The relative free energy difference from [**1**] to [**1**]$^{\bullet-}$ is calculated to be 12.8 kcal/mol (+0.556 eV) which corresponds to a potential of –1.06 V vs Fc/Fc^{+}. Upon the first reduction, [**1**]$^{\bullet-}$ can follow two possible paths: it can be either further reduced to [**1**]$^{2-}$ or protonated at the N core by tosic acid to yield [**1-H**]. Protonation to generate [**1-H**] is thermodynamically favored with a relative free energy of +2.39 kcal/mol (+0.104 eV), compared to going uphill +36.3 kcal/mol (+1.57 eV) to form [**1**]$^{2-}$.

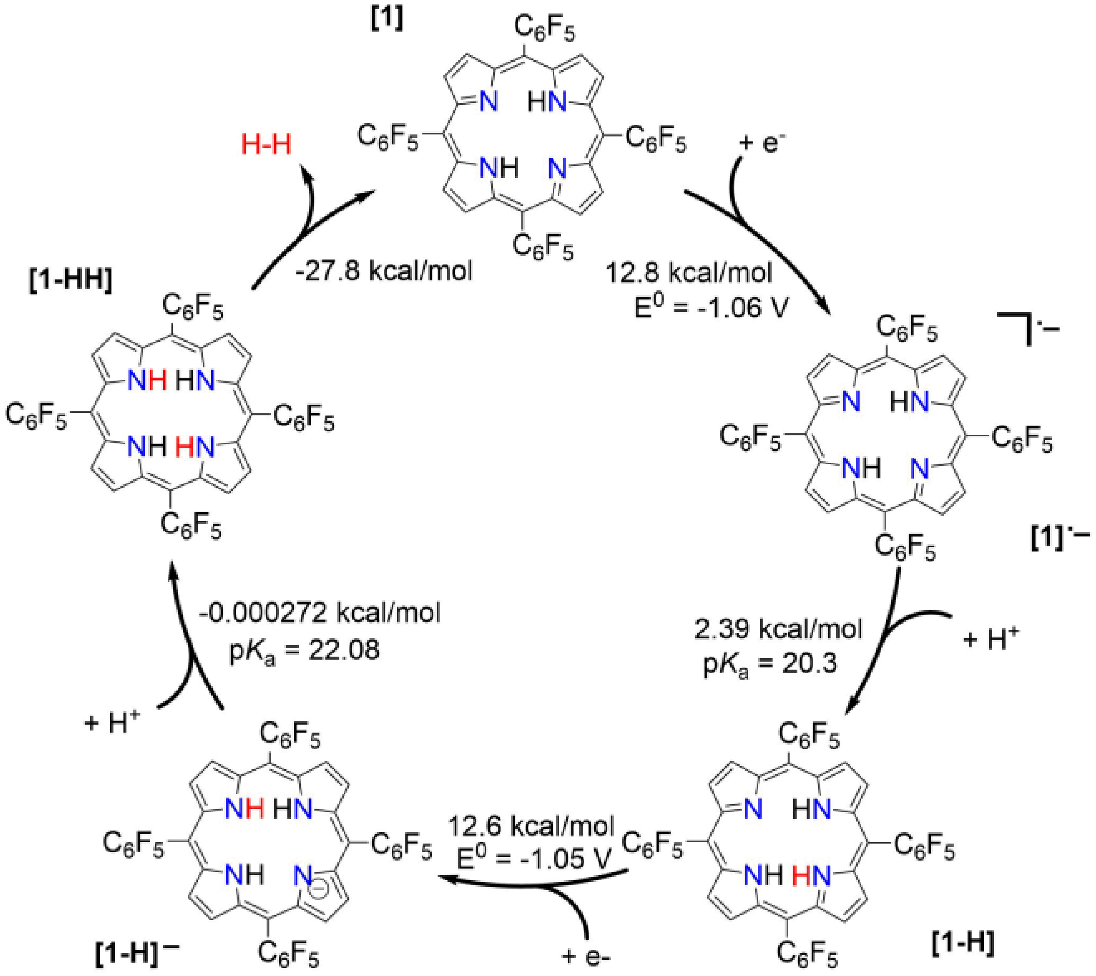

Scheme 2.2. Proposed catalytic cycle for H_2 evolution, following an *E-P-E-P* mechanism, with THF as solvent.

The calculated relative pK_a for the deprotonation of [**1-H**] is 20.3. Since the pK_a of tosic acid in THF is predicted to be 11.8, the reduced porphyrin is likely to get protonated. The first two steps of the proposed mechanism (*E*-*P*) are in agreement with our experimental observations. The next step can either be electron transfer or protonation, to yield [**1-H**]$^-$ or [**1-HH**]$^+$, respectively. While we cannot experimentally discern between these two pathways, [**1-H**]$^-$ is calculated to be thermodynamically favored by 8.91 kcal/mol when compared to generating [**1-HH**]$^+$. The following step yields [**1-HH**], which putatively produces H_2, and closes the cycle. The overall proposed mechanism is described by Scheme 2.2. Calculated relative pK_a's and redox potentials for all possible mechanistic pathways for H_2 generation are presented in Table 2.2. Additional benchmarking was performed with B3P86 and M062X functionals to evaluate the mechanistic pathways of hydrogen evolution using **[1]** as electrocatalyst. In addition, geometry optimizations were done using 6-31G**, and 6-311G** basis sets were assessed with all functionals. Table 2.3 and Table 2.4 display all thermodynamic parameters gather.

Table 2.2. Calculated redox potentials and pK_a's in THF using 6-31+G as basis set, values in parentheses correspond to the experimental values obtained in this work.

	6-31+G					
	B3LYP	**B3P86**	**M062X**	**B3LYP**	**B3P86**	**M062X**
Reaction	**E° (V vs Fc/Fc$^+$)**			**pK_a**		
$TsOH + AcO^- \rightarrow TsO^- + AcOH$				11.8	10.8	11.2
$[1] + e^- \rightarrow [1]^{\cdot -}$	–1.06 (–1.14)^a	-0.95	-1.10			
$[1]^{\cdot -} + e^- \rightarrow [1]^{2-}$	–2.08 (–1.54)^a	-1.99	-1.60			
$[1\text{-H}]^- + AcO^- \rightarrow [1]^{2-} + AcOH$				37.7	35.3	34.7
$[1\text{-HH}] + AcO^- \rightarrow [1\text{-H}]^- + AcOH$				22.1	21.6	21.0
$[1\text{-H}]^+ + AcO^- \rightarrow [1] + AcOH$				5.9	3.5	3.9
$[1\text{-HH}]^{2+} + AcO^- \rightarrow [1\text{-H}]^+ + AcOH$				–9.5	-11.1	-9.6
$[1\text{-H}]^+ + e^- \rightarrow [1\text{-H}]$	–0.21	-0.08	-0.20			
$[1\text{-HH}]^{2+} + e^- \rightarrow [1\text{-HH}]^+$	0.73	0.85	0.80			
$[1\text{-HH}]^+ + e^- \rightarrow [1\text{-HH}]$	–0.12	0.02	-0.05			
$[1\text{-H}] + e^- \rightarrow [1\text{-H}]^-$	–1.05	-0.99	-1.00			
$[1\text{-H}] + AcO^- \rightarrow [1]^{\cdot -} + AcOH$				20.3	18.3	19.6
$[1\text{-HH}]^+ + AcO^- \rightarrow [1\text{-H}] + AcOH$				6.3	4.6	5.2

[a] Experimental value

Table 2.3. Calculated redox potentials and pK_a's in THF using 6-31G** as basis set, values in parentheses correspond to the experimental values obtained in this work.

	6-31G**					
	B3LYP	**B3P86**	**M062X**	**B3LYP**	**B3P86**	**M062X**
Reaction	**E° (V vs Fc/Fc$^+$)**			**pK_a**		
TsOH + AcO$^-$ → TsO$^-$ + AcOH				13.5	13.9	13.6
[1] + e$^-$ → [1]$^{\cdot-}$	-1.08	-0.78	-0.88			
[1]$^{\cdot-}$ + e$^-$ → [1]$^{2-}$	-1.94	-1.85	-1.95			
[1-H]$^-$ + AcO$^-$ → [1]$^{2-}$ + AcOH				24.6	24.3	24.8
[1-HH] + AcO$^-$ → [1-H]$^-$ + AcOH				11.5	11.1	11.3
[1-H]$^+$ + AcO$^-$ → [1] + AcOH				7.93	-9.2	7.2
[1-HH]$^{2+}$ + AcO$^-$ → [1-H]$^+$ + AcOH				11.5	-23.5	13.5
[1-H]$^+$ + e$^-$ → [1-H]	-0.15	0.13	-0.13			
[1-HH]$^{2+}$ + e$^-$ → [1-HH]$^+$	0.86	1.20	1.10			
[1-HH]$^+$ + e$^-$ → [1-HH]	0.15	0.24	0.14			
[1-H] + e$^-$ → [1-H]$^-$	-0.92	-0.83	-0.93			
[1-H] + AcO$^-$ → [1]$^{\cdot-}$ + AcOH				16.3	17.1	16.1
[1-HH]$^+$ + AcO$^-$ → [1-H] + AcOH				-6.63	-7.05	-6.05

Table 2.4. Calculated redox potentials and pK_a's in THF using 6-311G** as basis set, values in parentheses correspond to the experimental values obtained in this work.

	6-311G**					
	B3LYP	**B3P86**	**M062X**	**B3LYP**	**B3P86**	**M062X**
Reaction	**E° (V vs Fc/Fc$^+$)**			**pK_a**		
TsOH + AcO$^-$ → TsO$^-$ + AcOH				11.7	10.9	11.4
[1] + e$^-$ → [1]$^{\cdot-}$	–1.04	-0.97	-1.15			
[1]$^{\cdot-}$ + e$^-$ → [1]$^{2-}$	–2.06	-2.01	-1.65			
[1-H]$^-$ + AcO$^-$ → [1]$^{2-}$ + AcOH				37.6	35.4	34.9
[1-HH] + AcO$^-$ → [1-H]$^-$ + AcOH				22.0	21.7	21.2
[1-H]$^+$ + AcO$^-$ → [1] + AcOH				5.8	3.6	4.1
[1-HH]$^{2+}$ + AcO$^-$ → [1-H]$^+$ + AcOH				–9.4	-11.2	-9.8
[1-H]$^+$ + e$^-$ → [1-H]	–0.19	-0.10	-0.25			
[1-HH]$^{2+}$ + e$^-$ → [1-HH]$^+$	0.71	0.87	0.85			
[1-HH]$^+$ + e$^-$ → [1-HH]	–0.11	0.04	-0.10			
[1-H] + e$^-$ → [1-H]$^-$	–1.03	-1.01	-1.05			
[1-H] + AcO$^-$ → [1]$^{\cdot-}$ + AcOH				20.2	18.2	19.8
[1-HH]$^+$ + AcO$^-$ → [1-H] + AcOH				6.2	4.7	5.4

Hydrogen production by **[P]** in MeCN is mechanistically different from that in THF with tosic acid. Experimentally, under acidic media the dication species **[P-HH]**$^{2+}$ is observed with a red shifted Soret band at 429 nm upon addition of tosic acid. Protonation of the porphyrin ring have been well studied. In acidic conditions, the macrocycle could exits as the free base **[P]**, monocation **[P-H]**$^{+}$ or dication **[P-HH]**$^{2+}$ species.[79–82] It is suggested that monoprotonation of the porphyrin ring requires the break of the planarity (Figure 2.12) of the macrocycle, once it takes place, the dication formation is readily accessible.[83,84]

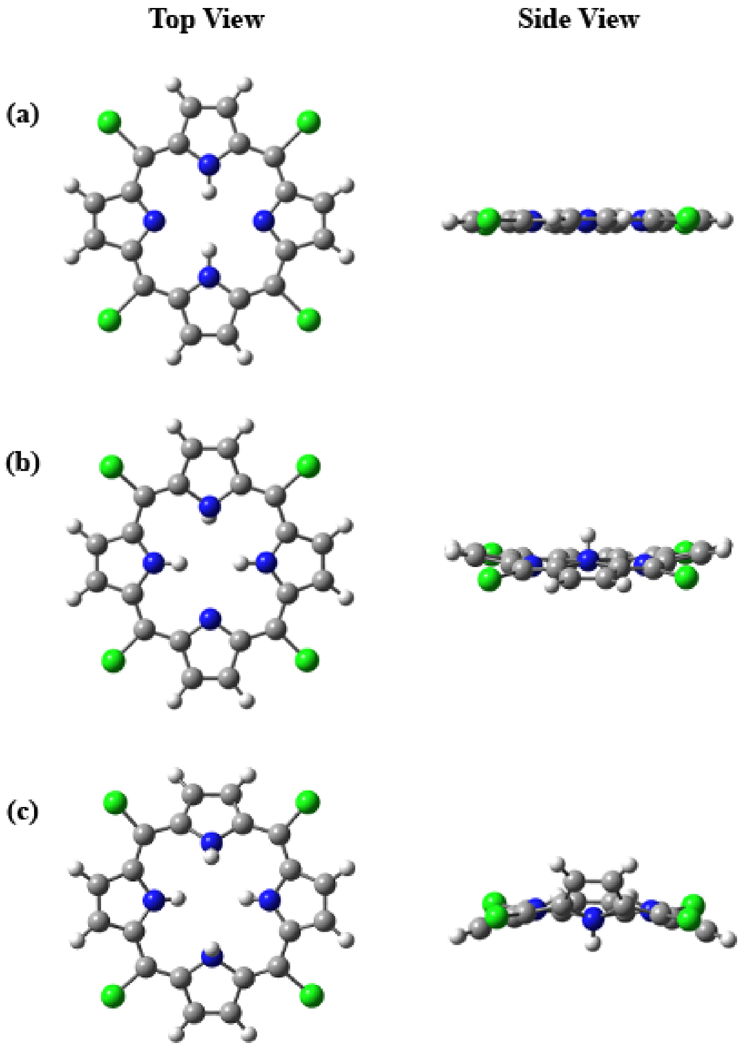

Figure 2.12. DFT optimized structures of the neutral species **1** (a) as well as the monoprotonated **[1-H]**$^{+}$ (b) and diprotonated **[1-HH]**$^{2+}$ (c) forms.

This simplifies the mechanism to yield one possible pathway, namely *P-P-E-E* which its individual steps are described in Figure 2.13 describes the free energy diagram corresponding to the pathway for hydrogen generation for **[1]** using tosic acid, and with respect to the TsOH/H_2 coupled in MeCN. The catalytic cycle, when MeCN is used as solvent, would start with the formation of the doubly protonated **[1-HH]$^{2+}$**. This compound would then be thermodynamically favorable to get reduced by either one two-electrons to yield **[1-HH]** or two sequential one-electron reductions (yielding **[1-HH]$^{+}$** and **[1-HH]**, respectively). The complete pathway is described by Scheme 2.3.

Pathway 1

$$\begin{aligned}
&[\mathrm{P}] + \mathrm{HA} \longrightarrow [\mathrm{P\text{-}H}]^{+} + \mathrm{A}^{-}\\
&[\mathrm{P}]^{+} + \mathrm{HA} \longrightarrow [\mathrm{P\text{-}HH}]^{2+} + \mathrm{A}^{-}\\
&[\mathrm{P\text{-}H}]^{2+} + e^{-} \longrightarrow [\mathrm{P\text{-}HH}]^{+} + \mathrm{A}^{-}\\
&[\mathrm{P\text{-}HH}]^{+} + e^{-} \longrightarrow [\mathrm{P\text{-}HH}]\\
&[\mathrm{P\text{-}HH}] \longrightarrow [\mathrm{P}] + \mathrm{H}_2
\end{aligned}$$

Scheme 2.3. Mechanistic pathway proposed for hydrogen generation in MeCN, with tosic acid as proton source.

Recent reports show that phlorins may be intermediates in HER processes when Ni porphyrin complexes are used.[38] Tetra-pentafluorophenyl phlorin has a strong absorption band in the Q region (centered at 655 nm)[85], which is absent in our samples even after long term electrolysis (more than 12 h). Thus, we cannot state that tetra-pentafluorophenyl phlorin is an intermediate species in our study. However, DFT treatment suggests we cannot rule it out.

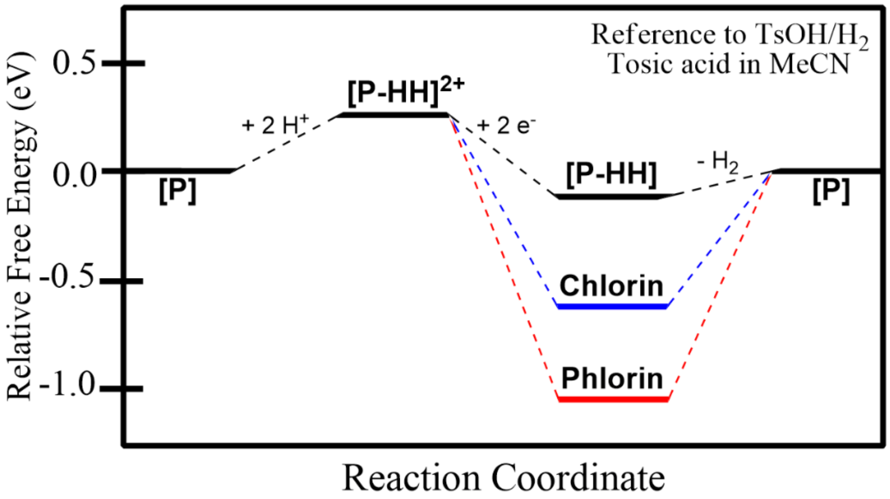

Figure 2.13. Free energy diagram of H_2 evolution catalyzed by **[1]** in acetonitrile with tosic acid as calculated by the Born-Haber cycles shown in Figure 2.2 and Figure 2.3. The free energies are plotted relative to the tosic acid/hydrogen ($TsOH/H_2$) couple.

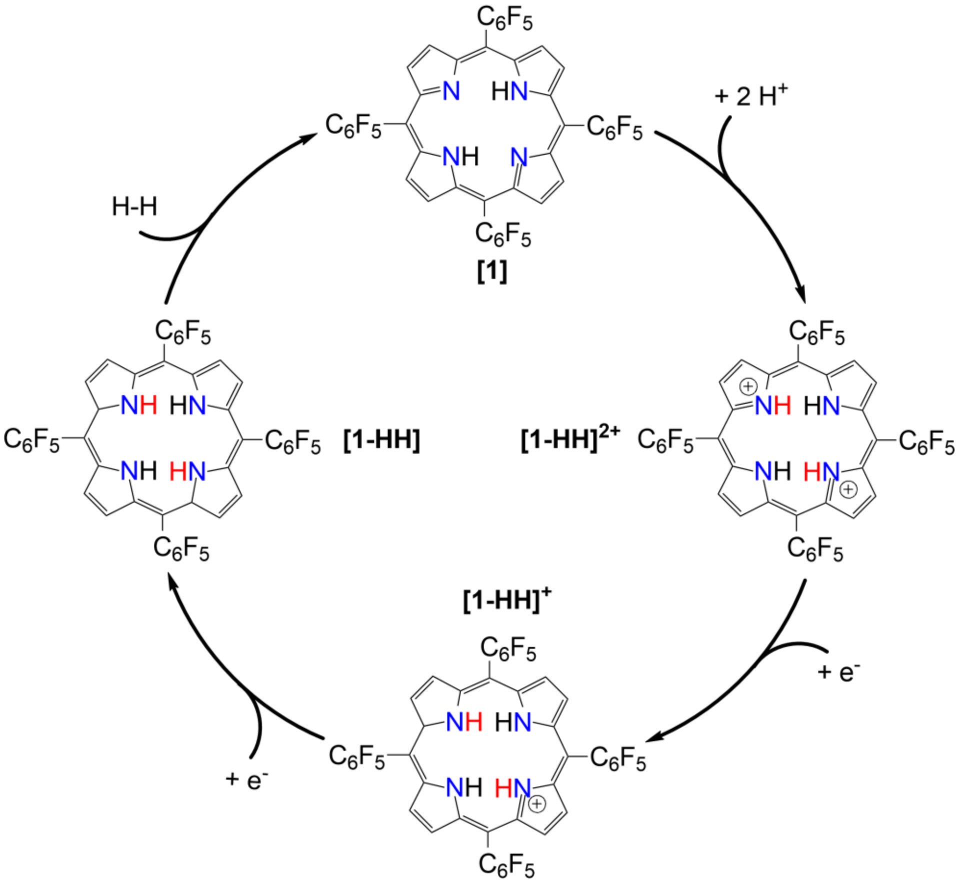

Scheme 2.4. Proposed catalytic cycle of H_2 evolution for tetra-pentafluorophenyl porphyrin and tosic acid, following a *P-P-E-E* mechanism and using MeCN as solvent.

In contrast, the UV-Vis spectrum signature of tetra-pentafluorophenyl chlorin (Soret band: 408 nm; Q-bands: 504 nm, 584 nm, 652 nm) was observed after 12 hours long term bulk electrolysis, indicating the generation of chlorin in the electrocatalytic process, which according to DFT calculations is accessible. The release of hydrogen gas by either species is however not thermodynamically favorable, suggesting that **[1]** is not regenerated and leading to a decomposition pathway.

2.5 CONCLUSION

We have studied the electrocatalytic generation of H_2 using a metal-free perfluorinated porphyrin. The catalytic activity was studied through cyclic voltammetry and controlled-potential electrolysis. Hydrogen is produced electrochemically at –1.31 V and –0.69 V vs Fc/Fc^+ in THF and MeCN respectively using tosic acid at 90% Faradaic yield. Electronic spectra and spectroelectrochemical experiments combined with thermodynamic calculations using density functional theory computations suggest that the most favorable mechanistic process is an *E-P-E-P* and a *P-P-E-E* sequence for HER under acidic conditions in THF and MeCN, respectively. This promising findings may contribute to open a new area for replacing noble metals by much more abundant organic compounds for the catalytic generation of hydrogen gas. It should be noted that this observed activity is limited to the meso-tetrapentafluorophenyl porphyrin with tosic acid and in THF and MeCN as solvents. We are currently working on the catalytic study of other substitution patterns (and other organic macrocycles) for the electrocatalytic production of hydrogen.

Chapter 3: Hydrogen Evolution Catalyzed by a Metal-Free Corrole: Experimental and Theoretical Mechanistic Study[2]

3.1 INTRODUCTION

Proton reduction by electrochemical methods represents an effective way to generate H_2 by converting electrical energy and storing it into chemical bonds.[86,87] Metalated macrocycles such as porphyrins [88,89] and corroles [90,91] have been studied for their ability to perform two-electron reductions of protons to H_2 by employing earth-abundant transition metals.[92–94] Metal-catalyzed hydrogen evolution reactions (HERs) typically proceed via protonation of the metal center.[87,95,96] Just as their metalated counterparts, free-base macrocycles can generate hydrogen gas at comparable reduction potentials.[45,46,97] We have previously demonstrated that free-base meso-tetra(pentafluorophenyl) porphyrin generates molecular hydrogen electrocatalytically under acidic conditions.[98] Spectroscopic and computational methods were employed in order to investigate the mechanistic pathway for hydrogen generation for this perfluorinated metal-free porphyrin in THF using *p*-toluenesulfonic acid (tosic acid) as proton source. We propose the most thermodynamically favorable pathway for hydrogen generation by calculating the relative free energy associated with the protonation and reduction steps. While metalloporphyrins have been reasonably well investigated for hydrogen generation, other metal-free analogues such as corroles remain an open area for exploration.

Corroles are contracted organic macrocycles characterized by three methine bridges and one direct pyrrole-pyrrole linked by the α-carbons similar to corrins.[99] Unlike corrins, corroles preserve the aromaticity of porphyrins despite the lack of one meso carbon compared to

---

[2] This chapter is excerpted with permission from a submitted manuscript: Nancy Rodríguez-López, Yanyu Wu, Dino Villagrán; Hydrogen Evolution Catalyzed by a Metal-Free Corrole: Experimental and Theoretical Mechanistic Study. **2019**. *Submitted.*

porphyrins. The extended π conjugation in the structure allows it to perform multi-electron redox chemistry.[100] In addition, these macrocycles have three NH protons in the core rather than two when compared to a free-base porphyrin having one basic nitrogen core that can act as proton acceptor.

Density functional theory (DFT) has become a powerful tool to analyze the electronic structure of chemical systems.[101,102] Several computational methods have been designed to study the catalytic mechanism of HER.[89,92,103] Those theoretical models focus on the determination of thermodynamic quantities such as proton dissociation constants (pK_as)[104,105] and reduction potentials (E°)[106,107] for the elucidation of free energy diagrams. Accurate calculations of these parameters play an important role in the elucidation of reaction mechanisms particularly when reaction intermediates are difficult to isolate.

Herein we utilize computational and experimental methods to study the electrocatalytic activity for the hydrogen evolution reaction catalyzed by free-base 5, 10, 15-tris(pentafluorophenyl)corrole, **[C-3H]**. We explore the different possible mechanistic pathways when **[C-3H]** is used as catalyst in the presence of both strong and weak acids (*p*-toluenesulfonic acid and benzoic acid) in acetonitrile (MeCN).

3.2 EXPERIMENTAL SECTION

3.2.1 Materials.

The synthesis of the free-base corrole was performed with reagents purchased from Acros Organics. Distillation of corrole was required prior to use. The electrochemical studies were carried out with dried and degassed solvents from a Pure Process Technology solvent purification system. Tetrabutylammonium hexafluorophosphate ($TBAPF_6$) and *p*-toluenesulfonic acid were acquired from Acros Organics. 5,10,15-tris(pentafluorophenyl)corrole, **[C-3H]** was synthesized following modified Lindsey's method[108] according to previously reported procedures[109].

3.2.2 Synthesis of 5,10,15-tris(pentafluorophenyl)corrole, [C-3H].

Trifluoroacetic acid (TFA), 5 mL, were added to 50 mL of DCM and placed in a round bottom flask containing pentafluorobenzaldehyde (1.96 g, 10.0 mmol). Pyrrole (1.40 mL, 20.0 mmol) was added to the mixture and stirred vigorously at room temperature for 10 min. The reaction mixture was diluted in 120 mL of DCM and a solution of p-chloranile (DDQ) in toluene (10.0 mL) was added to the reaction mixture with stirring. The reaction was protected from light and stirred at room temperature for five more minutes. The solution was passed over a chromatography column (silica, hexanes:dichloromethane 3:2) and further purified by column chromatography (silica, hexanes:dichloromethane 4:1). Solvent evaporation afforded the pure corrole which was recrystallized from pentane to give dark crystals (0.814 g, 9.8% yield). ^{1}H NMR (C_6D_6): 9.03(d, 2H), 8.85(d, 2H), 8.68(d, 2H), 8.52(s, 2H); UV–Vis (THF): λ_{max}/nm 409,564, 605.

3.2.3 Cyclic voltammetry.

The cyclic voltammetry measurements were collected using a CHI760D potentiostat, and 0.1 M tetrabutylammonium hexafluorophosphate ($TBAPF_6$) as the supporting electrolyte. Tetrabutylammonium hexafluorophosphate and *p*-toluenesulfonic acid were oven dried preceding its use. The cyclic voltammograms were carried out in a dry N_2-filled glovebox, with a three electrode set-up (a) 2 mm diameter glassy carbon working electrode, (b) Pt mesh counter electrode and (c) Ag/Ag$^+$(AgCl) reference electrode. We used ferrocene (Fc) as an internal standard by addition of 1 mM ferrocene to each measurement.

3.2.4 Other physical methods.

^{1}H NMR was obtained on a JEOL 600 MHz NMR spectrometer. The NMR spectrum was referenced to C_6D_6 residual solvent signal (7.16 ppm). The electronic absorption spectra were performed on a SEC2000 spectrometer with a VISUAL SPECTRA 2.1 software.

3.3 COMPUTATIONAL DETAILS

Theoretical data for all metal-free corrole derivatives were obtained from density functional theory (DFT) calculations. The molecular geometries were optimized in the gas phase with B3LYP (Becke's 3-parameter hybrid functional, coupled with the Lee-Yang-Parr correlational functional).[110,111] The 6-31+G, Pople basis set [112,113] was used for all atoms as implemented in Gaussian 09[114]. Vibrational frequencies were calculated at 298.15 K and 1 atm confirming the obtained geometries corresponded to a minima on the potential energy surface, and to find the zero-point and thermal energy contributions. The solvation model based on density (SMD) was used as executed by the Gaussian 09 suite to calculate the solvation free energies in acetonitrile using the gas phase geometry optimized species.[115] To ease computational expense, the pentafluorophenyl groups in all corroles were replaced with chlorine atoms. This substitution was chosen based on the similar electron-withdrawing properties of –Cl as compared to $-C_6F_5$, determined by their Hammett constants (0.23 and 0.27, respectively).[116] Additional benchmarking was performed using B3P86[110,117] and M062X[118] as functionals, with 6-31G*[113,119,120] and 6-31+G* as basis sets. We based our discussion on the results from the optimized solvated structures with B3LYP and 6-31+G. Cartesian coordinates for the optimized structures in the gas phase and all thermodynamic values are provided in the Supplementary Information. The computational methodology implemented is described below.

3.3.1 Reduction Free Energy Calculation.

The Born-Haber thermodynamic cycle in Scheme 3.1 is used for the calculation of reduction potentials, according to the $\Delta G^\circ_{(sol)}$ for a one-electron reduction reaction as shown in equation 3.1:

$$E^\circ = -\Delta G^\circ_{(sol)} / nF \qquad \text{Eq. 3.1}$$

where n refers to the number of transferred electrons, F is Faraday's constant (96 485 C/mol), and $\Delta G^\circ_{(sol)}$ is the free energy of reduction in solution. The thermodynamic cycle presented in Scheme 1 is use to obtain the reaction free energy in solution for the reduction of a molecule. $\Delta G^\circ_{(sol)}$ is obtained with the reaction free energy in the gas phase, $\Delta G^\circ(g)$, and the solvation energies of the oxidized and reduced macrocycles, ΔG°_{solv}[C-3H], and $\Delta G^\circ_{solv}[\text{C-3H}]^{\bullet-}$ as shown in equation 3.2.

$$\Delta G^\circ_{(sol)} = \Delta G^\circ_{(g)} + \Delta G^\circ_{solv}[\text{C-3H}]^{\bullet-} - \Delta G^\circ_{solv}[\text{C-3H}] - \Delta G^\circ_{solv}(e^-) \qquad \text{Eq. 3.2}$$

$$\begin{tikzcd}
\textbf{[C-3H]}\,(g) + e^-(g) \arrow[r, "\Delta G^o(g)"] \arrow[d, "\Delta G^o_{solv}\textbf{[C-3H]}"', "\Delta G^o_{solv}(e^-)"] & \textbf{[C-3H]}^{\bullet-}(g) \arrow[d, "\Delta G^o_{solv}\textbf{[C-3H]}^{\bullet-}"] \\
\textbf{[C-3H]}\,(sol) + e^-(sol) \arrow[r, "\Delta G^o(sol)"'] & \textbf{[C-3H]}^{\bullet-}(sol)
\end{tikzcd}$$

Scheme 3.1. Born-Haber thermodynamic cycle for the calculation of the free energy associated with the one-electron reduction.

The solvation free energy of the electron cannot be directly obtained from calculations. In this case, according to both ionic and electron conventions, the free energy of formation for the free electron is considered to be zero.[121] When the value for the reduction potential of the electron is obtained from the literature, the contribution to the $\Delta G^\circ_{solv}(e^-)$ is –0.868 kcal/mol at 298.15 K, which neglects the solvation free energy for the electron.[122] The calculated reduction potentials were reported relative to the ferrocene/ferrocenium couple (Fc/Fc^+). The standard hydrogen electrode (SHE) potential which has been determined to be 4.6 eV in acetonitrile[123], is 0.40 V more negative than that for the Fc/Fc^+ couple. Therefore, subtraction of 4.2 eV is necessary to make direct comparison to the cyclic voltammetry data collected.

3.3.2 Proton Dissociation Free Energy Calculation.

The proton dissociation constant, K_a, can be related to the free energy change for proton transfer according to equation 3.3:

$$pK_a = \Delta G^\circ_{(sol)} / 2.303RT \qquad \text{Eq. 3.3}$$

where $\Delta G^\circ_{(sol)}$ is the change in free energy for the proton dissociation reaction, R is the ideal gas constant, and T is the temperature (in K). We used the Born-Haber cycle presented in Scheme 3.2 to calculate the free energy change related to the proton dissociation of the macrocycle. It is difficult to calculate the free energy of the solvated proton with accuracy, hence a direct calculation of the free energy for the reaction cannot be performed. We considered the proton-exchange reaction of the acid (AH) and the free-base corrole (C) in order to obtain the reaction free energies of deprotonation, as shown in equation 3.4.

$$A^- + [C\text{-}4H]^+ \rightarrow AH + [C\text{-}3H] \qquad \text{Eq. 3.4}$$

The free energy in solution for the proton dissociation reaction can be calculated with respect to the reaction free energy of deprotonation of the corrole in the gas phase, $\Delta G^\circ(g)$, as well as the solvation free energies for the corrole, the acid, and its conjugated base, $\Delta G^\circ_{solv}([C\text{-}4H]^+)$,

$\Delta G°_{solv}(AH)$, $\Delta G°_{solv}(A^{-})$, respectively as shown in equation 3.5. The contribution of the proton towards the reaction free energy in solution has been previously reported to be –6.28 kcal/mol. [122]

$$\Delta G°_{(sol)} = \Delta G°_{(g)} + \Delta G°_{solv}(AH) + \Delta G°_{solv}([C\text{-}3H]) - \Delta G°_{solv}(A^{-}) - \Delta G°_{solv}([C\text{-}4H]^{+}) \qquad \text{Eq. 3.5}$$

$$\begin{tikzcd}
A^{-}(g) \arrow[d, "\Delta G^{o}_{solv}(A^{-})"] & + & \mathbf{[C\text{-}4H]}^{+}(g) \arrow[r, "\Delta G^{o}(g)"] \arrow[d, "\Delta G^{o}_{solv}\mathbf{[C\text{-}4H]}^{+}"] & AH(g) \arrow[d, "\Delta G^{o}_{solv}(AH)"] & + & \mathbf{[C\text{-}3H]}(g) \arrow[d, "\Delta G^{o}_{solv}\mathbf{[C\text{-}3H]}"] \\
A^{-}(sol) & + & \mathbf{[C\text{-}4H]}^{+}(sol) \arrow[r, "\Delta G^{o}(sol)"'] & AH(sol) & + & \mathbf{[C\text{-}3H]}(sol)
\end{tikzcd}$$

Scheme 3.2. Born-Haber cycle for the calculation of the free energy change of proton transfer from the proton source to the metal-free specie.

3.4 RESULTS AND DISCUSSION

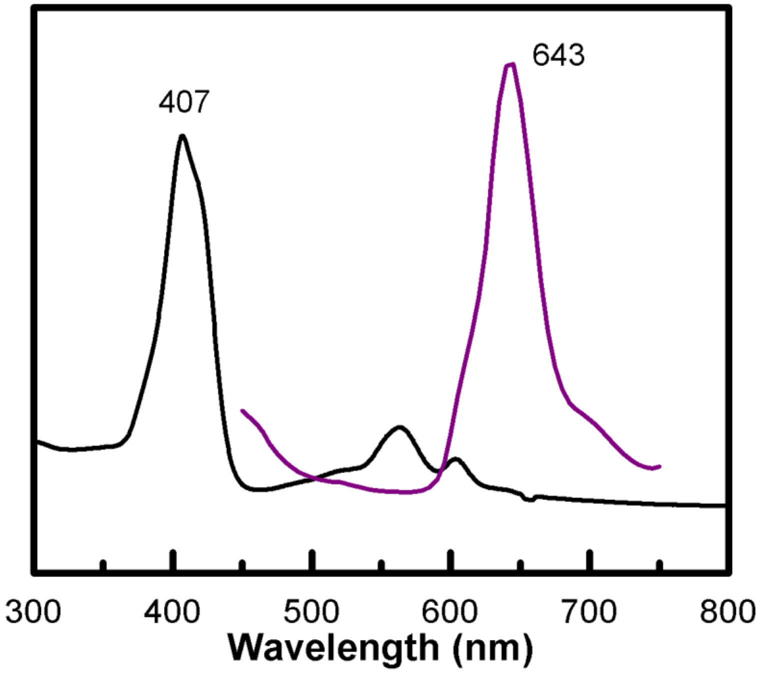

Figure 3.1. Absorption (Soret band 407 nm) and emission (643 nm) spectra of **[C-3H]** in MeCN at 22.8°C. The fluorescence spectrum was obtained by excitation at 400 nm.

Spectroscopy and Electronic Structure. In acetonitrile, **[C-3H]** exhibits a narrow and intense absorbance in the Soret region (409 nm) and two small Q-bands at 564 and 605 nm as shown in Figure 3.1. The Soret band for the free base corrole is not symmetric, which can be attributed to the lower symmetry of the macrocycle rings.[124] Free-base meso-triarylcorroles present strong fluorescence, commonly mirroring the absorption spectra.[125] Figure 3.1 displays the emission spectra of **[C-3H]** with an excitation at 400 nm, an intense band at 645 nm can be observed. These findings are in agreement with previously reported work on corrole monomers.[126,127]

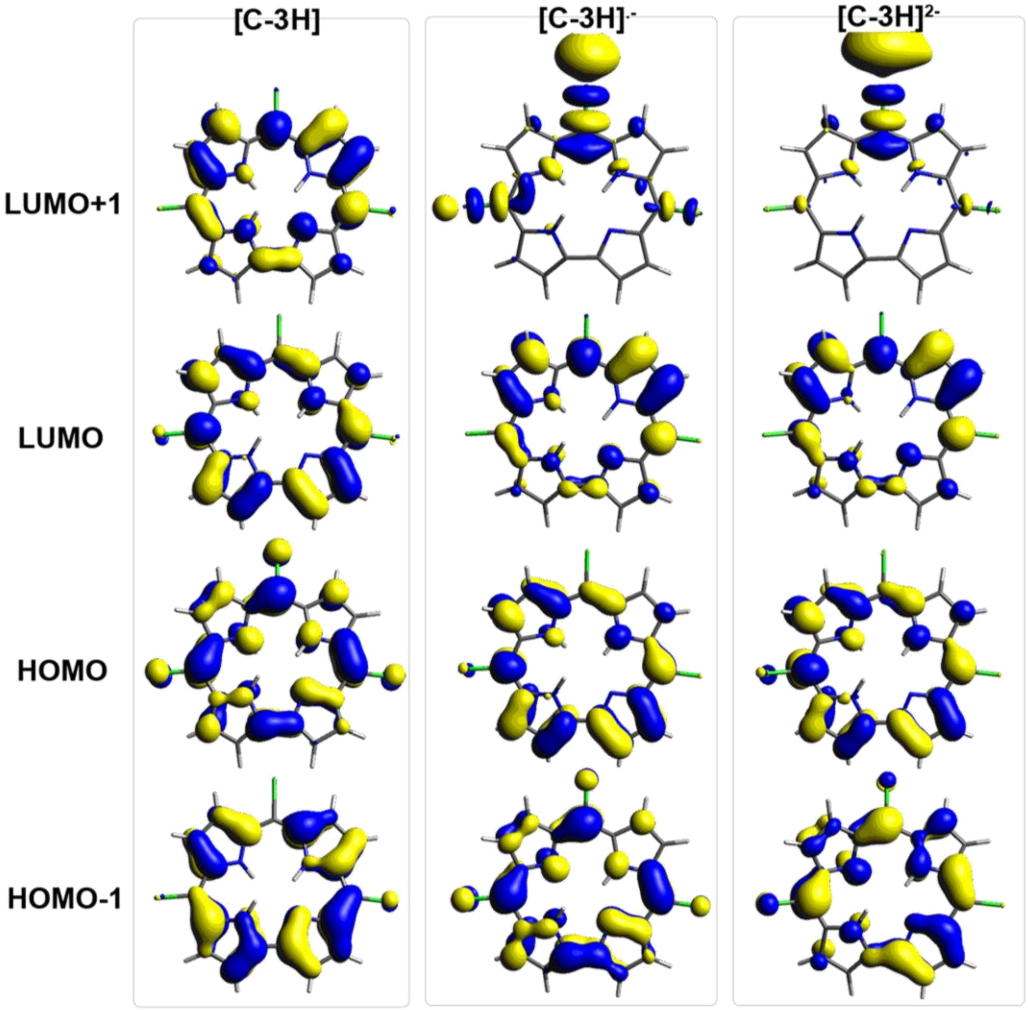

Figure 3.2. Contour plots of four frontier orbitals for **[C-3H]**, **[C-3H]**$^{\bullet-}$ and **[C-3H]**$^{2-}$ with 0.03 isosurface value calculated by DFT.

DFT calculations were performed on a model of the synthesized free-base corrole to elucidate the nature of the frontier molecular orbitals and the relative free energies of the reduction and protonation reactions. Fully optimized geometries of the neutral, **[C-3H]**, mono reduced, **[C-3H]**$^{\bullet-}$, and doubly reduced, **[C-3H]**$^{2-}$ free-base corrole are shown in Figure 1. The most stable form of **[C-3H]** consists of a bent structure with one of the pyrrolic rings slightly out-of-plane in accordance to x-ray crystallography data that shows that meso-substituted corroles exhibit tilting of one of the protonated pyrrole rings.[99] The observed bent structure is in agreement with the conformational properties of corroles where the lack of the meso carbon causes steric strain in the macrocycle forcing the molecule out-of-plane.[100]

The spectroscopic properties of corroles are understood in terms of Gouterman's four orbital model characterized by the electronic transitions between the HOMO and LUMO orbitals.[128,129] Removal of one meso-carbon alters both the symmetry (from D_{4h} to C_{2v}) and energy of the molecular orbitals. The degenerate HOMO and LUMO orbitals split into HOMO (b_1) and HOMO–1 (a_2), and LUMO (a_2) and LUMO+1 (b_1), respectively, as shown in Figure 1. The HOMO and LUMO energies, as well as the HOMO–LUMO energy gap ($\Delta E_{H–L}$) obtained from theoretical calculations for **[C-3H]**, **[C-3H]**$^{\bullet-}$ and **[C-3H]**$^{2-}$ are shown in Table 3.1. The calculated $\Delta E_{H–L}$ for **[C-3H]** (2.60 eV) is comparable to the energy gap reported for similar meso substituted free-base corroles.[130,131]

Table 3.1. HOMO and LUMO energies, and calculated HOMO–LUMO energy gap ($\Delta E_{H–L}$) for **[C-3H]**, **[C-3H]**$^{\bullet-}$ and **[C-3H]**$^{2-}$, values are in eV.

	[C-3H]	[C-3H]$^{\bullet-}$	[C-3H]$^{2-}$	**Ref. 41**	**Ref. 42**
LUMO	–2.993	0.633	3.847	–2.30	–2.595
HOMO	–5.592	–0.725	2.680	–4.76	–5.244
$\Delta E_{H–L}$	2.599	1.358	1.167	2.46	2.649

The frontier molecular orbitals for **[C-3H]** (Figure 3.2) show symmetry along the axis passing through the pyrrole-pyrrole link and the meso-carbon opposed to it. The electron density in these orbitals is localized mainly on the corrole ring and not on the substituents, with the exception of the HOMO. In contrast, the frontier orbitals for $\mathbf{[C\text{-}3H]}^{\bullet-}$ and $\mathbf{[C\text{-}3H]}^{2-}$ lose some of the symmetry observed in **[C-3H]**. In addition, the distribution of the electron density is irregular throughout the corrole, with LUMO+1 having most of the electron density on the substituents due to the electron withdrawing ability of the $–C_6F_5$ functional groups in the meso carbons.

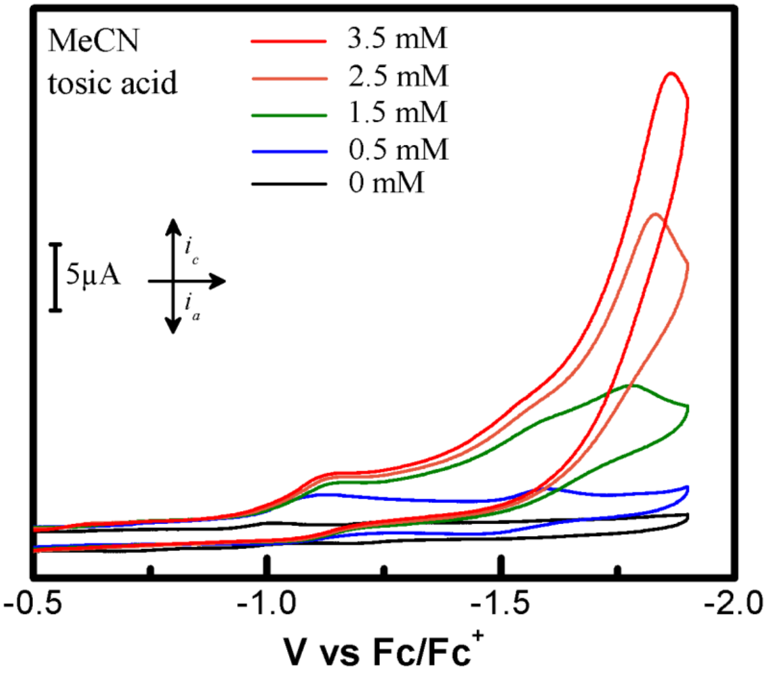

Figure 3.3. Cyclic voltammograms (scan rate: 100 mV/s) of **[C-3H]** in MeCN with no acid (black line) and with different concentrations of tosic acid. Glassy carbon as working electrode.

Cyclic Voltammetry and H_2 evolution. Cyclic voltammetry (CV) was performed in **[C-3H]** using acetonitrile as solvent to evaluate its electrocatalytic behavior. When no proton source is added, **[C-3H]** displays two well defined one-electron reversible reductions with half-wave potentials at $E_{1/2} = -0.86$ V and $E_{1/2} = -1.22$ V vs Fc/Fc^{+} corresponding to the reduction of **[C-3H]** to form **[C-3H]**$^{\cdot-}$ and **[C-3H]**$^{-2}$, respectively. Two different protons sources, *p*-toluenesulfonic acid and benzoic acid were introduced to evaluate the electrocatalytic properties of **[C-3H]** for proton reduction.

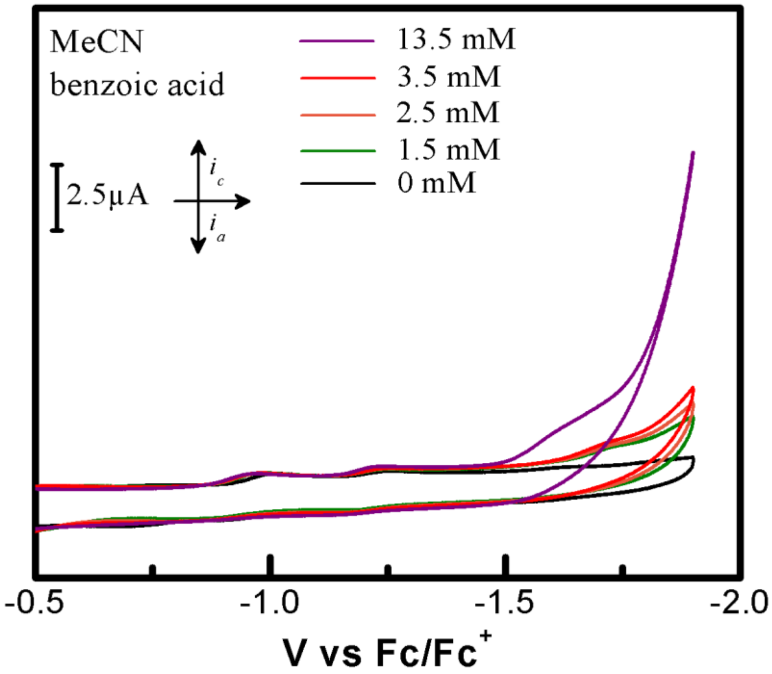

Figure 3.4. Cyclic voltammograms of **[C-3H]** in MeCN with no acid (black line) and with different concentrations of benzoic acid. (Scan rate: 100 mV/s; Working electrode: Glassy carbon)

Upon addition of *p*-toluenesulfonic acid (pK_a = 8.45 in MeCN)[132] both reduction potentials shift cathodically (Figure 3.3). At small acid concentrations, the first reduction potential shifts by ~200 mV while the second wave shifts ~300 mV. No relevant increase in current for the first reduction peak is observed with the addition of acid. Furthermore, we observed suppression of the cathodic peak (oxidation of the reduced species **[C-3H]**$^{\cdot-}$) due to protonation of **[C-3H]** to form **[C-4H]**$^{+}$. However, when higher concentrations of *p*-toluenesulfonic acid are introduced, an irreversible prewave at a potential near –1.51 V vs Fc/Fc^{+} appears along with a catalytic wave at

–1.83 V vs Fc/Fc$^+$ which increases in current response as *p*-toluenesulfonic acid is added to the solution. As previously reported for other catalytic systems, the potential of the formed prewave can significantly change from that of the reversible $E_{1/2}$ for the non- active species depending upon the rate constant of these two reactions.[133] These features on the cyclic voltammograms indicate the formation of a new species (due to an irreversible chemical reaction) during catalysis followed by electron transfer. Moreover, the lack of oxidation features in the return sweep for the catalytic system suggests the generated species is chemically irreversible, and therefore react to form other intermediates for the hydrogen generation process.[134]

On the other hand, in the presence of benzoic acid (pK_a = 20.7 in MeCN)[93] both of the reduction waves for **[C-3H]** remain constant, and an increase in current was only observed past the second reduction wave near –1.5 V vs Fc/Fc$^+$ (Figure 3.4). The peak corresponds to reduction of benzoic acid and its height is dependent on the increasing concentration of acid. No catalysis is observed near the first and second reduction potentials for the corrole ($E_{1/2}$ = –0.86 V and $E_{1/2}$ = –1.22 V vs Fc/Fc$^+$). It has been previously stablished that thermodynamically is not possible to reduce an acid at a potential more positive than its standard reduction potential.[135] The standard reduction potential in acetonitrile for benzoic acid is −1.36 V vs Fc/Fc$^+$ which indicates this free-base corrole cannot catalyze proton reduction under these conditions, and the observed current is likely due to the working electrode. Similar results were found when Fe_2(benzenedithiolate)$(CO)_6$ was used as catalysts in acetonitrile in the presence of weak acids.[136] The cyclic voltammograms obtained show that H_2 evolution can be catalyzed by **[C-3H]** under acidic media, using a strong acid such as *p*-toluenesulfonic acid, and it suggests that the rate of proton reduction in this system strongly depends on the pK_a of the proton source.

Pathway 1

$$\begin{aligned}
&\textbf{[C-3H]} + \mathrm{HA} \longrightarrow \textbf{[C-4H]}^{+} + \mathrm{A}^{-}\\
&\textbf{[C-4H]}^{+} + e^{-} \longrightarrow \textbf{[C-4H]}\\
&\textbf{[C-4H]} + e^{-} \longrightarrow \textbf{[C-4H]}^{-}\\
&\textbf{[C-4H]}^{-} - \mathrm{H_2} \longrightarrow \textbf{[C-2H]}^{-}\\
&\textbf{[C-2H]}^{-} + \mathrm{HA} \longrightarrow \textbf{[C-3H]} + \mathrm{A}^{-}
\end{aligned}$$

Pathway 2

$$\begin{aligned}
&\textbf{[C-3H]} + e^{-} \longrightarrow \textbf{[C-3H]}^{\bullet-}\\
&\textbf{[C-3H]}^{\bullet-} + e^{-} \longrightarrow \textbf{[C-3H]}^{2-}\\
&\textbf{[C-3H]}^{2-} + \mathrm{HA} \longrightarrow \textbf{[C-4H]}^{-} + \mathrm{A}^{-}\\
&\textbf{[C-4H]}^{-} - \mathrm{H_2} \longrightarrow \textbf{[C-2H]}^{-}\\
&\textbf{[C-2H]}^{-} + \mathrm{HA} \longrightarrow \textbf{[C-3H]} + \mathrm{A}^{-}
\end{aligned}$$

Pathway 3

$$\begin{aligned}
&\textbf{[C-3H]} + e^{-} \longrightarrow \textbf{[C-3H]}^{\bullet-}\\
&\textbf{[C-3H]}^{\bullet-} + \mathrm{HA} \longrightarrow \textbf{[C-4H]} + \mathrm{A}^{-}\\
&\textbf{[C-4H]} + e^{-} \longrightarrow \textbf{[C-4H]}^{2-}\\
&\textbf{[C-4H]}^{-} - \mathrm{H_2} \longrightarrow \textbf{[C-2H]}^{-}\\
&\textbf{[C-2H]}^{-} + \mathrm{HA} \longrightarrow \textbf{[C-3H]} + \mathrm{A}^{-}
\end{aligned}$$

Scheme 3.3. Proposed mechanistic pathways for hydrogen generation in MeCN, where tosic acid or benzoic acid are employed as proton source.

Hydrogen Evolution Mechanisms. Experimental studies have shown that 5,10,15-tris(pentafluorophenyl)corrole, **[C-3H]**, evolves hydrogen electrochemically at –1.22 V vs Fc/Fc$^+$ in acetonitrile with *p*-toluenesulfonic acid as proton source (Figure 3.3). We have previously demonstrated that another metal-free macrocycle, tetrapentafluorophenyl porphyrin, evolves hydrogen gas under acidic media. The electron-withdrawing group was necessary to bring the reduction potentials into a more positive range.[98]

Spectroscopic techniques and DFT calculations can give insight into the mechanistic pathway the hydrogen evolution reaction follows. Three possible sequential pathways (depicted in Scheme 3.3) were considered for HER mechanism with **[C-3H]** as electrocatalyst: *PEEP*, *EEPP*, and *EPEP*, where *P* stands for proton transfer from the acid to the corrole, and *E* stands for electron transfer. We limit the scope of the discussion to sequential electron and proton transfer processes. Relevant species to the sequential *E-P* mechanisms are shown in Scheme 3.4.

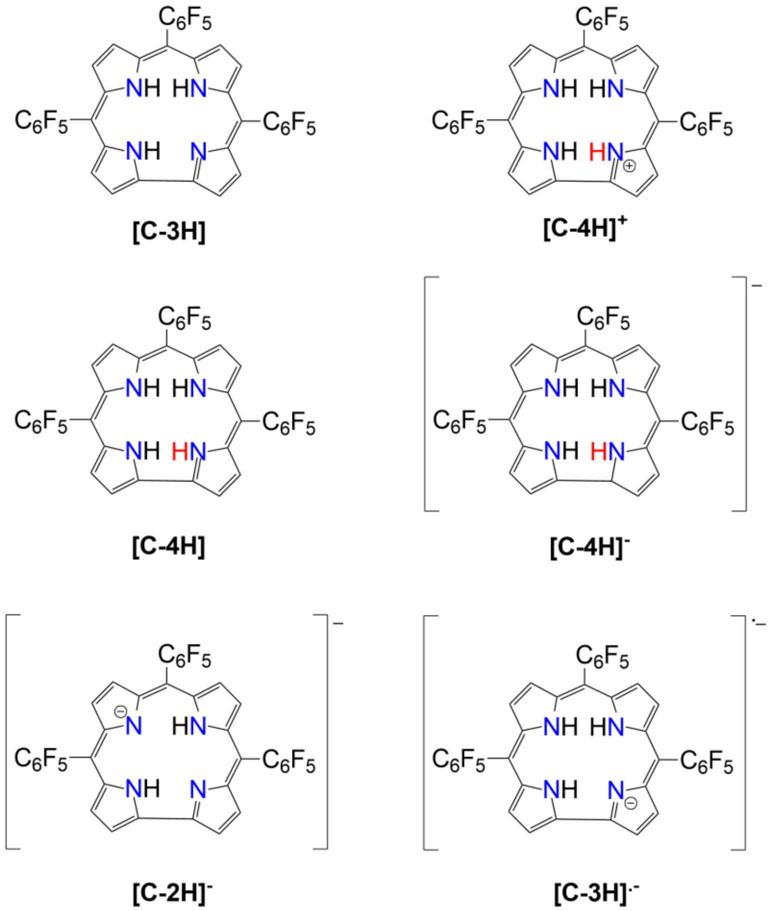

Scheme 3.4. Proposed metal-free corrole intermediates involved in the mechanistic pathways presented in Scheme 3.3.

As shown in Figure 3.1, **[C-3H]** exhibits a narrow and intense band in the Soret region (409 nm), and two small Q-bands at 564 and 605 nm in acetonitrile. When performing titration with *p*-toluenesulfonic acid in acetonitrile (Figure 3.5), the Soret band at 407 nm decreases while a new red-shifted band at 421 nm appears with an isosbestic point at 414 nm. These results combined with the cyclic voltammograms indicate that the first step of hydrogen generation in acetonitrile using *p*-toluenesulfonic acid as proton source is protonation of **[C-3H]** to yield **[C-4H]**$^+$. Meanwhile, when **[C-3H]** is titrated with benzoic acid the electronic spectra remains constant, indicating that in acetonitrile this proton source is not strong enough to protonate **[C-3H]** as supported by the cyclic voltammetry displayed in Figure 3.6.

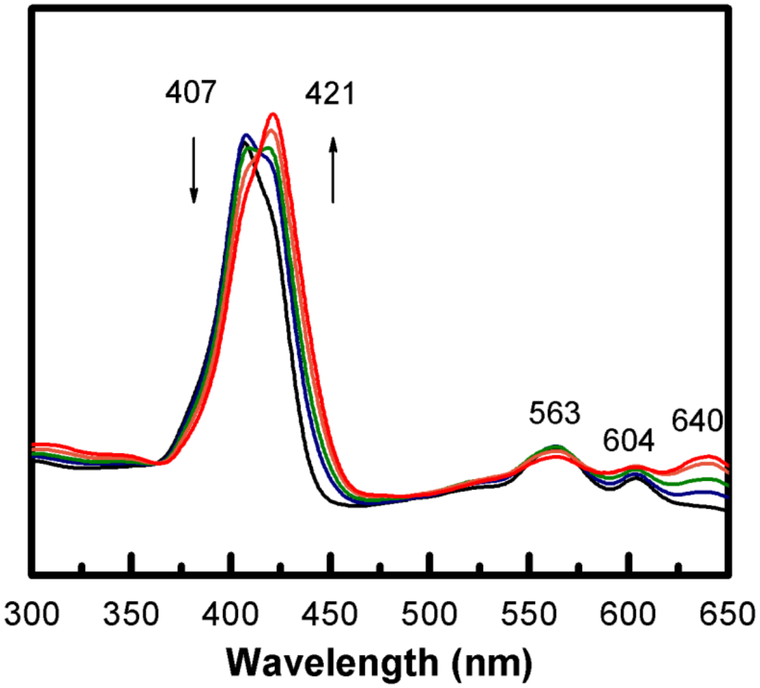

Figure 3.5. UV-Vis spectrum of **[C-3H]** in MeCN containing 0.1 M TBAPF$_6$ before and after titrating with tosic acid.

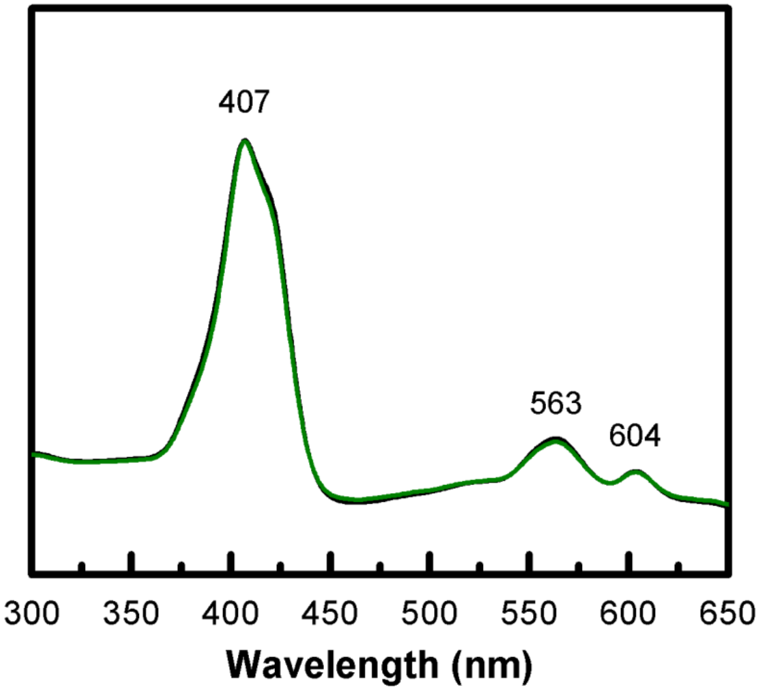

Figure 3.6. UV-Vis spectrum of **[C-3H]** in MeCN containing 0.1 M $TBAPF_6$ before and after titrating with benzoic acid.

The mechanistic pathway for hydrogen evolution using **[C-3H]** as electrocatalyst can be deduced with the aid of DFT computations by calculating the relative free energies associated with the reduction and protonation of relevant intermediates involved in the catalytic cycle. These relative free energies are used to calculate reduction potentials and pK_as. Figure 3.7 depicts the free energy diagram corresponding to the three proposed pathways for hydrogen generation by **[C-3H]** with *p*-toluenesulfonic acid as proton source (strong acid). These values are calculated with respect to the TsOH/H_2 coupled in acetonitrile. The calculated pK_a for *p*-toluenesulfonic acid in acetonitrile is 8.45, while the pK_a for **[C-3H]** is 10.2. The relative free energy obtained for the protonation step is +1.99 kcal/mol (+0.086 eV) opposed to +10.5 kcal/mol (+0.46 eV) for the reduction of **[C-3H]** to **[C-3H]**$^{\cdot-}$. Therefore, we establish that the first step in the catalytic cycle involves the protonation of **[C-3H]** to get species **[C-4H]**$^{+}$ consistent with the experimental data.

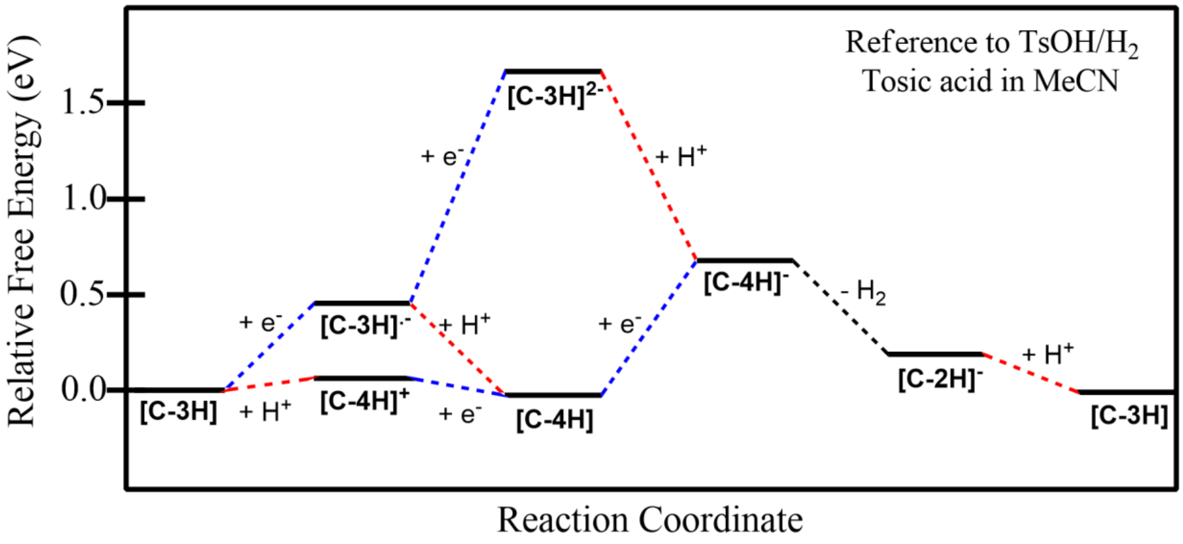

Figure 3.7. Free energy diagram of H_2 evolution catalyzed by **[C-3H]** in MeCN with tosic acid (pK_a = 8.45), and applied potential of –1.65 V vs Fc/Fc$^+$. As calculated by the Born-Haber cycles shown in Scheme 3.1 and Scheme 3.2.

According to the proposed mechanistic pathways depicted in Scheme 3.3, and based on the availability of N-core protonation sites on the neutral corrole, the next two steps in the mechanism are one-electron reductions of the macrocycle to form **[C-4H]** and **[C-4H]**$^–$. The reduction of the protonated corrole proceeds with a relative free energy of –3.46 kcal/mol (–0.15 eV) to yield **[C-4H]**. Once the formation of **[C-4H]** takes place, a second reduction of the macrocyle occurs with a calculated relative free energy of +16.9 kcal/mol (+0.74 eV). Hydrogen gas is tentatively evolved from the intermediate **[C-4H]**$^–$ obtaining thus **[C-2H]**$^–$. This species gets readily protonated (–11.0 kcal/mol, –0.48 eV) to regenerate **[C-3H]**, closing thus the catalytic cycle.

Additional benchmarking was performed with B3P86 and M062X functionals to evaluate the mechanistic pathways using corrole. In addition, geometry optimizations were done using 6-31G*, and 6-31+G* basis sets were assessed with all functionals. Table 3.2 display all thermodynamic parameters calculated (redox potentials and pK_a's) for the hydrogen evolution reaction in acetonitrile. The calculated reduction potentials and dissociation constants show variation between the different basis sets and functionals. Nevertheless, the general mechanistic steps when using tosic and benzoic acid does not change.

Table 3.2. Calculated redox potentials and pKa's in MeCN using tosic acid as proton source. Values in parentheses correspond to experimental values obtained in this work. Redox potentials and dissociation constants calculated with benzoic acid as proton source are identical.

	B3LYP	**B3LYP**	**B3LYP**
	6-31+G		
[**C-3H**] + e$^-$ → [**C-3H**]$^{\cdot -}$	–0.86 V (–0.96)^a	–0.75 V	–0.92 V
[**C-3H**]$^{\cdot -}$ + e$^-$ → [**C-3H**]$^{2-}$	–1.60 V(–1.22)^a	–1.41 V	–1.67 V
[**C-4H**]$^-$ + TsO$^-$ → [**C-3H**]$^{2-}$ + TsOH	25.3	19.1	20.0
[**C-3H**] + TsO$^-$ → [**C-2H**]$^-$ + TsOH	16.8	11.3	9.69
[**C-4H**]$^+$ + TsO$^-$ → [**C-3H**] + TsOH	10.2	10.5	8.78
[**C-4H**]$^+$ + e$^-$ → [**C-4H**]	–0.25 V	–0.16 V	–0.37 V
[**C-4H**] + e$^-$ → [**C-4H**]$^-$	–1.14 V	–1.00 V	–1.10 V
[**C-4H**] + TsO$^-$ → [**C-3H**]$^{\cdot -}$ + TsOH	17.5	12.2	10.3
	6-31G*		
[**C-3H**] + e$^-$ → [**C-3H**]$^{\cdot -}$	–1.00 V	–0.85 V	–0.90 V
[**C-3H**]$^{\cdot -}$ + e$^-$ → [**C-3H**]$^{2-}$	–1.73 V	–1.60 V	–1.65 V
[**C-4H**]$^-$ + TsO$^-$ → [**C-3H**]$^{2-}$ + TsOH	24.8	23.1	21.7
[**C-3H**] + TsO$^-$ → [**C-2H**]$^-$ + TsOH	13.1	12.2	11.0
[**C-4H**]$^+$ + TsO$^-$ → [**C-3H**] + TsOH	11.4	11.4	11.6
[**C-4H**]$^+$ + e$^-$ → [**C-4H**]	–0.37 V	–0.19 V	–0.24 V
[**C-4H**] + e$^-$ → [**C-4H**]$^-$	–1.19 V	–1.10 V	–1.12 V
[**C-4H**] + TsO$^-$ → [**C-3H**]$^{\cdot -}$ + TsOH	15.7	14.6	12.8
	6-31+G*		
[**C-3H**] + e$^-$ → [**C-3H**]$^{\cdot -}$	–1.12 V	–0.97 V	–1.04 V
[**C-3H**]$^{\cdot -}$ + e$^-$ → [**C-3H**]$^{2-}$	–1.74 V	–1.63 V	–1.69 V
[**C-4H**]$^-$ + TsO$^-$ → [**C-3H**]$^{2-}$ + TsOH	19.6	19.2	15.9
[**C-3H**] + TsO$^-$ → [**C-2H**]$^-$ + TsOH	10.3	9.5	7.9
[**C-4H**]$^+$ + TsO$^-$ → [**C-3H**] + TsOH	9.03	8.75	10.3
[**C-4H**]$^+$ + e$^-$ → [**C-4H**]	–0.54 V	–0.38 V	–0.41 V
[**C-4H**] + e$^-$ → [**C-4H**]$^-$	–1.27 V	–1.19 V	–1.30 V
[**C-4H**] + TsO$^-$ → [**C-3H**]$^{\cdot -}$ + TsOH	11.6	11.8	9.24

[a] Experimental value

3.5 CONCLUSION

In conclusion, we show that a metal-free perfluorinated corrole can electrocatalytically produce H_2 gas from organic acidic conditions in MeCN. Cyclic voltammetry was used to study its catalytic performance. Electrochemical production of hydrogen occurs at –1.22 V vs Fc/Fc^+ in acetonitrile using *p*-toluenesulfonic acid as proton source. Electronic spectra, spectroelectrochemical experiments, and theoretical calculations of thermodynamic parameters using density functional theory suggest that the lowest energy mechanism is *PEEP*. In addition, we found that the free-base corrole does not catalyzed proton reduction when a weaker acid, benzoic acid, is used as proton source. It should be noted the observed activity is limited to this free-base corrole in acetonitrile as solvent under these conditions.

Chapter 4: Study of Multielectron Redox Chemistry through Quadruply Bonded Non-Symmetric Dimolybdenum Systems

4.1 INTRODUCTION

Multielectron redox chemistry occurs widely in nature with the help of mid-to-late first row transition metals (eg. Fe, Co, Mn).[137–140] Based on the state and connectivity of the redox centers, there are two main mechanisms of electron transfer: Inner-sphere (ISET) and Outer-sphere (OSET) electron transfer (Scheme 4.1). This chapter will focus on the understanding of electron transfer by ISET.

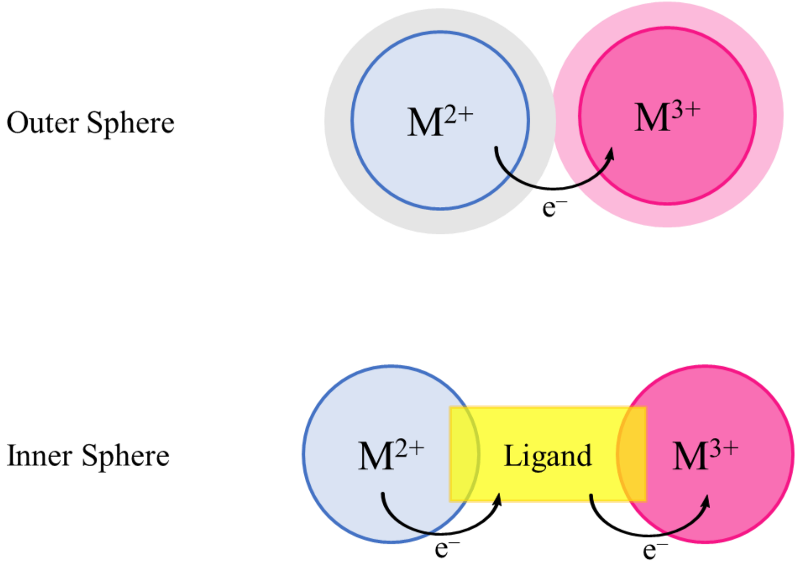

Scheme 4.1. Pictorial representation of inner-sphere and outer-sphere electron transfer.

Mixed valent (MV) compounds have been synthesized and studied for the understanding of multielectron redox chemistry through ISET. The most studied compound of this type is the Creutz–Taube (CT) ion (Scheme 4.2**)** first synthesized by Carol Creutz in the late 1960s.[141] The study of electron transfer using this complex gave Taube the Nobel Prize in 1983. This system is comprised by two ruthenium pentammine units connected by a pyrazine ligand thus completing the octahedral coordination sphere for each metal.[142] The CT ion is a symmetric system containing an odd number of electrons, the resulting unpaired electron may consequently be localized on one of the metal atoms (Ru^{2+}–L–Ru^{3+}), or delocalized over both metals ($Ru^{2.5+}$–L–$Ru^{2.5+}$) making both ruthenium centers equivalent.[143]

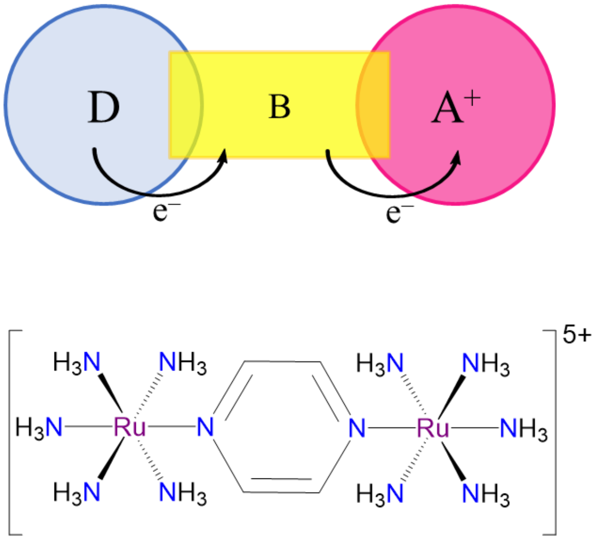

Scheme 4.2. Creutz–Taube ion, mixed-valent compound for the understanding of electron transfer.

Ever since the study of the CT ion, many mixed-valent systems have been prepared. They are categorized by the coupling of the metal centers and their ability to stabilize the MV species according to the Robin–Day classification.[144] The stability of the MV system is measured by the equilibrium constant, K_c, arising from the equilibrium between the fully oxidized and fully reduced species. This equilibrium constant represents the rate at which two MV compounds form a product where both elements (metals) go from different to equal oxidation states, as shown in Scheme 4.3.[145] According to this scheme, compounds demonstrating a weak electronic communication, with $K_c < 10^2$, belong to Class I. On the other hand, Class III comprises compounds with high electronic coupling and complete delocalization of the electron, such compounds have $K_c > 10^6$.

Finally, Class II compounds demonstrate some interaction between the metal centers with $10^2 < K_c < 10^6$, but the electron is predominantly localized on a single redox site.[146]

$$[\text{M-L-M}] + [\text{M}^+\text{-L-M}^+] \xrightleftharpoons{K_c} 2\,[\text{M-L-M}^+]$$

$$K_c = e^{\frac{\Delta E_{1/2}F}{RT}}$$

Class I	$K_c < 10^2$
Class II	$10^2 \leq K_c \leq 10^6$
Class III	$10^6 < K_c$

Scheme 4.3. Mixed-valent equilibrium and Robin–Day classification.

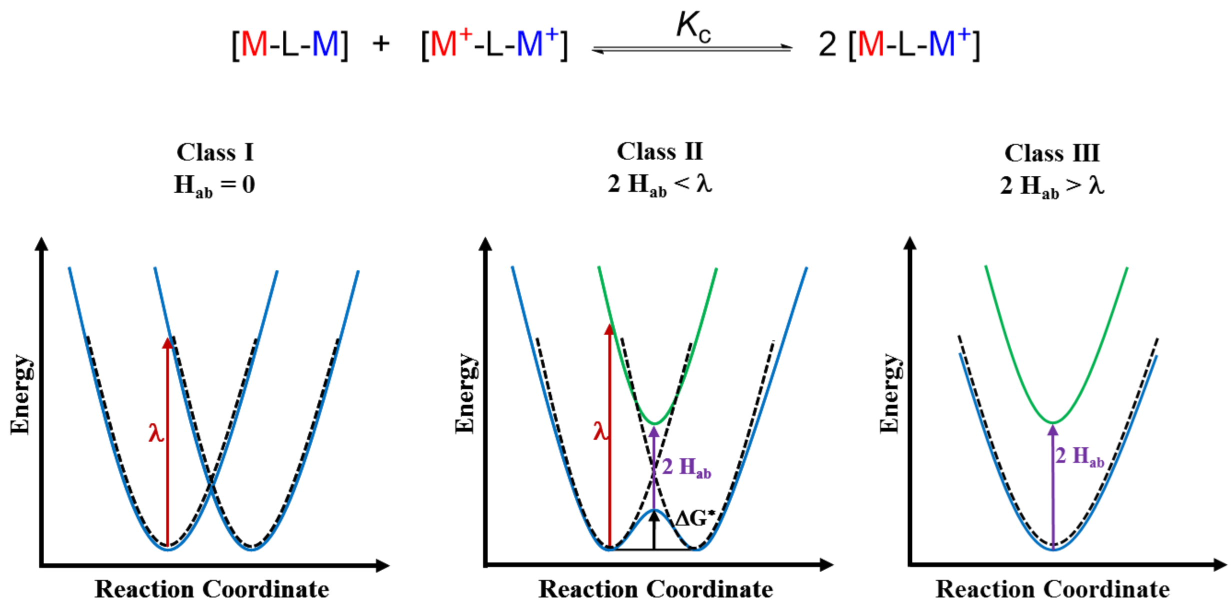

Figure 4.1. Potential energy curves according to Robin–Day classification, Class I (left), Class II (middle) and Class III (right).

In addition, we can study the kinetics and thermodynamics of these systems by Marcus–Hush theory (MHT). According to MHT we can represent both ends of the mixed-valent equilibrium by two parabolic wells, as shown in Figure 4.1. In Class I, where the electron is fully localized on one redox center (valence trapped), there is no overlap between the parabolas, and the reorganization energy (λ) due to electron transfer is large. In Class II, there is some overlap corresponding to the electronically coupled redox centers. In this case, the electron transfer process is defined by the activation energy required for the process. For Class III, the electron is fully delocalized throughout the system, and the activation energy for the transfer of the electron between the donor and acceptor is zero. In this system only one parabolic well is observed.

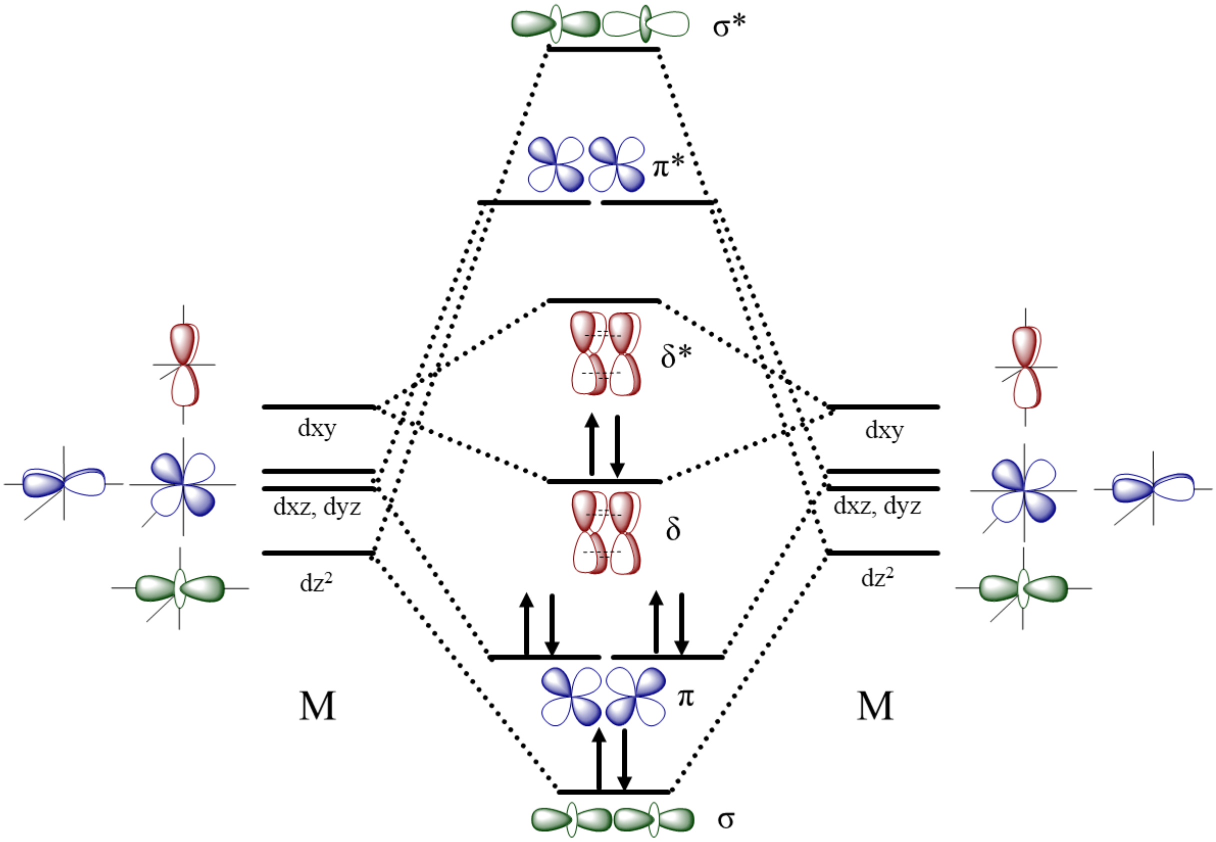

Figure 4.2. Molecular orbital diagram for D_{4h} bimetallic complex.

Of special interest are mixed-valent compounds presenting multiple metal-metal bonds. The first quadruple bonded compound, dirhenium (III) octachloride, was synthesized and characterized by Cotton et al. in the mid-1960s.[147–149] The electronic nature of the quadruple metal-

metal bond is assigned as such: σ-bond arising from the head-on overlap of the d_{z^2}–d_{z^2} orbitals, two degenerate π-bonds from the interaction of the d_{xz}–d_{xz} and d_{yz}–d_{yz} orbitals, and a δ-bond from the d_{xy}–d_{xy} face-to-face interaction. The electronic structure of a metal–metal quadruple bonded bimetallic complex is presented in Figure 4.2. A library of symmetrical bimetallic compounds using an array of metals, such as Ni, Cu, Cr, Mo, W, Re, Ru, Rh, Pd and Pt have been synthesized, characterized, and studied as platforms for electron transfer due to their ease of functionalization as well as their interesting and well stablished electrochemical properties.[150–153] These compounds so called *dimers-of-dimers* are of the type M_2–L–M_2, where M_2 is the multiple bonded unit, and L the bridging ligand. The removal of one electron from their δ-orbital can be tracked by spectroscopic means such as electron paramagnetic resonance and crystallography since the formal bond order decreases from 4 to 3.5 increasing thus the M–M bond distance. Moreover, the oxidation of Mo_2^{4+} proceeds without large rearrangement of the ligands making this electrochemical process often reversible.

$$[\text{M-L-M}] + [\text{M}^{+}\text{-L-M}^{+}] \xrightleftharpoons{K_c} 2\,[\text{M-L-M}^{+}]$$

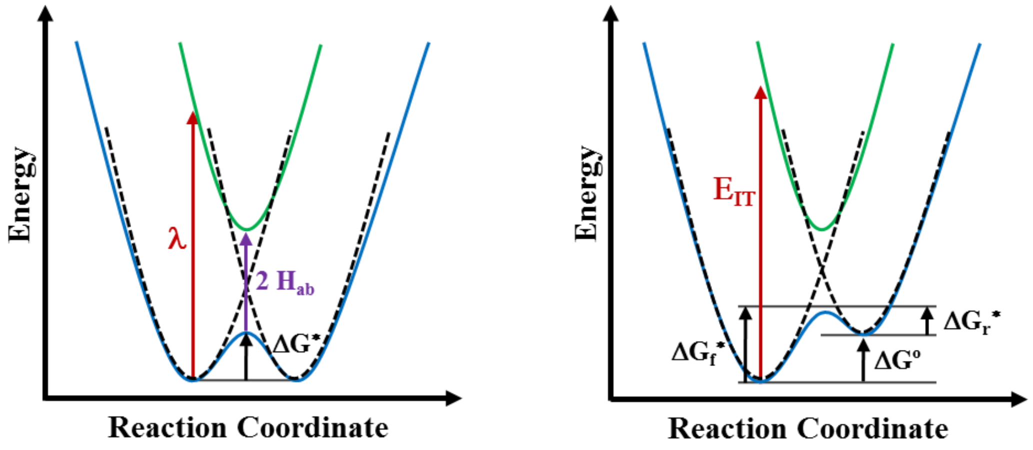

Figure 4.3. Marcus–Hush potential energy surfaces applied for (left) symmetrical and (right) non-symmetric systems.

Moreover, homobimetallic *dimers-of-dimers* reported so far are characterized to be symmetrical systems. The study of electronic communication in non-symmetric analogues has not been fully explored with only few examples in the literature.[154,155] According to Marcus theory, the main difference between symmetric and non-symmetric systems is the relative free energy of the parabolic wells, as depicted in Figure 4.3, considering that the donor and the acceptor are no longer equivalents. This could potentially decrease the activation energy required by increasing the electronic coupling and making the electron transfer process faster.

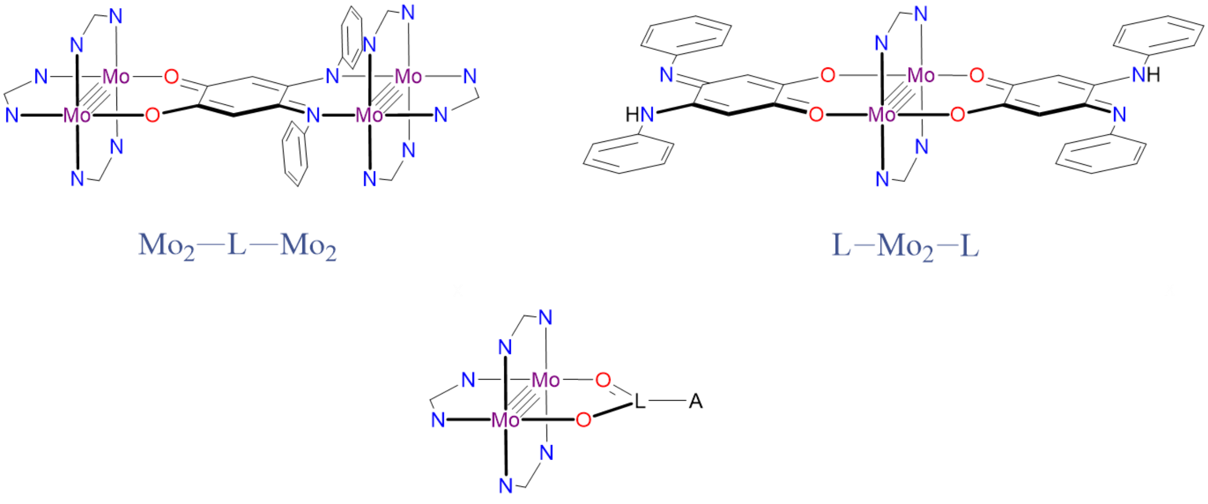

Mo_2—L—Mo_2

L—Mo_2—L

Mo_2—L—A

Scheme 4.4. Non-symmetric D–B–A systems.

We are interested in understanding the effect of non-symmetry on the electronic coupling of the donor and acceptor sites. In order to make non-symmetric complexes, either the metal unit or the bridging ligand can be asymmetrical (Scheme 4.4). In an attempt to obtain non-symmetric metal centers, a fullerene derivative and a non-symmetrical ligand were employed. The former would allow the study of the effect of a non-metallic redox active center in the electron transfer process. In contrast, the latter would allow the incorporation of a single metal as the second building unit by monodeprotonation of the ligand. By doing this, we could putatively tune the electronics of the system according to the metal used. On the other hand, making the bridging ligand non-symmetric facilitates the synthesis of the complexes by using the same procedure for preparation of the symmetric analogues.

4.2 EXPERIMENTAL SECTION

4.2.1 Materials and Methods.

All reactions and manipulations were conducted under a nitrogen atmosphere, using either a nitrogen drybox or standard Schlenk line techniques unless otherwise noted. Solvents used were purified under argon using a Pure Process Technology solvent purification system, or degassed under nitrogen. Commercially available chemicals methylithium (MeLi) and sodium methoxide ($NaOCH_3$) were purchased form Sigma Aldrich and used as received. The starting materials: *N*,*N*-dianisylformamidine (HDAniF)[156], $Mo_2(DAniF)_3(OAc)$[157], **I**, trans-$Mo_2(DAniF)_2(O_2CCH_3)_2$[158], **II**, 2,5-dihydroxy-4-phenylimino-2,5-cyclohexadien-1-one[159], **III**, and 2-hydroxy-5-phenylamino-4-phenylimino-2,5-cyclohexadien-1-one[159], **IV**, were prepared following reported procedures. The carboxylic fullerene derivative, **V**, was synthesized by Catalina Suarez from the Echegoyen group according reported procedure.[160]

4.2.2 Physical Measurements.

^{1}H NMR spectra were recorded on a Bruker 300 MHz and 400 MHz NMR spectrometer with chemical shifts (δ) referenced to the residual signal of $CDCl_3$ or C_6D_6. The Infrared spectra were measured on an Agilent Cary 630 FTIR Spectrometer. UV–Vis spectra were obtained using a SEC2000 Spectra System equipped with the Visual Spectra 2.1 software. Raman spectra were recorded on a Thermo Scientific DXR SmartRaman spectrometer using a laser at 532 nm. Matrix–

assisted laser desorption ionization (MALDI) mass spectra were collected using a Bruker Microflex LRF mass spectrometer.

4.2.3 Electrochemical Studies.

Electrochemical analyses by cyclic voltammetry (CV) and differential pulse voltammetry (DPV) were collected by using a CHI760D potentiostat with a Pt working and auxiliary electrodes, a Ag/AgCl reference electrode, 1mM solution of the compounds, and 0.10 M Bu_4NPF_6 (in THF or DCM) as electrolyte. Data was obtained with a scan rate of 100 mV/s. Ferrocene was added at the end of the run and used as internal standard.

4.2.4 X–Ray Structure Determination.

Crystals of **4** suitable for X–Ray diffraction analysis were prepared by diffusion of hexanes into a solution of **4** in THF. The crystal was mounted with a small amount of silicone grease and centered in the goniometer of a Bruker SMART APEX CCD system equipped with a graphite monochromator and a MoKα fine-focus tube (λ = 0.71073 Å). Data for the crystals was collected at 100 K. No crystal decay was observed during the collection. The frames were integrated with the Bruker SAINT Software package using a narrow-frame algorithm. Data were corrected for absorption effects using the multi-scan method (SADABS). The structure was solved and refined by direct methods using the Bruker SHELXTL Software Package. Crystallographic data for **4** is listed in Table 4.2, and relevant bond distances and angles for this compound are given in Table 4.3.

4.2.5 Synthesis of $[Mo_2(DAniF)_3]_2(C_{12}O_3NH_7)$, 1.

2,5-dihydroxy-4-phenylimino-2,5-cyclohexadien-1-one (16.0 mg, 0.074 mmol) and $Mo_2(DAniF)_3(OAc)$ (151 mg, 0.150 mmol) were placed in a 50 mL Schlenk flask with 10 mL of

THF. $NaOCH_3$ (0.45 mL) was then added to the flask slowly with stirring. The reaction mixture was then stirred for 5h at room temperature. The solvent was removed under reduced pressure and benzene was used to extract the compound. $[Mo_2(DAniF)_3]_2(C_{12}O_3NH_7)$, **1**, was washed with ether and hexanes. Yield: 171 mg, 54 %. ^1H NMR (δ – C_6D_6): 8.68 (s, 4H), 8.51 (s, 2H), 7.03 (s, 1H), 7.01 (s, 1H), 6.82-6.38 (53H), 3.22 (s, 24H), 3.18 (s, 12H). MALDI–TOF MS (m/z): Calcd. 2129.35 $[M+H^+]$, Found 2129.35 $[M+H^+]$. UV-Vis λ_{max}: 490, 420 nm.

4.2.6 Synthesis of $[Mo_2(DAniF)_3]_2(C_{18}O_2N_2H_{12})$, 2.

2-hydroxy-5-phenylamino-4-phenylimino-2,5-cyclohexadien-1-one (16.0 mg, 0.05 mmol) and $Mo_2(DAniF)_3(OAc)$ (112 mg, 0.110 mmol) were placed in a 50 mL Schlenk flask and dissolved in 10 mL THF. $NaOCH_3$ (0.4 mL) was then added to the reaction mixture slowly and with stirring. The mixture was stirred for 5h at room temperature. The solvent was removed under reduced pressure and benzene was used to extract the compound. $[Mo_2(DAniF)_3]_2(C_{18}O_2N_2H_{12})$, **2**, was washed with ether and hexanes. Yield: 141 mg, 58 %. ^1H NMR (δ – C_6D_6): 8.68 (s, 4H), 8.43 (s, 2H), 7.11 (s, 1H), 7.10 (s, 1H), 6.78–6.25 (58H), 3.24–3.10 (36H). MALDI–TOF MS (m/z): Calcd. 2205.4 $[M+H^+]$, Found 2205 $[M+H^+]$. UV–Vis λ_{max}: 704, 420 nm.

4.2.7 Synthesis of $Mo_2(DAniF)_3(C_{69}O_2NH_8)$, 3.

To a mixture of $Mo_2(DAniF)_3(OAc)$ (8.60 mg, 0.008 mmol) and the fullerene derivative (7.5 mg, 0.008 mmol) in 2 mL THF, $NaOCH_3$ (0.02 mL) was added slowly with stirring. The reaction mixture was stirred at room temperature for 2h. The solvent was then removed under reduced pressure and the residue was extracted with 5 mL DCM. Filtration and precipitation with hexanes yielded $Mo_2(DAniF)_3(C_{69}O_2NH_8)$, **3**. Yield: 2.33 mg, 15 %. ^1H NMR (δ – $CDCl_3$): 8.38 (s, 1H), 8.0 (s, 2H), 7.71 (d, 4H), 6.99 (d, 8H), 6.86 (d, 8H), 6.42 (d, 4H), 6.37 (d, 4H), 3.90 (s, 4H), 3.79 (s, 12H), 3.61 (s, 6H). MALDI–TOF MS (m/z): Calcd. 1842.2 [M+H$^+$], Found 1841.56 [M+H$^+$]. UV-Vis λ_{max}: 450 nm.

4.2.8 Synthesis of $Mo_2(DAniF)_3(C_{18}O_2N_2H_{12})$, 4.

2-hydroxy-5-phenylamino-4-phenylimino-2,5-cyclohexadien-1-one (29.8 mg, 0.103 mmol) and $Mo_2(DAniF)_3(OAc)$ (112 mg, 0.110 mmol) were placed in a 50 mL Schlenk flask and dissolved in 10 mL THF. $NaOCH_3$ (0.21 mL) was then added to the reaction mixture slowly and with stirring. The mixture was stirred for 5h at room temperature. The solvent was removed under reduced pressure and benzene was used to extract the compound. $Mo_2(DAniF)_3(C_{18}O_2N_2H_{12})$, **4**, was washed with ether and hexanes. Yield: 130 mg, 94 %. ^{1}H NMR (δ – $CDCl_3$): 8.70 (s, 1H), 8.45 (s, 1H), 8.32 (s, 2H), 7.41 (t, 4H), 7.36 (s, 2H), 7.22 (d, 4H), 7.11 (t, 2H), 6.57 (d, 8H), 6.43 (d, 8H), 6.21 (d, 4H), 6.18 (d, 4H), 3.72 (s, 12H), 3.66 (s, 6H). ESI MS (m/z): Calcd. 1247.25 [M+H$^+$], Found 1247.5 [M+H$^+$]. UV–Vis λ_{max}: 768 nm, 436 nm.

4.2.9 Synthesis of trans-$Mo_2(DAniF)_3[C_{18}O_2N_2H_{12}]_2$, 5.

2-hydroxy-5-phenylamino-4-phenylimino-2,5-cyclohexadien-1-one (148 mg, 0.512 mmol) and trans-$Mo_2(DAniF)_2(O_2CCH_3)_2$ (200 mg, 0.244 mmol) were placed in a 50 mL Schlenk flask and dissolved in 10 mL THF. $NaOCH_3$ (1.02 mL) was then added to the reaction mixture slowly and with stirring. The mixture was then stirred for 5h at room temperature. The solvent was removed under reduced pressure. DCM was added to extract the compound, followed by reduction of the solution (about 5 mL). Ethanol (50 mL) was added to precipitate the compound, which was later washed with ethanol and hexanes. $Mo_2(DAniF)_3[(C_{18}O_2N_2H_{12})]_2$, **5**, was washed with ether and hexanes. Yield: 300 mg, 95 %. ^{1}H NMR (δ – $CDCl_3$): 8.32 (s, 2H), 8.20 (s, 2H), 7.36 (s, 4H), 7.05 (d, 8H), 6.88 (t, 8H), 6.81 (d, 8H), 6.72 (d, 8H), 6.42 (t, 4H), 3.71 (s, 12H). UV–Vis λ_{max}: 727 nm, 394 nm.

4.3 COMPUTATIONAL DETAILS

Density Functional Theory (DFT) calculations were performed with the hybrid Becke–3 parameter exchange functional and the Lee-Yang-Parr nonlocal correlation functional (B3LYP) [110,111] implemented in the Gaussian 09 (Revision C.01)[114114] program suit. The Pople basis set, 6–31G*,[113,119,120] was used on non-metal atoms (carbon, nitrogen, oxygen, and hydrogen). An effective core potential (ECP) representing the $1s^2s^2p^3s^3p^3d^4p$ core was used for the molybdenum atoms, along with the associated double-ζ basis set (LANL2DZ).[161–164] Geometry optimization calculations were found to be minima in the potential energy surface as evidenced by the absence of imaginary vibrations in the frequency calculations. Electronic transition energies were computed for the neutral compounds using Time–Dependent Density Functional Theory (TD–DFT) method with the lowest 30 singlet excited states being considered.[165–171] All calculations were performed in a 44-processor PowerWolf PSSC supercomputer cluster running Linux Red Hat 4.1.2-54 located at the University of Texas at El Paso. Isosurface plots of frontier molecular orbitals were generated using the Avogadro software with isodensity values of 0.04.

4.4 RESULTS AND DISCUSSION

4.4.1 Non-symmetrical Mo_2 Dimer-of-Dimers, Mo_2–L–Mo_2 system

Molecular Design and Synthesis. As previously stated, an asymmetrical D–B–A system can be prepared by (1) connecting two identical redox centers to an asymmetric bridging ligand or (2) connecting different redox centers to a symmetrical bridging ligand. In the first section of this chapter, the study of electron transfer by a *dimer-of-dimers* will be done. Dianions of carboxylic acids, which led to low K_c values, are the commonly used ligands in this type of systems.[172,173] The dioxolene group and its derivatives have shown strong electronic communication between Mo_2 units.[174] Amidinates on the other hand, are attractive due to their stronger Lewis basicity when compared to their carboxylates analogues as well as their ability to modify the R substituent in the N atoms.[152,175,176]

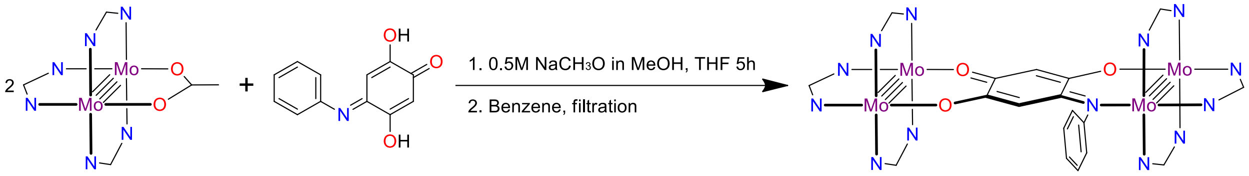

Scheme 4.5. Reaction conditions for synthesis of **1**.

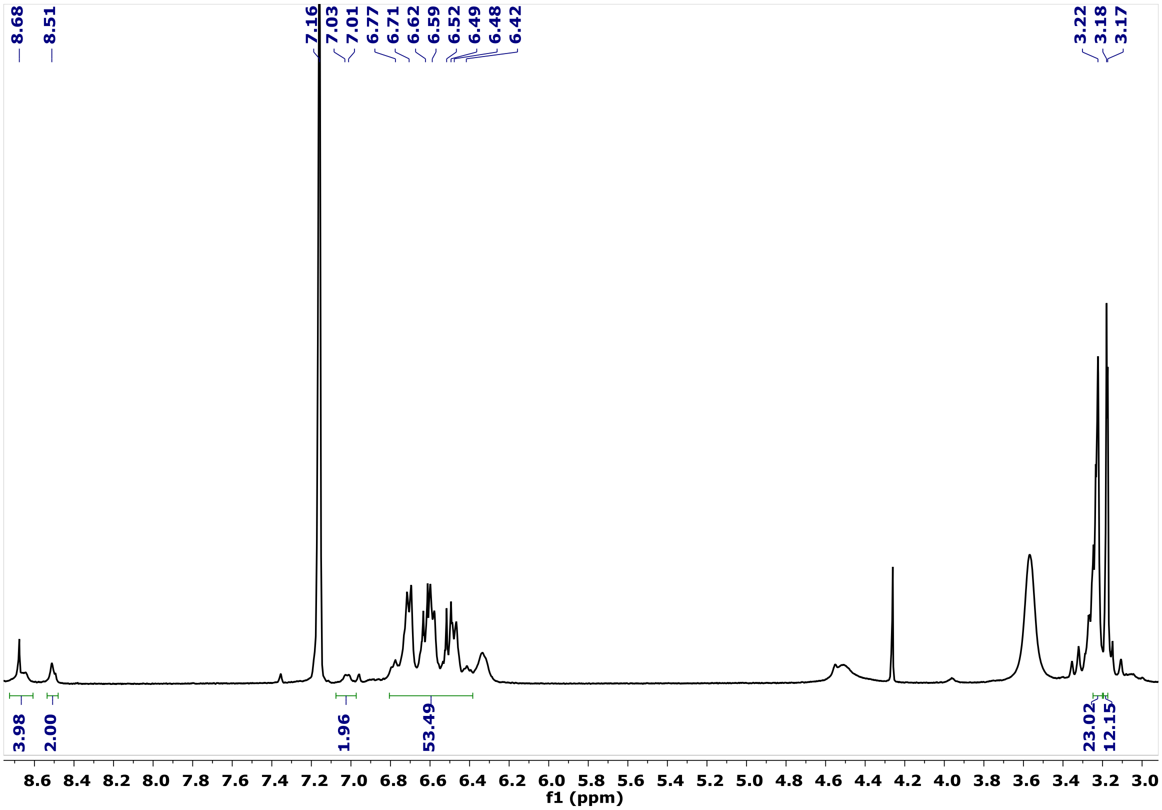

Figure 4.4. ^{1}H NMR for **1** in C_6D_6.

Compounds **1** and **2** were prepared by assembling two $[Mo_2(DAniF)_3]^+$ units with a non-symmetrical ligand. The coordination of the ligand yields products with two six-membered rings. The successive introduction of N atoms yielded two asymmetrical complexes, $[Mo_2(DAniF)_3]_2(C_{12}O_3NH_7)$, **1**, and $[Mo_2(DAniF)_3]_2(C_{18}O_2N_2H_{12})$, **2**. This method gives the advantage of performing the synthesis of the complexes in a one-pot reaction (Scheme 4.5 and Scheme 4.6) similar to the method developed for symmetric *dimers-of-dimers*.[177]

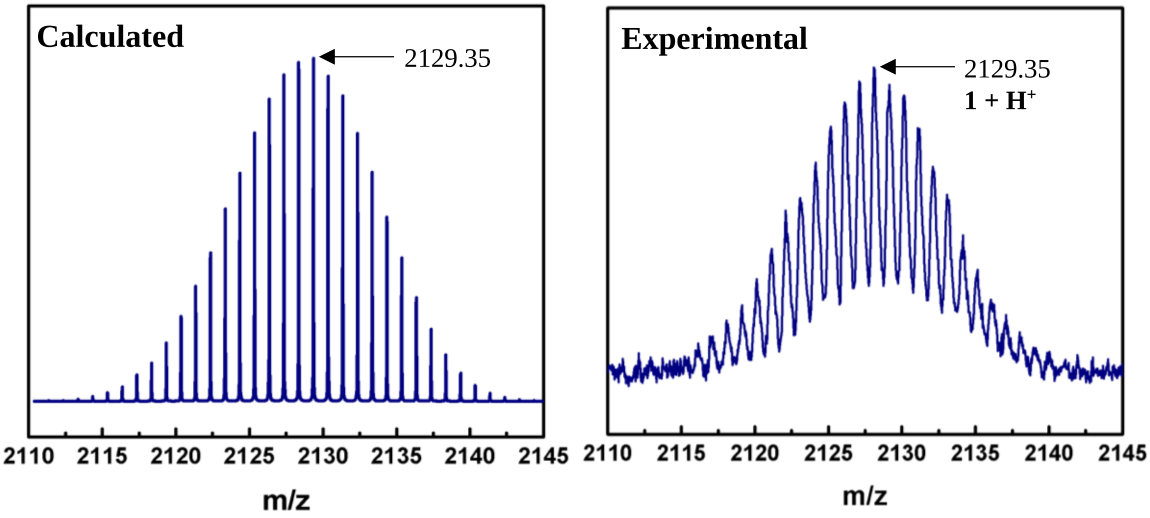

Figure 4.5. MALDI–TOF mass spectrum of **1**. (left) Average m/z calculated at 2129.35, and (right) detected m/z 2129.35.

The structure of $[Mo_2(DAniF)_3]_2(C_{12}O_3NH_7)$, **1**, in solution was confirmed by ^{1}H NMR spectroscopy, however the crystal structure for this compound was not obtained. The proton NMR is consistent with the structure of the molecule, with all signals having the expected chemical shifts (ppm) and relative intensities as presented in Figure 4.4. MALDI–TOF MS was performed for this complex, both the isotopic distribution and the predicted mass (m/z value calculated = 2129.35, experimental = 2129.35) were obtained and compared, as shown in Figure 4.5.

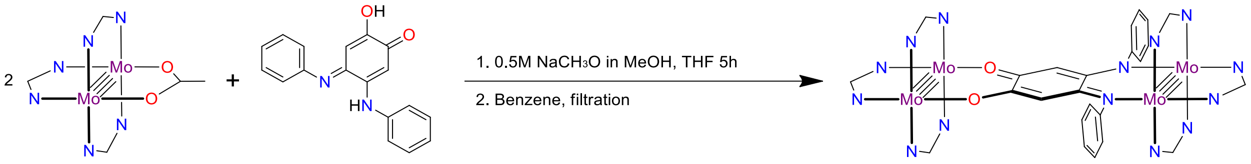

Scheme 4.6. Reaction conditions for synthesis of **2**.

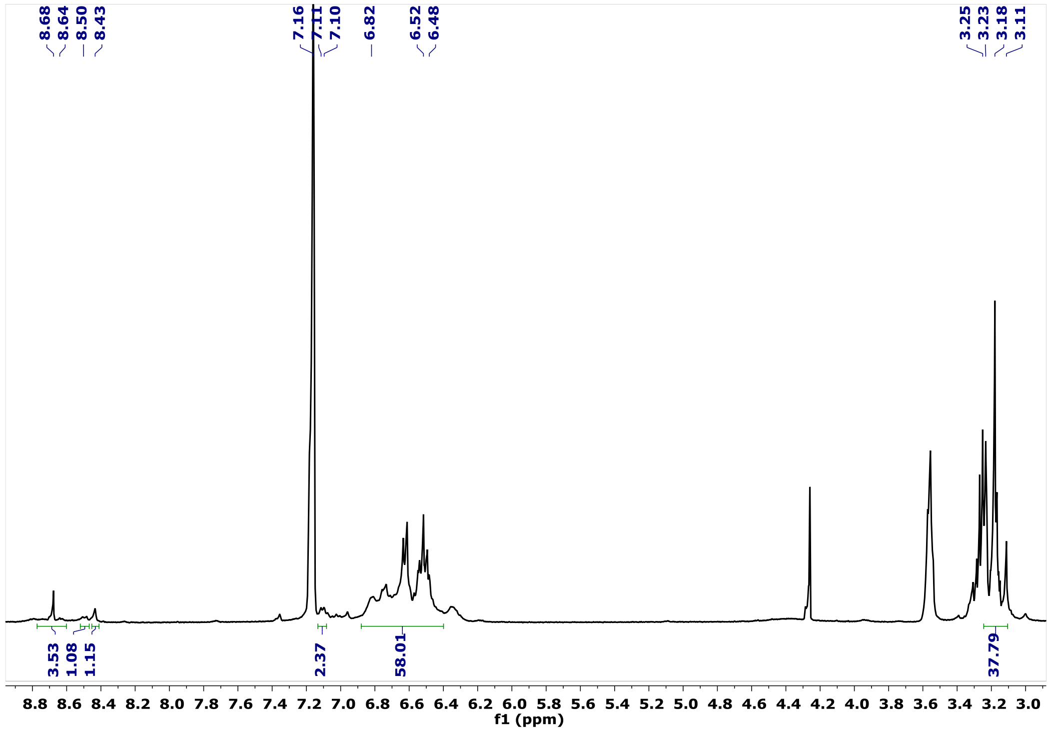

Figure 4.6. ^{1}H NMR for **2** in C_6D_6.

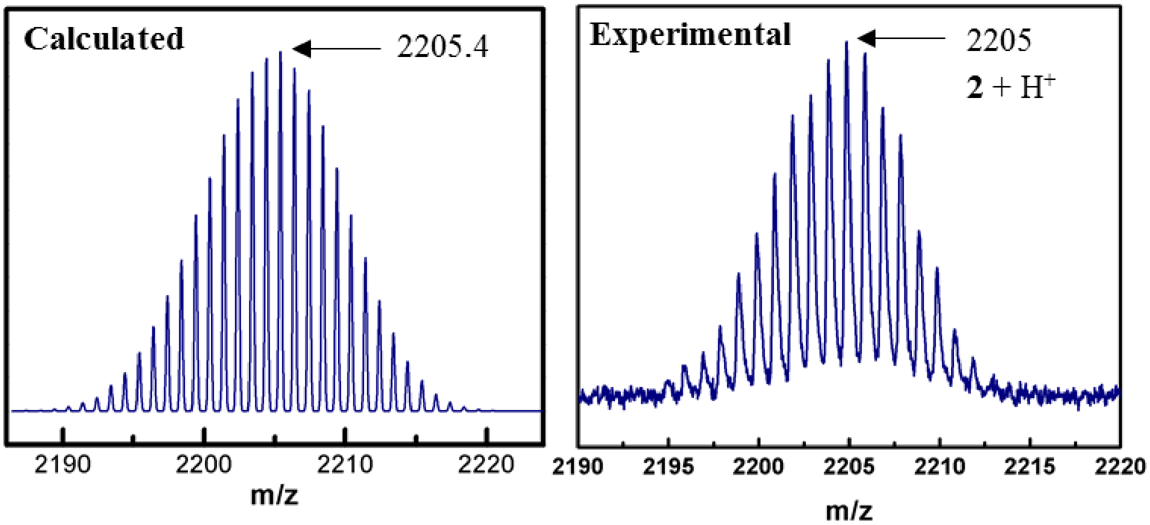

Figure 4.7. (Left) Calculated MS **2** with m/z value of 2205.4. (Right) MALDI–TOF mass spectra of **2** m/z found 2205.

The ^{1}H NMR of $[Mo_2(DAniF)_3]_2(C_{18}O_2N_2H_{12})$, **2**, (Figure 4.6) is consistent with the structure of the molecule. In addition, all the signals have the expected chemical shifts (ppm) and relative intensities. MALDI-TOF mass spectroscopy was performed on **2**, and is presented in Figure 4.7. Similar to what was observed for compound **1**, both the expected isotopic distribution and the predicted m/z for **2** (m/z value calculated = 2205.4, experimental = 2205) were observed.

Electrochemical Studies. The magnitude of the electronic communication in a Mo_2–L–Mo_2 system is mainly determined by two factors: the distance between the two Mo_2 units, and the nature of the linker.[157] The 2,5-dihydroxy-1,4-benzoquinone (H_2dhbq) ligand and its analogues have been reported to favor strong electronic communication in *dimers-of-dimers* because they present extended π* orbitals with energies similar to those of the transition metal orbitals.[178] Although several transition metal complexes with $dhbq^{2-}$ have been reported, only one non-symmetric analogue has been used in Mo_2–L–Mo_2 systems.[179]

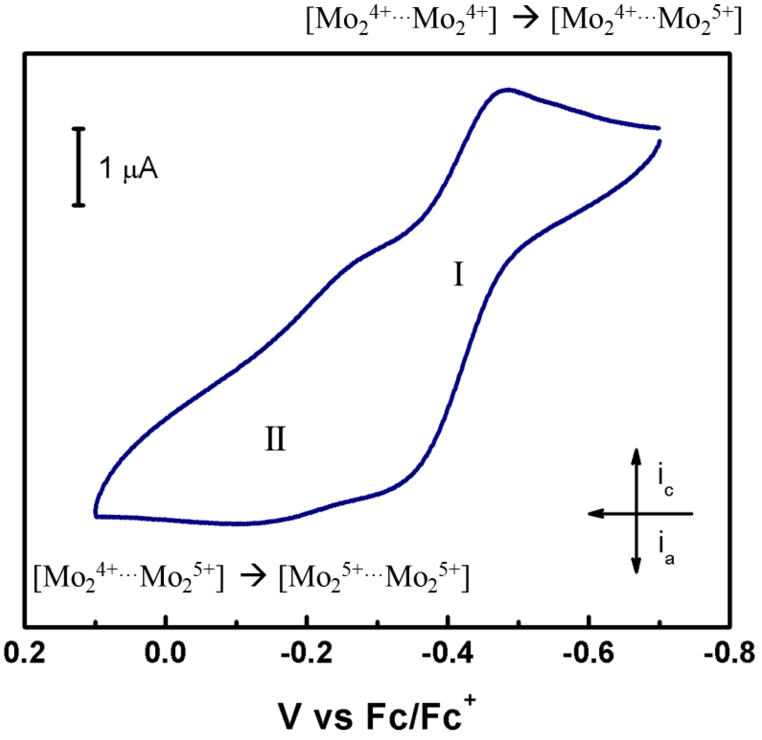

Figure 4.8. The cyclic voltammogram of **1**, with $E_{1/2}$ (I) = –0.405 V and $E_{1/2}$ (II) = –0.180 V. Data was obtained in THF solution with potentials referenced to Fc/Fc^+.

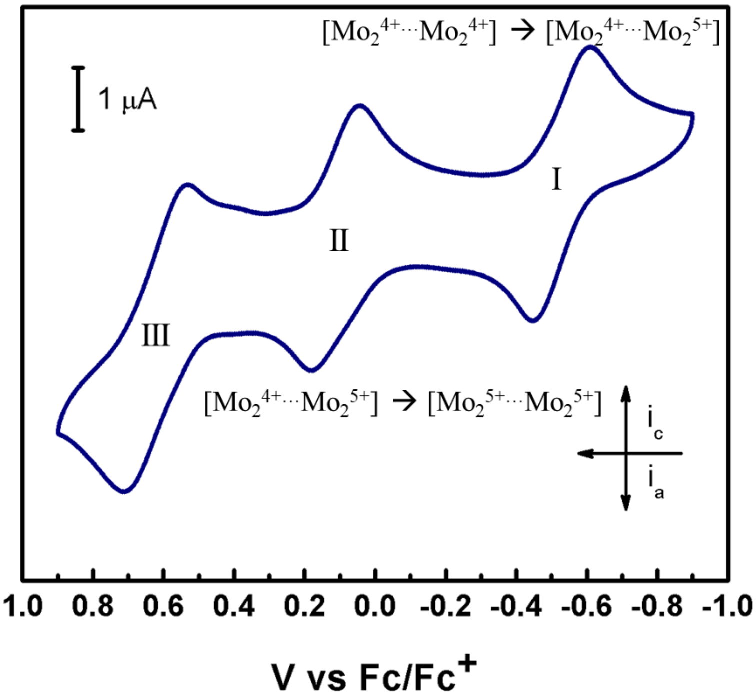

Figure 4.9. Cyclic voltammogram of **2**, with $E_{1/2}$ (I) = –0.523 V, $E_{1/2}$ (II) = 0.112 V and $E_{1/2}$ (III) = 0.625 V. Data was obtained in THF solution with potentials referenced to Fc/Fc^+.

Cyclic voltammetry was performed on **1** in order to evaluate the degree of communication in the Mo_2–L–Mo_2 system. Figure 4.8 presents two one-electron oxidations of the dinuclear metal centers for **1**, at $E_{1/2}$ (I) = –0.405 V vs Fc/Fc^+ corresponding to $[Mo_2^{4+}–L–Mo_2^{4+}] \rightarrow [Mo_2^{5+}–L–Mo_2^{4+}]$ and $E_{1/2}$ (II) = –0.180 V vs Fc/Fc^+ for $[Mo_2^{5+}–L–Mo_2^{4+}] \rightarrow [Mo_2^{5+}–L–Mo_2^{5+}]$. Cyclic voltammetry was performed on **2** in order to study the electronic interactions between the metal centers, and it is presented in Figure 4.9. Interestingly, three one-electron reversible oxidations with $E_{1/2}$ (I) = –0.523 V, $E_{1/2}$ (II) = 0.112 and $E_{1/2}$ (III) = 0.625 V vs Fc/Fc^+ are observed in the window provided by THF. Cyclic voltammetry of the ligand proves that the third oxidation event of **2** is ligand based, which exhibits an oxidation event at 0.625 V vs Fc/Fc^+. Therefore, the first two oxidations in **2** are metal based corresponding to $[Mo^{4+}–Mo^{4+}] \rightarrow [Mo^{5+}–Mo^{4+}]$ and $[Mo^{5+}–Mo^{4+}] \rightarrow [Mo^{5+}–Mo^{5+}]$. The potential separations ($\Delta E_{1/2}$) between the Mo_2 redox sites are within the range of the symmetrical analogue.[174] The CV of **2** shows the oxidation potentials for the two dimolybdenum units are separated by 635 mV. The internal potential difference between the bimetallic centers increases the potential separation and the electronic interaction. Replacing two O atoms by N atoms increases the $\Delta E_{1/2}$ value to 635 mV (**2**) from 225 mV in the monosubstituted version **1**.

The comproportionation constant (K_c) and the free energy changes ($\Delta G^o{}_c$) are derived from the electrochemical data obtained, $\Delta E_{1/2}$ (Table 4.1). A $\Delta G^o{}_c$ larger than 10^3 for an asymmetrical complex indicates that the singly oxidized *dimer-of-dimer* is thermodynamically more stable in solution.[180] K_c for the comproportionation equilibrium involving the species studied can be derived from the separation of the potentials between the two redox couples ($\Delta E_{1/2}$). The equilibrium constant is exponentially related to $\Delta E_{1/2}$ ($K_c = e^{\Delta E1/2\ /\ 25.69}$), and it measures the stability of the mixed-valent species [Mo^{5+}–L–Mo^{4+}]. Calculation of K_c using $\Delta E_{1/2}$ = 225 mV, gives a value of $K_c = 6.36 \times 10^3$. According to the Robin–Day classification, this compound belongs to Class II meaning the Mo_2 units present low electronic coupling. On the other hand, K_c for **2** is derived to be 5.4×10^{10}. The magnitude of the equilibrium constant indicates that both bimetallic units, which are linked by the conjugated organic ligand, are strongly coupled, and according to the Robin–Day scheme it belongs to a Class III complex.

Table 4.1. Derived thermodynamic parameters for the comproportionation equilibriums from the electrochemical measurements of **1** and **2**.

	$\Delta E_{1/2}$ (mV)	K_c	$\Delta G^\circ{}_c$ (cm^{-1})
1	225	6.36×10^3	–1814
2	635	5.43×10^{10}	–5116

Spectroscopic Properties. The asymmetric compounds show dark green color. The electronic spectra for the neutral complexes, **1** and **2**, show a pronounced absorption in the visible region and a high energy absorption in the ultraviolet region. Figure 4.10 show the absorption spectra for **1** and its precursors. There is no low energy absorption observed for **I**, and the shoulder at 445 nm is known to be the δ → δ∗ transition arising from an electron excitation from HOMO to LUMO, while the ligand shows a π → π∗ transition at 498 nm.

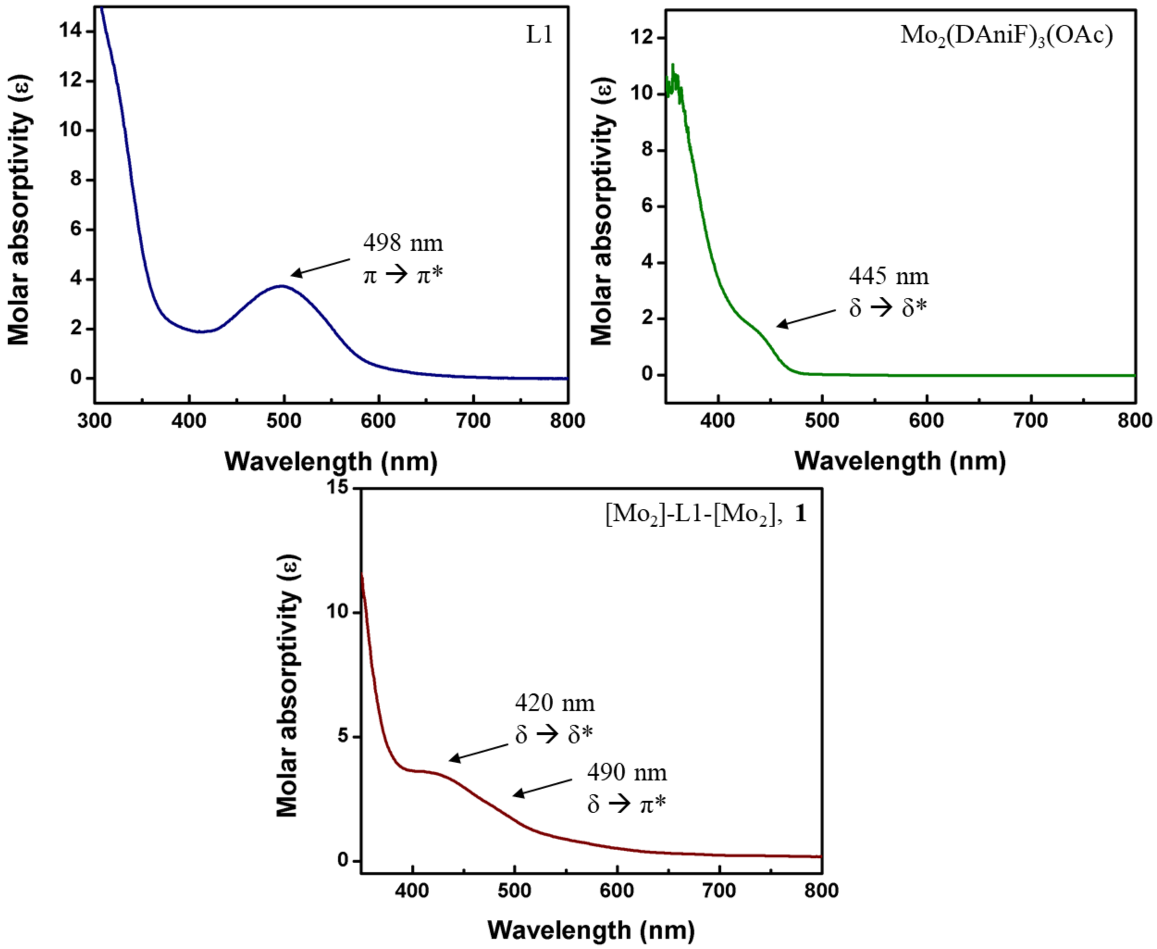

Figure 4.10. Absorption spectra for (Top left) Ligand, (Top right) **I**, and (Bottom) **1** in solvent.

It has been found that for symmetric compounds of the M_2–L–M_2 type, a δ → π∗ transition corresponding to the metal-to-ligand charge transfer (MLCT) dominates the electronic spectra in the visible region.[151,154] This is a consequence of the interaction between the δ-orbital of the Mo_2 unit and the π-orbital of the linker, where the π∗ orbital of the ligand is lower in energy than the δ∗ orbital of the metal. The symmetrical dioxolene presents an absorption band at 1128 nm related to the HOMO → LUMO excitation. Similarly, compound **1** presents an absorption band at 490 nm assigned to the MLCT. Figure 4.11 displays the absorption spectra of **2** and its precursors. In this case, the ligand shows a π → π∗ transition at 360 nm, while **2** has a MLCT band at 704 nm. The existence of the low energy MLCT band is critical for the electronic communication between the bimetallic units by facilitating an electron-hopping or hole-hopping pathway.[181] These transitions in **1** and **2** are consistent with the strong electronic coupling in these compounds.

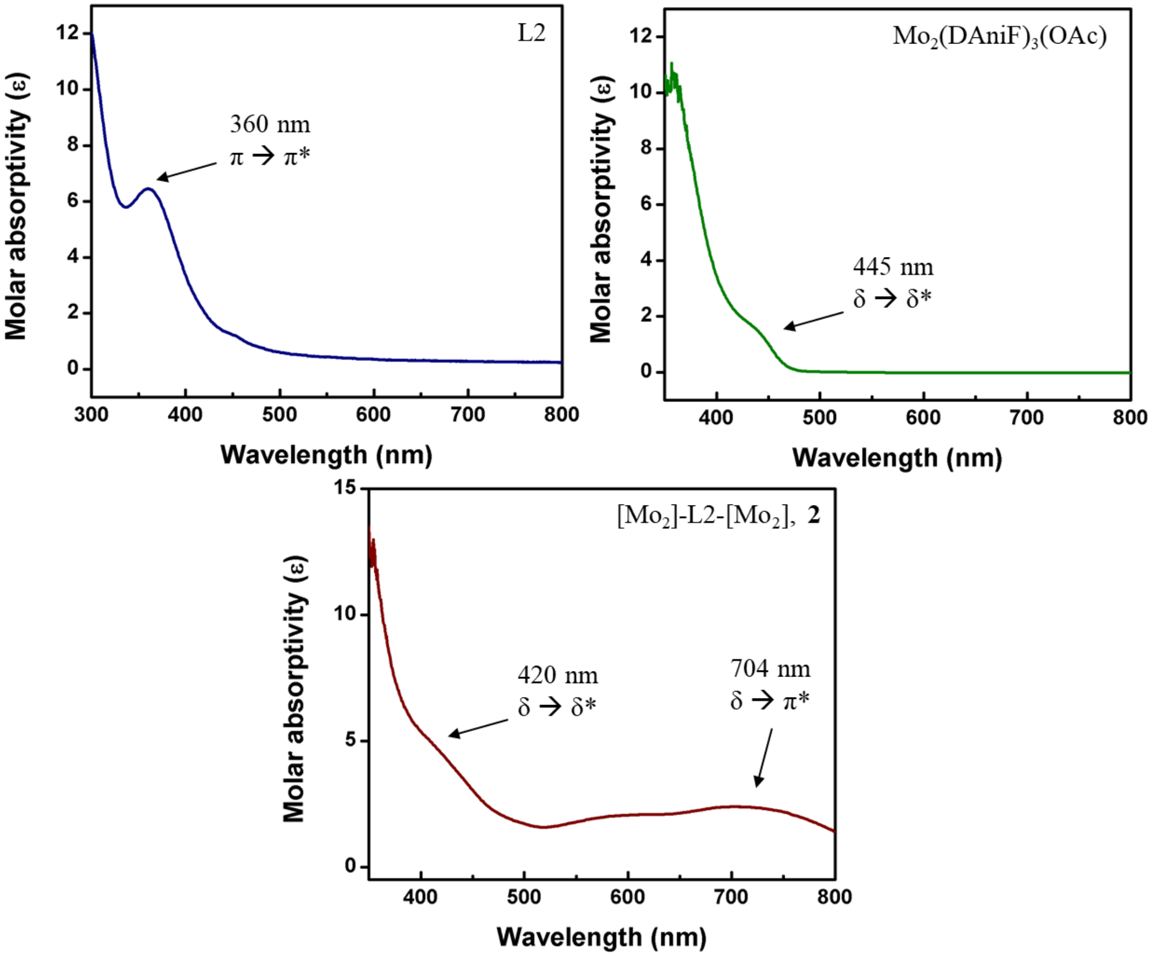

Figure 4.11. Absorption spectra for (Top left) Ligand, (Top right) **I**, and (Bottom) **2** in solvent.

DFT Calculations. Theoretical calculations were done to gain insight in the electronics of the system. The geometry optimizations were carried out on model compounds where the aryl groups of the formamidinates were replaced by H atoms. The vibrational frequency analysis on the optimized models indicated that the geometries are minima on the potential energy surfaces due to the absence of imaginary frequencies. In Mo_2–L–Mo_2 the frontier orbitals are typically composed of the in-phase and out-of-phase Mo_2 δ-orbitals interacting with the π-orbitals of the ligand. The greater the interaction between the dimolybdenum unit and the ligand the larger the HOMO–HOMO-1 separation due to orbital stabilization, decreasing thus the HOMO–LUMO energy gap ($\Delta E_{H\text{-}L}$) and enhancing the Metal-to-Ligand charge transfer (MLCT). For both compounds, the HOMO presents large metal contribution while the LUMO has mainly ligand character with small metal contribution from the dimolybdenum units. Therefore, as stated above, the HOMO → LUMO transition corresponds to a metal-to-ligand charge transfer band.

We can observe in Figure 4.12 that the HOMO-1 for **1** presents mixing of δ-orbital and the empty ligand π*-orbital. Molecular orbital analysis of the HOMO and HOMO-1 show that this orbitals are mainly metal based and their energy difference is 0.837 eV. The HOMO is formed by the in-phase combination of the δ-orbitals in the Mo_2 units which interact with the occupied π*-orbital of the linker. Meanwhile, the HOMO-1 and LUMO arise from the out-of-phase combination of the δ-orbitals of the Mo_2 units with an empty π* orbital of the linker. On the other hand, the LUMO and HOMO-2 are mainly ligand based. Significant ligand character is also present in the HOMO, which allows for electron delocalization between the two dimolybdenum units as observed experimentally.

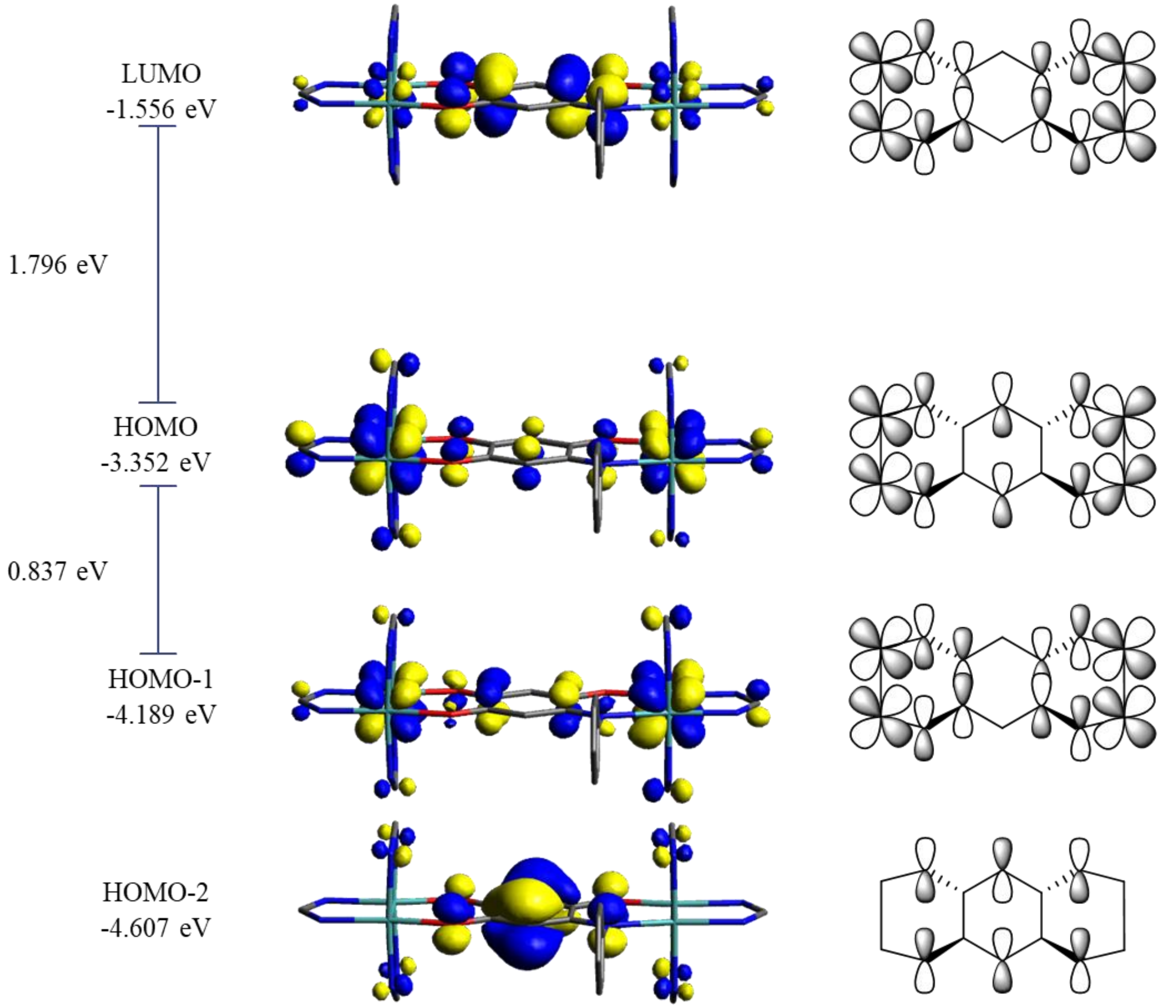

Figure 4.12. Contour plots and molecular orbital representation of four frontier orbitals for **1**, with energy for all orbitals.

Similarly to compound **1**, molecular orbital analysis of **2** (Figure 4.13) indicate the HOMO is formed by the in-phase combination of the δ-orbitals in the Mo_2 units, which interact with the occupied π* orbital of the linker. Again, the HOMO-1 and LUMO are formed by the out-of-phase combination of the δ-orbitals of the Mo_2 units with an empty π*-orbital of the linker. In the same way, the LUMO and HOMO-2 have mainly ligand character. Moreover, ligand character is also observed in the HOMO which allows for the electron delocalization detected experimentally.

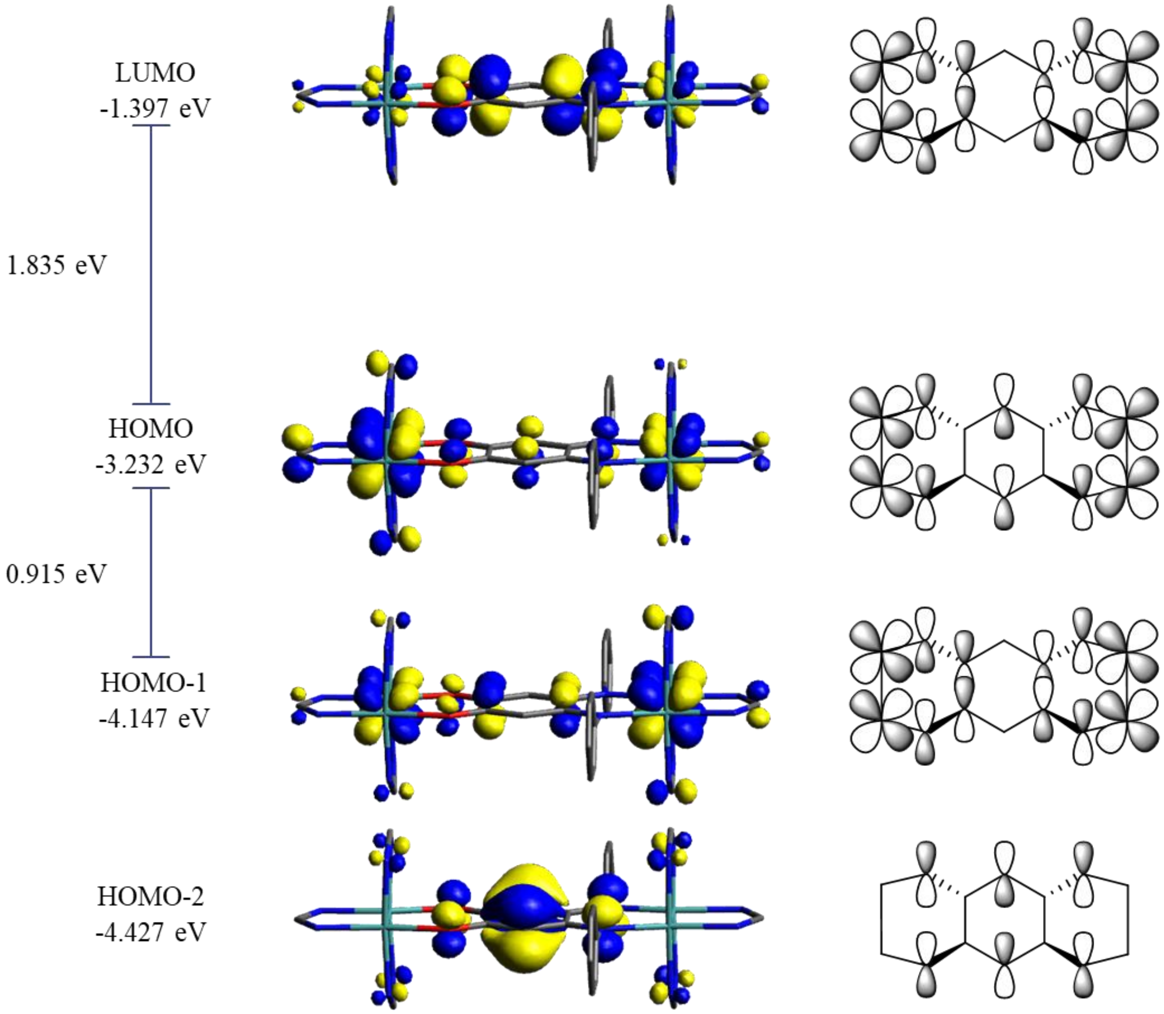

Figure 4.13. Contour plots and molecular orbital representation of four frontier orbitals for **2**, with energy for all orbitals.

The structure of the HOMO, as shown in Figure 4.12 and Figure 4.13, agree with a strong interaction between the dimolybdenum units and the linkers, with significant influence from the linker to both the HOMO and HOMO-1. The molecular orbitals show some asymmetrical character by presenting unbalanced electron density in the Mo_2 units and the ligand. On the HOMO for **1** and **2**, higher electron density is found on the Mo_2 site with more O atoms; while on the HOMO-1 the charge is distributed in the opposite manner.

The energy gap between the HOMO and HOMO-1 ($\Delta E_{H\text{–}H\text{-}1}$) is directly related to the interaction between the Mo_2 centers.[182–184] In the symmetric dioxolene analogue, the $\Delta E_{H\text{–}H\text{-}1}$ is 0.98 eV, the largest number obtained for dimers with Mo.[174] The calculated values for $\Delta E_{H\text{–}H\text{-}1}$ for **1** and **2** are 0.837 and 0.915 eV, respectively; suggesting the electronic coupling of the dimolybdenum units in **2** may be stronger than that on **1**. This result is consistent with the larger separation between the redox potentials waves in **2** than in **1**. In both systems, the energies of the linkers' π-orbitals are far-below the HOMO-1, indicating hole-hopping does not have a large contribution to the electronic coupling.

4.4.2 Electronic Communication between a Fullerene Derivative and a Dimolybdenum Unit, Mo_2–L–C_{60} system

Molecular Design and Synthesis. Dinuclear metallic systems, like the ones shown in the previous section, have been studied for the understanding of electronic communication in a D–B–A system. Relative to symmetrical systems, less work is known for the study of electron transfer through asymmetrical systems, especially those with mixed metallic and organic redox sites.[185–187] Therefore, the nature of the charge transfer in these systems in not well understood.

Fullerenes are well-known electron acceptors[188] which possess good thermal stability resulting in their application in organic solar cells[189] and superconductors[190]. These three-dimensional materials exhibit small reorganization energies during electron transfer processes, achieving ultrafast charge transfer.[191] In this section, we report the study of electron transfer through a non-symmetrical D–B–A system where a quadruple bonded dimolybdenum and a fullerene (C_{60}) serve as electron donor an acceptor, respectively. In an attempt to incorporate the two different redox sites to a single molecule, the C_{60} cage needed to be functionalized with a chelating group that could bind to the dimolybdenum unit. The synthesis for this fullerene derivative was carried out by the Echegoyen group at UTEP. The introduction of a pending carboxylate in the fullerene derivative allowed for the one-pot synthesis of the asymmetric complex using **I** as starting material (Scheme 4.7), similar to the preparation of **1** and **2** from the previous section. Compound **3** was obtained as an orange powder in 15% yield. The proposed structure of **3** was confirmed by spectroscopic analyses, ^{1}H NMR and MS.

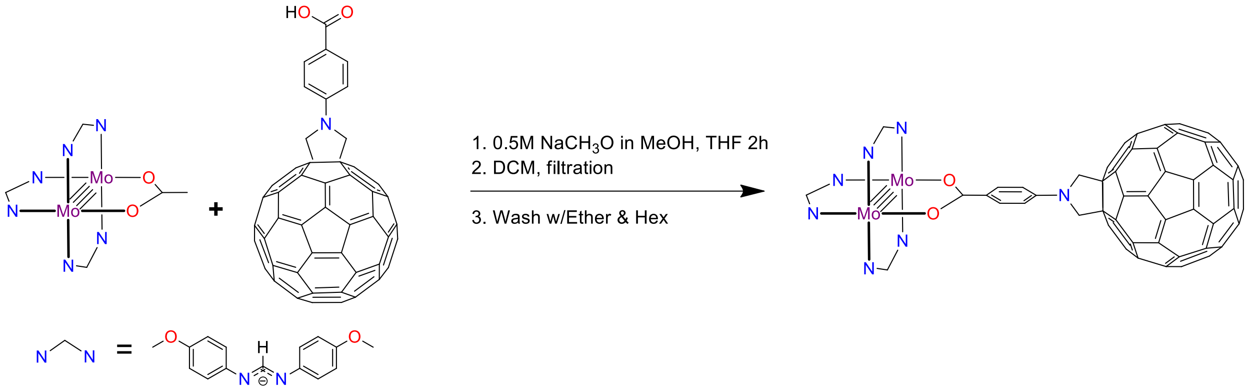

Scheme 4.7. Reaction conditions for synthesis of **3.**

For $Mo_2(DAniF)_3(C_{69}O_2NH_8)$, **3**, the room-temperature ^{1}H NMR is consistent with the structure of the molecule, with all signals having the expected chemical shifts (ppm) and relative intensities (2:1 ratio for the protons in the formamidinate ligands). Using ^{1}H NMR (Figure 4.14) we were able to identify different resonances corresponding to the carboxylate fullerene derivative and the bimetallic unit. There are two singlets at 8.38 ppm and 8.0 ppm that correspond to the protons of the formamidinate ligand. Additionally, there are two singlets at 3.79 ppm and 3.61ppm corresponding to the protons on methoxy group of the formamidinate ligands. On the other hand, the signal at 3.90 ppm is related to the protons from the pyrrolidine of the fullerene derivative. Moreover, the characteristic isotopic distribution for a complex presenting a dimolybdenum unit was observed in the mass spectra of **3**. The MALDI–MS in Figure 4.15 shows the calculated average mass of 1842.2, and the obtained m/z value of 1841.56 for **3**. Compound **3** is soluble in common polar solvents which facilitates the spectroscopic and electrochemical analysis. Although red crystals were obtained for **3**, the diffraction of the crystal was too weak to resolve the structure.

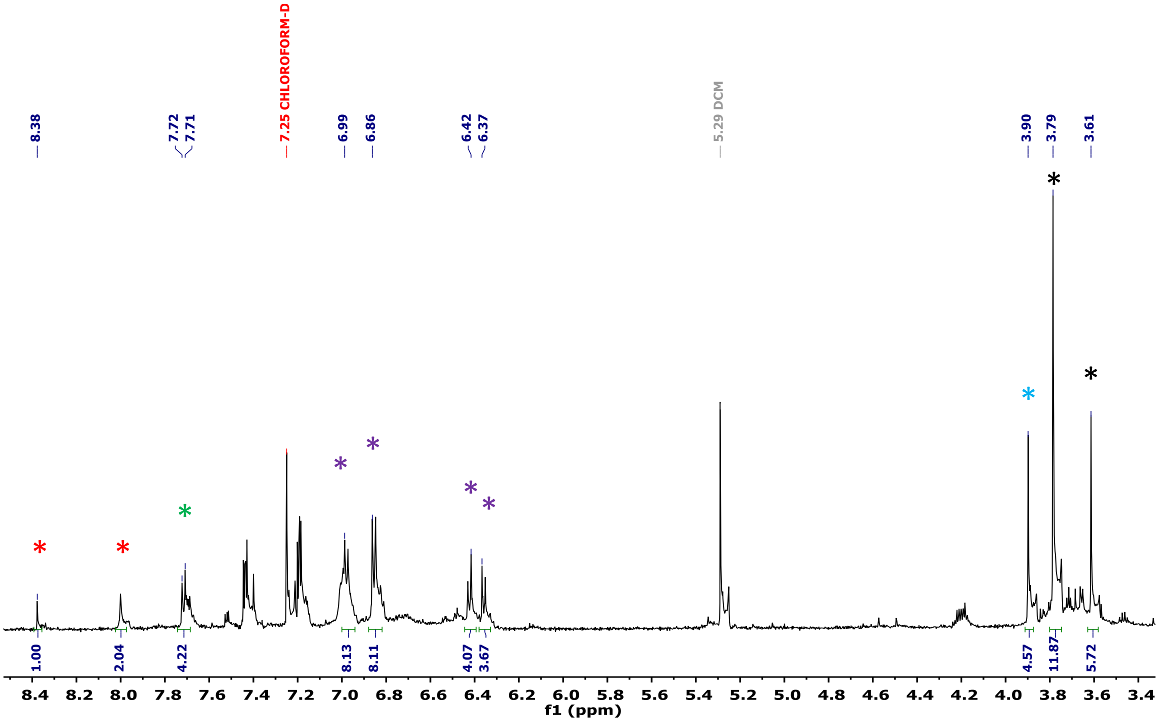

Figure 4.14. ^{1}H NMR for **3** in $CDCl_3$.

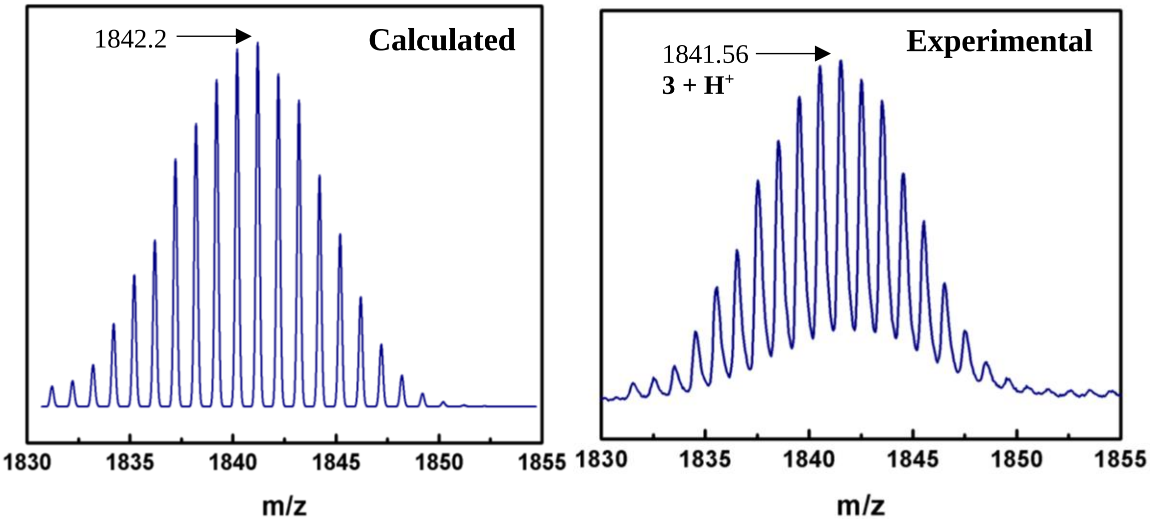

Figure 4.15. MALDI–TOF MS of **3** with m/z (left) calculated at 1842.2, and (right) detected at 1841.56.

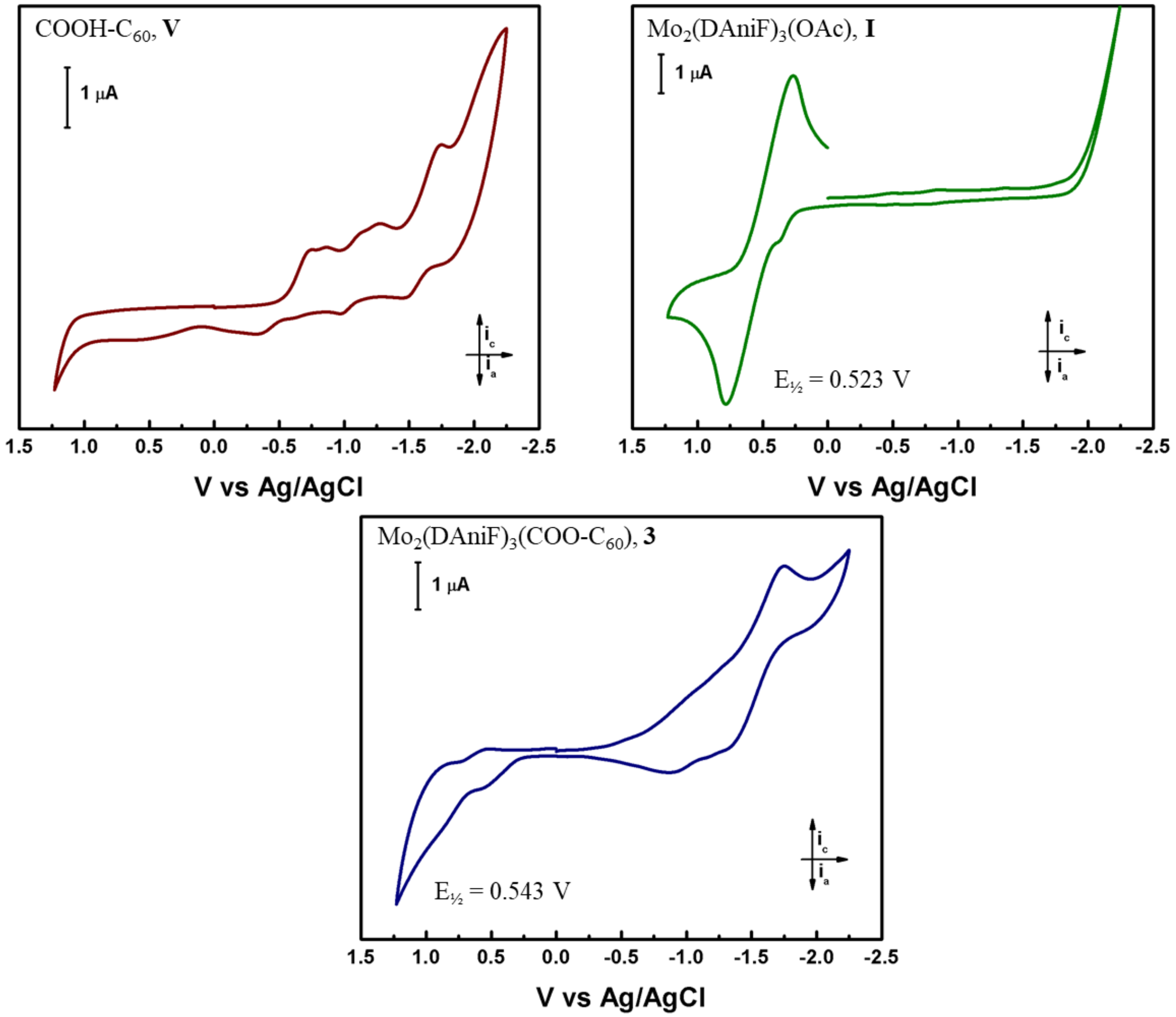

Figure 4.16. Cyclic voltammogram of (Top left) C_{60} derivative, (Top right) **I**, and (Bottom) **3**, with $E_{1/2} = –0.543$ V. Data was obtained in THF solution with potentials referenced to Ag/Ag$^+$.

Electrochemical Studies. Figure 4.16 displays the cyclic voltammograms (CV) for **I**, **V**, and **3** in THF. C_{60} fullerenes can be reduced by up to six electrons due to the presence of triply degenerate lowest unoccupied molecular orbitals.[192,193] The CV scan in the cathodic direction for **V** is dominated by four quasireversible reduction waves in the range of −0.5 to −2 V vs Ag/AgCl. Compound **3** show an amphoteric redox behavior with waves at both oxidation and reduction sides. This compound exhibits one reversible oxidation at $E_{1/2} = –0.543$ V vs Ag/AgCl, while the reduction events are dominated by C_{60} reduction waves. Quadruple-bonded dimolybdenum centers typically present a one-electron reversible event at 0.4–0.7 V vs Ag/AgCl.[185] This suggests the oxidation process found for **3** in Figure 4.16 corresponds to oxidation of the Mo_2 center due to the $Mo_2^{4+} \rightarrow Mo_2^{5+}$ process. Upon assembly of the fullerene derivative with the Mo_2 unit, the reduction processes of the fullerene cage differ from those observed for **V**. Two quasireversible reductions are observed in the CV for **3**. The integration of these waves, when compared to the one-electron oxidation of Mo_2, suggest that the reduction around –1.0 V and –1.5 V vs Ag/AgCl correspond to one- and three-electron transfer processes, respectively. Presumably, significant $Mo_2^{5+} \rightarrow C_{60}$ charge transfer occurs in the electrochemically generated radical species, and thus, the change in the reduction waves for the fullerene derivative could be attributed to electronic interaction between the donor and acceptor. Therefore, in the monocation radicals the organic redox center serves as electron acceptor, while the Mo_2 center is the electron donor.

Spectroscopic Properties. UV–Vis spectroscopy was done for **3** and its precursors, and their electronic spectra is presented in Figure 4.17. The carboxylic fullerene derivative (Top left) presents a strong band in the UV region, as well as two weak signals around 355 nm and 430 nm which are characteristic of fullerene mono-adducts.[194] $Mo_2(DAniF)_3(OAc)$, **I**, (Top right) shows a strong band in the UV region that corresponds to a metal-to-ligand charge transfer (MLCT) transition, as well as a weak band at 445 nm assigned to the $\delta \rightarrow \delta^*$ transition. The MLCT transition comes from the interaction between the δ orbital of the Mo_2 center and the π* orbital of the linker. The electronic spectrum of **3** (Bottom) presents a strong band in the UV region as well as a pronounced broad absorption band in the visible region. This band is likely due to the $\delta(Mo_2)$ to π^*(ligand) transitions (MLCT). This MLCT transition has been observed in other studies for dimolybdenum systems.[154,195–197] An additional absorption band around 350 nm is observed for **3**, which could be assigned to transitions within the ligand and C_{60}, similarly to that observed for **V**.

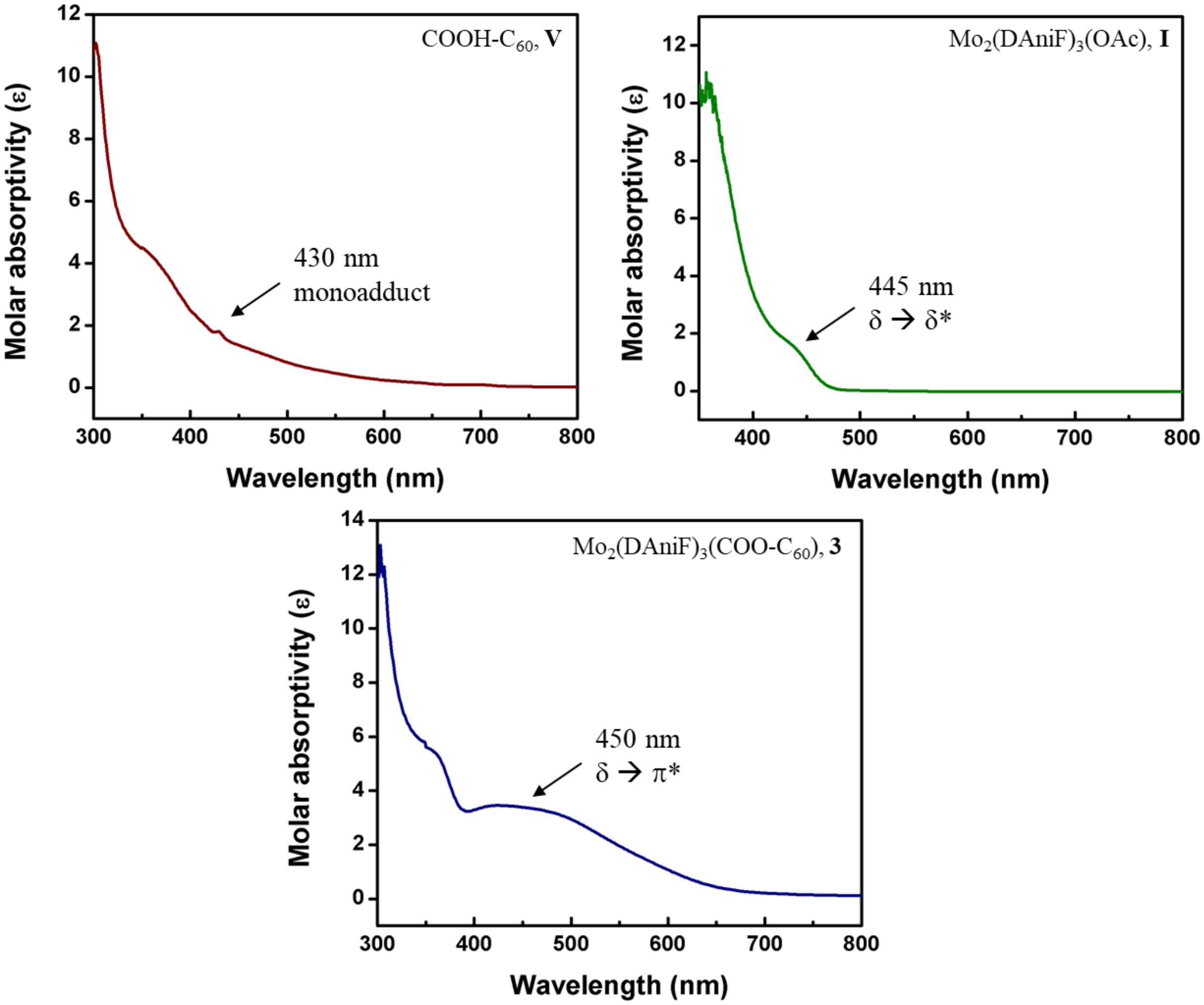

Figure 4.17. UV–Vis spectra of (Top left) C_{60} derivative, **V**, (Top right) **I**, and (Bottom) **3**.

DFT Calculations. Density Functional Theory (DFT) calculations were performed to gain insight into the ground state geometry, electronic structure, and nature of the frontier orbitals of **3**. Figure 4.18 shows that the HOMO for this compound is based mainly on the δ bonding orbital of the Mo_2 center, while the LUMO is dominated by the π*-orbital of the fullerene cage. The HOMO-12, HOMO-13 and HOMO-15 correspond to the metal d-orbitals forming the quadruple bond, one σ- and two π-orbitals, respectively. The composition of the HOMO and LUMO confirms that the oxidation wave at 0.543 V in the electrochemical measurement correspond to the $Mo_2^{5+/4+}$ redox process, while the observed reduction waves are associated to the fullerene. Time–Dependent Density Functional Theory (TD–DFT) calculations corroborates that this band comes from the HOMO → LUMO transition, and as a result shows MLCT character.

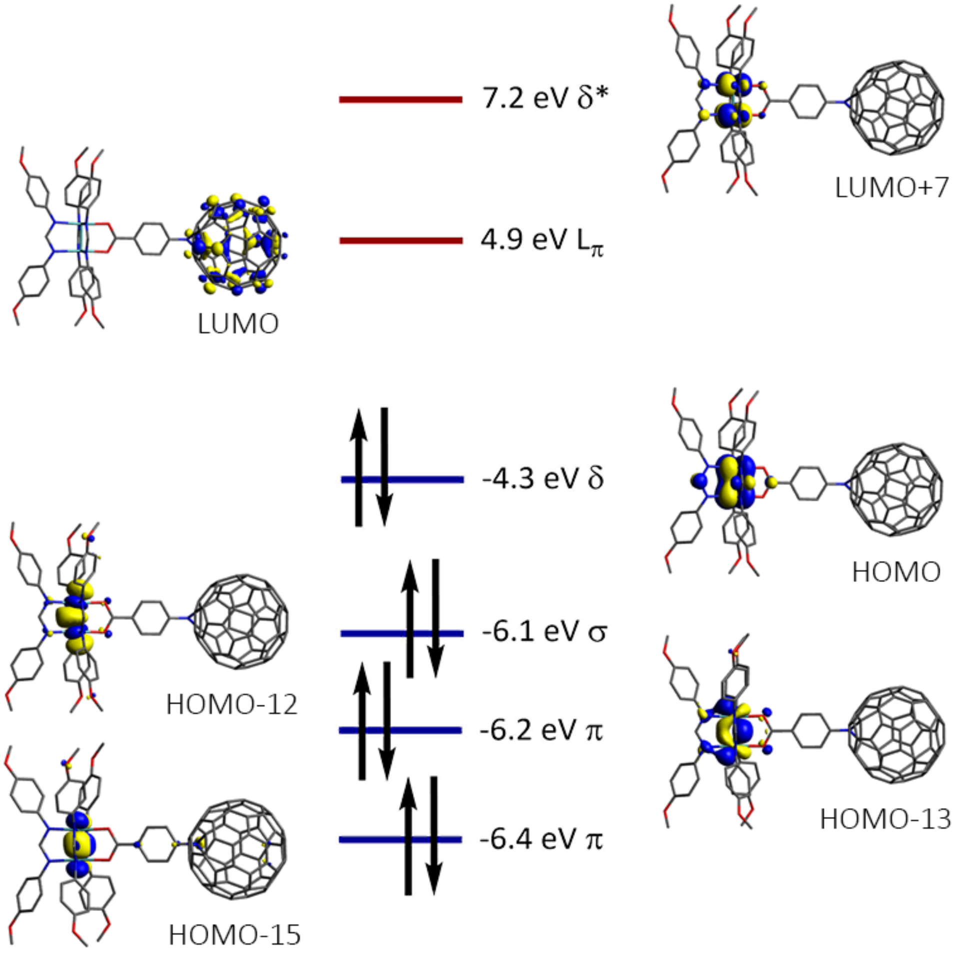

Figure 4.18. Contour plots of the frontier and d-orbitals of **3**, with isosurface value of 0.4.

4.4.3 Electron Transfer through a Dimolybdenum Unit, L–Mo_2–L system

Molecular Design and Synthesis. Mixed valent compounds, as shown in the previous sections, are comprised of two redox centers separated by a bridge, where the redox centers are typically metal centers and the bridge is an organic linker. The Robin–Day classification for mixed valent compounds equally applies to systems where the redox centers are either inorganic or organic in nature. While in M_2–L–M_2 complexes the organic linker bridge serves to couple the redox active metal centers, in L–M_2–L systems the M_2 δ-orbital tentatively couples the ligands forming a ligand-based mixed valent complex. Previously reported work has shown evidence of such ligand-based mixed valent systems for *trans* $M_2(T^iPB)_2L_2$ compounds where M = Mo or W and L = an azulene carboxylate[198,199] or thienyl carboxylate[200]. These compounds have shown that the charge in the MV system is either localized over both ligands or localized on one, and can be described in terms of the Robin–Day scheme.[201–203]

We synthesized and studied two compounds wherein the double-substituted quinone, **IV**, is attached to a Mo_2^{4+} center. In compound **4** one quinone is attached, while in compound **5** there are two quinones in trans-position. As previously observed, this quinone present one-electron oxidation in Mo_2–L–Mo_2 systems. In addition, data obtained from the cyclic voltammetry indicates that this ligand allowed for delocalization of the charge in the MV system. Therefore, this ligand is suitable to further study the influence of M_2 δ-ligand π-conjugation. We expect to observe a localized charge for **4**, and either localized charge on one ligand or delocalized charge over two ligands for the trans compound **5**.

The monosubstituted complex, **4**, was prepared from the reaction between $Mo_2(DAniF)_3(OAc)$, **I**, where DAniF = *N*,*N′*-di-(*p*-anisyl)formamidinate, and 1.5 equivalents of the ligand, **IV**, in THF (Scheme 4.8). The lability of the acetate ligand allowed the replacement by **IV**, moreover we propose the obtained connectivity of the ligand to the dimolybdenum is favored by steric factors. Compound **4** was isolated by precipitation upon addition of hexanes to a benzene concentrated solution yielding a green compound in 94% yield. **4** is air-sensitive and soluble in most organic solvents. The mass spectra for monosubstituted complex, M_2–L, showed the expected isotopic distribution and predicted mass (m/z value calculated = 1247.25, experimental = 1247.5) as shown in Figure 4.19.

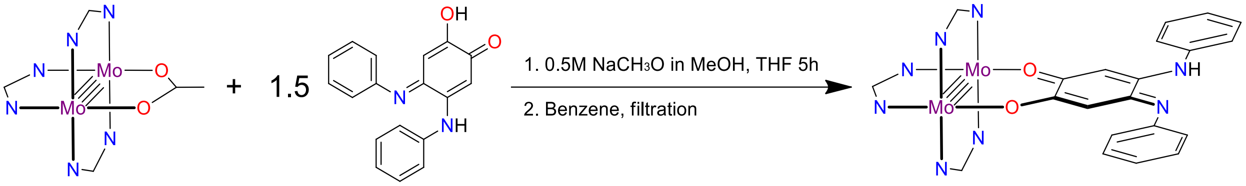

Scheme 4.8. Reaction conditions for synthesis of **4.**

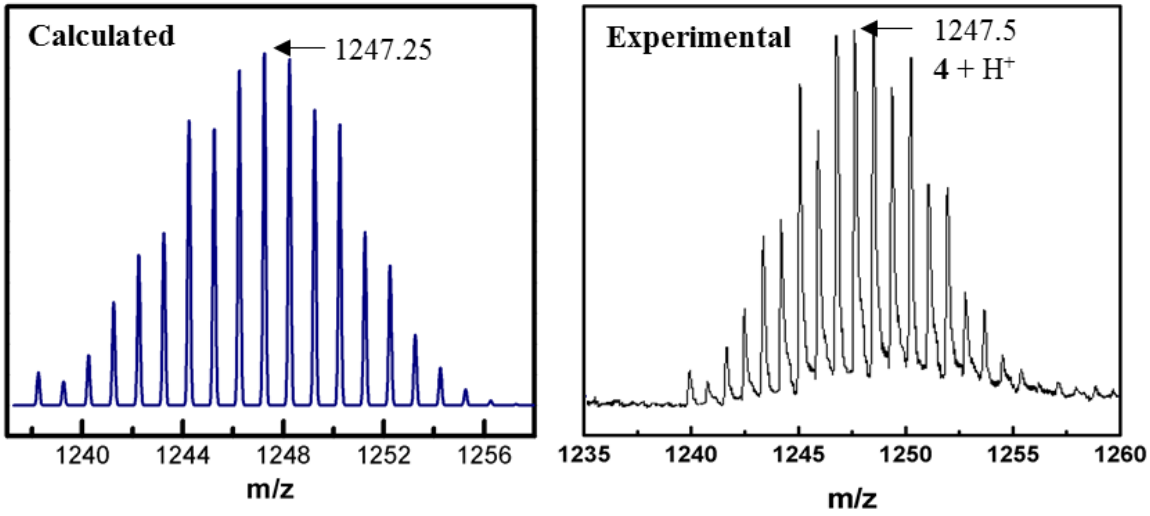

Figure 4.19. MS spectra of **4** with m/z (Left) calculated at 1247.25, and (Right) detected at 1247.5.

On the other hand, complex **5** was prepared from the reaction between trans-$Mo_2(DAniF)_2(OAc)_2$, **II**, and two equivalents of the organic linker **IV** in THF (Scheme 4.9). This compound was isolated by precipitation upon addition of ethanol to a concentrated solution of **5** in DCM. The dark green compound was obtained in 95% yield. We were able to identify the compound by mean of ^{1}H NMR. Figure 4.20 show a singlet at 8.20 ppm corresponding to the protons of the formamidinate ligand. There is a signal at 3.71 ppm assigned to the methoxy group protons of the ancillary ligand. In addition, the signals between 6.42 and 7.36 ppm correspond to those for the aromatic protons in the quinone and formamidinate. Compound **5** is soluble in most organic solvents and does not react with chlorinated ones. This compound is air-sensitive but stable as a solid under inert atmosphere at room temperature.

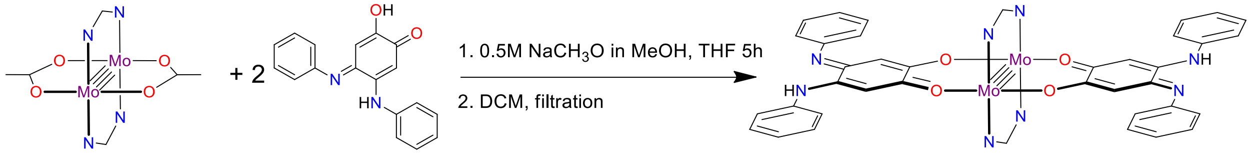

Scheme 4.9. Reaction conditions for synthesis of **5**.

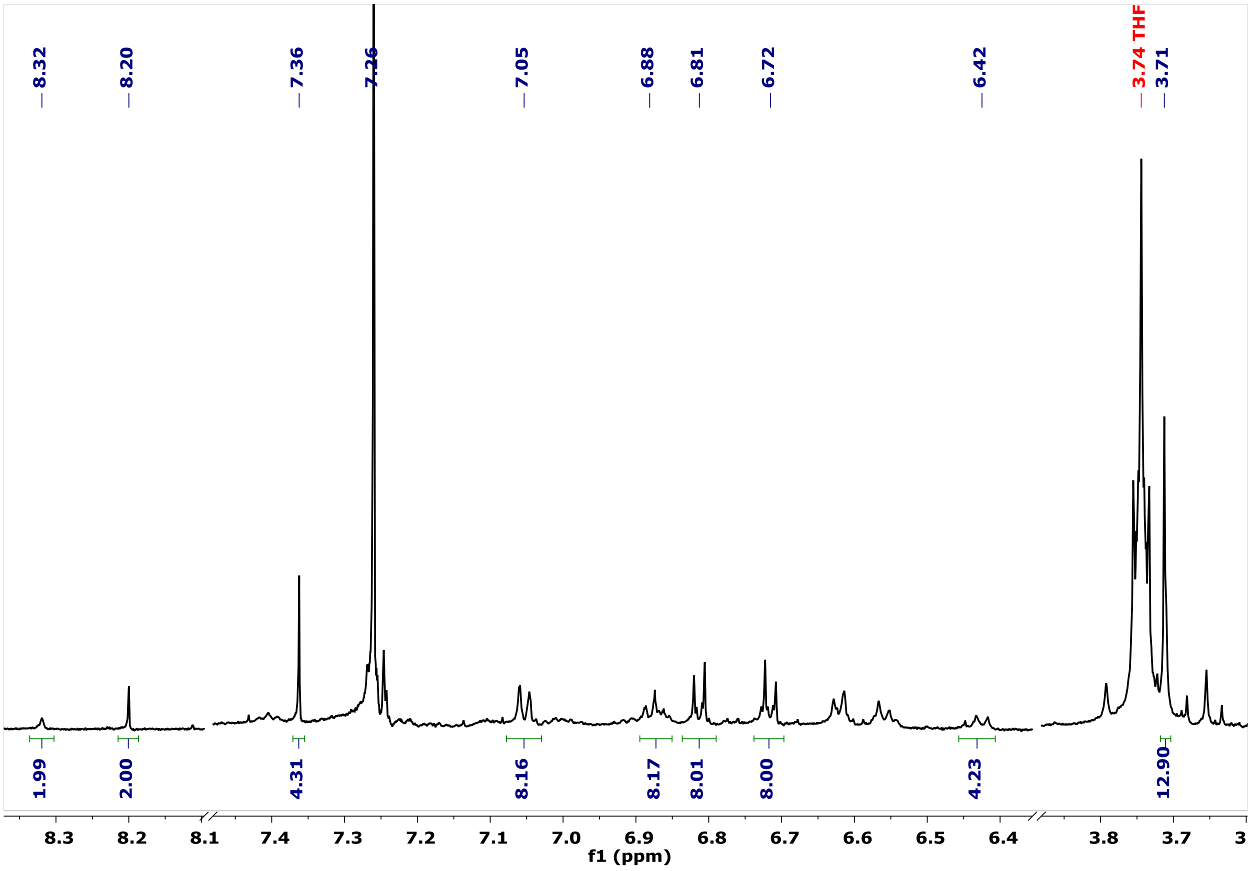

Figure 4.20. ^{1}H NMR for **5** in CDCl$_3$.

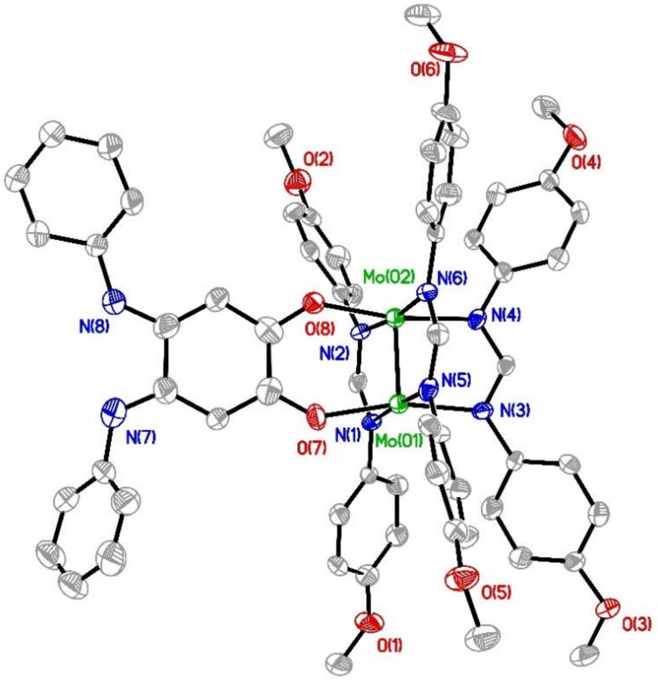

Figure 4.21. Crystal structures for **4** with ellipsoids drawn at 50% probability level. All hydrogen atoms have been omitted for clarity.

Structural Determinations. Single crystals of **4** suitable for X–Ray analysis were obtained by slow diffusion of hexanes into a THF solution of **4** at room temperature. The structure of **4** provided in Figure 4.21 shows a paddlewheel structure with three formamidinate ligands and one substituted quinone ligand. **IV** is connected to the Mo_2 center through its O-end potentially due to steric hindrance. Crystallographic information pertinent to this compound is given in Table 4.2, while selected bond distances and angles are given in Table 4.3. This compound crystallizes in the triclinic space group $P\bar{1}$ with Z = 2. The integration of the data using a triclinic unit cell yielded a total of 31404 reflections to a maximum θ angle of 28.37° (0.75Å resolution), of which 14410 were independent (average redundancy 2.179, completeness = 97.2%, R_{int} = 12.86%, R_{sig} = 26.29%) and 6213 (43.12%) were greater than $2\sigma(F^2)$. The final cell dimensions of a = 13.7542(19) Å, b = 13.9223(19) Å, c = 16.798(2) Å, α = 111.969(2)°, β = 90.539(2)°, γ =

96.427(2)°, volume = 2959.7(7) Å^3, are based upon the refinement of the XYZ-centroids of 2796 reflections above 20 σ(I).

Table 4.2. X–ray crystallographic data for **4**.

	4
Formula	$C_{67}H_{67}Mo_2N_8O_9$
FW, g·mol^{-1}	1320.16
Crystal system	Triclinic
Space group	$P\bar{1}$
a (Å)	13.7542(19)
b (Å)	13.9223(19)
c (Å)	16.798(2)
α (deg)	111.969(2)
β (deg)	90.539(2)
γ (deg)	96.427(2)
V (Å^3)	2959.7(7)
Z	2
d_{calc} (g·cm^{-3})	1.481
μ (mm^{-1})	0.491
2θ (deg)	1.31–28.37
λ, Å	0.71073
T, K	100(2)
GOF	0.955
R1,[a] wR2($I > 2\sigma(I)$)[b]	0.0970, 0.1724

[a] $R1 = \sum||F_o| - |F_c||/\sum|F_o|$. [b] $wR2 = [\sum[w(F_o^2 - F_c^2)^2]/\sum w(F_0^2)^2]^{1/2}$, $w = 1/[\sigma^2(F_o^2) + (aP)^2 + bP]$, where $P = [\max(F_o^2 \text{ or } 0) + 2(F_c^2)]/3$.

Table 4.3. Selected bond lengths (Å) and bond angles (°) for **4**.

	4
Mo(1) – Mo(2)	2.1077(10)
Mo(1) – N(1)	2.162(6)
Mo(1) – N(3)	2.121(6)
Mo(1) – O(7)	2.060(5)
Mo(2) – O(8)	2.079(5)
N(1)–C(1)–N(2)	119.9(8)
N(3)–C(16)–N(4)	119.8(7)
O(7)–Mo(1)–Mo(2)	99.33(16)
O(7)–Mo(1)–N(3)	166.5(2)

The Mo–Mo bond distance of **4**, 2.1077(10) Å, falls within the range of 2.06–2.17 Å, which corresponds to that of a typical Mo_2 quadruple bonded compound.[204,205] This Mo–Mo bond distance is comparable to that of the previously reported *dimer-of-dimers* (2.1051(4) Å) where the symmetrical non-innocent ligand 2,5-dihydroxy-1,4-benzoquinone was used as the bridging linker.[174] The Mo–O bond distances, 2.060(5) and 2.079(5) Å, are shorter than those in compounds with other O-donor linkers, 2.114(3) Å in $Mo_2(DAniF)_3(CH_3N(O)CC(O)NCH_3)Mo_2(DAniF)_3$ for example.[182] However, the average Mo–N bond distance in **4**, 2.149(6) Å, is within the usual range. The organic linker is essentially planar with the phenyl ring of the –NPh groups out-of-plane.

The six-membered ring on the substituted quinone ligand shows variation in the C–C distances similar to those found in the symmetric benzoquinone series of *dimer-of-dimers*.[174] The average C–C bonds in the ring, 1.404 Å, is similar to the distance found in a phenyl ring. On the other hand, the C–C distance on the N-end, 1.512 Å, closely resembles a single bond in an oxalate group, 1.51(1) Å.[173] These differences suggest that the electron density is not fully delocalized in the ring. However, the C–O distances of 1.278 and 1.274 Å are shorter than a typical single bond but longer that a double bond, which indicates some degree of electron delocalization. Moreover, the short Mo–O distance, Å, shows a strong interaction between the Mo_2 unit and the ligand.

Electrochemical Studies. Compound **4** and **5** show redox activity in DCM. The cyclic voltammogram for **4** and **5** are shown in Figure 4.22 and Figure 4.23, respectively. The first oxidation of **4** occurs at $E_{1/2}$ (I) = –0.03 V vs Fc/Fc^+. Quadruple-bonded dimolybdenum units usually present a one-electron reversible event between 0.4–0.7 V vs Ag/AgCl.[185] This process is then assigned to oxidation of the Mo_2 center due to the $Mo_2^{4+} \rightarrow Mo_2^{5+}$ process. This first oxidation occurs 0.13 V lower than that for **5**, this is consistent with the expected relative energies of the Mo_2 δ-orbitals, similar to the observed energies for the mono and trans Mo_2 complexes with 9,10-

anthraquinone carboxylate ligands.[206] Moreover, a second redox wave at $E_{1/2}$ (II) = 0.465 V was assigned to an oxidation of the organic linker. The integration of the second reduction wave (when compared to the one-electron oxidation of Mo^{5+}) corresponds to a one-electron transfer process.

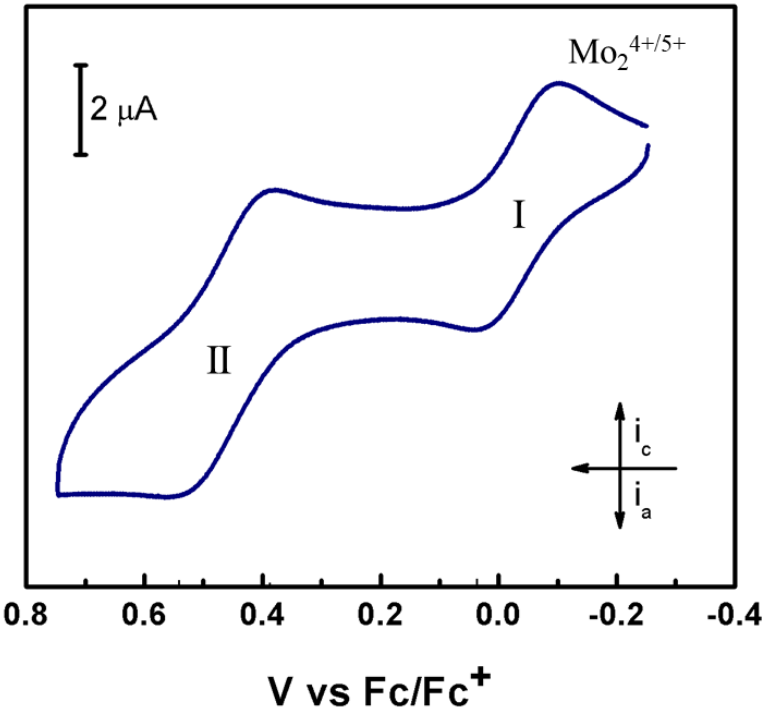

Figure 4.22. Cyclic voltammogram of **4**, with $E_{1/2}$ (I) = –0.03 V and $E_{1/2}$ (II) = 0.465 V. Data was obtained in a DCM solution of **4** with potentials referenced to Fc/Fc$^+$.

As shown in Figure 4.22, two redox events are observed for **4** suggesting the ligands in the trans compound **5** could be electronically coupled through $M_2(\delta)$–ligand π-conjugation. In contrast, the CV of **5** (Figure 4.23) shows two redox events at $E_{1/2}$ (I) = –0.017 V and $E_{1/2}$ (II) = 0.148 V. Similarly to the first event for **4**, the first oxidation of **5** is assigned to oxidation of the Mo_2 center due to the $Mo_2^{4+} \rightarrow Mo_2^{5+}$ process. If the ligands were to be electronically coupled through the dimolybdenum center, a separation of each one-electron ligand oxidation is expected. The second oxidation event at 0.148 V corresponds to a two-electron oxidation associated to oxidation of the ligands, this wave shows slight splitting. The appearance of a single event indicates that the ligands are not considerably coupled through the Mo_2 unit.

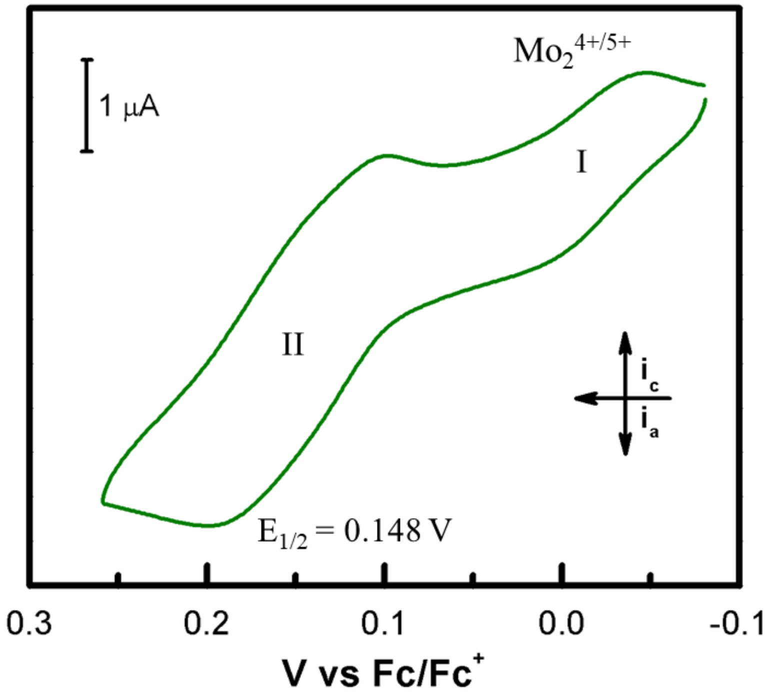

Figure 4.23. Cyclic voltammogram of **5**, with $E_{1/2}$ (I) = –0.017 V and $E_{1/2}$ (II) = 0.148 V. Data was obtained in a DCM solution of **5** with potentials referenced to Fc/Fc^+.

Spectroscopic Properties. The room temperature electronic absorption spectra of **4** and **5** in THF are shown in Figure 4.24 and Figure 4.25, respectively. These compounds are highly colored and show two absorption bands in the visible region assigned to the M_2 δ to π^*-ligand MLCT transitions. Compound **4** has a low MLCT transition at 768 nm and a higher energy MLCT transition at 436 nm. The absorption bands in compound **5** are blue-shifted to 394 and 727 nm. The lowest energy absorptions are assigned to the transition involving the fully allowed HOMO to LUMO transition similar to previously reported M_2–L and L–M_2–L compounds.[199,201,203] This is consistent with the δ-orbital in **4** having higher in energy due to the interaction with formamidinate ligands.

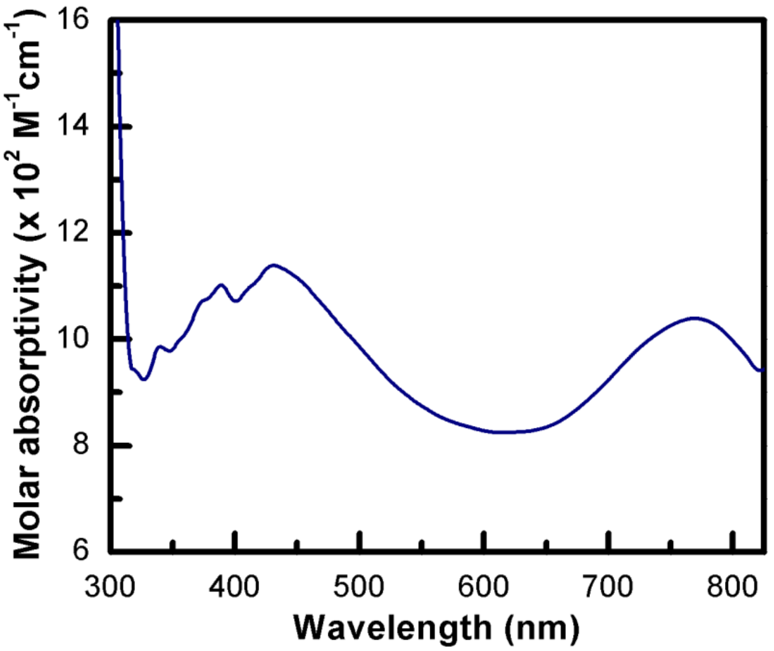

Figure 4.24. Absorption spectra of compound **4** measured at room temperature in THF.

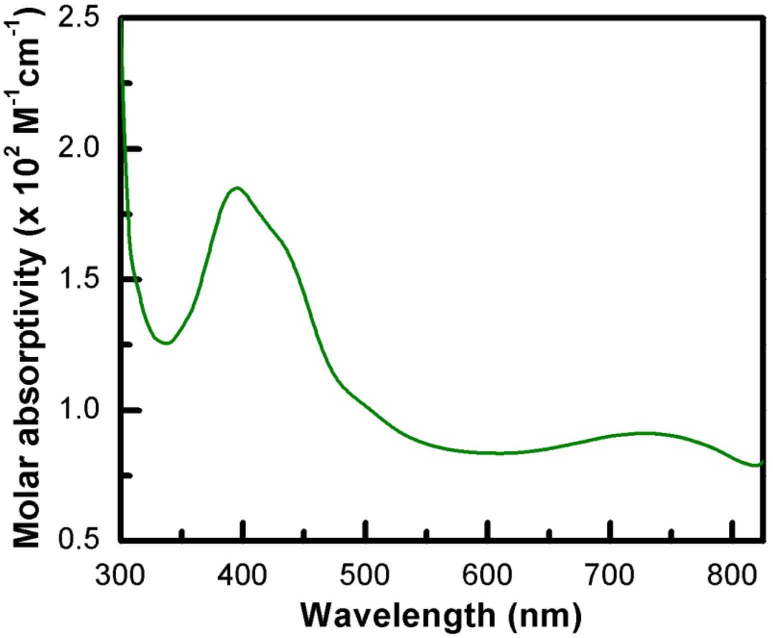

Figure 4.25. Absorption spectra of compound **5** measured at room temperature in THF.

Electronic Structure Calculations. Density Functional Theory (DFT) calculations were performed to gain insight into the ground state geometry, electronic structure, and nature of the frontier orbitals of **4** and **5**. The geometry optimizations were carried out on model compounds where the aryl groups of the formamidinates were replaced by H atoms. The absence of imaginary frequencies on the vibrational frequency analysis of the optimized models indicate the geometries are on a minima on the potential energy surface. The frontier molecular orbitals on model compounds for **4** and **5** are depicted in Figure 4.26 and Figure 4.27, respectively.

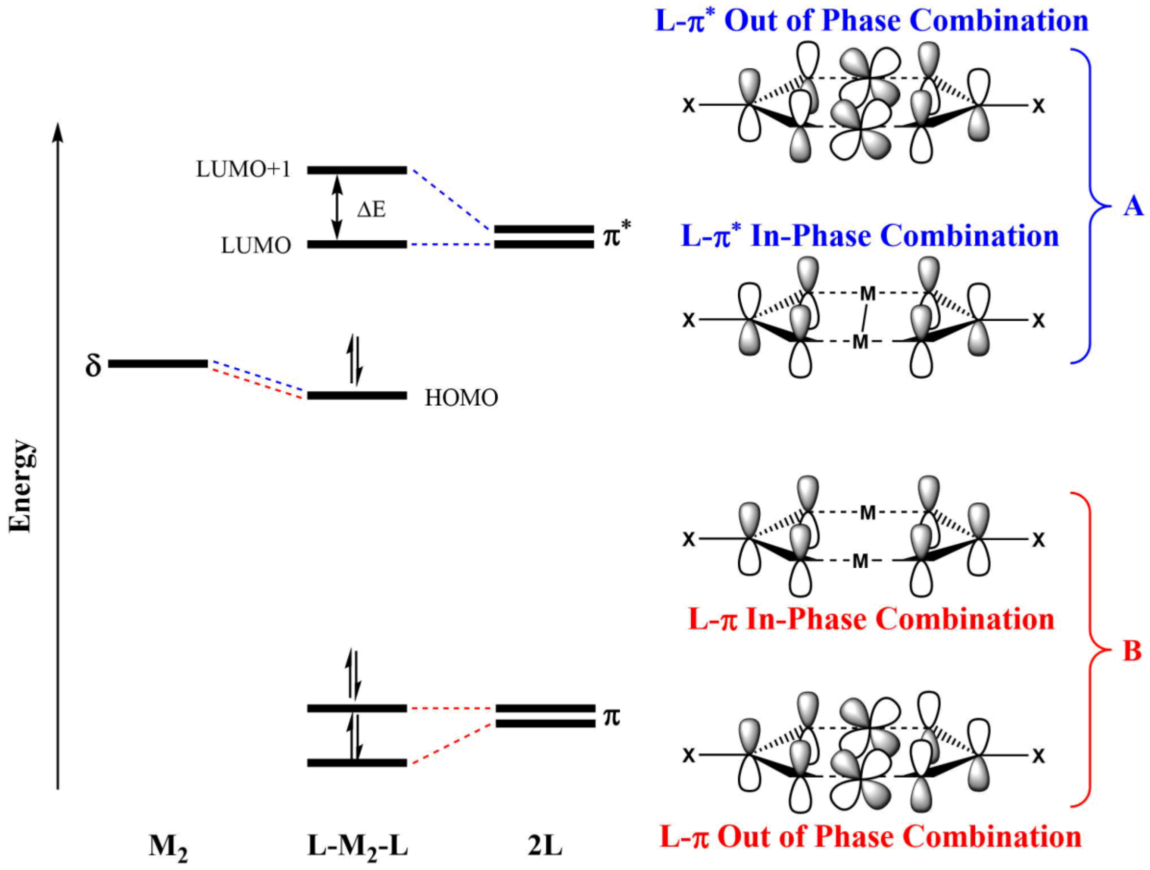

Scheme 4.10. Frontier molecular orbitals for a L−M_2−L system.

As shown for *dimers-of-dimers* at the beginning of the chapter, the bridging ligand can potentially couple the redox centers suggesting that in a L−M_2−L system, where L is a conjugated π-ligand, the M_2 δ-orbital could couple the ligands. Therefore, the anion of the complex can be considered a mixed valent system. It has been previously stablished that the electronic coupling on these organic π-systems (L−M_2−L) originates from the interaction of the M_2 δ-orbital π-orbitals of the ligands in trans position, as depicted in Scheme 4.10.[203] The interaction of the molecular orbitals for the bimetallic unit and the empty orbitals of the ligands in *A* show that the LUMO and LUMO+1 are the in-phase combination of the ligands, and the out-of-phase combination of the π* orbitals with the M_2 δ-orbital, respectively. The out-of-phase combination matches the symmetry of the metal center creating a metal-to-ligand backbonding interaction. Meanwhile, the interaction observed in *B* corresponds to that of the filled π-orbitals of the ligands with the M_2 δ-orbital. In this case, the HOMO-1 is the in-phase combination of the ligand orbitals, while the HOMO-2 is formed by the out-of-phase combination of the L π-orbitals and the M_2 δ-orbital.

As expected, the HOMO for both compounds is the Mo_2 δ orbital with some ligand mixing. The δ-orbital in model compound **4** is higher in energy than the same orbital for **5** by about 0.1 eV. This has been previously reported on similar systems[206] where the difference in energy has been attributed to the presence of formamidinate ligands raising the δ and δ* orbitals as a reflection of the relative electronegativities of N versus O atom. The LUMO for **4** is the ligand based π* with some Mo_2 δ contribution, while the LUMO for **5** is ligand based involving the in-phase combination of the substituted quinone ligand π*-orbitals. The obtained molecular orbitals support the assignment of the lowest energy bands observed for **4** and **5** as MLCT transitions from HOMO to LUMO. Moreover, for **4** the LUMO+1 and LUMO+2 are the metal based δ*- and σ*-orbitals. Meanwhile, the LUMO+1 and LUMO+2 orbitals for **5** are the combination of the out-of-phase π* of the ligand in trans position with the Mo_2 δ, and the Mo_2 δ*-orbital respectively.

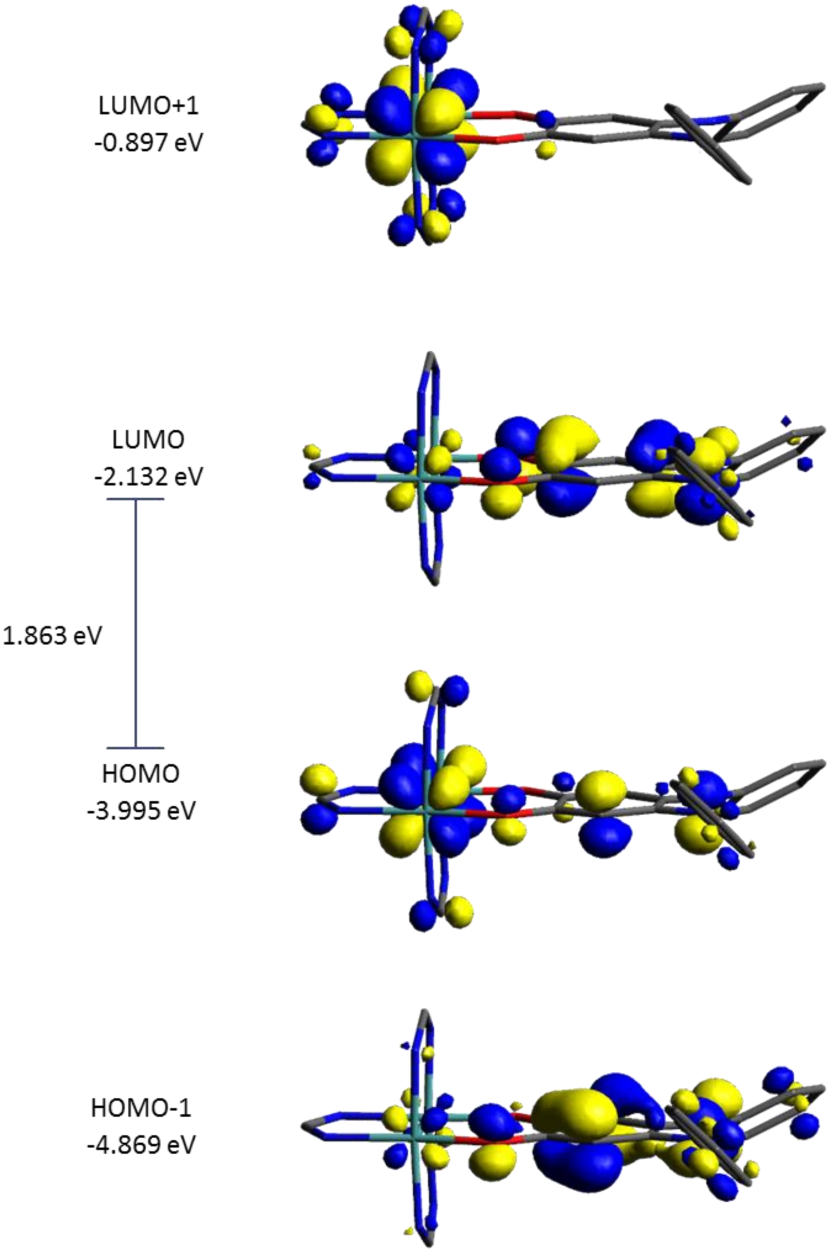

Figure 4.26. Contour plots and molecular orbital representation of four frontier orbitals for **4**, with energy for all orbitals.

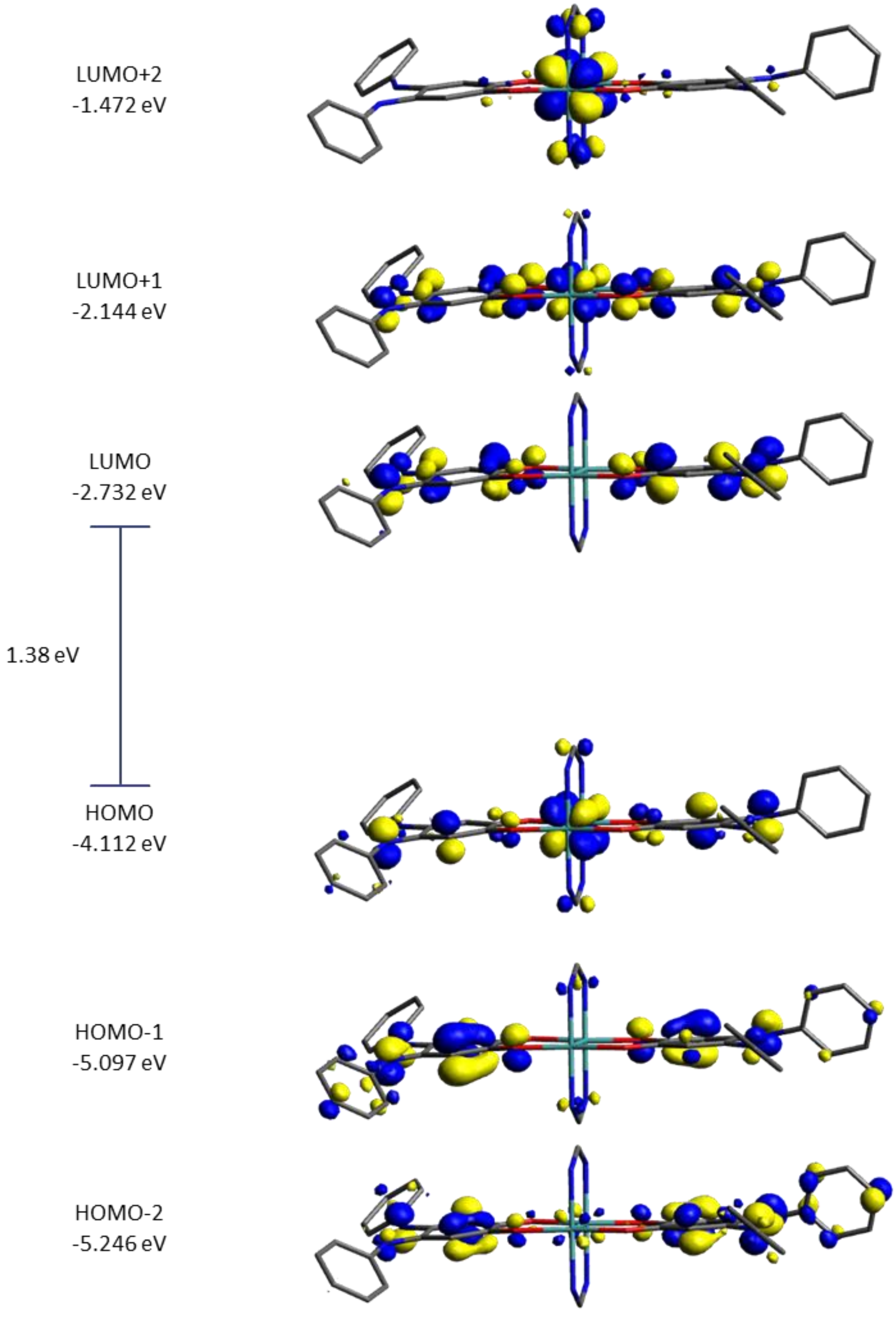

Figure 4.27. Contour plots and molecular orbital representation of four frontier orbitals for **5**, with energy for all orbitals and isosurface value of 0.45.

Time dependent DFT calculations were performed for both models which predicted two transition in the visible region. The lower energy refers the HOMO to LUMO transition associated with the MLCT. Compound **4** presents a high energy absorption from HOMO to LUMO due to the allowed MLCT. On the other hand, the higher energy absorption band is due to electronic transitions form the HOMO-1 to the LUMO. For **5** the higher energy absorption band is due to the excitation from the HOMO to the LUMO+2 which refers to Mo_2 $\delta \rightarrow \delta^*$ transition. Molecular orbital calculation on the anion of these compounds places the single electron in the LUMO of the neutral complexes and have delocalized charge over the complex for **4** and the trans ligands for **5**.

4.4 CONCLUSION

Multimetallic building blocks have been of interest for the study of multielectron redox chemistry due to their interesting and well-studied electrochemical properties. We have created three types of non-symmetric systems utilizing metal-metal quadruple bonded dimolybdenum units in an attempt to better understand multielectron redox processes. Additionally, a family of non-symmetric ligands (2,5-dihydroxy-4-phenylimino-2,5-cyclohexadien-1-one, and 2-hydroxy-5-phenylamino-4-phenylimino-2,5-cyclohexadien-1-one) was synthesized and characterized for the preparation of *dimers-of-dimers* using dimolybdenum units as redox centers. Electrochemical studies on $[Mo_2(DAniF)_3]_2(C_{12}O_3NH_7)$, **1**, and $[Mo_2(DAniF)_3]_2(C_{18}O_2N_2H_{12})$, **2**, displayed two one-electron and three one-electron oxidations, respectively. Calculation of their comproportionation constants ($K_c = 6.36 \times 10^3$ and $K_c = 9.7 \times 10^{10}$) categorized **1** as Class II, and **2** as Class III on the Robin–Day classification. Oxidized species (by one and two electrons) for both compounds need to be synthesized in order to study the electronic communication in a mixed valent system analogue to the Creutz–Taube ion.

We studied the effect of a non-metallic redox active unit in the electronics of a M_2−L−C_{60} system, where a C_{60} cage is used as the second active site. For that purpose, $Mo_2(DAniF)_3(C_{69}O_2NH_8)$, **3**, was synthesized and characterized by ^{1}H NMR and MALDI-TOF mass spectrometry. In addition, the electronic spectrum of this compound presents a strong band in the UV region corresponding to a metal-to-ligand charge transfer transition from the interaction of the δ orbitals of the [Mo_2] core with the π* orbitals of the bridging ligand. Compound **3** also presented a δ → δ* transition at 470 nm, which is within the range (400−500 nm) for a quadruple bonded dimolybdenum. Cyclic voltammetry on **3** showed a one-electron oxidation of the dimolybdenum unit, as well as reduction events typically not observed in these systems and that have been assigned to reductions of the fullerene cage. More characterizations are still needed for this compound, such as IR, Raman and single crystal XRD.

Finally, we presented the study of charge transfer in a system where the donor and acceptor were non-symmetric organic units, and the bridging ligand in charge of the coupling was a dimolybdenum center. The synthesized compounds, **4** and **5**, were characterized by means of ^{1}H NMR, mass spectrometry or single crystal X-Ray diffraction. One-electron oxidation of the Mo_2^{4+} unit was observed for both compounds at –0.03 V for **4** and –0.017 V for **5**. In addition, a second a one-electron oxidation event was observed for **4** while a two-electron oxidation wave was observed for **5** as expected. The appearance of only one wave for the oxidation of the ligands in **5** suggest the ligands are not significantly coupled. The absorption spectra for the compounds show two intense bands in the visible region related to MLCT electronic transitions which were supported by theoretical calculations. One-electron reduced species for **4** and **5** need to be studied in order to further understand the electronic communication in a mixed valent system analogue to the Creutz–Taube ion.

Chapter 5: Redox Potential Tuning of Dimolybdenum Systems through Systematic Substitution by Guanidinate Ligands[3]

5.1 INTRODUCTION

The chemistry of metal-metal bonded bimetallic complexes has been enhanced by the use of bidentate ligands like carboxylates, amidinates and guanidinates.[207] The nature of such supporting ligands has a strong effect on the oxidation states, redox potentials, and electronic properties of the compound.[208] The increased attention to guanidinate ligands is a result of their capability to stabilize higher oxidation states in bimetallic complexes.[209–215] This ability is a result of the delocalization of the charge across the guanidinate backbone.[216,217]

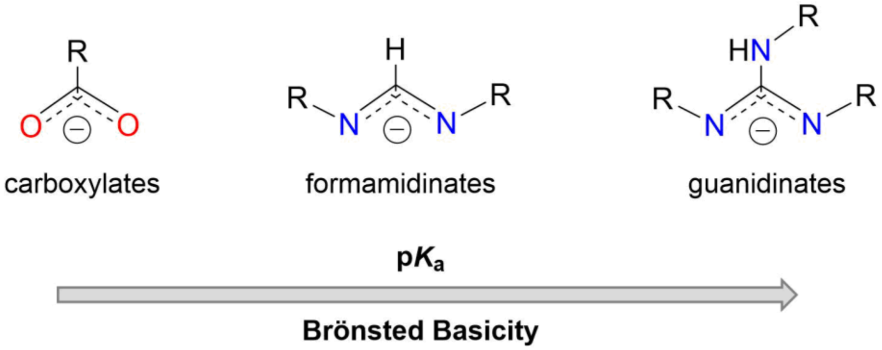

Scheme 5.1. Structure of common structural ligands used in multiple bonded bimetallic complexes: carboxylate, formamidinate and guanidinate ligands.

Of special interest is the bicyclic hpp ligand (hpp is the anion of 1,3,4,6,7,8-hexahydro-2H-pyrimido[1,2-a]pyrimidine) due its high Brönsted basicity (Scheme 5.1),[218,219] which allows it to stabilize the most easily ionizable family of complexes. $W_2(hpp)_4$, $W_2(TMhpp)_4$, $W_2(TEhpp)_4$ present onset ionization energies (3.51, 3.45, and 3.40 eV respectively) lower than the ionization energy for the cesium atom (3.89 eV).[207,220,221] The low ionization energies for compounds

---

[3] This chapter is excerpted with permission from a submitted manuscript: Nancy Rodríguez-López, Nathalie Metta, Alejandro Metta, Dino Villagrán; Redox Potential Tuning of Dimolybdenum Systems through Systematic Substitution by Guanidinate Ligands. **2019**. *Submitted.*

containing hpp have been associated with the strong antibonding interaction between the π orbitals of the ligand and the δ orbitals of the M_2^{4+} unit,[220] therefore destabilizing the M_2^{4+} core and favoring the oxidation to yield M_2^{5+} and M_2^{6+} species.[218,222,223] Consequently, large cathodic shifts in the redox potentials of bimetallic compounds of the M_2L_4 type are observed when the hpp ligand is introduced in the system.[207]

Research on bicyclic guanidinate ligands has centered on enhancing the solubility of complexes in a variety of organic solvents[221,223] as well as fine-tuning their electronic and electrochemical properties.[224,225] The individual effect of the ligands on the electronic properties of the system has been explored in similar bimetallic complexes by systematic replacement of the ancillary ligands.[158,226] Prior work with carboxylate and formamidinate ligands in dimolybdenum complexes has revealed that when carboxylates are systematically replaced by formamidinate ligands there is an increase in the stability of the oxidized species as well as a shift in the reduction potentials.[150] Previous results showed a remarkable capacity of hpp for fine-tuning the redox potential of Mo_2^{4+} unit in M_2L_4 complexes. When bicyclic guanidinates are introduced in dimolybdenum paddlewheel complexes the most stable specie is the triple bonded Mo_2^{6+}.[213] Nonetheless, a study where formamidinates have been systematically replaced by guanidinate ligands has not been reported. Thus, the effect of the substitution on the electronic structure and reduction potentials of the dimolybdenum center has not been explored.

Herein we report the synthesis, characterization, and study of a series of compounds of the form $Mo_2(DAniF)_n(hpp)_{4-n}$. We have synthesized and characterized dimolybdenum paddlewheel units with different proportions of formamidinate and guanidinate ligands in an attempt to fine-tune the electronic structure of these compounds, and to gain a better understanding of the electron donor properties of basic ligands such as acetates, formamidinates, and guanidinates when attached to a bimetallic system. The degree of tuning was quantified by exploring their electrochemical properties and comparing their prospective redox potentials, Raman shifts, and electronic absorption. Density Functional Theory (DFT) studies were performed to compare the respective energies of the compounds and to understand their electronic structure. The effect of the substitution on the electronic structures of the dimetal core was investigated using x-ray diffraction, electrochemistry, Raman, and UV-vis spectroscopies, which were correlated with the results from DFT calculations.

5.2 EXPERIMENTAL SECTION

5.2.1 General Procedures.

All synthetic procedures and materials handling were conducted under N_2 atmosphere using a drybox or standard Schlenk techniques unless otherwise noted. All the used solvents were dried and degassed using a Pure Process Technology solvent purification system. The materials used for the study HDAniF,[156] $Mo_2(O_2CCH_3)_4$ **(I)**,[227] $Mo_2(DAniF)_3(O_2CCH_3)$[157] **(II)**, $Mo_2(DAniF)_4$ **(III)**,[228] trans-$Mo_2(DAniF)_2(O_2CCH_3)_2$,[158] $[Mo_2(DAniF)(MeCN)_6](BF_4)_3$,[226] were prepared following literature procedures. 1,3,4,6,7,8-Hexahydro-2H-pyrimido[1,2-a]pyrimidine (Hhpp) and other commercially available chemicals were used as received.

5.2.2 Physical Measurements.

Elemental analyses were performed by Midwestern Mircrolab, LLC., Indianapolis, Indiana, and Galbraith Laboratories, Inc., Knoxville, Tennessee. UV-Vis spectra were collected on a SEC2000 Spectra System with the Visual Spectra 2.1 software from 300 to 800 nm. Infrared spectra were recorded on an Agilent Cary 630 FTIR Spectrometer. Raman spectra were obtained on a Thermo Scientific DXR SmartRaman spectrometer using a 532 nm laser. ^1H NMR spectra were recorded on a Bruker 300 MHz and 400 MHz NMR spectrometer with chemical shifts referenced to the residual protic signal of C_6D_6. Electrochemical analyses by cyclic voltammetry were performed in THF using a CHI760D Potentiostat with a Pt working electrode, Pt mesh auxiliary electrode, Ag/Ag^+ reference electrode, a scan rate of 100 mV/s, and 0.1 M $TBAPF_6$ as electrolyte. Ferrocene was added at the end of the run as internal standard.

5.2.3 X-Ray Structure Determination.

Suitable crystals for x-ray diffraction were prepared by diffusion of hexanes into THF solutions of **1** and **2**. Each crystal was mounted with a small amount of silicone grease and centered in the goniometer of a Bruker SMART APEX CCD system equipped with a graphite monochromator and a MoKα fine-focus tube ($\lambda = 0.71073$ Å). Data for all crystals were collected at 100 K with no crystal decay observed during the collection. The frames were integrated with Bruker SAINT Software package using a narrow-frame algorithm. Data were corrected for absorption effects via multi-scan method (SADABS). All structures were solved and refined by direct methods using the Bruker SHELXTL Software Package. Crystallographic data for **1** and **2** are listed in Table 5.3, while the Mo-Mo distances for these compounds are given in Table 5.1.

5.2.4 Synthesis of $Mo_2(DAniF)_3(hpp)$, 1.

A mixture of yellow $Mo_2(DAniF)_3(O_2CCH_3)$ (1.02 g, 1.00 mmol) and Hhpp (0.139 g, 1.00 mmol) was dissolved in 40 mL of THF. While stirring, 2.00 mL of a 0.5 M solution of $NaOCH_3$ in methanol was slowly added. The color turned first to red then to brown. The reaction was stirred for 5 h at room temperature producing white crystalline sodium acetate. After removal of the solvent under reduced pressure, the residue was extracted with 20 mL of dichloromethane; filtration removed NaO_2CCH_3. The volume of the filtrate was reduced to about 5 mL with vacuum evaporation. Ethanol (10 mL) was added to the residue with vigorous stirring. A bright yellow solid and a dark brown supernatant solution were obtained. After decanting, the solid was washed with ethanol (2 x 10 mL), followed by 10 mL of hexanes, and dried under vacuum. Yield: 901 mg, 82%. ^{1}H NMR (δ in C_6D_6): 1.74 (q, 4H, -2C*H*$_2$), 2.87 (t, 4H, -2C*H*$_2$), 3.21 (s, 6H, -OC*H*$_3$) 3.22 (s, 12H, -OC*H*$_3$), 3.45 (t, 4H, 2C*H*$_2$), 6.56 (d, 4H, aromatic C-*H*) 6.59 (d, 4H, aromatic C-*H*), 6.65 (d, 8H, aromatic C-*H*), 6.68 (d, 8H, aromatic C-*H*), 8.55 (s, 2H, -NC*H*N-), 8.58 (s, 1H, -NC*H*N-). UV-Vis λ_{max}: 412 nm. Raman (cm^{-1}): $v = 487$. Anal. Calcd for $Mo_2C_{52}N_9O_6H_{57}$: C, 56.99; N, 11.5; H, 5.24. Found: C, 56.79; N, 11.27; H, 5.35.

5.2.5 Synthesis of trans-Mo$_2$(DAniF)$_2$(hpp)$_2$, 2.

A mixture of yellow trans-Mo_2(DAniF)$_2$(O_2CCH_3)$_2$ (0.500 g, 0.610 mmol) and Hhpp (0.160 g, 1.15 mmol) was dissolved in 40 mL of THF. While stirring 2.30 mL of a 0.5 M solution of $NaOCH_3$ in methanol was added slowly. The color turned orange, upon further stirring the solution turned a brighter shade of orange. The reaction was stirred for 5 h. After 5 h, the stirring was stopped and solution was allowed to settle. An orange solid and a dark brown supernatant solution were obtained. After decanting, the solid was washed with diethyl ether (2 x 10 mL) and dried under vacuum. Yield: 495 mg, 83 %. ^{1}H NMR (δ in C_6D_6): 1.79 (q, 8H,-2C*H*$_2$), 2.91 (t, 8H, -2C*H*$_2$), 3.28 (s, 12H, -OC*H*$_3$), 3.59 (t, 8H, -2C*H*$_2$), 6.65 (d, 8H, aromatic C-*H*), 6.75 (d, 8H, aromatic C-*H*), 8.41 (s, 2H, -NC*H*N-). UV-Vis λ_{max}: 442 nm. Raman (cm^{-1}): $v = 494$. Anal. Calcd for $Mo_2C_{44}N_{10}O_4H_{54}$: C, 53.99; N, 14.31; H, 5.56. Found: C, 53.81; N, 14.07; H, 5.47. ESI–MS: *m*/*z*: 982.40.

5.2.6 Synthesis of Mo$_2$(DAniF)(hpp)$_3$, 3.

To a mixture of purple [Mo_2(DAniF)(CH_3CN)$_6$](BF_4)$_3$ (0.600 g, 0.650 mmol) and Hhpp (0.270 g, 1.95 mmol) in THF, NaOMe (3.90 mL) 0.5M in MeOH was added dropwise. The color turned bright orange upon addition of the sodium salt. The reaction was stirred for 5 h. After 5 h, the stirring was stopped and the solution was allowed to settle. An orange solid could be seen at the bottom and the supernatant was decanted. Solid was washed with diethyl ether (2 x 10 mL) and dried under vacuum. Yield: 395 mg, 73%. ^{1}H NMR (δ in C_6D_6): 1.26 (q, 8H, -2C*H*$_2$), 1.41 (q, 4H-2C*H*$_2$), 2.34 (t, 8H, -2C*H*$_2$), 2.87 (t, 8H, -2C*H*$_2$), 3.33(s, 6H, -OC*H*$_3$), 3.45, (t, 4H, 2C*H*$_2$), 3.58 (t, 4H, 2C*H*$_2$), 6.62 (d, 4H, aromatic C-*H*), 8.68 (s, 1H, -NC*H*N-). UV-Vis λ_{max}: 450 nm. Raman (cm^{-1}): $v = 505$.

5.3 COMPUTATIONAL DETAILS

Density Functional Theory (DFT) calculations were performed with the hybrid Becke-3 parameter exchange functional and the Lee-Yang-Parr nonlocal correlation functional (B3LYP)[110,111] as implemented by Gaussian 09[114] (Revision C.01) program suit. Double-ζ-quality basis set (cc-pvdz)[229–233] was used on nonmetal atoms (carbon, nitrogen, oxygen, and hydrogen). An effective core potential (ECP) representing the $1s^2s^2p^3s^3p^3d^4p$ core was employed for the molybdenum atoms, along with the associated double-ζ basis set (LANL2DZ).[161–164] The absence of imaginary vibrations in the frequency calculations for all compounds indicated the gas phase geometry optimizations were a minima in the potential energy surface. Polarizability derivatives (Raman intensities) were computed using the keyword Freq=Raman in the Gaussian 09 package. Time-Dependent Density Functional Theory (TD-DFT) was used to calculate the electronic transition energies for the lowest 15 singlet excited states of all neutral compounds.[165–171] All calculations were performed in a 44-processor PowerWolf PSSC supercomputer cluster running Linux Red Hat 4.1.2-54 located at the University of Texas at El Paso. Isosurface plots of frontier molecular orbitals were generated using the Avogadro software with isodensity values of 0.04.

5.4 RESULTS AND DISCUSSION

Molecular Design and Syntheses. Redox tuning can be studied through ligand substitution by taking advantage of the well-defined redox properties of quadruply bonded Mo_2 complexes. An overview of the synthetic routes followed for the synthesis of all involved compounds is shown in Scheme 5.2 where **1** – **3** are placed in bold line boxes. Other species compared in the study are written off as **I** – **IV** and can be found in dashed line boxes. The depicted reactions are listed with the italicized lower case letters ***a*** – ***h***. The letters O and N are used to depict the oxygen and nitrogen atoms found in the ancillary ligands (acetates, formamidinates and guanidinates), while L refers to an acetonitrile molecule in an equatorial position. A brief description of the reactions for the synthesis of each species can be found on the caption for Scheme 5.2. The use of carboxylates and formamidinate ligands allows compounds bearing different patterns of ancillary ligands; one carboxylate and three formamidinates as well as two carboxylates and two formamidinates in either cis or trans configuration. The remaining carboxylates in such precursors could be replaced by the more basic guanidinates to afford the anticipated compounds.

As reported[227], the starting material $Mo_2(OAc)_4$, **I**, can be used to synthesize $Mo_2(DAniF)_3(OAc)$, **II**. The stoichiometric addition of the more basic formamidinate ligand (HDAniF) compared to acetate allows their substitution to afford **II** (Scheme 5.2, route ***a***). Compound **1** was synthesized by replacing the acetate ligand in **II** with the bicyclic guanidinate hpp (Scheme 5.2, following conditions in ***b***). $Mo_2(DAniF)_3(hpp)$, **1**, was obtained with 82% yield as a yellow powder. Compound **1** is considerably stable as a solid under inert atmosphere. It does not react with chlorinated solvents, and it is soluble in donor solvents like THF, as well as aromatic solvents such as benzene.

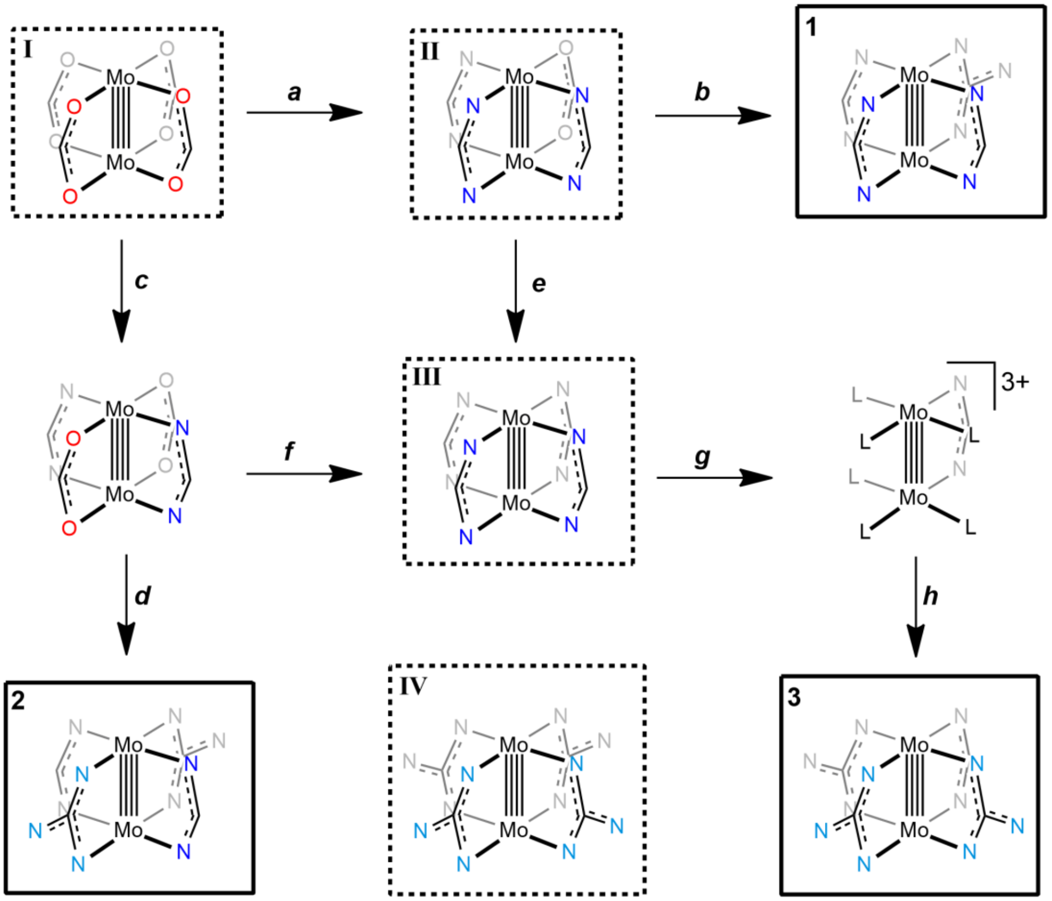

Scheme 5.2. Reaction conditions for obtaining compounds **1**–**3** are as follow: (a) mixing **I** with 3 equiv of HDAniF and $NaOCH_3$ in THF; (b) reaction of **II** with 1 equiv of Hhpp and $NaOCH_3$ in THF; (c) addition of 2 equiv of HDAniF and $NaOCH_3$ to **I** in THF; (d) addition of 2 equiv of Hhpp and $NaOCH_3$ in THF to trans-$Mo_2(DAniF)_2(OAc)_2$; (e) reaction of **II** with one equiv of HDAniF and $NaOCH_3$ in THF; (f) reaction of trans-$Mo_2(DAniF)_2(OAc)_2$ with 2 equiv of HDAniF and $NaOCH_3$ in THF; (g) mixing **III** with 3 equiv of HBF_4 in CH_3CN; (h) addition of 3 equiv of Hhpp and $NaOCH_3$ to $[Mo_2(MeCN)_6](BF_4)_3$ in THF.

The synthesis of the trans isomer $Mo_2(DAniF)_2(hpp)_2$, **2**, was performed similarly to **1**. Precise control of the stoichiometry for the synthesis of precursor trans-$Mo_2(DAniF)_2(OAc)_2$ was fundamental (Scheme 5.2, conditions in ***c***), excess formamidinate would otherwise react to yield **III**. Once the precursor was successfully obtained, the replacement of the acetate ligands by hpp was completed (Scheme 5.2, following reaction conditions in ***d***). Trans-$Mo_2(DAniF)_2(OAc)_2$, **2**, was obtained as an orange powder with 83% yield. Compound **2** is stable in the solid state under inert atmosphere. It reacts with chlorinated solvents, and is only partially soluble in other solvents. While we were not able to isolate the cis isomer, no interconversion from the trans to cis configuration was detected.

In contrast to the direct synthetic pathway of **1** and **2**, $Mo_2(DAniF)(hpp)_3$, **3**, was prepared through an indirect route (Scheme 5.2). In order to afford **3**, precursor $Mo_2(DAniF)_2(CH_3CN)_6^{3+}$ was first obtained by reacting tetrafluoroboric acid, HBF_4, and $Mo_2(DAniF)_4$, **III** (Scheme 5.2, reaction conditions in ***g***)[228]. The removal of formamidinates is more difficult compared to the displacement of acetate groups in **I** due to their increased basicity which requires stronger reactants (HBF_4) than NaOMe used in the displacement of acetates in **I**. Compounds with the formula $Mo_2(DAniF)_{4\text{-}n}(CH_3CN_{eq})_{2n}$, are useful since acetonitrile molecules can be easily displaced in substitution reactions.[158] Presumably, in the substitution of $^{-}$DAniF by CH_3CN, HBF_4 protonates the formamidinate ligand to a monodentate intermediate, while a neutral acetonitrile occupies the open coordination site.[226] Finally, the MeCN ligands are substituted by hpp to obtain $Mo_2(hpp)_3(DAniF)$, **3**, as an orange powder in 73% yield (Scheme 5.2, reaction ***h***). This compound is partially soluble in most donor and aromatic solvents.

Structural Determinations. Single crystals suitable for crystallography were obtained by diffusion of hexanes into a THF solution of the compounds. The structures of **1** and **2** provided in Figure 5.1 show a paddlewheel structure with formamidinate and guanidinate structural ligands. Figure 5.1a shows the molecular structure of $Mo_2(DAniF)_3(hpp)$, **1**, with selected bond distances and angles given in Table S1. Compound **1** crystallizes in the monoclinic space group $P2_1/c$ with Z = 8. The M–M dimolybdenum bond distance 2.0844(6) Å falls within the range of 2.06–2.17 Å, which corresponds to that of a typical Mo_2 quadruple bonded compound.[204,205]

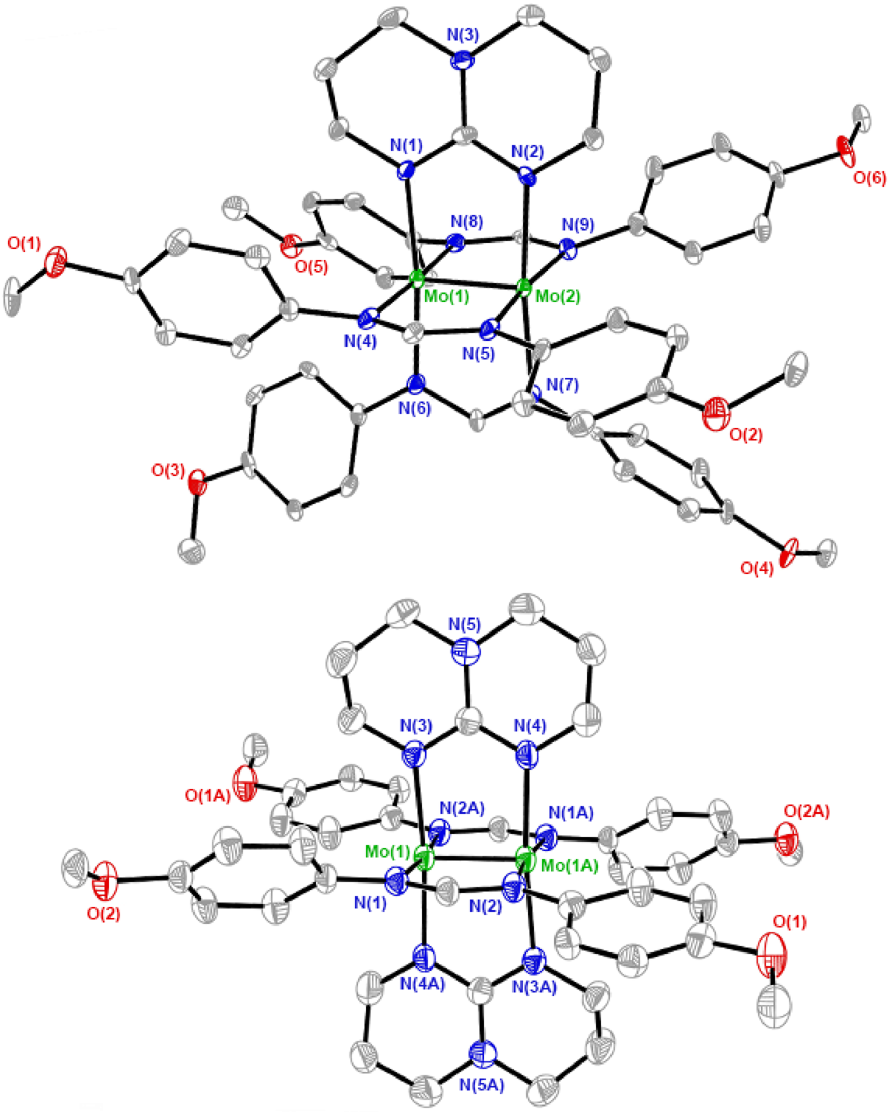

Figure 5.1. Crystal structures for **1** and **2** with ellipsoids drawn at 50% probability level. All hydrogen atoms have been omitted for clarity.

The replacement of the acetate ligand in the starting material $Mo_2(DAniF)_3(O_2CCH_3)$, **II**, by the guanidinate ligand to form **1**, showed to affect the metal–metal bond distance. Compared to the reported Mo–Mo bond on **II**, of 2.0892(8) Å, the metal–metal distance was shortened by 0.048 Å. The $Mo–N_{hpp}$ bond distance in **1** is in average 2.131 Å, while the bond lengths for the formamidinate nitrogen atoms $Mo–N_{trans}$ and $Mo–N_{cis}$ are 2.165 Å and 2.153 Å, respectively. The bond distances found trans to guanidinate nitrogen atoms are slightly longer than those cis to them.

This lengthening trend of trans groups is similar to the trans influence of both guanidinate and formamidinate groups relative to carboxylates.[158,234,235] Meanwhile, the average N–C bond lengths were 1.357 Å for $^{-}$hpp and 1.331 Å for $^{-}$DAniF, which are consistent with the delocalized charge in these bonds.

Table 5.1. Selected Mo-Mo bond lengths (Å) for compounds **I–III** and **1–3**.

	Experimental	**Calculated**
I	2.0934(8) [236]	–
II	2.0892(8) [157]	–
III	2.0964(5) [228]	–
1	2.0844(6)	2.12328
2	2.0784(6)	2.11451
3		2.10730
IV	2.067(1) [207]	–

Table 5.2. Selected bond lengths (Å) and angles for compounds **1** and **2**.

	1	**2**
Mo–Mo	2.0844(6)	2.0784(6)
Mo–Mo–N$_{\text{hpp}}$	92.80	92.84
Mo–Mo–N$_{\text{DAniF}}$	92.96	92.89
Mo–N$_{\text{hpp}}$	2.131(4)	2.138(3)
Mo–N$_{\text{trans}}$	2.165(4)	
Mo–N$_{\text{cis}}$	2.153(4)	2.158(3)

Compound **2**, where two guanidinates in trans configuration have been introduced in the system, crystallizes in the triclinic space group $P\bar{1}$. The molecule occupies a special position (Z = 1) having the center of the M–M bond sit on an inversion point. Therefore, the two Mo_2 units are crystallographically equivalent. Figure 5.1b shows the molecular structure for trans-$Mo_2(DAniF)_2(hpp)_2$, **2**, with selected bond distances and angles given in Table 5.2. The Mo–Mo distance of 2.0784(6) Å is shorter than that in **1** by 0.006 Å as expected from the addition of a second hpp unit. The Mo–N_{hpp} bond distance in **2** is in average 2.138(3) Å, whereas that for Mo–N_{DAniF} is 2.158(3) Å. Single crystals grown of **3** were too small for adequate data collection.

Table 5.3. X-ray crystallographic data for **1** and **2**.

	$Mo_2(DAniF)_3(hpp)$, 1	***trans*-$Mo_2(DAniF)_2(hpp)_2$, 2**
Formula	$C_{52}H_{58}Mo_2N_9O_6$	$C_{44}H_{52}Mo_2N_{10}O_4$
FW, g·mol^{-1}	1096.95	976.83
Crystal system	Monoclinic	Triclinic
Space group	$P2_1/c$	P-1
a **(Å)**	36.375(4)	9.7483(7)
b **(Å)**	12.0680(14)	10.6331(7)
c **(Å)**	23.043(3)	11.4180(8)
α (deg)	90	65.7350(10)
β (deg)	106.056(2)	86.1570(10)
γ (deg)	90	74.3210(10)
V (Å^3)	9720.6(19)	1037.51(12)
Z	8	1
d_{calc} (g·cm^{-3})	1.499	1.563
μ (mm^{-1})	0.577	0.662
2θ (deg)	1.17 – 25.00	1.96 – 27.43
λ, Å	0.71073	0.71073
T, K	100(2)	100(2)
GOF	0.951	1.036
R1,[a] wR2($I > 2\sigma(I)$)[b]	0.0553, 0.1416	0.0483, 0.1072

[a] $R1 = \sum||F_o| - |F_c||/\sum|F_o|$. [b] $wR2 = [\sum[w(F_o^2 - F_c^2)^2]/\sum w(F_0^2)^2]^{1/2}$, $w = 1/[\sigma^2(F_o^2) + (aP)^2 + bP]$, where $P = [\max(F_o^2 \text{ or } 0) + 2(F_c^2)]/3$.

The C–N and C–C bond distances observed in the guanidinate ligands for all complexes are comparable. In addition, a distance of ~1.45 and ~1.51 Å was observed for the C–N and C–C bonds in the formamidinate ligands, respectively. On the other hand, the two equivalent C–N bonds of the CN_3 unit are shorter, with bond length of ~1.34 Å. This observation is in agreement with the atoms in the hpp core being sp^2 hybridized causing the guanidine core to demonstrate planarity (~178.9°). In addition, the shorter Mo–N_{hpp} distance for the hpp ligand when compared to the Mo–N distance for the formamidinate ligand is a reflection of the stronger binding of hpp due to the higher basicity of the ligand.

Electrochemical Studies. Dimolybdenum paddlewheel structures typically show a one-electron oxidation that leads to the formation of a Mo_2^{5+} unit.[237] However, when hpp is used as ligand in $Mo_2(hpp)_4$, **IV**, two one-electron oxidations are observed.[213] Thus, to understand the ability of hpp to stabilize higher oxidation states the electrochemical properties of **I**, **II** and **III**, and **1**, **2** and **3** were studied. Cyclic voltammograms (CV) for the studied compounds and their precursors are depicted in Figure 5.2 and Figure 5.3, respectively. Electrochemical data for the compounds presented in this work as well as precursors **I**, **II**, **III** and **IV** are given in Table 3, all redox potentials have been referenced versus the ferrocene/ferrocenium couple (Fc/Fc^+). Compound **I** shows a one-electron reversible event with half-wave potential ($E_{1/2}$) at –0.120 V, which corresponds to the reversible oxidation of Mo_2^{4+} to Mo_2^{5+}. Similarly, **II** and **III** display a one-electron oxidation with an $E_{1/2}$ = –0.286 V and $E_{1/2}$ = –0.381 V, respectively. Replacement of one formamidinate by a guanidinate ligand in **1** shifts the Mo_2^{4+} to Mo_2^{5+} oxidation potential half a volt in the negative direction ($E_{1/2}$ = –0.754 V vs Fc/Fc^+) when compared to **II** and **III**. The lower oxidation potential of **1** is expected due to the increase on the electron density on the metal center as a result of the increase basicity of hpp.[219]

Table 5.4. Redox potentials in volts (vs Fc/Fc^+) for Mo_2L_4 compounds **I** – **IV** and **1** – **3**.

	$E^2_{1/2}$ (Mo_2^{6+}/Mo_2^{5+})	$E^1_{1/2}$ (Mo_2^{5+}/Mo_2^{4+})
I	–	–0.120
II	–	–0.286
III	–	–0.381[228]
1	–	–0.754
2	–0.693	–0.988
3	–0.763	–1.136
IV	–0.968[213]	–1.795[213]

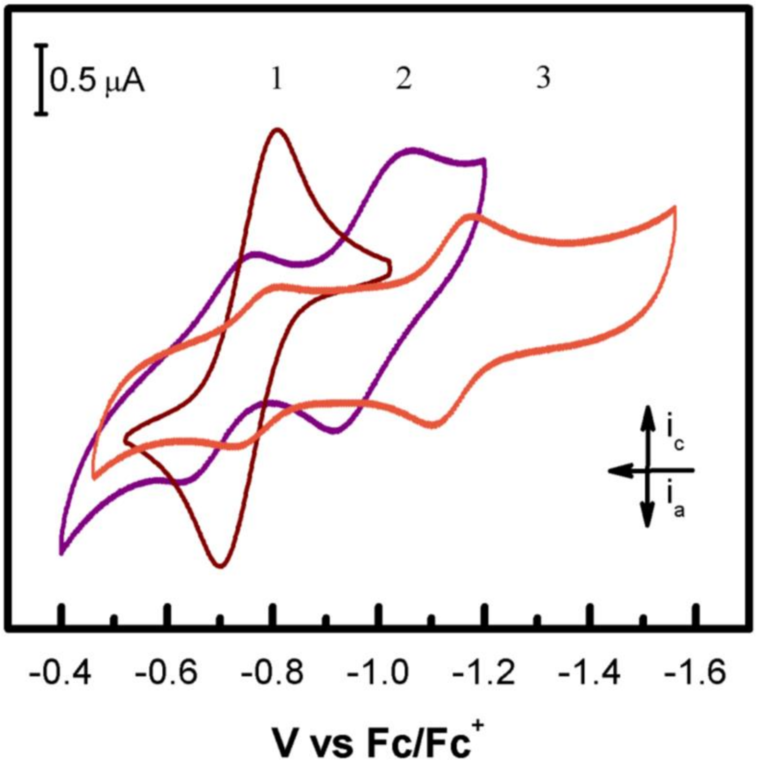

Figure 5.2. Cyclic voltammograms for **1**, **2**, and **3** in THF with potentials referenced to Fc/Fc$^+$.

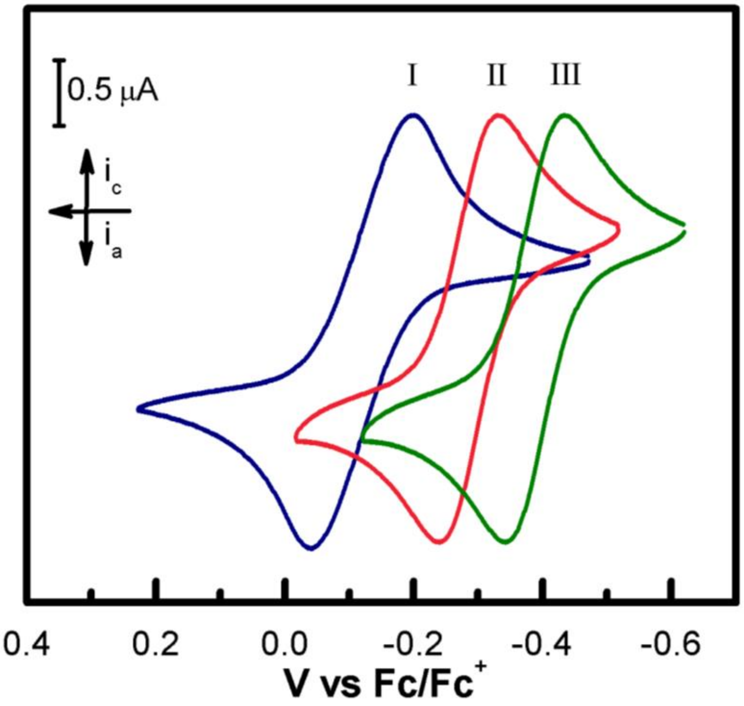

Figure 5.3. Cyclic voltammograms for **I**, **II** and **III** in THF with potentials referenced to Fc/Fc$^+$.

The bicyclic guanidinate, hpp, has shown the ability to stabilize higher oxidation states in bimetallic complexes due to its π-donor nature and increased basicity.[221,238] The CV for $Mo_2(hpp)_4$, **IV**, shows two reversible one-electron redox events at $E_{1/2}{}^2$ = –0.968 V and $E_{1/2}{}^1$ = –1.795 V corresponding to the reduction of Mo_2^{6+} to Mo_2^{5+} and Mo_2^{5+} to Mo_2^{4+}, respectively.[213] The charge stabilization ability of hpp can be observed when a second guanidinate is introduced in **2**. Two one-electron reversible redox processes are obtained at $E_{1/2}$ (1) = –0.988 V and $E_{1/2}$ (2) = –0.693 V, analogous to those for **IV**. The half-wave potentials, $E_{1/2}$ (2) and $E_{1/2}$ (1) were assigned to the reduction of Mo_2^{6+} to Mo_2^{5+} and Mo_2^{5+} to Mo_2^{4+}, respectively. Therefore, the major specie at the resting point must be the doubly oxidized Mo_2^{6+} species. The reduction potential at –0.693 V (Figure 5.2) indicates that the oxidation of **2**$^+$ is easier than that of **I** and **III**. The measured half-wave potential for the $[Mo_2]^{4+/5+}$ pair in **2** is significantly more negative than that of **1** by 0.234 V. Moreover, the poorer solubility of **2** compared to that of **I**, **II** and **1** in THF causes a considerable decrease of the current in the cyclic voltammogram.

Replacement of a third formamidinate by hpp in **3** shows a similar voltammogram to that of **2** with two one-electron reversible redox events at $E_{1/2}$ = –0.763 V and $E_{1/2}$ = –1.136 V. Analogous to **2**, these processes correspond to the reduction of Mo_2^{6+} to Mo_2^{5+} and Mo_2^{5+} to Mo_2^{4+}, respectively. The redox potential for the $[Mo_2]^{5+/4+}$ pair in **3** is 0.148 V more negative than in **2**. This trend continues when the final formamidinate is replaced to get **IV** where the $E_{1/2}$ for the reduction of Mo_2^{5+} to Mo_2^{4+} occurs at –1.795 V vs Fc/Fc$^+$.

The systematic substitution of formamidinates by guanidinates allows to probe the ability of hpp to destabilize the quadruple bond. The measured $E_{1/2}$ for the Mo_2^{4+} to Mo_2^{5+} oxidation shifts cathodically as guanidinates are added to the Mo_2^{4+} unit. It is evident the guanidinate ligand, hpp, tunes the redox potentials of these bimetallic molybdenum systems due to the high basicity of the anion along with its ability to strongly interact with the Mo_2^{n+} core via its delocalized π electrons in the central $C(N)_3$ unit.[238] Therefore, the δ bonding orbital gets destabilized upon increasing the electron-donating ability of the ancillary ligand. The redox properties of these series of compounds show the increase in basicity from $^-$OAc < $^-$DAniF < $^-$hpp, with the guanidinate being the most basic. Consequently, the guanidinate ligands are the most difficult to substitute while acetates are the most easily ones due to their increased lability. Moreover, a trans influence is noticed proportional to the basicity of the ligand, such influence is also manifested in the Mo–N bond distance (Table 5.2).

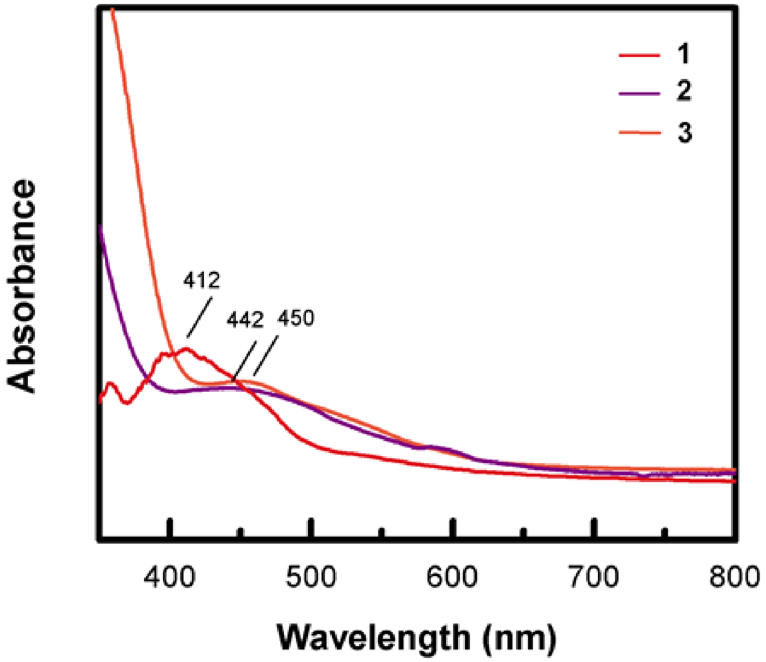

Figure 5.4. UV-Vis Spectra of compounds **1–3**.

Spectroscopic Properties. The UV-Vis spectra of compounds **1** – **3** show two absorption peaks: one near the UV region (~300 nm) and one in the visible region (~450 nm). The low energy transition in the region of 400–600 nm, assigned to Mo_2 δ → Mo_2 δ*, has been well established in the literature for quadruply bonded paddlewheel dimolybdenum compounds.[226,239,240] The energy of this transition relies on the nature of the ancillary ligands.[241] The absorption spectra of **1** – **3** are shown in Figure 5.4. Compound **1** shows a band at 412 nm, arising from the δ → δ* transition. Similarly, compounds **2** and **3** presented a band at 442 nm and 450 nm, respectively. A detailed electronic transition analysis was performed using time-dependent density functional theory (TD–DFT) calculations (*vide supra*).

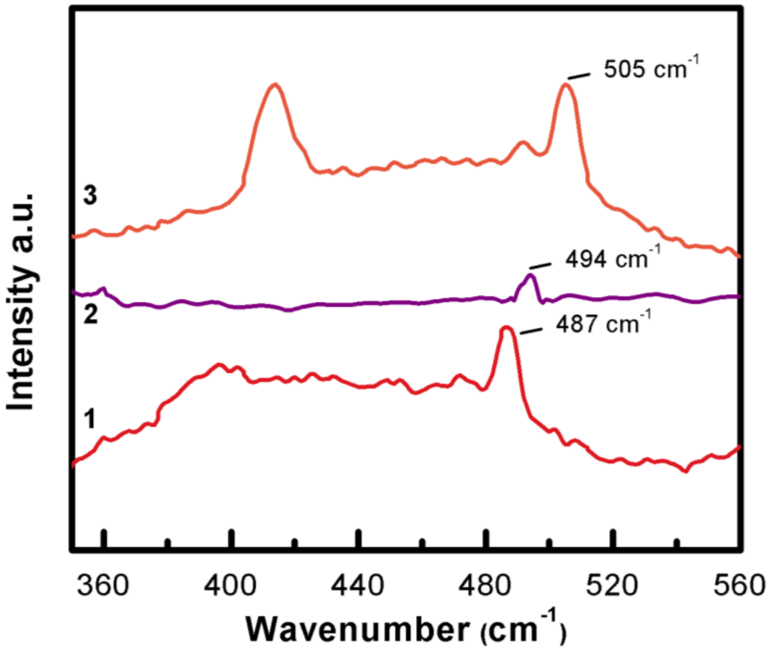

Figure 5.5. Raman spectra of compounds **1** (bottom), **2** (middle) and **3** (top).

Raman spectroscopy was used to further probe the electronic structure of the strength of the metal–metal bond in **1** – **3**. The spectra were obtained with a laser excitation of 532 nm and it is found in Figure 5.5. For non-axially substituted carboxylate dimolybdenum complexes such as **I**, the band associated with the symmetric *v*(Mo–Mo) vibration appears at 404 cm^{-1} (Figure 5.6), while for the halide species is 342±8 cm^{-1}.[242] The strongest Raman signal was assigned to the Mo–Mo stretching mode as supported by DFT calculations. The *v*(Mo–Mo) of **1** shows a Raman shift at 487 cm^{-1}. The trans isomer, **2**, gives the Mo–Mo shift at 494 cm^{-1}. Finally, compound **3**, has a

Mo–Mo vibration at 505 cm^{-1}. This complex shows strong fluorescence, which accounts for the high intensity detected. The sequential addition of guanidinate ligands shifts the *v*(Mo–Mo) Raman signal, this observation is consistent with the destabilization of the Mo–Mo bond due to the high basicity and electron donating abilities of guanidinate ligands.[243]

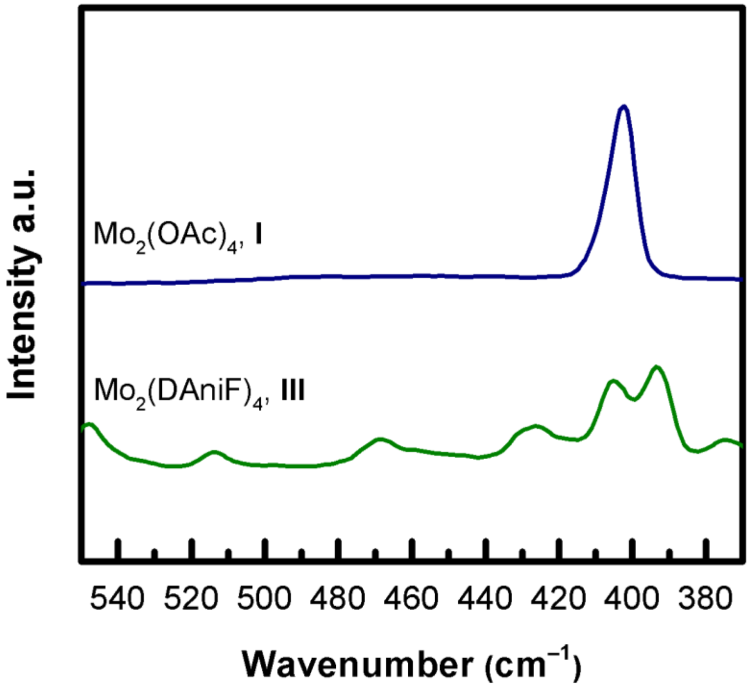

Figure 5.6. Raman spectra of compounds **I** (top) and **III** (bottom).

DFT Calculations. Density Functional Theory (DFT) calculation were performed on all precursors **I** – **IV** and all synthesized compounds, **1** – **3**, to gain insight into the electronic structure of their Mo_2 cores, their ground state geometries, and the nature of their frontier orbitals. The gas phase geometry optimizations were performed using the crystal structure parameters as the starting point for the calculations. The calculated gas-phase Mo–Mo bond distance for **1** is 2.12328 Å, which is analogous to the experimentally obtained 2.0844(6) Å. For **2**, the DFT obtained metal–metal bond is 2.11451 Å while the experimental one is 2.0784(6) Å. Meanwhile, the calculated

Mo–Mo bond for **3** is 2.10730 Å. The shortening of the M–M bond distance is consistent with the greater overlap of the δ bond due to the addition of guanidinates as ancillary ligands. This effect is described by the linear relationship of the M–M bond distance with the number of guanidinate ligands surrounding the bimetallic center (Figure 5.7). The fitting of the data gives a correlation coefficient of (R^2) 0.947. Another correlation is also observed between the energy of the $\delta \rightarrow \delta^*$ transition and the metal–metal bond distance. As the metal–metal bond length increases the energy of the $\delta \rightarrow \delta^*$ transition increases as well. There is a consistent overestimation of the Mo–Mo bond by about 0.04 Å, which has been well established in the literature when B3LYP and other functionals are employed.[221,244]

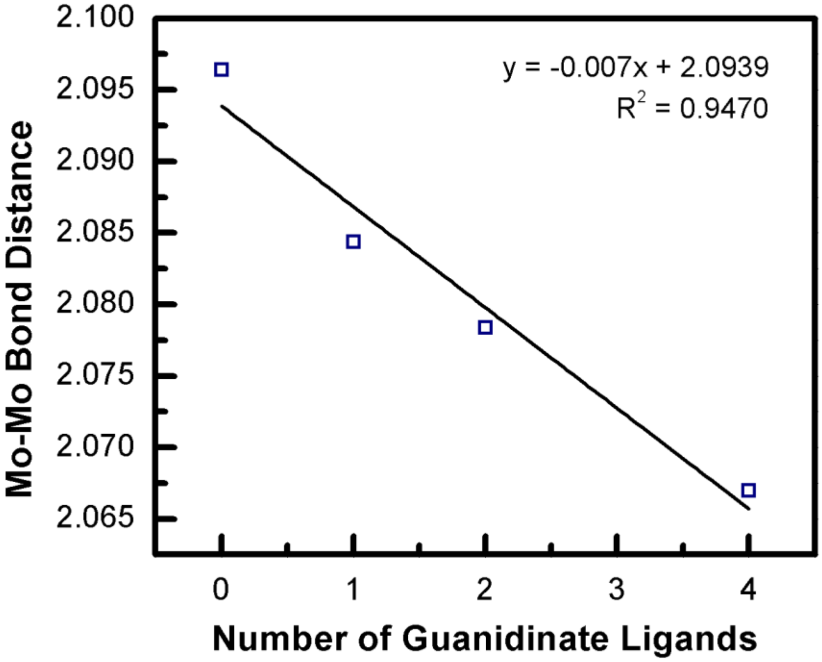

Figure 5.7. Plot of the dependence of the Mo–Mo bond distance on the number of guanidinates in **III**, **1**, **2**, **3**, and **IV**. The squares are the measured values, and the solid line are the least square fit for the data.

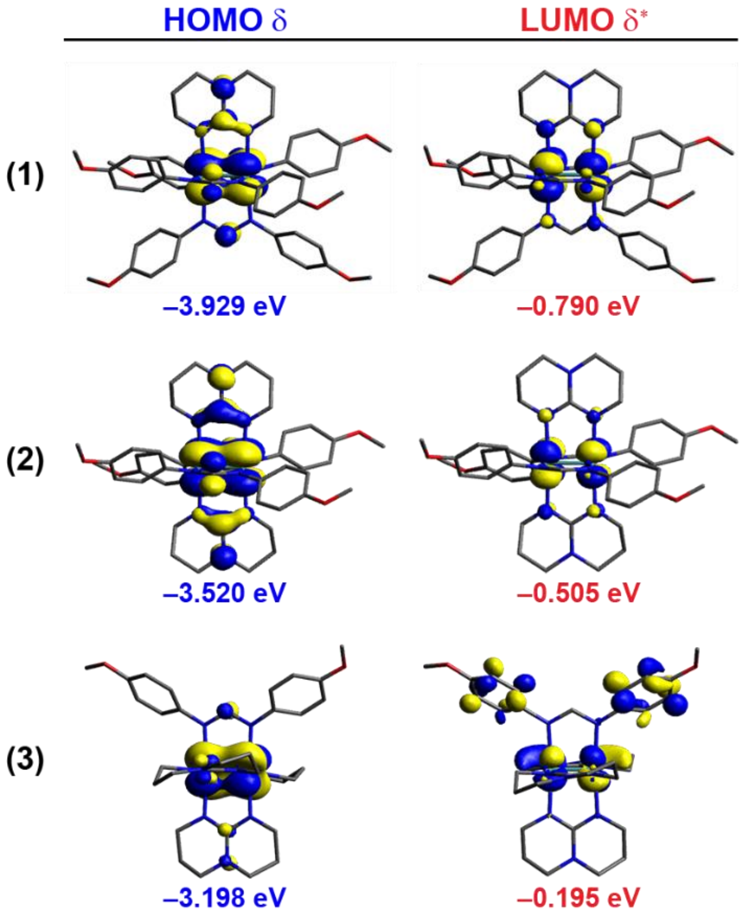

Figure 5.8. Illustration of the HOMO and LUMO for compound **1 – 3** with 0.04 contour calculated by DFT.

Figure 5.8 depicts the HOMO and LUMO orbitals for compounds **1** – **3**. The highest occupied molecular orbital (HOMO) for all the compounds was established as a metal based δ orbital with some degree of mixing with the ligands. The composition of the HOMO attributes the lower redox potential wave in the cyclic voltammograms for **1** – **3** to the $Mo_2^{5+/4+}$ process. On the other hand, the lowest unoccupied molecular orbital (LUMO) is a metal based δ* orbital, except in $Mo_2(hpp)_4$ where the LUMO is a metal based σ* while the LUMO+1 is the δ*.[245] A molecular orbital diagram for the frontier molecular orbitals of the $Mo_2(DAniF)_{4-n}(hpp)_n$ (n = 0, 1, 2, 3, 4) molecules is given in Figure 5.9 which allows a comparison of relative energies for **III**, **1**, **2**, **3** and **IV**. The highest HOMO energy observed was at –2.813 eV for $Mo_2(hpp)_4$ (**IV**), with 64% metal character, while the lowest and most stable orbital is that for $Mo_2(DAniF)_4$ (**III**) with an onset HOMO δ energy of –4.32 eV and 75% metal character.

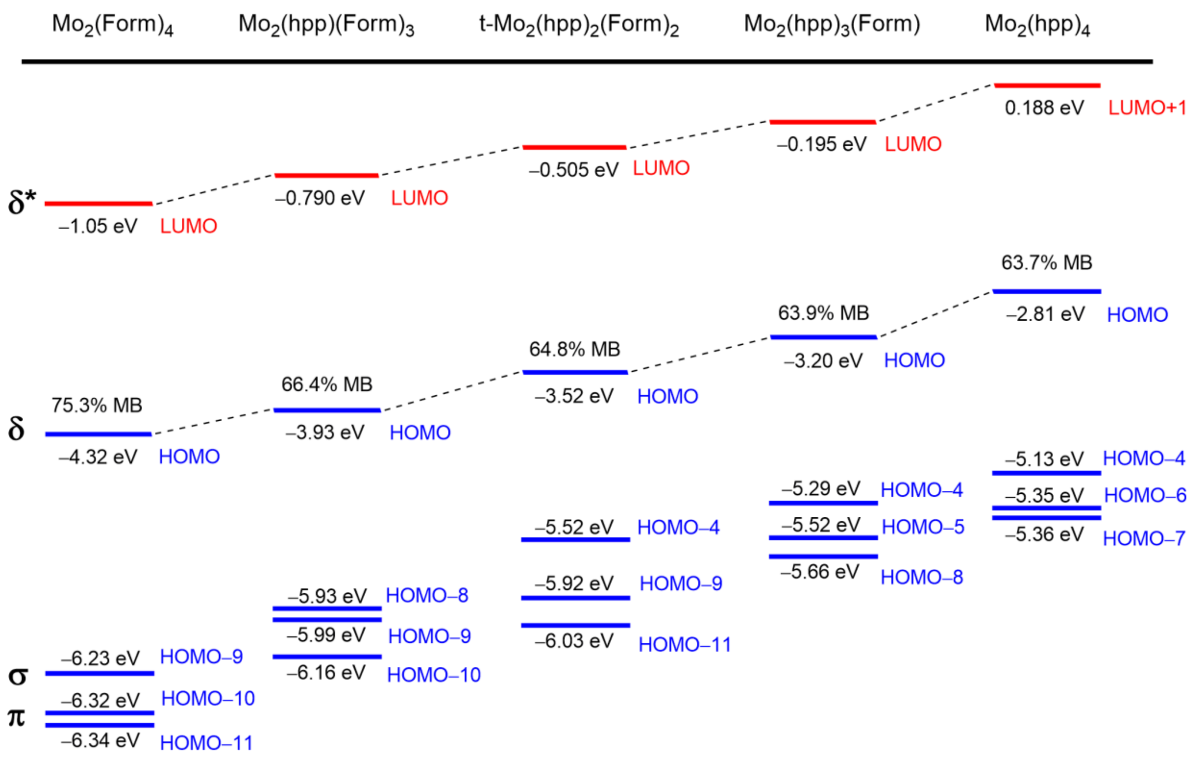

Figure 5.9. Diagram shows the respective relative energies of the metal orbitals of **III**, **1**, **2**, **3** and **IV**. The metal based character of the delta HOMO Orbital is displayed.

The electronic structure of **1** shows that the HOMO (–3.929 eV) is metal based (66%) with δ character. Contrary to typical paddlewheel complexes, the σ orbital is found to be less stable than the π orbitals, at –5.932 eV (HOMO–8). The HOMO–9 and HOMO–10 (at –5.997 eV and –6.156 eV, respectively) are the π orbitals showing strong ligand interaction between the guanidinate N atoms and the metal center. The LUMO of **1** is the metal based δ* found at –0.790 eV. Compound **2**, has an onset LUMO energy of –0.505 eV, 0.285 eV higher in energy than that for **1**. The Mo_2 unit makes the largest contribution to the HOMO with 65% at –3.520 eV. Similar to **1**, the σ orbital

(HOMO–4) is less stable than the π orbitals at –5.515 eV. Finally, the HOMO–9 and HOMO–11 are found at –5.921 and –6.027 eV, respectively. On the other hand, **3** has a HOMO energy of –3.198 eV. Interestingly, the metal character of the compound decreases again with respect to **1** and **2**, to 64%. Once again the σ orbital is found before the π orbitals at –5.290 eV (HOMO–4), while HOMO–5 and HOMO–8 are found at –5.516 and –5.655 eV, respectively.

The reduction potentials for this series are also linearly correlated to the number of guanidinates in the complexes and the onset energy of the HOMOs with R^2 of 0.9228 (Figure 5.10a) and 0.9258 (Figure 5.10b), respectively. Comparison between the energy levels of the metal based frontier orbitals for **III**, **1**, **2**, **3** and **IV** show that the relative energy of such orbitals increases from that of the tetraformamidinate paddlewheel compound, **III**, to that of the tetraguanidinate one, **IV**. The large energy range of the HOMO (~1.5 eV) show that substitution of $^{-}$DAniF for $^{-}$hpp results in a large change in the electronic structure of the paddlewheel compounds. This trend correlates with the ligand electronic donor ability that increases gradually as formamidinates get replaced by the cyclic guanidinate hpp. Furthermore, the systematic addition of electron donating hpp ligands results in a smaller HOMO–LUMO energy gap decreasing the metal character of the δ orbitals (HOMO) due to a greater mixing of metal- and ligand-based orbitals.[241] The magnitude of the half-wave potential for the synthesized compounds follows the order **1** < **2** < **3** based on their HOMO energies as the number of guanidinates are introduced in the system. This observation is in agreement with the obtained electrochemical data, where the destabilization of the Mo_2^{4+} core is reflected in the negative shift of the redox potentials, favoring the formation of the M_2^{5+} and M_2^{6+} species.

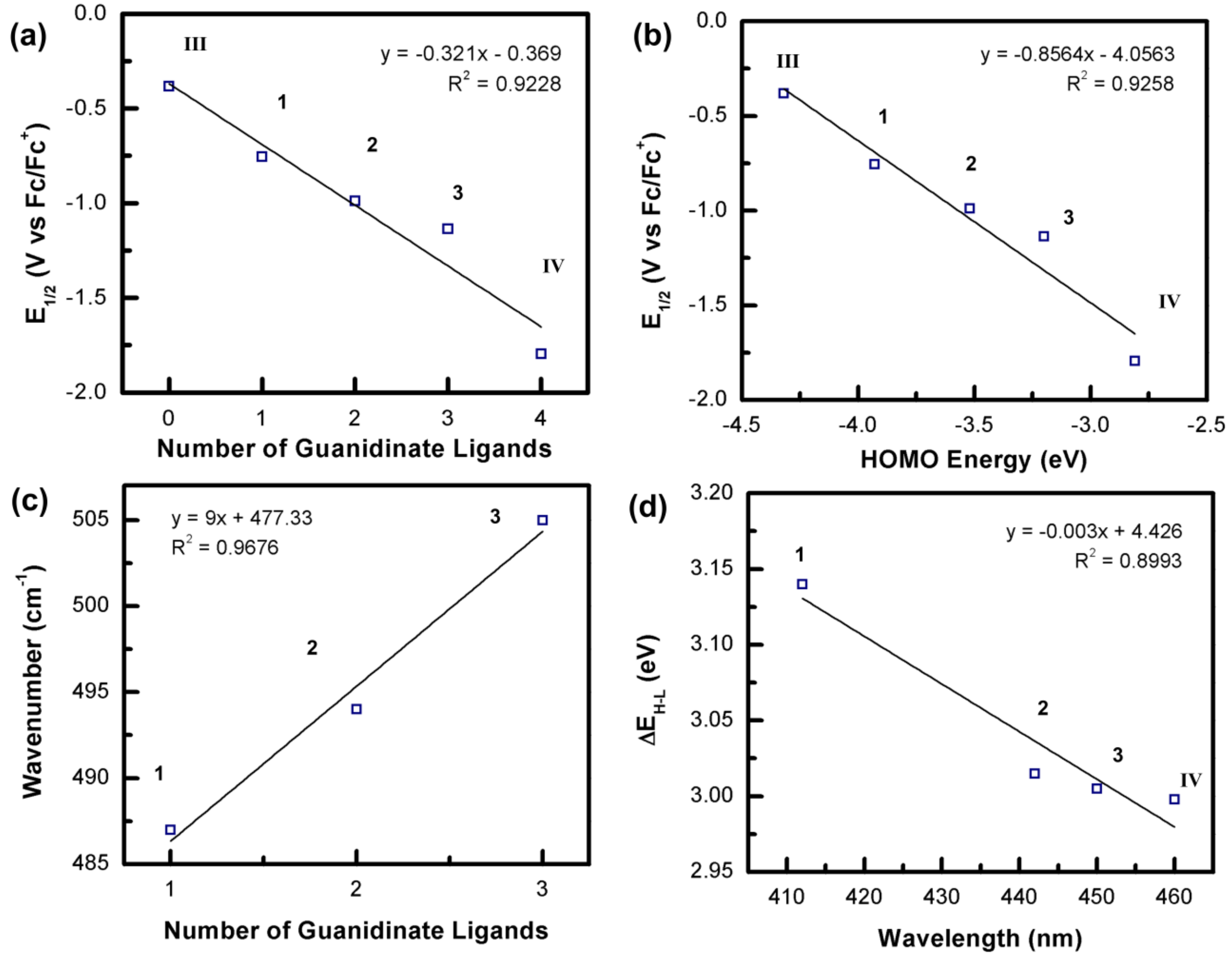

Figure 5.10. Plot of the dependence of (a) half-wave potentials ($E_{1/2}$) on the number of guanidinates around the Mo_2 core with zero being the tetra-formamidinate **III**; (b) potential separation ($E_{1/2}$) on the calculated energy of the highest occupied molecular orbitals for **III**, **1**, **2**, **3**, and **IV**; (c) the Raman shifts for the ν(Mo–Mo) stretch on the guanidinate ligands for **1**, **2**, and **3**; (d) the lowest energy absorption band associated to the $\delta \rightarrow \delta^*$ electronic transition on the calculated HOMO–LUMO energy gap for **1**, **2**, **3**, and **IV**. The squares are the measured values, and the solid line are the least square fit for the data.

Table 5.5. Experimental and calculated Raman shifts for ν(Mo–Mo).

	Experimental (cm^{-1})	Calculated (cm^{-1})
I	404	–
III	404	407
1	487	489
2	494	492
3	505	510
IV	–	501

Density functional theory was used to help assign the *v*(Mo–Mo) vibrational modes. Table 5.5 presents the experimental and calculated Raman shifts of the *v*(Mo–Mo). We can observe that the frequencies for the dimolybdenum stretch in compounds **1** – **3** are between 487 and 505 cm^{-1}. Compared to the vibration of the tetraacetate moiety, the higher frequency of the vibration for **1** – **3** can be attributed to a smaller Mo–Mo bond and the increase in the metal–metal bond strength.[246] The calculated Raman shifts obtained by DFT show an increase in the frequency for the dimolybdenum stretch as a function of the number of guanidinates being substituted with a correlation coefficient (R^2) of 0.9676 (Figure 5.10c) consistent with the reduction of the HOMO–LUMO gap. Nonetheless, the difference in the calculated frequencies between compounds **1** and **3** is 21 cm^{-1} (0.06 kcal/mol).

Table 5.6. UV–Vis λ_{max} for **I**, **III**, **1**, **2**, **3** and **IV**.

	Experimental (nm)	**Calculated (nm)**
I	303[247]	
III	430[228]	
1	412	520
2	442	542
3	450	572
IV	460[248]	

Time-dependent density functional theory calculations were performed on the geometry optimized compounds **1** – **3** to help assign the lowest energy transition observed in the UV-Vis spectra for each compound. Absorption spectra of **1** shows a band at 412 nm arising from the δ → δ* transition. Similarly, **2** presented a band at 442 nm while the same signal appeared at 450 nm for **3**. These bands corresponds to the HOMO → LUMO transition calculated to be 520, 542 and 572 nm for **1**, **2** and **3**, respectively. A bathochromic shift is present in the electronic absorption spectra for these molecules as guanidinates are substituted in the Mo–Mo center, from the tetraformamidinate **III** (430 nm) to the tetraguanidinate complex **IV** (460 nm) as depicted in Figure 5.10d with a correlation coefficient (R^2) of 0.8993. This feature is attributed to the delocalization of the uncoordinated nitrogen lone pair into the ligand π system which narrows the HOMO–LUMO energy gap as observed in the calculated relative energies in Figure 5.9.[249] Meanwhile, the higher energy transition observed at 290, 295, and 330 nm for **1**, **2**, and **3** respectively were calculated at 375, 362, and 358 nm. These high energy transitions correspond to $\delta \rightarrow \pi_M^*$ transition for **1**, $\pi_M \rightarrow \delta^*$ in the case of **2**, and $\delta \rightarrow \pi_L$ for **3**. Experimental and calculated wavelengths for the δ to δ* transition of **I**, **III**, **1**, **2**, **3** and **IV** are displayed in Table 5.6.

5.5 CONCLUSION

A series of quadruple bonded dimolybdenum compounds was successfully synthesized and characterized. Compounds **1** and **2** were structurally characterized by single crystal x-ray crystallography presenting a Mo–Mo distance of 2.0844(6) and 2.0784(6) Å, respectively. Data obtained from Raman Spectroscopy shows an increase in Raman Shift with the addition of guanidinate ligands, 487, 494, and 505 cm^{-1} for **1**, **2** and **3**, respectively. Electrochemical studies showed that $Mo_2^{4+/5+}$ redox process can be tuned over a range of nearly 0.4V due to the increased ligand basicity. In addition, we have shown the ability of hpp to stabilize higher oxidation states for the Mo_2 unit. The addition of two and three guanidinate ligands shows the ability for these complexes to perform multi-electron redox chemistry. DFT calculations depict strong influence in the guanidinate ligand in the difference in energy levels between the compounds. These observations show greater metal−ligand mixing as formamidinates were replaced by guanidinates, thus reducing the metal character of the HOMO. Moreover, the decrease in energy for the $\delta \rightarrow \delta^*$ transition (as guanidinates are introduced to the Mo_2 core) is in agreement with an increase in the d orbitals overlap and bond strength, hence shortening the Mo–Mo bond distances.

Chapter 6: Chemistry of Digold (I) and Digold (II) Formamidinate Complexes

6.1 INTRODUCTION

Since the discovery of the Re–Re quadruple bond in $ReCl_8^{2-}$ the chemistry of bimetallic compounds with metal-metal bonds has evolved into an important field of chemistry.[150] The nature of their metal-metal interactions and their dependence on coordinating ligands have been explored by studying their spectroscopic, electronic, and magnetic properties. Gold chemistry has been the subject of study over the past years due to the interesting potential applications. [250–254] Moreover, the chemistry of gold bimetallic complexes is of especial interest due to their compelling structural and optical properties.[255] These complexes have led to dinuclear oxidative addition and the formation of metal-mental gold(II) bonds.[256]

Oxidative addition is an important reaction describing the exchange of one or two electrons between a metal center and the molecule being added.[257] This process leads to increased oxidation states and coordination numbers of the metallic unit. The oxidative addition in dinuclear systems can be influenced by the distance between the metal centers.[258] Bridging ligands have been employed to hold the metal atoms in close proximity while stabilizing an intermediate or final product. Oxidative addition reactions of dinuclear gold(I) have been studied using ylides, thiolates, formamidinates, and guanidinates.[256,259] It has been found that in these systems the close proximity of the gold centers is essential to stabilize the d^9 system upon oxidation to form Au(II)-Au(II).[256] For this reason, factors that modify the electronic structure of the gold atoms or the nature of the ligands are considered.[260,261]

Fackler and coworkers have explored oxidative addition in digold systems containing C–P–C, C–P–S and N–C–N bridging monoanionic ligands.[256,258] Although work has been done using these ligands, digold-nitrogen compounds, Au(II)–N, are less common. The formation of dinuclear gold (II) products substantially depends on the type of ligands used. Electron delocalization through the π-system of the ligands has been associated to the stabilization of Au(II) complexes. Amidinates have shown to be promising ligands to bring metal center to close proximity, and stabilizing digold (II) compounds through delocalization of the electron density.[262] The use of sterically bulky groups in the ligand is necessary to isolate the dinuclear species.[263]

Ligand control over transition metal complexes is crucial in homogeneous catalysis[257,264] and electron transfer reactions[265]. This control can be determined by the nature of the coordinating atoms, steric factors, and substituent effects in the periphery. In a classical two-state model (D–B–A), the electron-donating ability of the donor, the electron-withdrawing ability of the acceptor, and the electron-transfer ability of the bridge are major factors controlling the electron transfer process and its mechanism. The bridging-ligand mediated electronic coupling and electron transfer has been explored by modification of its length, conjugation and conformation.[157,266–268] To probe donor and acceptor properties, a variety of metals have been employed as redox centers in D–B–A systems.[157,172,269–271] Nonetheless, variation of the peripheral ligands on the metal unit can potentially modify the energy of the orbitals, modulating thus redox potentials and photophysical properties of the unit.[272,273] Therefore, the electron transfer process can be influenced through inductive effects on the ancillary ligands (away from the first coordination sphere) with minimum change in the coordination geometry.

Dinuclear compounds have been successfully used as antitumor agents[274], platforms for supramolecular structures[275], and catalysts[276,277]. The electronic structure of the dinuclear center plays an important role in these applications, thus the ability to fine-tune the electronics of these systems may lead to new developments in the above mentioned areas. Ren's work has shown that the redox potentials on Mo_2L_4 and Ni_2L_4 formamidinate complexes is sensitive to variations on the substituents on the periphery.[208,278] Although important, systematic studies of substituent effects on the electronic and photophysical properties of bimetallic centers are scarce.

6.2 EXPERIMENTAL SECTION

6.2.1 Materials and Methods.

All manipulations were carried under normal atmosphere at room temperature unless otherwise stated. All glassware was oven dried prior to use. The materials used $CDCl_3$, tetrahydrothiophene(THT), hydrogen tetracholoaurate(III) ($H[AuCl_4]•4H_2O$), acetic acid, *m*-anisidine, *p*-anisidine, triethylorthoformate, 4-chloroaniline, and 2,6-diisopropylaniline were purchased from Sigma-Aldrich. Au(THT)Cl[35], and HDippF[43] were prepared according to literature procedures. Triphenylguanidine, HCl, THF, DCM, ethanol, hexanes, ethyl acetate, and diethyl ether were purchased from Fischer Scientific and used as received.

6.2.2 Physical Measurements.

^1H NMR spectra were recorded on a Bruker 400 MHz NMR spectrometer, and on a JEOL 600 MHz NMR spectrometer. UV-Vis spectra was recorded on a SEC2000 Spectra System with the Visual Spectra 2.1 software. The proton chemical shifts (δ) of all gold complexes were referenced to the residual protic signal of $CDCl_3$ solvent. Infrared spectra were recorded on an Agilent Cary 630 FTIR Spectrometer. Mass Spectra were collected using a JEOL AccuTOF JMS-T100LC under ESI+ mode spectrometer.

6.2.3 Electrochemical Studies.

Electrochemical analyses by cyclic voltammetry (CV) and differential pulse voltammetry (DPV) were collected using a CHI760D potentiostat with a Pt working and auxiliary electrodes, a Ag/AgCl reference electrode, 1mM solution of the compounds, and 0.10 M Bu_4NPF_6 (in DCM) as electrolyte. Data was obtained with a scan rate of 100 mV/s, and ferrocene was added at the end of the run as internal standard.

6.2.4 X-Ray Structure Determination.

Crystals of **II**, **III**, **1**, **2**, **3**, **4**, and **5** suitable for X-Ray diffraction analysis were prepared by slow evaporation of solutions of **1** – **5**. The crystals were mounted and centered in the goniometer of either a Bruker SMART APEX CCD or a Bruker D8 Venture system equipped with a graphite monochromator and a MoKα fine-focus tube ($\lambda = 0.71073$ Å). Data for **III**, **IV**, **1**, **2**, **3**, and **4** were collected at 100 K, while the data for **II** and **5** were collected at 296 and 300.27 K, respectively. No crystal decay was observed during the collection. The frames were integrated with Bruker SAINT software package using a narrow-frame algorithm. Data were corrected for absorption effects using the multi-scan method (SADABS). All structures were solved and refined using the Bruker SHELXTL Software Package. Crystallographic data for **1** – **3** are listed in Table 6.1, while the crystallographic data for **4**, and **5** are listed in Table 6.3. Relevant bond distances for compounds **1** – **3** are given in Table 6.2, while those for **4** and **5** are given in Table 6.4. Crystallographic data for **II**, **III**, and **IV** are listed in Table 6.5.

6.2.5 Synthesis of Ethyl (*N*-2,6-diisopropylphenyl) formimidate (DippFm), I.

2,6-diisopropylaniline (0.159 mol) was mixed with triethylorthoformate (2 mol equiv.) in a 50 mL round-bottom flask. The reaction was heated for 3 h at 140°C while distilling ethanol. A brown oil was obtained at the end of the reaction. The excess triethylorthoformate was then distilled off, leaving a dark orange oil. Yield = 30.34 g, 82%. $R_f = 0.95$ ^{1}H NMR δ (ppm in $CDCl_3$): 7.13 (t, 2H, aromatic C-H), 7.08 (d, 1H, aromatic C-H), 4.42 (q, 2H, C-H), 3.04 (sept., 2H, C-H), 1.44, t, 3H, C-H), 1.19 (d, 12H, C-H). ESI-MS (*m/z*): Calcd. 233.17 [L], Found 233.35 [L]

6.2.6 Synthesis of *N*-3-methoxyphenyl, *N'*-2,6-diisopropylphenyl-formamidine (H^{m}DippAF), II.

DippFm, **I**, (0.1025 mol), 1 equiv. of *m*-anisidine, and catalytic amounts of HCl (0.05 equiv. –approx. 1-2 drops-) were mixed in a 50 mL round-bottom flask. The reaction mixture was heated at 140^{o}C until theoretical amounts of ethanol were collected. A dark orange oil was obtained as a product. Silica column chromatography was run with ethyl acetate: hexanes (1:5). Clear crystals were grown from the collected fractions. The crystals were washed with hexanes (3 x 20 mL). Yield = 12.72 g, 40%. R_f = 0.95 ^{1}H NMR δ (ppm in $CDCl_3$): 9.98 (s, 1H, N-H), 7.93 (s, 1H, NC*H*N-), 7.18 (d, 2H, aromatic C-H), 7.14 (t, 1H, aromatic C-H), 7.08 (t, 1H, aromatic C-H), 6.49 (d, 1H, aromatic C-H), 6.43 (d, 1H, aromatic C-H), 6.26 (s, 1H, aromatic C-H), 3.41 (s, 1H, -OCH$_3$), 3.27 (sept., 2H, C-H), 1.20 (d, 12H, C-H). ESI-MS (*m/z*): Calcd. 310.20 [L], Found 311.16 [LH$^+$].

6.2.7 Synthesis of *N*-2,6-diisopropyphenyl, *N'*-4-chloro-formamidine (ClHDippF), III.

In a 50mL round bottom flask, DippFm (18.2 mmol) and 1 eq. of 4-chloroaniline, along with catalytic amounts of HCl (1 drop). The reaction mixture was heated at 140^{o}C for 1.5 h while distilling ethanol. The red brown product mixture was run in a 5:1 hexanes: ethyl acetate chromatography column. Clear crystals were grown from the corresponding elutions. The crystals were washed with hexanes (3x20mL). Yield: 2.4 g, 42%. R_f = 0.58 ^{1}H NMR δ (ppm in $CDCl_3$): 8.75 (s, 1H, N-H), 7.77 (s, 1H, NC*H*N-), 7.27 (d, 2H, aromatic C-H), 7.18 (t, 1H, aromatic C-H), 6.83 (d, 1H, aromatic C-H), 3.21 (sept., 2H, C-H), 1.20 (d, 12H, C-H). ESI-MS (*m/z*): Calcd. 314.15 [L], Found 315.20 [LH$^+$].

6.2.8 Synthesis of N-3-methoxyphenyl, *N'*-4-methoxyphenyl-formamidine (^{m,p}HDAniF), IV.

Triethylorthoformate (81.2 mmol), *p*-anisidine (1 mol equiv.) and *m*-anisidine (1 mol equiv.) were mixed in a 100mL round-bottom flask. The reaction mixture was heated at 140^{o}C while distilling ethanol until the theoretical amount of ethyl alcohol was collected. Diethyl ether was added to the brown oily product mixture to precipitate a white solid. Sonication helped to separate better the precipitate from the liquor. The white powder was washed with ether (3x30 mL) and hexanes (2x30 mL). Yield = 9.334 g, 45%. R_f = 0.22. ^{1}H NMR δ (ppm in $CDCl_3$): 9.74 (s, 1H, N-H), 8.18 (s, 1H, NC*H*N-), 7.18 (t, 1H, aromatic C-H), 7.01 (d, 2H, aromatic C-H), 6.86, (d, 2H, aromatic C-H), 6.61 (d, 2H, aromatic C-H), 6.53 (s, 1H, aromatic C-H), 3.80 (s, 3H, -OCH3), 3.67 (s, 3H, -OCH3). ESI-MS (*m/z*): Calcd. 256.12 [L], Found 257.87 [LH^+].

6.2.9 Synthesis of $Au_2H(DippF)_2Cl$, 1.

HDippF (500 mg, 1.37 mmol) and NaOH (55 mg, 1.37 mmol) were placed in a 50 mL flask with 20 mL of THF. The reaction mixture was stirred at room temperature for 24 h. Au(THT)Cl (440 mg, 1.37 mmol) was added to the solution and stirred for 12 h. The purple suspension was filtered, and a yellow filtrate was collected. Slow evaporation of the solution yielded yellow crystals suitable for X-Ray Diffraction. Yield: 476 mg, 30%. ESI-MS (*m/z*): Calcd. 1157.47 [MH^+], Found 1157.48 [MH^+].

6.2.10 Synthesis of $Au_2(DippF)_2$, 2.

In a 50 mL flask a solution of HDippF (0.180 g, 0.493 mmol), and NaOH (0.0190 g, 0.493 mmol), were stirred THF (10 mL) at room temperature for 2 hours to create the sodium salt. Au(THT)Cl (0.160 g, 0.499 mmol) was then added to the solution and stirred for an additional 12 hours. After completion, solution had turned a grayish color and black residue could be seen against wall. Reaction was left to settle and the supernatant was decanted off. Solid was washed with a minimal amount of hexanes. Crystals suitable for X-Ray Diffraction were grown from a saturated solution of diethyl ether. Yield: 436 mg, 74%. ^{1}H NMR (δ in $CDCl_3$): 1.18 (d, 24H, $CH(CH_3)_2$), 1.35 (d, 24H, $CH(CH_3)_2$), 3.75 (sept, 8H, $CH(CH_3)_2$), 7.02 (m, 12H, C_6H_3), 7.46 (s, 2H, NC*H*N). ESI-MS (*m/z*): Calcd. 1121.50 [MH^+], Found 1121.53 [MH^+]. UV-Vis λ_{max}: 343 nm. IR 3350 (w), 3062 (s), 2960 (m), 1634 (s), 1596 (d), 1437 (d), 1382 (s), 1346 (d), 1246 (s), 1181 (d), 1056 (m), 964 (s), 879 (s), 801 (s) 754 (s), 690 (m). Anal. Calcd. for $Au_2C_{50}N_4H_{70}C_{l2}$: C, 50.38; H, 5.92; N, 4.70. Found: C, 51.13; H, 6.33; N, 4.25.

6.2.11 Synthesis of $Au_2(DippF)_2(Cl)_2$, 3.

Compound **1** (g, mmol) was dissolved in 30 mL of a DCM:Hex (5:1) mixture and let to evaporate. Yellow crystals were obtained within 72h. Yield: 98.1 mg, 20%. ^{1}H NMR (δ in $CDCl_3$): 7.99 (s, 2H, -NC*H*N-), 7.13 (t, 4H, -C*H*-), 7.03 (d, 8H, -C*H*-), 3.59 (sept, 8H, -C*H*), 1.47 (d, 24H, -C*H*$_3$), 1.30 (d, 24H, -C*H*$_3$). ESI-MS (*m/z*): Calcd. 1157.47 [M – Cl^- + H^+], Found 1157.53 [M – Cl^- + H^+]. UV-Vis λ_{max}: 470, 350, 243 nm.

6.2.12 General procedure for the synthesis for Au_2L_2 compounds. Synthesis of $Au_2(^{m}DippAF)_2$, 4.

HDippAF (110 mg, 0.322 mmol) and NaOH (12.9 mg, 0.322 mmol) were placed in a flask with 10 mL DCM. The reaction mixture was stirred at room temperature for 24 h. Au(THT)Cl (g, mmol) was added to the solution and stirred for 12 h. The dark suspension was filtered and the yellow filtrate collected. Slow evaporation of the solution yielded crystals suitable for X-Ray Diffraction. Yield: 424 mg, 26%. ^{1}H NMR (δ in $CDCl_3$): 8.15 (s, 2H, -NC*H*N-), 7.14 (t, 2H, -C*H*), 7.12 (d, 2H, -C*H*), 7.09 (s, 2H, -C*H*), 7.07 (d, 2H, -C*H*), 6.87 (t, 2H, -C*H*), 6.81 (d, 2H, -C*H*), 6.60 (d, 2H, -C*H*), 3.78 (s, 6H, -OC*H*$_3$), 3.62 (sept, 4H, C-*H*), 1.26 (d, 12H, -C*H*$_3$), 1.22 (d, 12H, -C*H*$_3$). ESI-MS (*m/z*): Calcd. 981.3 [M – OCH_3], Found 981.14 [M – OCH_3]. UV-Vis λ_{max}: 360, 303 nm.

6.2.13 Synthesis of $Au_2(ClDippF)_2$, 5.

Colorless crystals. Yield: 1.17 g, 72%. ^{1}H NMR (δ in $CDCl_3$): 8.06 (s, 2H, -NC*H*N-), 7.21 (d, 4H, -C*H*-), 7.14 (d, 4H, -C*H*-), 7.09 (d, 4H, -C*H*-), 6.82 (t, 2H, -C*H*-), 3.59 (sept, 4H, -C*H*), 1.26 (d, 12H, -CH_3), 1.22 (d, 12H, -CH_3). ESI-MS (*m/z*): Calcd. 1021.24 [MH^+], Found 1021.25 [MH^+]. UV-Vis λ_{max}: 374 nm.

6.2.14 Synthesis of $Au_2(^{m,p}DAniF)_2$, 6.

155 mg of light yellow powder were collected. Yield: 37%. ^{1}H NMR (δ in $CDCl_3$): 8.28 (s, 2H, -NC*H*N-), 7.04 (d, 2H, -C*H*), 7.00 (d, 2H, -C*H*), 6.96 (s, 2H, -C*H*), 6.73 (d, 4H, -C*H*), 6.58 (d, 4H, -C*H*), 6.47 (t, 2H, -C*H*), 3.69 (s, 6H, -C*H*), 3.63 (s, 6H, -OCH_3). ESI-MS (*m/z*): Calcd. 905.16 [MH^+], Found 905.2 [MH^+]. UV-Vis λ_{max}: 384 nm.

6.3 COMPUTATIONAL DETAILS

Density Functional Theory (DFT) calculations were performed with the hybrid Becke-3 parameter exchange functional and the Lee-Yang-Parr nonlocal correlation functional (B3LYP)[110,111] implemented in the Gaussian 09 (Revision C.01)[114] program suit. The Pople basis set, 6-31G*,[119,279–281] was used on non-metal atoms (carbon, nitrogen, oxygen, chlorine, and hydrogen), while the associated double-ζ basis set (LANL2DZ)[161–164] was used for the gold atoms. Geometry optimization calculations were found to be minima in the potential energy surface as evidenced by the lack of imaginary vibrations in the frequency calculations. Electronic transition energies were computed on the optimized geometries for the neutral compounds using Time-Dependent Density Functional Theory (TD-DFT) method with the lowest 30 singlet excited states being considered.[165–171] All calculations were performed in a 44-processor PowerWolf PSSC supercomputer cluster running Linux Red Hat 4.1.2-54 located at the University of Texas at El

Paso. Isosurface plots of frontier molecular orbitals were generated using Avogadro software with isodensity values of 0.045.

6.4 RESULTS AND DISCUSSION

6.4.1 Oxidative Addition in a Dinuclear Au(I) Formamidinate Complex, $Au_2(DippF)_2$

Molecular Design and Synthesis. The dinuclear compounds **1** and **2** were synthesized by the reaction of Au(THT)Cl with the sodium salt of diisopropyl formamidine in a 1:1 ratio using THF, and in the presence of air in 30% and 74% yield. On the other hand, compound **3** was synthesized by dissolving **1** in DCM:Hex (5:1) solution and letting evaporate over a period of 72 hours in 20% yield. **3** can be also synthesized by metathesis of Au(THT)Cl with sodium formamidinate in a 1:1 ratio, and using DCM as solvent. A scheme of the reactions for the synthesis of **1** and **3** are presented in Scheme 6.1. Compounds **1** – **3** decompose to elemental gold in the presence of light but are otherwise stable to air and moisture in the solid state.

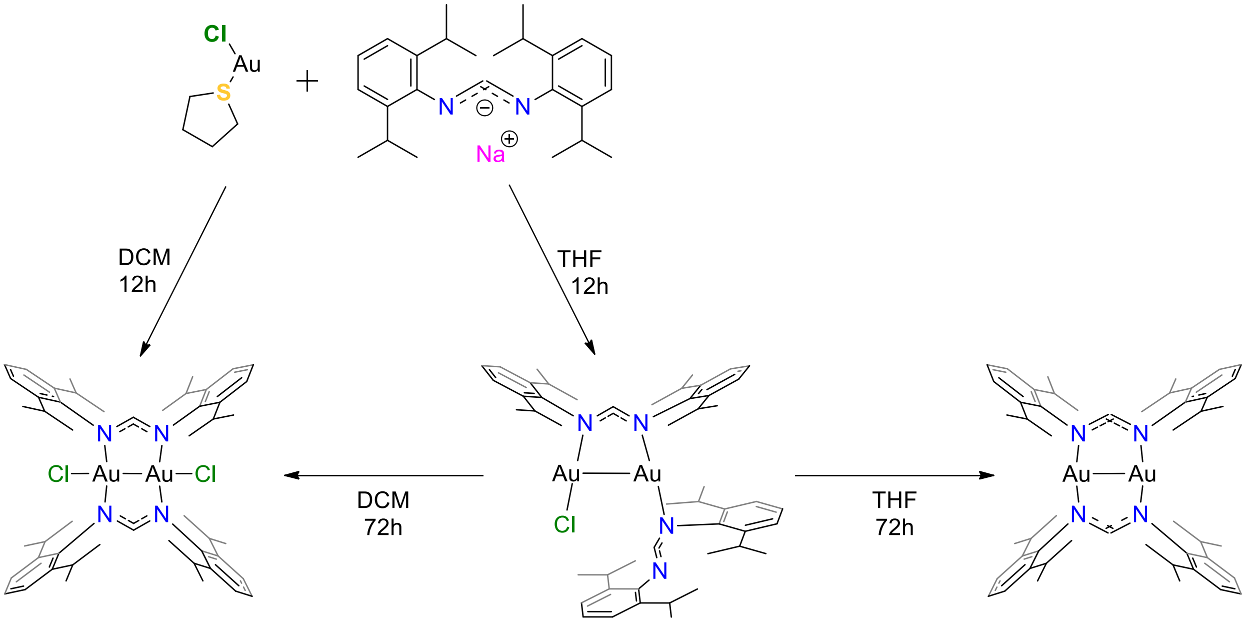

Scheme 6.1. Reaction conditions for the synthesis of **1** – **3**.

The structure of **1** – **3** in solution was confirmed by ^{1}H NMR spectroscopy and single crystal X-Ray crystallography. The proton NMR is consistent with the structure of the molecule with all signals having the expected chemical shifts (ppm) and relative intensities. ^{1}H NMR for **3** (Figure 6.1) show a singlet at 7.99 ppm and 7.46 ppm respectively for the methine protons suggesting the formamidinate ligands are related by symmetry. ESI-MS was performed on **1** and **3**, and are presented in Figure 6.2, Figure 6.3, and Figure 6.4. The compounds show the expected isotopic distribution and the predicted m/z. The calculated *m/z* for **1** + H^+ is 1157.47 (experimental *m/z* = 1157.48), while the ESI-MS for **2** and **3** *m/z* value was calculated 1121.50 and 1157.47, and experimental 1121.53 and 1157.53. The mass spectrum of **3** shows that the dichloride species easily loses a chlorine atom (*m/z* = 1157.53).

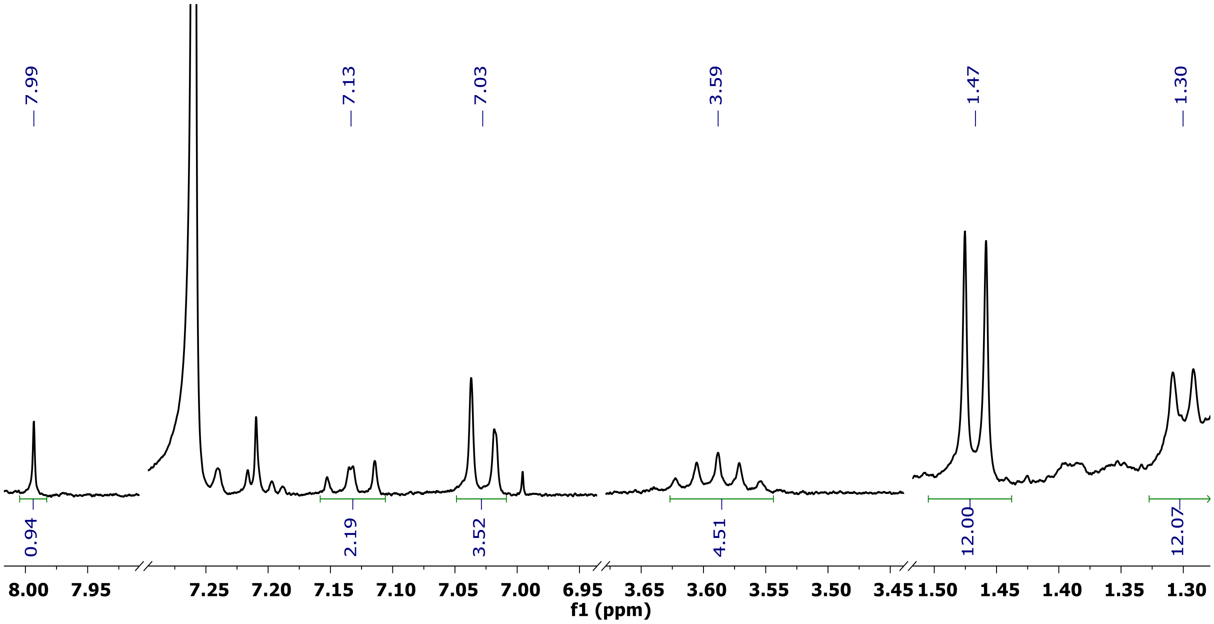

Figure 6.1. ^{1}H NMR for **3** in $CDCl_3$.

The mechanism of the reaction has not been carefully studied, but the presence of air and the use of chlorinated solvent are required to oxidize Au(I) to Au(II) yielding the dichloride compound **3**. This type of reactions has been previously observed by Fackler et al, in a similar digold (II) compound, $Au_2(hpp)_2Cl_2$.[262] The oxidation of Au(I) occurs spontaneously in the synthesis when DCM is used as solvent, similarly to the reported Au(II) hpp complex.[263] In THF on the other hand, **1** is initially formed which later undergoes a self-redox reaction to form Au(0) and the Au(II) product.

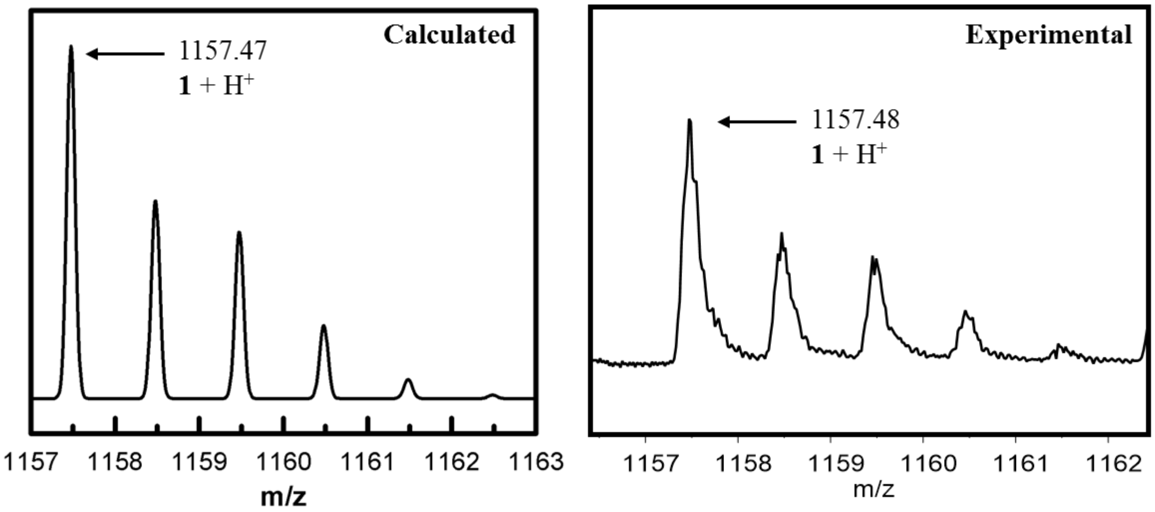

Figure 6.2. ESI-MS of **1**, (left) average *m/z* calculated at 1157.47, and (right) detected *m/z* 1157.48 corresponding to **1** + H^+.

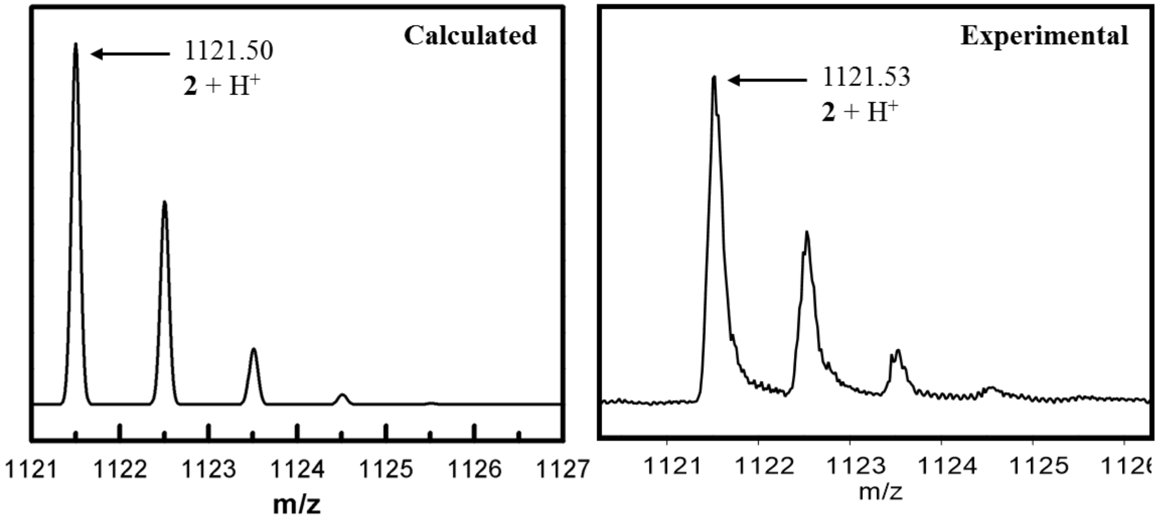

Figure 6.3. ESI-MS of **2**, (left) average *m/z* calculated at 1121.50, and (right) detected *m/z* 1121.53 corresponding to **2** + H^+.

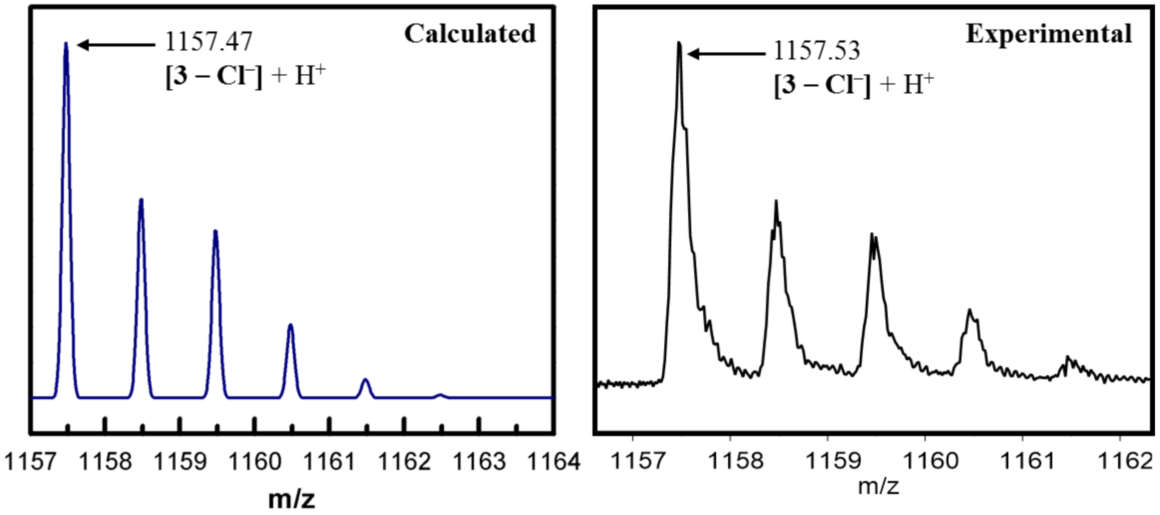

Figure 6.4. ESI-MS of **3**, (left) average *m/z* calculated at 1157.47, and (right) detected *m/z* 1157.53 corresponding to $[\mathbf{3} - Cl^-] + H^+$.

Structural Determinations. Single crystals suitable for crystallography were obtained by slow evaporation of the concentrated solutions of **1** – **3**. The structures of **1** – **3** are provided in Figure 6.5, while selected bond lengths and angles are presented in Table 6.1 and Table 6.2. Compound **1** crystallizes in the monoclinic space group C 2/c with Z = 8. The Au···Au distance of 2.9714(5) Å is similar to the only other reported structure of this type, [Au$_3$(2,6-Me2-form)$_2$(THT)Cl], where the Au···Au distance is ~3.01 Å.[263] Opposite to **1**, [Au$_3$(2,6-Me2-form)$_2$(THT)Cl] has a trinuclear gold center, nonetheless the geometry and Au···Au distance was found to be comparable. The formation of the dinuclear compound was possible due to steric hindrance of the bulky diisopropyl groups in the ortho position of the formamidinate ligand.

On the other hand, compound **2** crystallizes in the orthorhombic P b c n space group with Z = 4. The Au···Au distance of 2.7464(7) Å is analogous to that of [Au$_2$(2,6-Me$_2$-form)$_2$], 2.711(3) Å.[263] The Au–N bond distances are 2.036(5) and 2.043(5) Å, which are considered normal when compared to the reported 2.035(7) Å, and 2.0675 and 2.015 Å for [Au_2(2,6-Me_2-form)$_2$] [263] and $Au_2[(Me_3SiN)_2C(Ph)]_2$.[282]

Complete chlorination of **2**, significantly decreases the Au–Au distance to 2.5303(3) Å for **3**. The dinuclear Au(II) complex **3**, $Au_2(DippF)_2(Cl)_2$, crystallizes in the tetragonal P4_2/n space group with Z = 4. The Au–Au bond distance is within the range of previously reported Au(II)–Au(II) complexes, between 2.48 and 2.57 Å.[256] The decrease in the gold–gold distance from ~3.01 Å for Au(I) complexes results from the formation of two Au–Cl bond and a single Au–Au bond, forming a stable d^9–d^9.[283] The Au–Cl bond is 2.3660(11) Å comparable to the distance found in other Au(II) structures.[263,284]

Table 6.1. X–ray crystallographic data for **1**, **2** and **3**.

	1	**2**	**3·THF**
Empirical formula	$C_{50}H_{71}Au_2ClN_4$	$C_{50}H_{70}Au_2N_4$	$C_{58}H_{86}Au_2Cl_2N_4O_2$
Formula weight (g·mol^{-1})	1157.49	1121.03	1336.14
Crystal system	Monoclinic	Orthorhombic	Tetragonal
Space group	C 2/c	P b c n	P4_2/n
a (Å)	37.7736(16)	18.530(6)	21.3553(10)
b (Å)	10.8675(4)	15.238(5)	21.3553(10)
c (Å)	27.7954(11)	17.038(6)	12.8298(6)
α (deg)	90	90	90
β (deg)	94.5320(10)	90	90
Υ (deg)	90	90	90
V (Å^3)	11374.5(8)	4811.0(3)	5851.0(6)
Z	8	4	4
d_{cal} (g·cm^{-3})	1.352	1.548	1.517
μ (mm^{-1})	5.231	6.128	5.142
2θ (deg)	1.08 – 25.00	1.73 – 30.00	1.35 – 28.31
λ (Å)	0.71073	0.71073	0.71073
T (K)	100(2)	296(2)	100(2)
GOF	1.020	1.031	1.063
R1,[a] wR2($I > 2\sigma(I)$)[b]	0.0466, 0.1000	0.0392, 0.0876	0.0349, 0.0875

[a]R1 = $\sum||F_o| - |F_c||/\sum|F_o|$. [b]wR2 = $[\sum[w(F_o^2 - F_c^2)^2]/\sum w(F_0^2)^2]^{1/2}$, $w = 1/[\sigma^2(F_o^2) + (aP)^2 + bP]$, where $P = [\max(F_o^2 \text{ or } 0) + 2(F_c^2)]/3$.

Table 6.2. Selected bond lengths (Å) and bond angles (°) for **1**, **2** and **3**.

	1	**2**	**3·THF**
Au(1) – Au(2)	2.9714(5)		
Au(1) – Au(1A)		2.7464(7)	2.5303(3)
Au(1) – Cl(1)	2.265(2)		2.3660(11)
Au(1) – N(1)	2.024(7)	2.036(5)	2.014(4)
Au(1) – N(2)		2.043(5)	2.030(4)
Au(2) – N(2)	2.005(6)		
Au(2) – N(3)	2.013(6)		
Au(1)–Au(1A)–N(1)		85.24(14)	86.24(10)
Au(1)–Au(2)–N(1)	80.8(2)		
Au(1)–Au(1A)–N(2)		83.97(13)	88.33(11)
Au(1)–Au(2)–N(2)	81.6(2)		
Au(1)–Au(2)–N(3)	104.53(18)		
N(1)–Au(1)–N(2A)		169.20(19)	174.57(15)
N(1)–C(1)–N(2)	125.9(8)	126.3(5)	125.7(4)
N(1)–Au(1)–Cl(1)	178.1(2)		93.71(11)
Cl(1)–Au(1)–Au(1A)			179.78(3)
Au(1)–Au(2)–Cl(1)	101.06(6)		

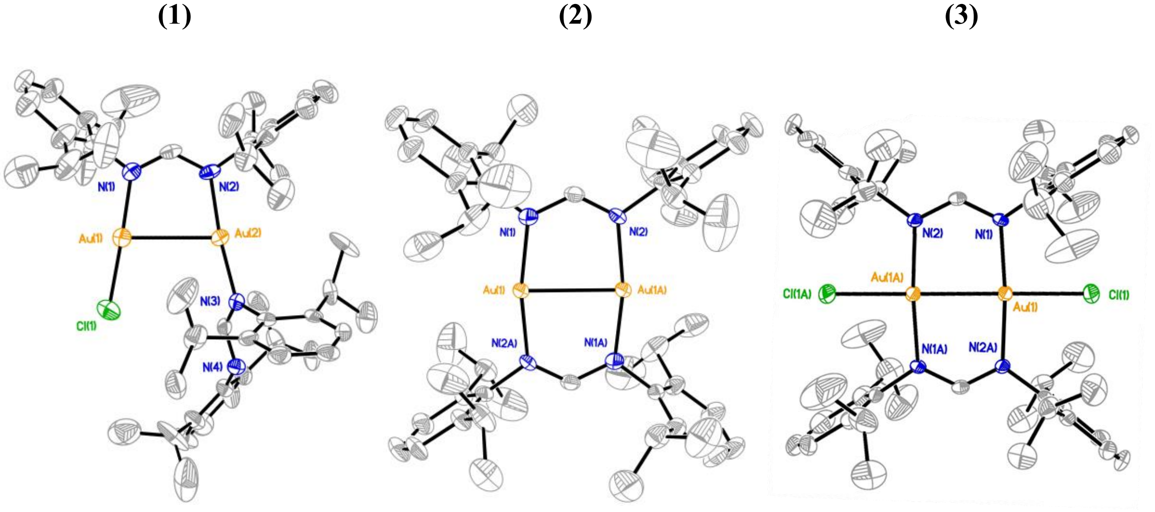
(1) **(2)** **(3)**

Figure 6.5. Crystal structures for **1**, **2** and **3** with ellipsoids drawn at 35% probability level. All hydrogen atoms have been omitted for clarity.

Electrochemical Studies. Compound **2** and **3** show redox activity in DCM. The cyclic voltammogram for **2** and **3** are shown in Figure 6.6 and Figure 6.7 respectively. The CV of **2** reveals a non-reversible one-electron oxidation at $E_{1/2}$ = 0.15 V vs Fc/Fc$^+$. On the other hand, a one-electron redox event occurs for **3** at $E_{1/2}$ = 0.843 V vs Fc/Fc$^+$.

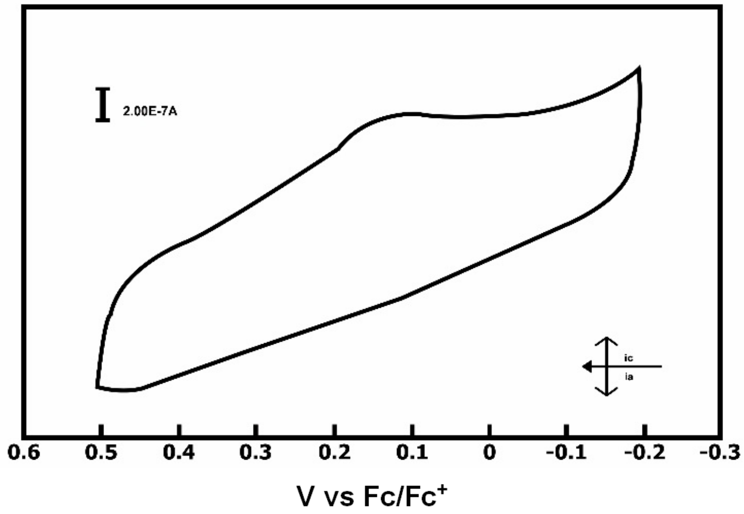

Figure 6.6. Cyclic voltammogram of **2**, with $E_{1/2}$ = 0.15V. Data was obtained in a DCM solution of **2** with potentials referenced to Fc/Fc$^+$.

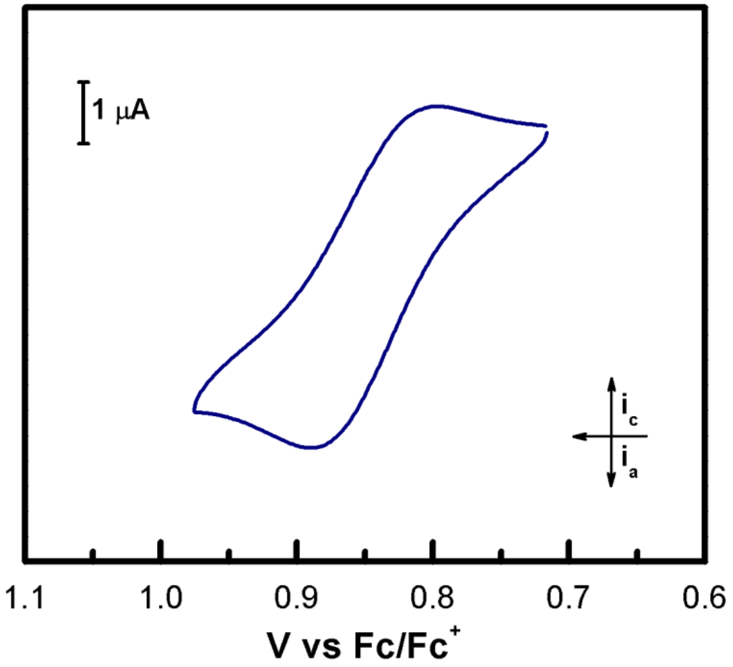

Figure 6.7. Cyclic voltammogram of **3**, with $E_{1/2}$ = 0.843 V. Data was obtained in a DCM solution of **3** with potentials referenced to Fc/Fc$^+$.

Spectroscopic Properties. The electronic spectrum of **2** is depicted in Figure 6.8. One absorption band that tails into the blue is observed peaking at 343 nm which provides the yellow color to **2**. The electronic spectrum of **3** is shown in Figure 6.9. Three absorption bands at 243, 350 and 470 nm are observed for **3**. The low energy absorption bands suggest an electronic transition from the HOMO to LUMO.

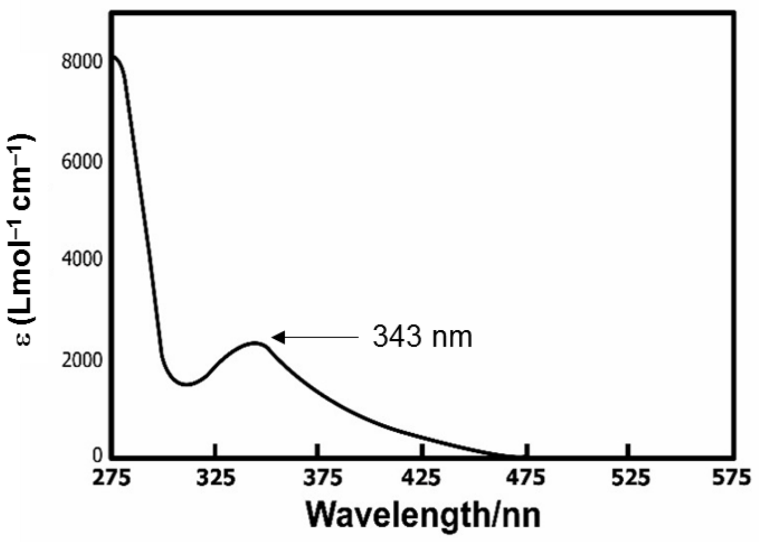

Figure 6.8. Absorption spectra for **2** in DCM.

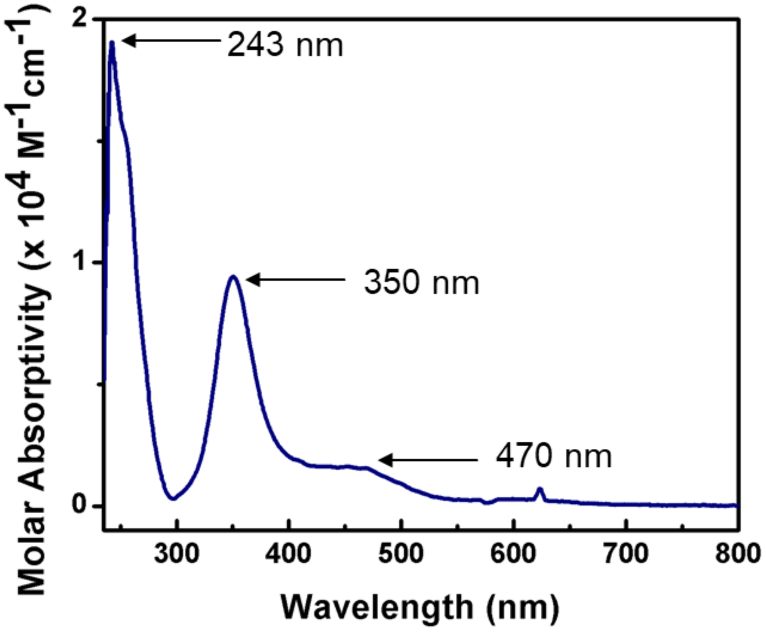

Figure 6.9. Absorption spectra for **3** in DCM.

DFT Calculations. Density Functional Theory (DFT) calculations were performed on compounds **2** and **3** to gain insight into the electronic structure of their Au_2 cores, the ground state geometries, and the nature of their frontier orbitals. Geometry optimizations were done using the crystal structure parameters as the starting point for the calculations. The absence of imaginary frequencies on the vibrational frequency analysis of the optimized models indicate the geometries are on a minima on the potential energy surface. The calculated gas-phase Au–Au bond distance for **3** is 2.59708 Å, which is comparable to the experimentally observed 2.5303(3) Å. Meanwhile, the calculated Au···Au distance for **2** is 2.82902 Å with and experimental value of 2.7385(7) Å. The shortening of the M–M distance (**2** → **3**) is consistent with the oxidative addition of Cl^- to the molecule. There is a consistent overestimation of the Au···Au distance of ~0.07 Å, which has been well established in the literature when B3LYP and other functionals are employed.[221,244]

The ground state for the dinuclear gold (I) species, **2**, is calculated to be a HOMO (–5.523 eV) with δ metal–metal antibonding, and a LUMO (–0.746 eV) with mainly ligand character. This suggests that oxidation of the dinuclear complex is due to the $[Au(I)–Au(I)]^+$ redox process, and that the electronic transition observed for **2** in Figure 6.8 corresponds to the MLCT. These electronic structures and frontier orbitals are similar to previously studied Au(I) and Au(II) complexes with the guanidinate hpp ligand.[262]

Figure 6.10 shows that the HOMO (–6.264 eV) for **3** corresponds to the π*-orbital of the formamidinate ligand, while the LUMO (–3.919 eV) is dominated by the σ*-orbital ($d_{x^2-y^2}$) of the metal center with some ligand character. The composition of the HOMO confirms that the oxidation wave shown in Figure 6.7 at $E_{1/2}$ = 0.843 V corresponds to the ligand redox process. Based on the HOMO energy, the magnitude of the half-wave potential would be expected to follow the order **2** < **3**. This observation is in agreement with the obtained electrochemical data, where the stabilization of the HOMO is reflected in the positive shift of the redox potential. Moreover, the HOMO and LUMO energy gap (ΔE_{H-L}) matches the energy of the absorption band (LMCT) in the spectrum of Figure 6.9 which is calculated to be 2.638 eV vs 2.345 eV obtained from theoretical calculations.

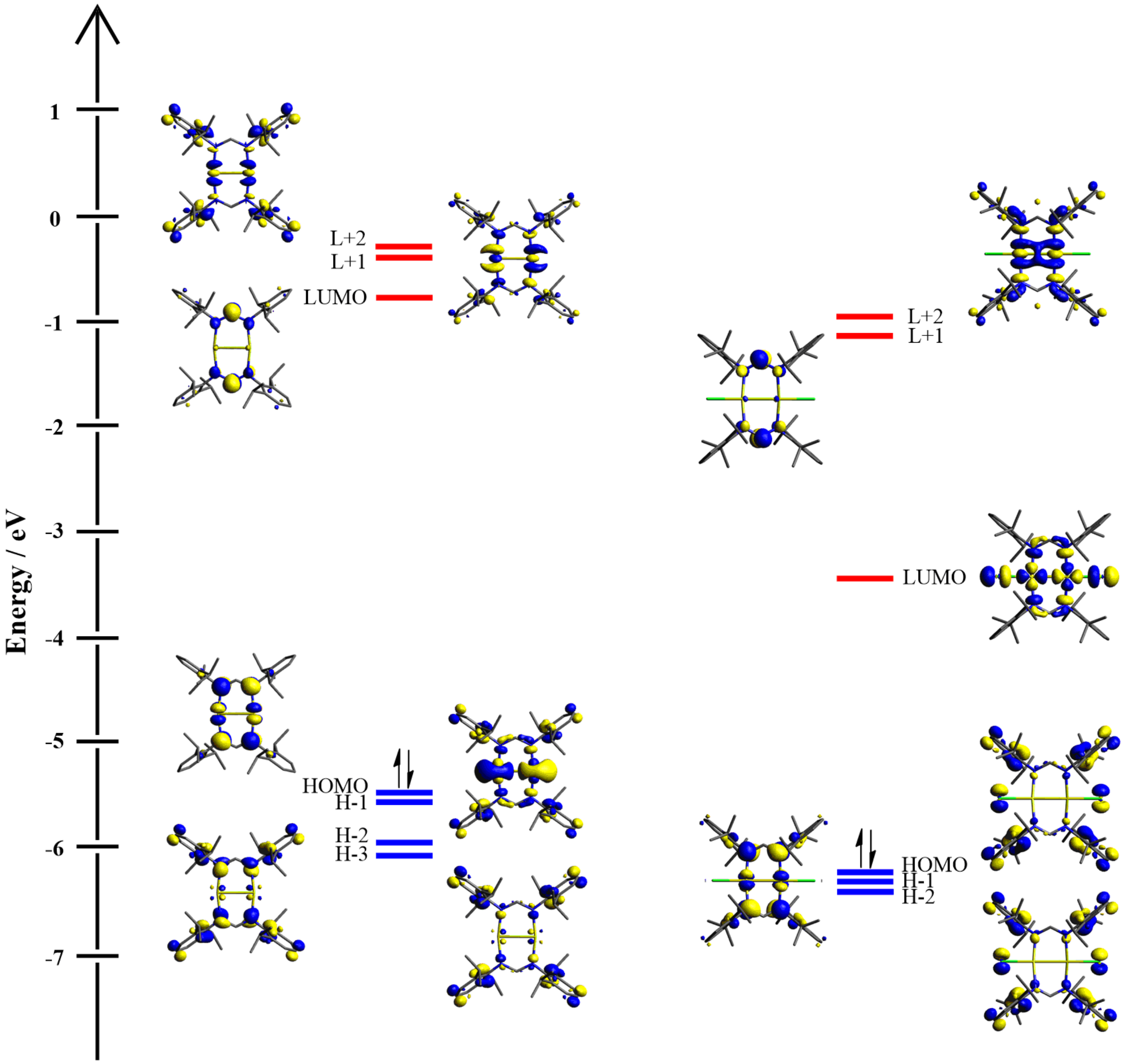

Figure 6.10. Contour plots and molecular orbital representation of four frontier orbitals for **2** and **3**, with energy for all orbitals.

6.4.2 Electronic Tuning of Digold Compounds via Remote Substituent Effect

Molecular Design and Synthesis. Compounds **4** – **6** (numbered according to the aryl substituents R and R': **4** (R = 2,6-$CHMe_2$, R' = *m*-OMe), **5** (R = 2,6-$CHMe_2$, R' = *p*-Cl), and **6** (R = *p*-OMe, R' = *m*-OMe) were prepared using the ligands depicted in Scheme 6.2 as outlined in Scheme 6.3. The substituents were chosen based on their electron-withdrawing and donating abilities as well as their steric hindrance which would potentially allow the formation of a coordinately unsaturated Au(I) complex. Hammett constants for these asymmetric formamidinates were calculated assuming that the additivity of Hammett constants holds (values are shown in Table 6.6).[285–287]

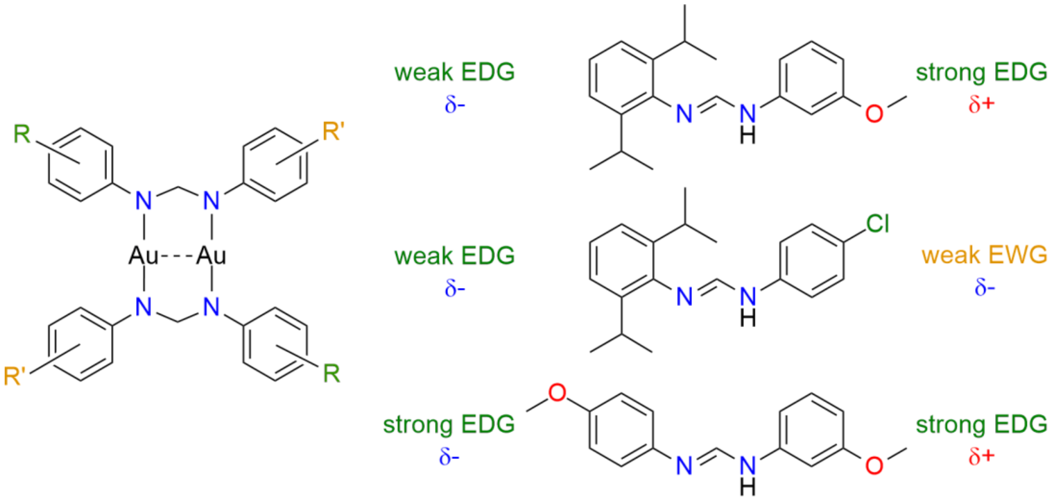

Scheme 6.2. Asymmetric ligands used in this study.

The bidentate formamidinate ligand is an excellent candidate for this study since the asymmetric derivatives can be readily prepared. The proposed formamidinates could potentially probe different electronic environments for the metal centers. If connected properly, the ligands may favor a more electron-rich environment for one Au atom. In addition, the capability of formamidines to support bimetallic compounds has been well documented in this work and previously published studies.[235,288,289] The dinuclear compounds **4** – **6** were synthesized by metathesis of the sodium salt of the asymmetric formamidinate ligands with Au(THT)Cl in a 1:1 ratio using DCM, and in the presence of air in 26%, 72%, and 37% yield. These compounds decompose to elemental gold in the presence of light but are otherwise stable to air and moisture in the solid state.

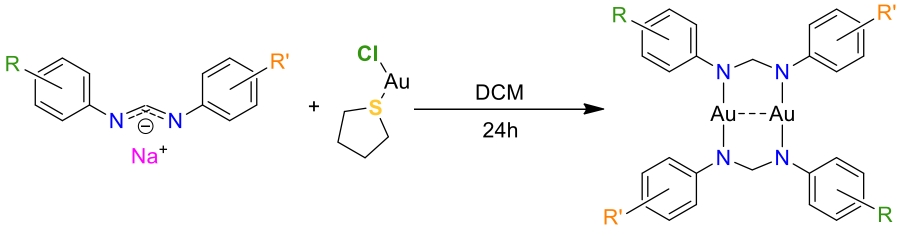

Scheme 6.3. General reaction scheme for the synthesis of **4** – **6**.

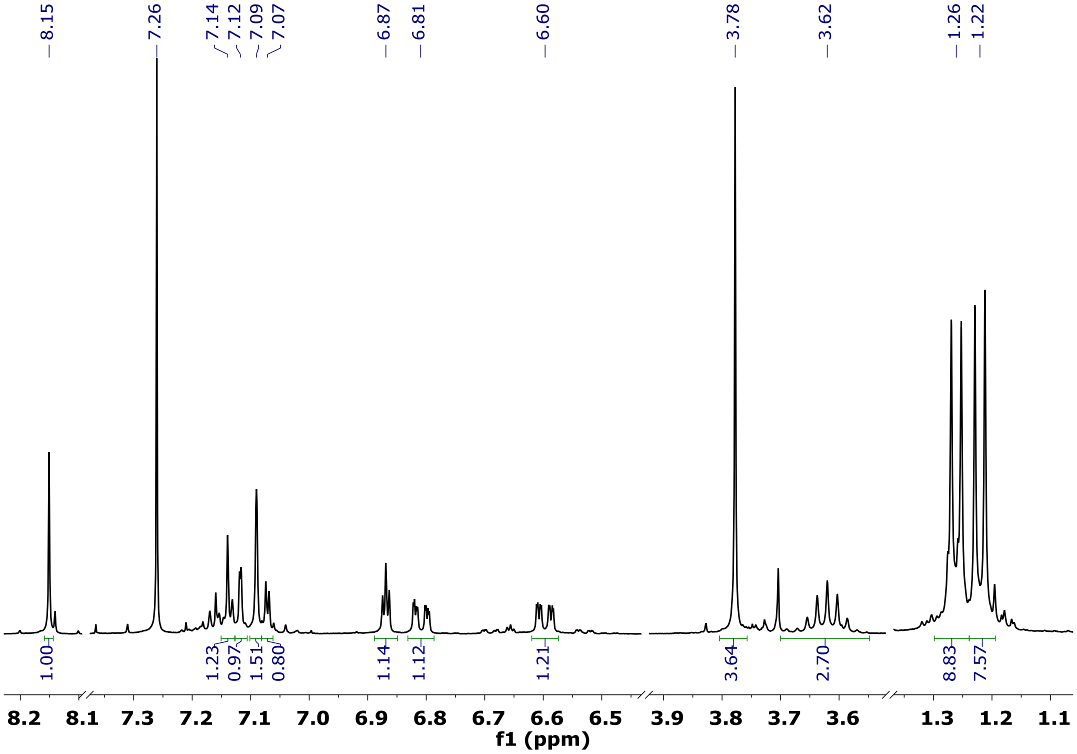

Figure 6.11. ^{1}H NMR for **4** in $CDCl_3$.

The structure of **4** – **6** was confirmed by ^{1}H NMR spectroscopy and single crystal X-Ray crystallography (**4** and **5**). The proton NMR is consistent with the structure of the molecule with all signals having the expected chemical shifts (ppm) and relative intensities. ^{1}H NMR for **4** (Figure 6.11), **5** (Figure 6.12), and **6** (Figure 6.13) show a singlet at 8.15 ppm, 8.06 ppm, and 8.28 ppm respectively for the methine protons on the formamidinate. This observation suggests the formamidinate ligands are related by symmetry in the complex.

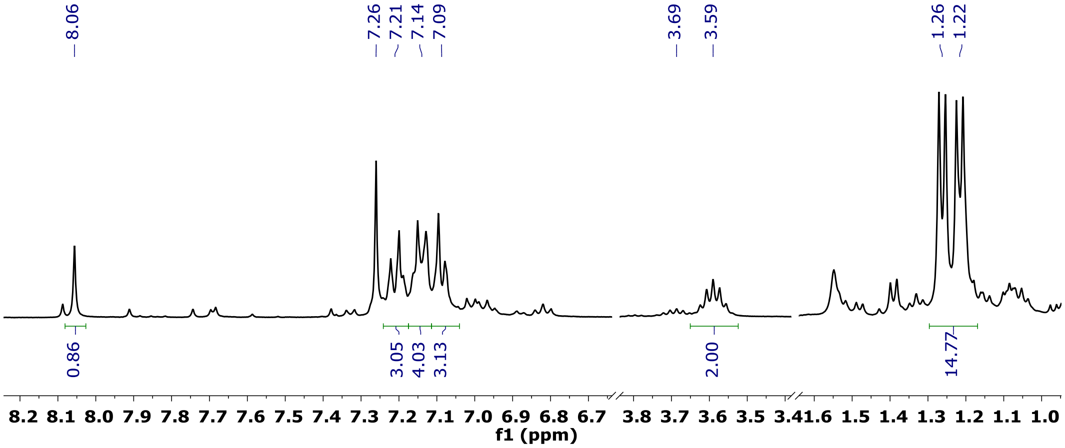

Figure 6.12. ^{1}H NMR for **5** in $CDCl_3$.

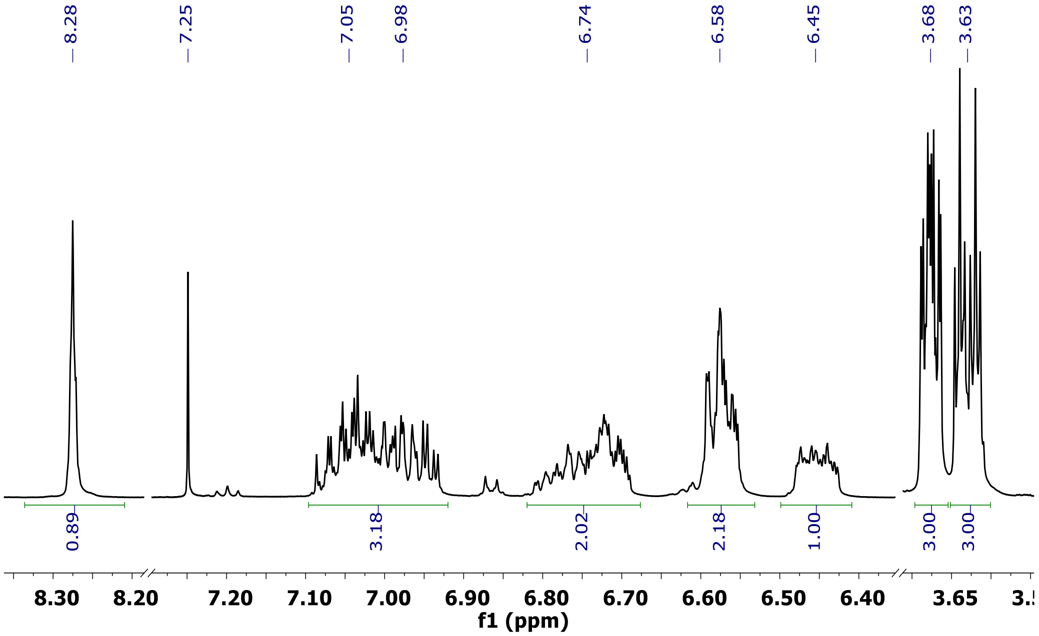

Figure 6.13. ^{1}H NMR for **6** in $CDCl_3$.

ESI-MS was performed on **4** – **6**, and are presented in Figure 6.14, Figure 6.15 and Figure 6.16. All compounds show the expected isotopic distribution and the predicted m/z. The calculated *m/z* for **4** – OCH_3 is 981.3 and experimental *m/z* = 981.14, while for **5** + H^+ *m/z* value was calculated = 1021.24 and experimental = 1021.25, and for **6** *m/z* value was calculated = 905.16 and experimental = 905.20.

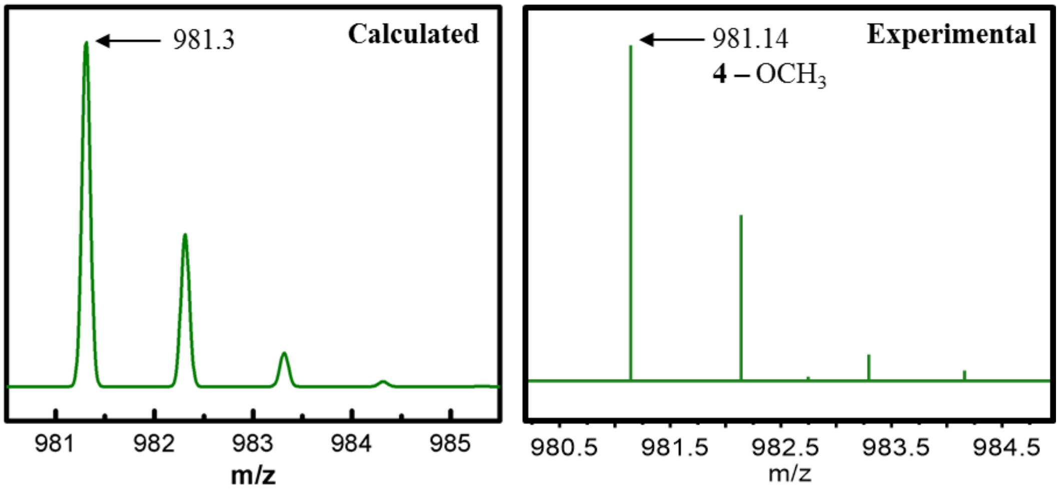

Figure 6.14. MS spectra of **4** with m/z (Left) calculated at 981.3, and (Right) detected at 981.14.

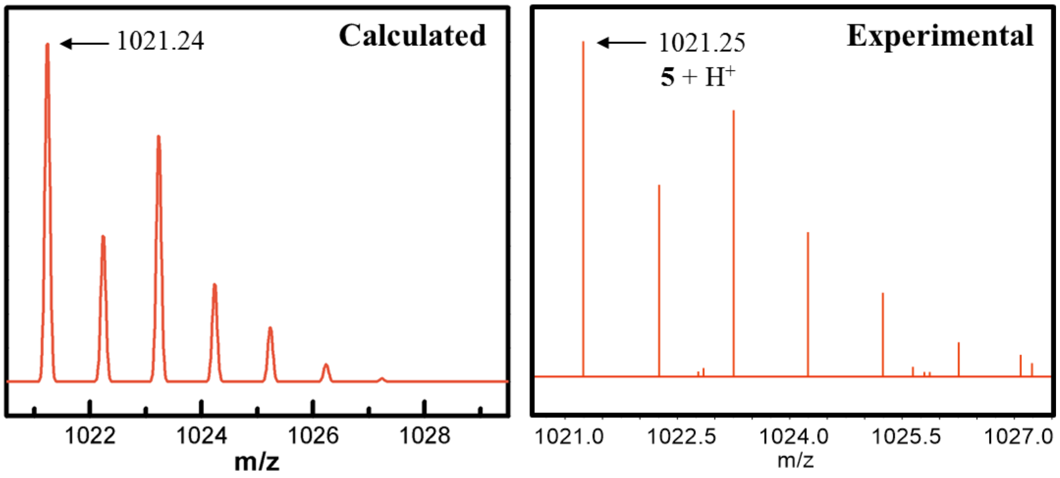

Figure 6.15. MS spectra of **5** with m/z (Left) calculated at 1021.24, and (Right) detected at 1021.25.

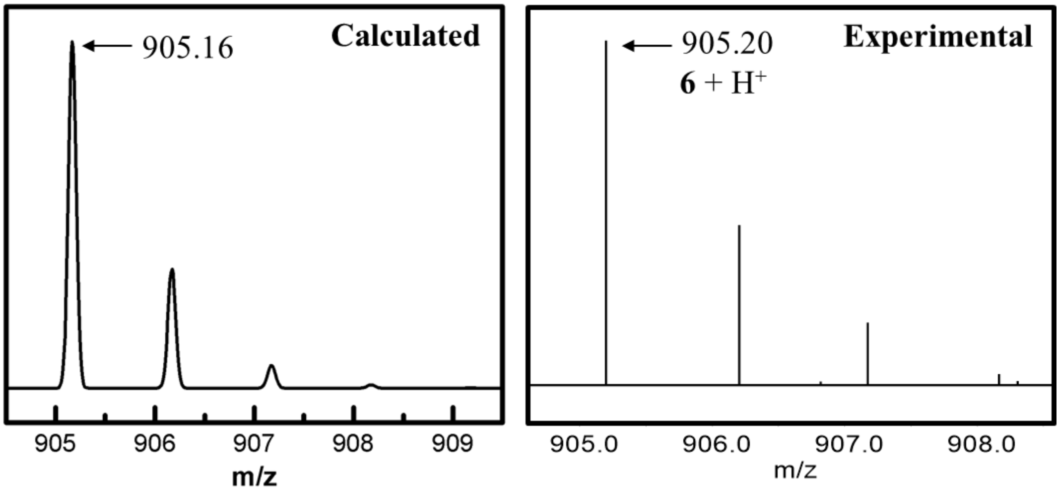

Figure 6.16. MS spectra of **6** with m/z (Left) calculated at 905.16, and (Right) detected at 905.20.

Structural Determinations. Single crystals suitable for X-Ray crystallography were obtained by slow evaporation of a DCM solution of the compounds. The structures of **4** and **5** show a dinuclear gold(I) structure with formamidinate structural ligand, and open coordination on the gold axial position. Figure 6.17 and Figure 6.18 show the molecular structure of $Au_2(^{m}DippAF)_2$, **4**, and $Au_2(ClDippF)_2$, **5**, with selected bond distances and angles given in Table 6.3 and Table 6.4. In addition, crystallographic data for the synthesized ligands are presented in Table 6.5. The dinuclear complex **4** crystallizes in the orthorhombic P b c a space group with Z = 4. The Au···Au distance is 2.7281(3) Å while the N−Au−N angle is 170.12(11)°.

On the other hand, compound **5** crystallized in the monoclinic P 2_1/c group with Z = 2. The Au···Au distance in **5** is 2.7431(11) Å, and the N−Au−N angle is 169.6(5)°. The obtained Au···Au distances (~2.7 Å) and Au−N bond distances (~2.04 Å) for **4** and **5** are consistent with those found for the only other dinuclear gold (I) compound reported with formamidinate ligands.[284] The similar distances indicate the Au – N covalent bond is unperturbed by the inductive effect of the remote substituents. To our knowledge compounds **4** − **6** are the first examples of asymmetrically bridged dinuclear gold(I) nitrogen complexes.

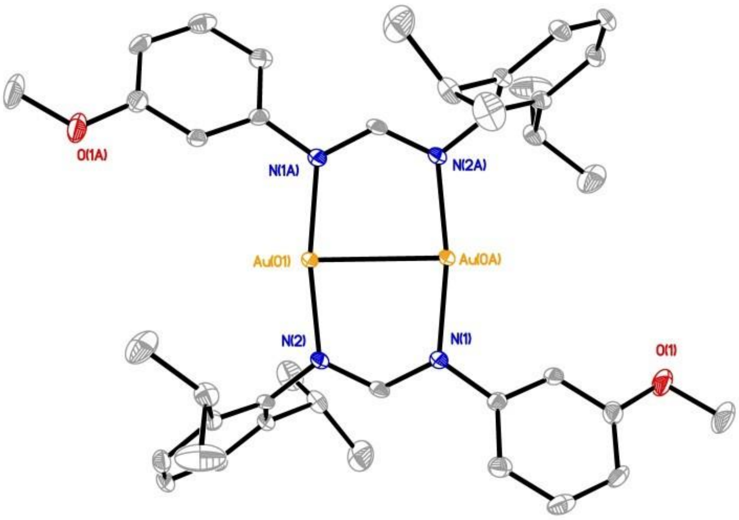

Figure 6.17. Crystal structures for **4** with ellipsoids drawn at 50% probability level. All hydrogen atoms have been omitted for clarity.

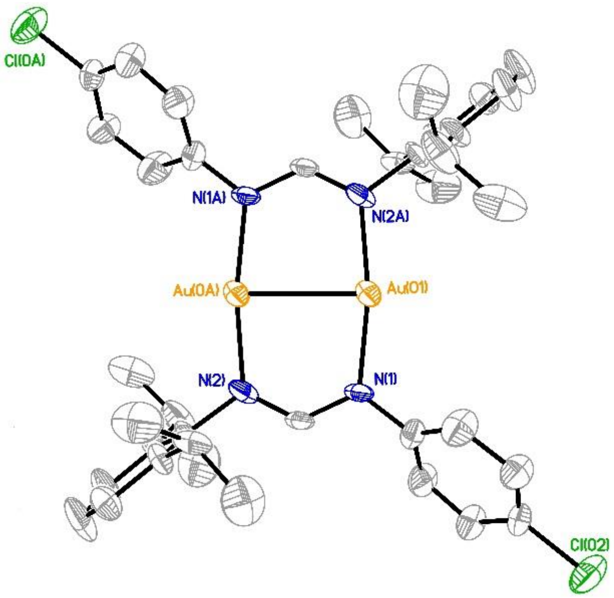

Figure 6.18. Crystal structures for **5** with ellipsoids drawn at 50% probability level. All hydrogen atoms have been omitted for clarity.

Table 6.3. X–ray crystallographic data for **4** and **5**.

	4	**5**
Empirical formula	$C_{40}H_{50}Au_2N_4O_2$	$C_{38}H_{44}Au_2Cl_2N_4$
Formula weight (g·mol^{-1})	1012.77	1021.60
Crystal system	Orthorhombic	Monoclinic
Space group	P b c a	P 2_1/c
a (Å)	15.2373(5)	12.4586(6)
b (Å)	11.4164(4)	6.4504(3)
c (Å)	21.2037(7)	23.6655(12)
α (deg)	90	90
β (deg)	90	103.829(2)
Υ (deg)	90	90
V (Å^3)	3688.5(2)	1846.70(16)
Z	4	2
d_{cal} (g·cm^{-3})	1.824	1.837
μ (mm^{-1})	7.985	8.112
2θ (deg)	1.92 – 27.50	2.13 – 25.00
λ (Å)	0.71073	0.71073
T (K)	100(2)	100(2)
GOF	1.074	1.082
R1,[a] wR2($I > 2\sigma(I)$)[b]	0.0216, 0.0541	0.0856, 0.2135

[a] $R1 = \sum||F_o| - |F_c||/\sum|F_o|$. [b] $wR2 = [\sum[w(F_o^2 - F_c^2)^2]/\sum w(F_0^2)^2]^{1/2}$, $w = 1/[\sigma^2(F_o^2) + (aP)^2 + bP]$, where $P = [\max(F_o^2 \text{ or } 0) + 2(F_c^2)]/3$.

Table 6.4. Selected bond lengths (Å) and bond angles (°) for **4**.

	4	**5**
Au(1) – Au(1A)	2.7281(3)	2.7431(11)
Au(1) – N(1)	2.038(3)	2.041(12)
Au(1) – N(2)	2.024(3)	2.024(13)
Au(1)–Au(1A)–N(1)	84.50(8)	84.2(4)
Au(1)–Au(1A)–N(2)	85.74(8)	85.5(4)
N(1)–Au(1)–N(2A)	170.12(11)	169.6(5)
N(1)–C(1)–N(2)	127.4(3)	129.9(13)

Table 6.5. X–ray crystallographic data for **II**, **III** and **IV**.

	II	**III**	**IV**
Empirical formula	$C_{20}H_{26}N_2O$	$C_{19}H_{23}ClN_2$	$C_{15}H_{16}N_2O_2$
Formula weight (g·mol^{-1})	310.43	314.84	256.30
Crystal system	Orthorhombic	Monoclinic	Monoclinic
Space group	P c c n	P 2_1/n	P 2_1/c
a (Å)	22.979(9)	10.4967(15)	7.2915(9)
b (Å)	23.219(8)	8.6681(8)	5.7809(7)
c (Å)	14.790(6)	19.6010(18)	30.593(4)
α (deg)	90	90	90
β (deg)	90	97.012(2)	95.398(2)
Υ (deg)	90	90	90
V (Å^3)	7891.(5)	1770.1(3)	1283.8(3)
Z	16	4	4
d_{cal} (g·cm^{-3})	1.045	1.181	1.326
μ (mm^{-1})	0.064	0.215	0.089
2θ (deg)	4.988 – 42.23	4.655 – 43.86	5.35 – 58.02
λ (Å)	0.71073	0.71073	0.71073
T (K)	296(2)	100(2)	100(2)
GOF	1.020	1.019	1.028
R1,^{a} wR2($I > 2\sigma(I)$)^b	0.0589, 0.2178	0.0464, 0.1316	0.0484, 0.1468

^{a}R1 = $\sum||F_o| - |F_c||/\sum|F_o|$. ^{b}wR2 = $[\sum[w(F_o^2 - F_c^2)^2]/\sum w(F_0^2)^2]^{1/2}$, $w = 1/[\sigma^2(F_o^2) + (aP)^2 + bP]$, where $P = [\max(F_o^2 \text{ or } 0) + 2(F_c^2)]/3$.

Electrochemical Studies. The redox behavior of the digold compounds **4** – **6** has been examined by cyclic voltammetry (Figure 6.19), and relevant experimental parameters are listed in Table 6.6. The half-wave potentials have been referenced versus the ferrocene/ferrocenium couple (Fc/Fc$^+$). Compound **4** shows a one-electron reversible event with $E_{1/2}$ = 0.602 V, which corresponds to the reversible oxidation of [Au(I)···Au(I)] to [Au(I)···Au(I)]$^+$. Similarly, **5** and **6** display a one-electron oxidation with an $E_{1/2}$ = 0.806 V and $E_{1/2}$ = 0.328 V, respectively. This oxidation can be attributed to the removal of an electron from the Au···Au δ∗ antibonding orbital, and its half-wave potential provides a reliable measure of the HOMO energy.

Table 6.6. Experimental results for **4 – 6**.

	4	**5**	**6**
Au···Au (experimental / Å)	2.7281(3)	2.7431(11)	~2.70
Au···Au (calculated / Å)	2.829	2.828	2.823
σ	–0.03	0.08	–0.15
δ (ppm)	8.15	8.06	8.28
$E_{1/2}$ (mV)	602	806	328
λ_{max} (nm)	360	374	384

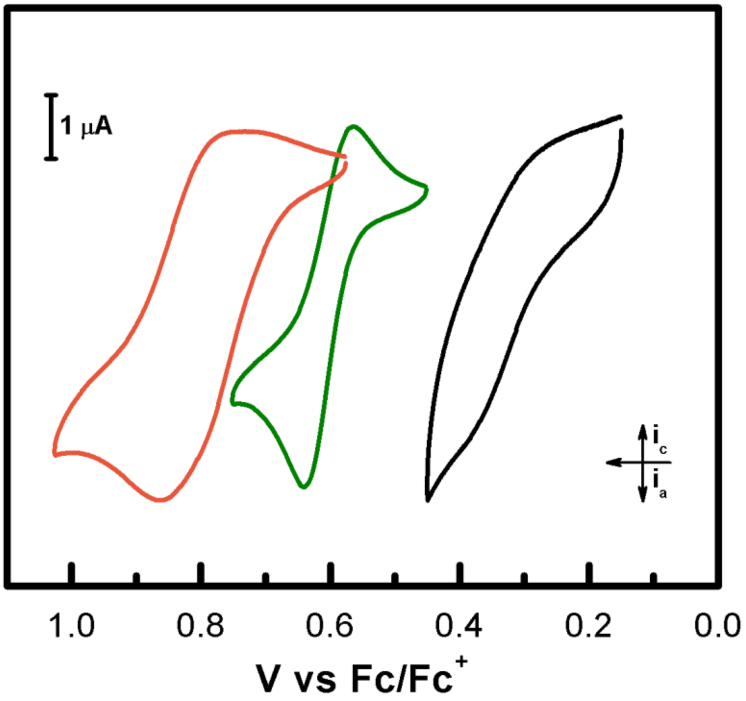

Figure 6.19. Cyclic voltammogram of **4**, **5**, and **6**, with $E_{1/2}$ = 0.602 V, $E_{1/2}$ = 0.806 V, and $E_{1/2}$ = 0.328 V. Data was obtained in DCM solutions of **4** – **6** with potentials referenced to Fc/Fc$^+$.

The degree of tuning in bimetallic complexes has been previously quantified by the correlation of the redox potential ($E_{1/2}$) of the synthesized compounds with the Hammett constant of their ligand substituents.[278,290] A gradual anodic-shift in $E_{1/2}$ is observed as the electron-withdrawing ability of the ligand increases (increasing σ), this trend is similar to those obtained for a dimolybdenum and dinickel series.[208,278,290,291] There is good correlation between $E_{1/2}$ and the

Hammett parameter *σ* as shown in Figure 6.20. The substituent constants (σ) for the series of asymmetric formamidinate ligands were calculated based on the Hammett constants for the corresponding substituents according to values reported in the literature.[116] According to previous reports, an increase in the electron-withdrawing ability of the substituents in symmetrical formamidinate ligands result in less electron density on the bimetallic core and therefore a more positive potential for the oxidation couple, $Au_2^{3+/2+}$. The trend in the $E_{1/2}$ is as expected, shifting towards positive potentials for the $Au_2^{3+/2+}$ couple when moving from electron-donating to electron-withdrawing groups. This suggests the δ∗-bonding orbital gets destabilized upon increasing the electron-donating ability of the ancillary ligand. Therefore, the substitution of the ancillary formamidinate ligands allowed the tuning of the redox properties of the Au_2 center.

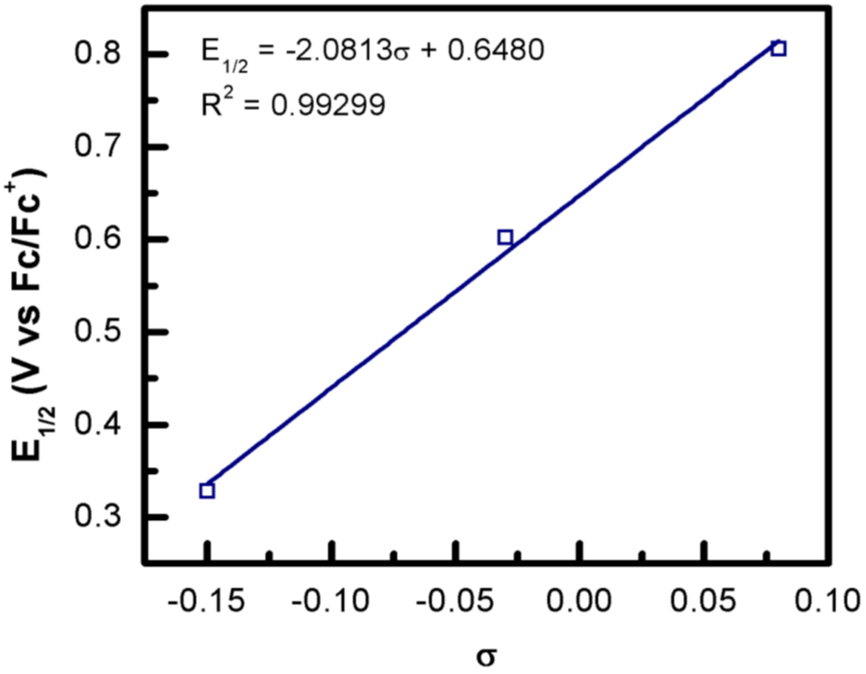

Figure 6.20. Plot of half-wave potentials ($E_{1/2}$) versus the Hammett substituent parameter (σ) for **4** – **6**. The squares are the measured values, and the solid line is the least-squares fit. All $E_{1/2}$ are referenced to Fc/Fc^+. Linear fit of the data gives a correlation coefficient (R^2) of 0.99299.

Spectroscopic Properties. The UV-Vis spectra of compounds **4**, **5**, and **6** show an absorption peak in the visible region at 360, 374, and 384 nm respectively. This low energy band can be assigned to the HOMO to LUMO electronic transition. The absorption spectra of **4**, **5**, and **6** are shown in Figure 6.21, Figure 6.22, and Figure 6.23. The stronger electron-donating ability of the methoxy groups in the asymmetric formamidinate ^{m,p}HDAniF renders **6** the lowest electronic transition energy (384 nm). In contrast, compound **5** displays a higher-energy absorption band (374 nm) due to the presence of an electron-withdrawing substituent (–Cl). The influence of aryl substituents on the charge transfer energy is similar to that observed in other metal complexes.[172]

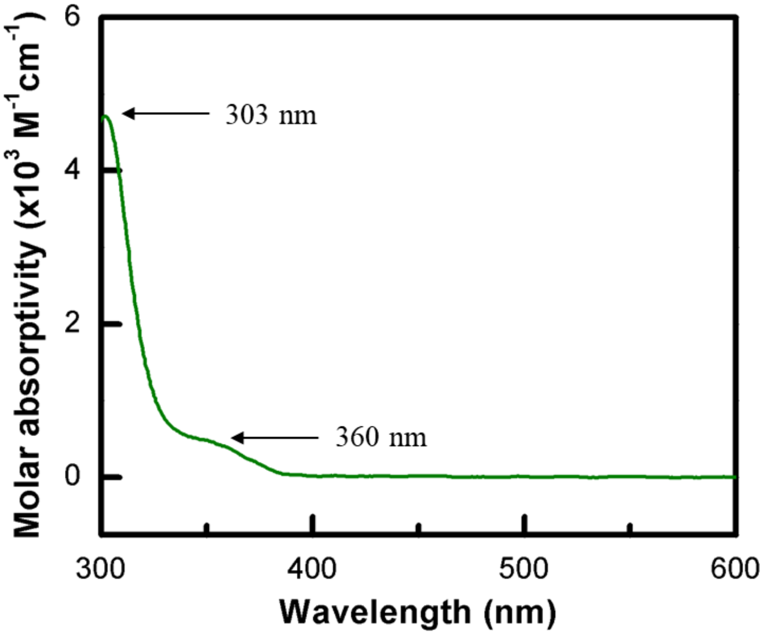

Figure 6.21. Absorption spectra of compound **4** measured at room temperature in THF.

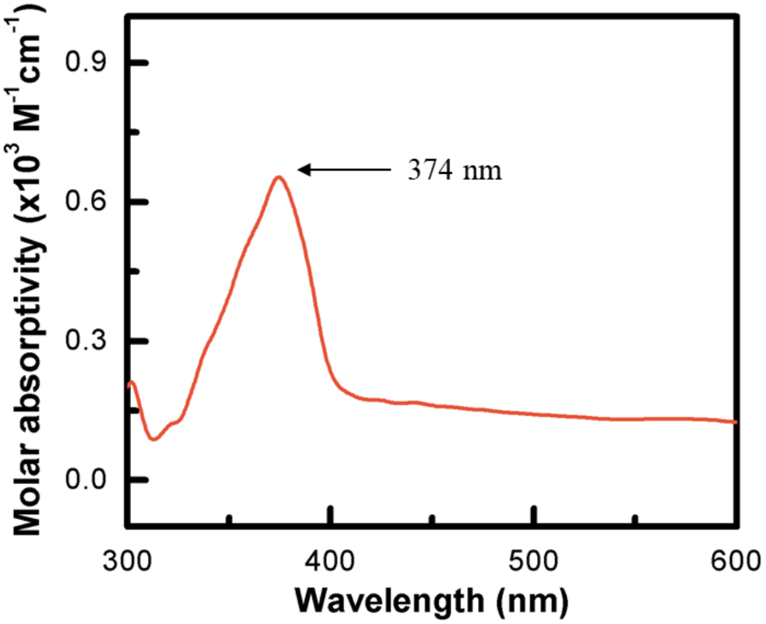

Figure 6.22. Absorption spectra of compound **5** measured at room temperature in THF.

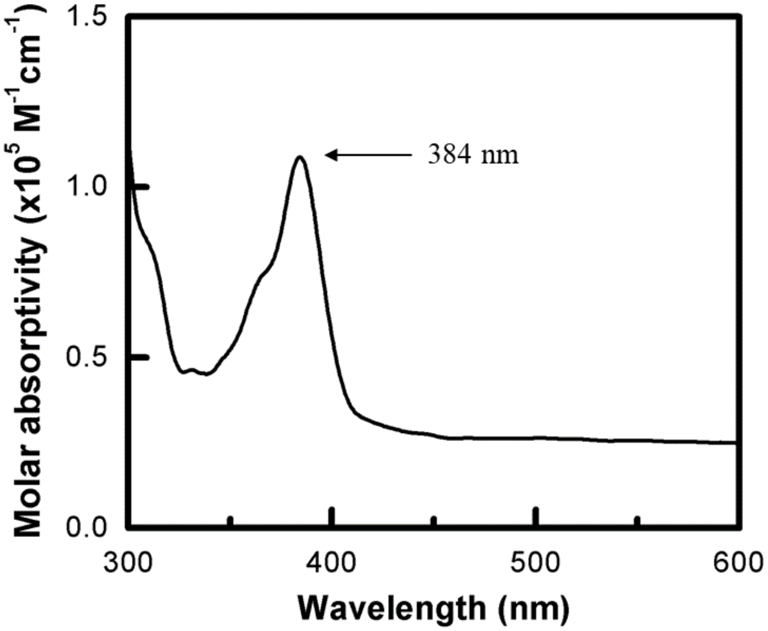

Figure 6.23. Absorption spectra of compound **6** measured at room temperature in THF.

Electronic Structure Calculations. Density Functional Theory (DFT) calculation were performed on compounds **4** – **6** to gain insight into the electronic structure of their Au_2 cores, the ground state geometries, and the nature of their frontier orbitals. Geometry optimizations were done using the crystal structure parameters as the starting point for the calculations for compounds **4** and **5**. The calculated gas-phase Au···Au distance for **4** is 2.82941 Å which is comparable to the experimentally observed 2.7281(3) Å. For **5**, the DFT obtained metal–metal distance is 2.82765 Å while the experimental one is 2.7431(11) Å. Meanwhile, the calculated Au···Au distance for **6** is 2.82339 Å. There is a consistent overestimation of the Au···Au distance by ~0.1 Å, which has been established when B3LYP and other functionals are employed.[221,244]

Figure 6.24 depicts the HOMO and LUMO orbitals for compounds **4** – **6**. The highest occupied molecular orbital (HOMO) for all the compounds was found to be a metal based δ*-orbital with some degree of ligand mixing. The asymmetric nature of the ligand can be observed in the uneven charge distribution on the HOMO due to the electron withdrawing nature of the substituents and/or their position in the ring. The HOMO for compounds **4** and **5** show no charge delocalization over the diisopropyl phenyl substituent. The composition of the HOMO confirms that the redox event in the cyclic voltammograms for **4** – **6** is attributed to the $Au_2^{2+/3+}$ process. The excellent linear correlation observed between the $E_{1/2}$ and the σ indicates the HOMO energy is affected by the remote substituents in the series. On the other hand, the lowest unoccupied molecular orbital (LUMO) is a ligand based π*-orbital. In these orbitals, uneven distribution of the charge is also present. The highest HOMO energy observed was at –4.976 eV for **6**, while the lowest and most stable occupied orbital is that for **5** with an onset HOMO δ* energy of –5.592 eV. The addition of electron withdrawing ancillary ligands stabilizes the HOMO ground state. The electronic structure of **4** shows that the HOMO (–5.523 eV) is metal based with δ* character. The LUMO of **4** is the ligand based π* found at –0.743 eV. Compound **5**, has an onset LUMO energy of –1.090 eV, 0.347 eV higher in energy than that for **4**. The Au···Au unit makes largest contribution to the HOMO at –5.592 eV. In addition, **6** has a HOMO and LUMO energies of –4.976 eV and –0.717 eV, respectively.

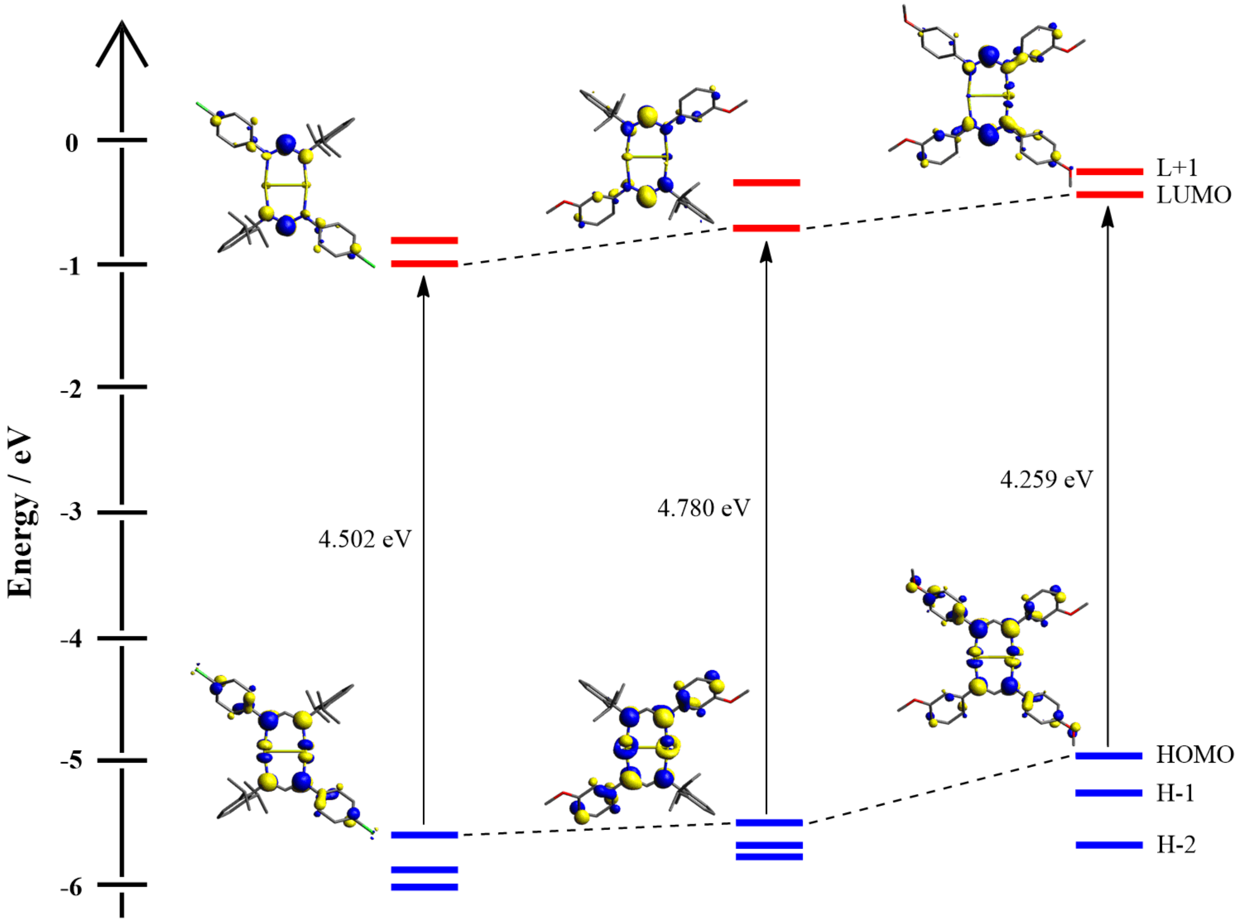

Figure 6.24. Contour plots and molecular orbital representation of four frontier orbitals for **4** – **6**, with energy for all orbitals and isosurface value of 0.45.

Time-dependent density functional theory calculations were performed on the geometry optimized **4** – **6** to help assign the lowest energy transition observed in the UV-Vis spectra for each compound. Absorption spectra of **4** shows a band at 360 nm arising from a metal to ligand charge transfer (MLCT) transitions from the occupied Au-based antibonding orbitals to the empty π-antibonding orbitals of the formamidinates with some metal mixing (δ* → δ*+Lπ*) transition. Similarly, **5** presented a band at 374 nm while the same signal appeared at 384 nm for **6**. These bands corresponds to the HOMO → LUMO+1 transition calculated to be 289, 305 and 314 nm for **4**, **5** and **6**, respectively.

6.5 CONCLUSION

In the first part of this chapter, we were able to obtain a gold(I) complex by using bulky groups (diisopropyl groups) as aryl substituents in the 2 and 6 position of the ring. The steric effects of these groups promoted the formation of the digold unit with axial open coordination sites. In addition, oxidative addition of Cl_2 to **2** yielded the digold(II) complex **3**. Compounds **1** – **3** were synthesized and characterized by ^{1}H NMR, ESI-MS, and single crystal X-Ray diffraction presenting Au – Au distances of 2.9714(5), 2.7385(7), and 2.5303(3) Å consistent with digold (I) and digold(II) species for **2** and **3** respectively. Electrochemical studies showed a non-reversible one-electron oxidation at $E_{1/2}$ = 0.15 V vs Fc/Fc$^+$ for **2**, and a one-electron reversible oxidation for **3** at $E_{1/2}$ = 0.843 V vs Fc/Fc$^+$. According to the nature of the HOMO, these events were assigned as oxidations of the Au_2 center and ligand for **2** and **3** respectively. In addition, the calculated ΔE_{H-L} were comparable to the lowest energy transition observed by UV-Vis, and were assigned as MLCT and LMCT for **2** and **3**.

In the second part of this chapter, a series of three Au(I)···Au(I) complexes with different formamidinate ligands (ArNCHNAr') was synthesized and characterized. These complexes share a common molecular skeleton, but vary the substituents in the aryl groups (Ar = *p*-XC_6H_5) **4** (R = 2,6-$CHMe_2$, R' = *m*-OMe), **5** (R = 2,6-$CHMe_2$, R' = *p*-Cl), and **6** (R = *p*-OMe, R' = *m*-OMe). Compounds **4** and **5** were structurally characterized by single crystal X-ray crystallography presenting Au···Au distances of 2.7281(3) and 2.7431(11) Å, respectively. The proposed ligands were selected (1) to present steric hindrance in the structure allowing the formation of the digold complex instead of a tetramer, and (2) to vary the electron-donating and withdrawing ability changing accordingly the Hammett constant (σ). Electrochemical studies showed that $Au_2^{2+/3+}$ redox process can be tuned due to inductive effects. To our knowledge, this is the first systematic study of remote substitution effects on digold(I) compounds with formamidinate ligands. The one-electron oxidation observed for **4**, **5**, and **6** at 0.602, 0.806, and 0.328 V corresponded to removal of an electron form the metal-based HOMO, and presented excellent linear correlation with the calculated Hammett constant. It was observed that the addition of electron-withdrawing substituents stabilized the metal-based δ^* HOMO. We have successfully utilized remote substituents to control the redox potential of a series of digold(I) complexes.

Chapter 7: Conclusion

The study of electron transfer in multielectron redox processes is crucial for the understanding of the chemistry behind energy conversion. For this purpose in Chapter 2 the electrocatalytic generation of hydrogen gas from acidic organic solutions using free-base meso-tetra(pentafluorophenyl)porphyrin was described. The electrocatalytic activity of the porphyrin was evaluated in THF and MeCN solutions and using *p*-toluenesulfonic acid as proton source. Hydrogen gas was produced at –1.31 vs Fc/Fc^+ in THF, and –0.69 V vs Ag/Ag^+ MeCN using *p*-toluenesulfonic acid at 90% Faradaic yield. We demonstrated by UV–Vis, spectroelectrochemical measurements and DFT calculations the ability of this porphyrin as electrocatalyst for homogeneous proton reduction. The data obtained from the spectroscopic and spectroelectrochemical measurements along with DFT provided the necessary information to build a mechanistic pathway for hydrogen generation. The most thermodynamically favorable pathway was found to be *E*-*P*-*E*-*P* and a *P*-*P*-*E*-*E* sequence (where *E* is a reduction process, and *P* protonation of the macrocycle) for HER under acidic conditions in THF and MeCN, respectively.

Although porphyrins have been well investigated as electrocatalysts for hydrogen generation, much less work is known for other analogues such as corroles. In Chapter 3, we utilized spectroscopic and theoretical calculation by DFT to evaluate the ability of 5, 10, 15-tris(pentafluorophenyl)corrole to generate hydrogen has under acidic organic media. The electrocatalytic ability of this corrole was assessed through cyclic voltammetry, where hydrogen gas was produced at –0.82 V vs Fc/Fc^+ in MeCN using tosic acid as proton source. The mechanism for HER was obtained with aid of spectroscopic data and DFT calculations. Out results suggested that the most favorable mechanistic pathway was a *P-E-E-P* sequence for tosic acid when performed in MeCN.

Numerous multielectron redox processes require the use of heterogeneous catalysts containing transition metals. It is difficult to obtain mechanistic information when heterogeneous catalysts are employed. Nonetheless, molecular systems can be used as platforms to study the basics of small molecule activation by reducing the catalytic process to the molecular level. Electron transfer via ISET in two-state models (D–B–A) is presented in Chapter 4, where three different non-symmetric systems utilizing metal-metal quadruple bonded dimolybdenum units were assessed. In the first part, a family of non-symmetric ligands (2,5-dihydroxy-4-phenylimino-2,5-cyclohexadien-1-one, and 2-hydroxy-5-phenylamino-4-phenylimino-2,5-cyclohexadien-1-one) was synthesized and characterized for the preparation of *dimers-of-dimers*. Electrochemical studies on $[Mo_2(DAniF)_3]_2(C_{12}O_3NH_7)$ and $[Mo_2(DAniF)_3]_2(C_{18}O_2N_2H_{12})$ displayed multielectron redox processes with two one-electron and three one-electron oxidations, respectively. Calculation of their comproportionation constants based on the data obtained by cyclic voltammetry ($K_c = 6.36 \times 10^3$ and $K_c = 9.7 \times 10^{10}$) regarded $[Mo_2(DAniF)_3]_2(C_{12}O_3NH_7)$ and $[Mo_2(DAniF)_3]_2(C_{18}O_2N_2H_{12})$ as Class II and Class III on the Robin–Day classification.

We studied the effect of a non-metallic redox active unit in the electronics of the D–B–A system, where a C_{60} fullerene cage was used as the second active site. $Mo_2(DAniF)_3(C_{69}O_2NH_8)$ was synthesized and characterized by ^{1}H NMR and MALDI-TOF mass spectrometry. The electronic spectrum gave information on the electronic communication in the two-state model, showing a strong band in the UV region that corresponded to a MLCT transition from the interaction of the δ orbitals of the Mo_2 core with the π^* orbitals of the bridging ligand, this transition was assigned based on the nature of the HOMO and LUMO and supported by TDDFT calculations. Cyclic voltammetry on this complex showed a one-electron oxidation of the dimolybdenum unit at 0.543 V vs Ag/Ag^+, as well as reduction events associated to reductions of the fullerene cage. The loss of symmetry on the reduction events for this complex suggests communication between the donor and acceptor sites in the form of $Mo_2^{5+} \rightarrow C_{60}$ charge transfer.

Moreover a study of charge transfer in a D–B–A system where both the donor and acceptor were non-symmetric organic units while the bridging ligand in charge of the coupling was a dimolybdenum center is presented. We synthesized and characterized $Mo_2(DAniF)_3(C_{18}O_2N_2H_{12})$ and *trans*-$Mo_2(DAniF)_3[C_{18}O_2N_2H_{12}]_2$ by means of ^1H NMR, mass spectrometry and single crystal X-Ray diffraction. One-electron oxidation of the Mo_2^{4+} unit was observed for both compounds at –0.03 and –0.017 V vs Fc/Fc$^+$ for $Mo_2(DAniF)_3(C_{18}O_2N_2H_{12})$ and *trans*-$Mo_2(DAniF)_3[C_{18}O_2N_2H_{12}]_2$ respectively. In addition, a second oxidation event was observed for the mono and trans complexes at 0.465 and 0.148 V vs Fc/Fc$^+$ respectively. Integration of these redox waves showed a one-electron and two-electron oxidation for $Mo_2(DAniF)_3(C_{18}O_2N_2H_{12})$ and *trans*-$Mo_2(DAniF)_3[C_{18}O_2N_2H_{12}]_2$. The presence of only one wave for the oxidation of the ligands in the trans complex suggested the ligands are not considerably coupled. In addition, UV-Vis spectra for the compounds showed two intense bands in the visible region related to MLCT electronic transitions as supported by DFT calculations.

Moreover, Chapter 5 and Chapter 6 present fundamental studies of ligand effects on the electronic properties of bimetallic systems used as platforms for the understanding of multielectron redox processes. Chapter 5 reported the synthesis and characterization of a series of compounds of the form $Mo_2(DAniF)_n(hpp)_{4-n}$ by ^1H NMR and X-Ray diffraction. In an attempt to fine-tune the electronic structure of $Mo_2(DAniF)_3(hpp)$, *trans*-$Mo_2(DAniF)_2(hpp)_2$ and $Mo_2(DAniF)(hpp)_3$, and to gain a better understanding on the electron donor properties of basic ligands (formamidinates and guanidinates) when attached to bimetallic systems different proportions of formamidinate and guanidinate ligands were employed. The degree of tuning was quantified by exploring their electrochemical properties and comparing their redox potentials. Cyclic voltammetry showed that the $Mo_2^{4+/5+}$ redox process can be tuned over a range of nearly 0.4 V due to the increased ligand basicity with $E_{1/2}$ of –0.754, –0.988, and –1.136 V vs Fc/Fc^+ in THF for $Mo_2(DAniF)_3(hpp)$, *trans*-$Mo_2(DAniF)_2(hpp)_2$, and $Mo_2(DAniF)(hpp)_3$. In addition, *trans*-$Mo_2(DAniF)_2(hpp)_2$ and $Mo_2(DAniF)(hpp)_3$ displayed multielectron redox chemistry due to stabilization of higher oxidation states in the Mo_2 unit by hpp. Data obtained from Raman Spectroscopy presented an increase in Raman Shift with the addition of hpp at 487, 494, and 505 cm^{-1} for $Mo_2(DAniF)_3(hpp)$, *trans*-$Mo_2(DAniF)_2(hpp)_2$ and $Mo_2(DAniF)(hpp)_3$, respectively. DFT studies depicted strong influence of hpp in the energy levels of the orbitals between the compounds, showing greater metal−ligand mixing as formamidinates were replaced by guanidinates, and therefore a decrease in metal character on the HOMOs. Moreover, the reduction of the HOMO – LUMO energy gap ($\delta \rightarrow \delta^*$ transition) as guanidinates are introduced to the Mo_2 core is in agreement with an increase in the bond strength and shortening the Mo–Mo bond distances.

Chapter 6 explored the reactivity and ligand influence in the electronic properties of digold systems. It has been found that digold (II) complexes stabilize the d^9 system upon oxidative addition, unlike mononuclear gold complexes that tend to disproportionate to Au(I) and Au(III). Ligand control over these complexes is crucial to enable the formation of digold systems, and tune their electronic properties and reactivity. This control can be determined by the nature of the coordinating atoms, steric factors, and substituent effects in the periphery. In the first part of this chapter, we explored oxidative addition in a digold (I) compound, $Au_2(DippF)_2$. Compounds $Au_2(DippF)_2$ and $Au_2(DippF)_2Cl_2$ were successfully synthesized and characterized by ^1H NMR, ESI-MS, and X-Ray diffraction, presenting Au···Au distances of 2.7385(7) and 2.5303(3) Å consistent with digold (I) and digold(II) species. The cyclic voltammograms showed a one-electron reversible oxidation for Au_2(DippF)$_2$ at $E_{1/2}$ = 0.843 V vs Fc/Fc$^+$, and a non-reversible one-electron oxidation at $E_{1/2}$ = 0.15 V vs Fc/Fc$^+$ for Au_2(DippF)$_2$Cl$_2$, assigned as oxidations of the Au_2 center and ligand, respectively. In addition, UV-Vis spectra for the compounds showed a high energy bands assigned to MLCT and LMCT electronic transitions as supported by TDDFT calculations.

Variation of the peripheral ligands on the metal unit can potentially modify the energy of the orbitals, modulating thus redox potentials and photophysical properties of the unit without large geometry rearrangement. Although important, systematic studies of substituent effects on the electronic and photophysical properties of bimetallic gold complexes are scarce. A series of three Au(I)-Au(I) complexes with different formamidinate ligands (ArNCHNAr') was synthesized and characterized. These complexes share a common molecular skeleton, but vary the substituents in the aryl groups (Ar = RC$_6$H$_5$, Ar = R'C$_6$H$_5$) Au_2(^{m}DippAF)$_2$ (R = 2,6-CHMe$_2$, R' = *m*-OMe), Au_2(ClDippF)$_2$ (R = 2,6-CHMe$_2$, R' = *p*-Cl), and Au_2(^{m,p}DAniF)$_2$ (R = *p*-OMe, R' = *m*-OMe). Compounds Au_2(^{m}DippAF)$_2$, Au_2(ClDippF)$_2$, and Au_2(^{m,p}DAniF)$_2$ were synthesized and structurally characterized by ^{1}H NMR, ESI-MS, and single crystal X-Ray diffraction presenting Au···Au distances of 2.7281(3) and 2.7431(11) Å, for Au_2(^{m}DippAF)$_2$ and Au_2(ClDippF)$_2$ respectively. Cyclic voltammetry showed that the $Au_2^{2+/3+}$ redox process can be tuned due to inductive effects, displaying a one-electron oxidation for Au_2(^{m}DippAF)$_2$, Au_2(ClDippF)$_2$, and Au_2(^{m,p}DAniF)$_2$ at 0.602, 0.806, and 0.328 V vs Fc/Fc$^+$ in DCM. An excellent linear correlation was found between the reduction potentials and the calculated Hammett constants. Furthermore, the addition of electron-withdrawing substituents stabilized the metal-based δ^* HOMO.

References

(1) Monthly Energy Review - April 2016. *US Energy Inf. Adm.* **2016**, 235.

(2) Lewis, N. S.; Nocera, D. G. Powering the Planet: Chemical Challenges in Solar Energy Utilization. *Proc. Natl. Acad. Sci.* **2006**, *103* (43), 15729–15735. https://doi.org/10.1073/pnas.0603395103.

(3) Seh, Z. W.; Kibsgaard, J.; Dickens, C. F.; Chorkendorff, I.; Nørskov, J. K.; Jaramillo, T. F. Combining Theory and Experiment in Electrocatalysis: Insights into Materials Design. *Science* **2017**, *355* (6321). https://doi.org/10.1126/science.aad4998.

(4) Gray, H. B. Powering the Planet with Solar Fuel. *Nat. Chem.* **2009**, *1* (1), 7–7. https://doi.org/10.1038/nchem.141.

(5) Hoffert, M. I.; Caldeira, K.; Jain, A. K.; Haites, E. F.; Harvey, L. D. D.; Potter, S. D.; Schlesinger, M. E.; Schneider, S. H.; Watts, R. G.; Wigley, T. M. L.; et al. Energy Implications of Future Stabilization of Atmospheric CO2 Content. *Nature* **1998**, *395* (6705), 881–884. https://doi.org/10.1038/27638.

(6) Lewis, N. S.; Crabtree, G. *Basic Research Needs for Solar Energy Utilization: Report of the Basic Energy Sciences Workshop on Solar Energy Utilization, April 18-21, 2005*; Lewis, N. S., Crabtree, G., Nozik, A. J., Wasielewski, M. R., Alivisatos, P., Eds.; US Department of Energy, Office of Basic Energy Science: Washington, DC, 2005.

(7) Layton, B. E. A Comparison of Energy Densities of Prevalent Energy Sources in Units of Joules Per Cubic Meter. *Int. J. Green Energy* **2008**, *5* (6), 438–455. https://doi.org/10.1080/15435070802498036.

(8) U.S. energy-related CO2 emissions fell slightly in 2017 - Today in Energy - U.S. Energy Information Administration (EIA) https://www.eia.gov/todayinenergy/detail.php?id=36953 (accessed May 16, 2019).

(9) Norby, R. J.; Luo, Y. Evaluating Ecosystem Responses to Rising Atmospheric CO2 and Global Warming in a Multi-Factor World. *New Phytol.* **2004**, *162* (2), 281–293.

(10) Eggleton, T.; Eggleton, R. A. *A Short Introduction to Climate Change*; Cambridge University Press, 2013.

(11) Change, N. G. C. Carbon Dioxide Concentration | NASA Global Climate Change https://climate.nasa.gov/vital-signs/carbon-dioxide (accessed May 16, 2019).

(12) Cherubini, F.; Peters, G. P.; Berntsen, T.; Strømman, A. H.; Hertwich, E. CO2 Emissions from Biomass Combustion for Bioenergy: Atmospheric Decay and Contribution to Global Warming. *GCB Bioenergy* **2011**, *3* (5), 413–426. https://doi.org/10.1111/j.1757-1707.2011.01102.x.

(13) World Energy Outlook 2016 https://www.iea.org/newsroom/news/2016/november/world-energy-outlook-2016.html (accessed Oct 19, 2019).

(14) Barber, J. Photosynthetic Energy Conversion: Natural and Artificial. *Chem. Soc. Rev.* **2008**, *38* (1), 185–196. https://doi.org/10.1039/B802262N.

(15) Tsao, J.; Lewis, N.; Crabtree, G. Solar Energy. Sandia National Laboratory 2006.

(16) Siegbahn, P. E. M. Structures and Energetics for O2 Formation in Photosystem II. *Acc. Chem. Res.* **2009**, *42* (12), 1871–1880. https://doi.org/10.1021/ar900117k.

(17) Gust, D.; Moore, T. A.; Moore, A. L. Solar Fuels via Artificial Photosynthesis. *Acc. Chem. Res.* **2009**, *42* (12), 1890–1898. https://doi.org/10.1021/ar900209b.

(18) Staffell, I.; Scamman, D.; Abad, A. V.; Balcombe, P.; Dodds, P. E.; Ekins, P.; Shah, N.; Ward, K. R. The Role of Hydrogen and Fuel Cells in the Global Energy System. *Energy Environ. Sci.* **2019**, *12* (2), 463–491. https://doi.org/10.1039/C8EE01157E.

(19) Qiao, Y.; Jiang, K.; Deng, H.; Zhou, H. A High-Energy-Density and Long-Life Lithium-Ion Battery via Reversible Oxide–Peroxide Conversion. *Nat. Catal.* **2019**, *2* (11), 1035–1044. https://doi.org/10.1038/s41929-019-0362-z.

(20) Zhu, Z.; Kushima, A.; Yin, Z.; Qi, L.; Amine, K.; Lu, J.; Li, J. Anion-Redox Nanolithia Cathodes for Li-Ion Batteries. *Nat. Energy* **2016**, *1* (8), 1–7. https://doi.org/10.1038/nenergy.2016.111.

(21) Liang, C. C.; Barnette, L. H. A High Energy Density Solid-State Battery System. *J. Electrochem. Soc.* **1976**, *123* (4), 453–458. https://doi.org/10.1149/1.2132855.

(22) Zhang, J.; Jiang, G.; Xu, P.; Kashkooli, A. G.; Mousavi, M.; Yu, A.; Chen, Z. An All-Aqueous Redox Flow Battery with Unprecedented Energy Density. *Energy Environ. Sci.* **2018**, *11* (8), 2010–2015. https://doi.org/10.1039/C8EE00686E.

(23) Badwal, S. P. S.; Giddey, S. S.; Munnings, C.; Bhatt, A. I.; Hollenkamp, A. F. Emerging Electrochemical Energy Conversion and Storage Technologies. *Front. Chem.* **2014**, *2*. https://doi.org/10.3389/fchem.2014.00079.

(24) Cook, T. R.; Dogutan, D. K.; Reece, S. Y.; Surendranath, Y.; Teets, T. S.; Nocera, D. G. Solar Energy Supply and Storage for the Legacy and Nonlegacy Worlds. *Chem. Rev.* **2010**, *110* (11), 6474–6502. https://doi.org/10.1021/cr100246c.

(25) Nocera, D. G. Chemistry of Personalized Solar Energy. *Inorg. Chem.* **2009**, *48* (21), 10001–10017. https://doi.org/10.1021/ic901328v.

(26) Walter, M. G.; Warren, E. L.; McKone, J. R.; Boettcher, S. W.; Mi, Q.; Santori, E. A.; Lewis, N. S. Solar Water Splitting Cells. *Chem. Rev.* **2010**, *110* (11), 6446–6473. https://doi.org/10.1021/cr1002326.

(27) Costentin, C.; Nocera, D. G. Self-Healing Catalysis in Water. *Proc. Natl. Acad. Sci.* **2017**, *114* (51), 13380–13384. https://doi.org/10.1073/pnas.1711836114.

(28) Merki, D.; Vrubel, H.; Rovelli, L.; Fierro, S.; Hu, X. Fe, Co, and Ni Ions Promote the Catalytic Activity of Amorphous Molybdenum Sulfide Films for Hydrogen Evolution. *Chem. Sci.* **2012**, *3* (8), 2515–2525. https://doi.org/10.1039/C2SC20539D.

(29) Lu, Z.; Wang, H.; Kong, D.; Yan, K.; Hsu, P.-C.; Zheng, G.; Yao, H.; Liang, Z.; Sun, X.; Cui, Y. Electrochemical Tuning of Layered Lithium Transition Metal Oxides for Improvement of Oxygen Evolution Reaction. *Nat. Commun.* **2014**, *5*, 4345. https://doi.org/10.1038/ncomms5345.

(30) Wang, M.; Chen, L.; Sun, L. Recent Progress in Electrochemical Hydrogen Production with Earth-Abundant Metal Complexes as Catalysts. *Energy Environ. Sci.* **2012**, *5* (5), 6763–6778. https://doi.org/10.1039/C2EE03309G.

(31) Yu, L.; Lin, J.; Zheng, M.; Chen, M.; Ding, Y. Homogeneous Electrocatalytic Water Oxidation at Neutral PH by a Robust Trinuclear Copper(II)-Substituted Polyoxometalate. *Chem. Commun.* **2018**, *54* (4), 354–357. https://doi.org/10.1039/C7CC08301G.

(32) Faber, M. S.; Lukowski, M. A.; Ding, Q.; Kaiser, N. S.; Jin, S. Earth-Abundant Metal Pyrites (FeS2, CoS2, NiS2, and Their Alloys) for Highly Efficient Hydrogen Evolution and Polysulfide Reduction Electrocatalysis. *J. Phys. Chem. C* **2014**, *118* (37), 21347–21356. https://doi.org/10.1021/jp506288w.

(33) Fukuzumi, S.; Hong, D. Homogeneous versus Heterogeneous Catalysts in Water Oxidation. *Eur. J. Inorg. Chem.* **2014**, *2014* (4), 645–659. https://doi.org/10.1002/ejic.201300684.

(34) Costentin, C.; Passard, G.; Savéant, J.-M. Benchmarking of Homogeneous Electrocatalysts: Overpotential, Turnover Frequency, Limiting Turnover Number. *J. Am. Chem. Soc.* **2015**, *137* (16), 5461–5467. https://doi.org/10.1021/jacs.5b00914.

(35) Bediako, D. K.; Solis, B. H.; Dogutan, D. K.; Roubelakis, M. M.; Maher, A. G.; Lee, C. H.; Chambers, M. B.; Hammes-Schiffer, S.; Nocera, D. G. Role of Pendant Proton Relays and Proton-Coupled Electron Transfer on the Hydrogen Evolution Reaction by Nickel Hangman Porphyrins. *Proc. Natl. Acad. Sci.* **2014**, *111* (42), 15001–15006. https://doi.org/10.1073/pnas.1414908111.

(36) Solis, B. H.; Hammes-Schiffer, S. Theoretical Analysis of Mechanistic Pathways for Hydrogen Evolution Catalyzed by Cobaloximes. *Inorg. Chem.* **2011**, *50* (21), 11252–11262. https://doi.org/10.1021/ic201842v.

(37) Lee, C. H.; Dogutan, D. K.; Nocera, D. G. Hydrogen Generation by Hangman Metalloporphyrins. *J. Am. Chem. Soc.* **2011**, *133* (23), 8775–8777. https://doi.org/10.1021/ja202136y.

(38) Solis, B. H.; Maher, A. G.; Dogutan, D. K.; Nocera, D. G.; Hammes-Schiffer, S. Nickel Phlorin Intermediate Formed by Proton-Coupled Electron Transfer in Hydrogen Evolution Mechanism. *Proc. Natl. Acad. Sci.* **2016**, *113* (3), 485–492. https://doi.org/10.1073/pnas.1521834112.

(39) Mondal, B.; Sengupta, K.; Rana, A.; Mahammed, A.; Botoshansky, M.; Dey, S. G.; Gross, Z.; Dey, A. Cobalt Corrole Catalyst for Efficient Hydrogen Evolution Reaction from H2O under Ambient Conditions: Reactivity, Spectroscopy, and Density Functional Theory Calculations. *Inorg. Chem.* **2013**, *52* (6), 3381–3387. https://doi.org/10.1021/ic4000473.

(40) Zhang, W.; Lai, W.; Cao, R. Energy-Related Small Molecule Activation Reactions: Oxygen Reduction and Hydrogen and Oxygen Evolution Reactions Catalyzed by Porphyrin- and Corrole-Based Systems. *Chem. Rev.* **2017**, *117* (4), 3717–3797. https://doi.org/10.1021/acs.chemrev.6b00299.

(41) Hu, X.; Brunschwig, B. S.; Peters, J. C. Electrocatalytic Hydrogen Evolution at Low Overpotentials by Cobalt Macrocyclic Glyoxime and Tetraimine Complexes. *J. Am. Chem. Soc.* **2007**, *129* (29), 8988–8998. https://doi.org/10.1021/ja067876b.

(42) McCrory, C. C. L.; Uyeda, C.; Peters, J. C. Electrocatalytic Hydrogen Evolution in Acidic Water with Molecular Cobalt Tetraazamacrocycles. *J. Am. Chem. Soc.* **2012**, *134* (6), 3164–3170. https://doi.org/10.1021/ja210661k.

(43) Maher, A. G.; Passard, G.; Dogutan, D. K.; Halbach, R. L.; Anderson, B. L.; Gagliardi, C. J.; Taniguchi, M.; Lindsey, J. S.; Nocera, D. G. Hydrogen Evolution Catalysis by a Sparsely Substituted Cobalt Chlorin. *ACS Catal.* **2017**, *7* (5), 3597–3606. https://doi.org/10.1021/acscatal.7b00969.

(44) Cao, R. Hydrogen and Oxygen Evolution Reactions Catalyzed By Single Site Metal Porphyrins and Corroles. *Meet. Abstr.* **2018**, *MA2018-01* (12), 967–967.

(45) Patra, B. C.; Khilari, S.; Manna, R. N.; Mondal, S.; Pradhan, D.; Pradhan, A.; Bhaumik, A. A Metal-Free Covalent Organic Polymer for Electrocatalytic Hydrogen Evolution. *ACS Catal.* **2017**, *7* (9), 6120–6127. https://doi.org/10.1021/acscatal.7b01067.

(46) Manton, J. C.; Hidalgo, D.; Frayne, L.; Brandon, M. P.; Vos, J. G.; Pryce, M. T. Electrocatalytic Hydrogen Evolution Using Metal-Free Porphyrins. *Int. J. Hydrog. Energy* **2018**, *43* (41), 18843–18849. https://doi.org/10.1016/j.ijhydene.2018.08.017.

(47) Belkova, N. V.; Epstein, L. M.; Filippov, O. A.; Shubina, E. S. Hydrogen and Dihydrogen Bonds in the Reactions of Metal Hydrides. *Chem. Rev.* **2016**, *116* (15), 8545–8587. https://doi.org/10.1021/acs.chemrev.6b00091.

(48) Hernandez, J. A.; George, S. J.; Rubio, L. M. Molybdenum Trafficking for Nitrogen Fixation. *Biochemistry* **2009**, *48* (41), 9711–9721. https://doi.org/10.1021/bi901217p.

(49) Hollander, J.; Spialter, L. The Reduction of Carbon Dioxide. *J. Chem. Educ.* **1958**, *35* (9), 446. https://doi.org/10.1021/ed035p446.

(50) Zhao, Q.; Betley, T. A. Synthesis and Redox Properties of Triiron Complexes Featuring Strong Fe–Fe Interactions. *Angew. Chem. Int. Ed.* **2011**, *50* (3), 709–712. https://doi.org/10.1002/anie.201005198.

(51) Abe, T.; Taguchi, F.; Imaya, H.; Zhao, F.; Zhang, J.; Kaneko, M. Highly Active Electrocatalysis by Cobalt Tetraphenylporphyrin Incorporated in a Nafion Membrane for Proton Reduction. *Polym. Adv. Technol.* **1998**, *9* (9), 559–562. https://doi.org/10.1002/(SICI)1099-1581(199809)9:9<559::AID-PAT818>3.0.CO;2-1.

(52) Bhugun, I.; Lexa, D.; Savéant, J.-M. Homogeneous Catalysis of Electrochemical Hydrogen Evolution by Iron(0) Porphyrins. *J. Am. Chem. Soc.* **1996**, *118* (16), 3982–3983. https://doi.org/10.1021/ja954326x.

(53) Grass, V.; Lexa, D.; Savéant, J.-M. Electrochemical Generation of Rhodium Porphyrin Hydrides. Catalysis of Hydrogen Evolution. *J. Am. Chem. Soc.* **1997**, *119* (32), 7526–7532. https://doi.org/10.1021/ja964100+.

(54) Solis, B. H.; Hammes-Schiffer, S. Proton-Coupled Electron Transfer in Molecular Electrocatalysis: Theoretical Methods and Design Principles. *Inorg. Chem.* **2014**, *53* (13), 6427–6443. https://doi.org/10.1021/ic5002896.

(55) Collman, J. P.; Wagenknecht, P. S.; Lewis, N. S. Hydride Transfer and Dihydrogen Elimination from Osmium and Ruthenium Metalloporphyrin Hydrides: Model Processes for Hydrogenase Enzymes and the Hydrogen Electrode Reaction. *J. Am. Chem. Soc.* **1992**, *114* (14), 5665–5673. https://doi.org/10.1021/ja00040a028.

(56) Marinescu, S. C.; Winkler, J. R.; Gray, H. B. Molecular Mechanisms of Cobalt-Catalyzed Hydrogen Evolution. *Proc. Natl. Acad. Sci.* **2012**, *109* (38), 15127–15131. https://doi.org/10.1073/pnas.1213442109.

(57) Fonda, H. N.; Gilbert, J. V.; Cormier, R. A.; Sprague, J. R.; Kamioka, K.; Connolly, J. S. Spectroscopic, Photophysical, and Redox Properties of Some Meso-Substituted Free-Base Porphyrins. *J. Phys. Chem.* **1993**, *97* (27), 7024–7033. https://doi.org/10.1021/j100129a017.

(58) Handbook of Porphyrin Science (Volumes 31 – 35) http://www.worldscientific.com/worldscibooks/10.1142/8560 (accessed Jan 24, 2017).

(59) Aronoff, S. Perchloric. Acid Titrations of Porphyrins in Nitrobenzene. *J. Phys. Chem.* **1958**, *62* (4), 428–431. https://doi.org/10.1021/j150562a013.

(60) Hibbert, F.; Hunte, K. P. P. Kinetic and Equilibrium Studies of the Protonation of Meso-Tetraphenylporphyrin in Dimethyl Sulphoxide–Water. *J. Chem. Soc. Perkin Trans. 2* **1977**, *0* (12), 1624–1628. https://doi.org/10.1039/P29770001624.

(61) Lindsey, J. S.; Hsu, H. C.; Schreiman, I. C. Synthesis of Tetraphenylporphyrins under Very Mild Conditions. *Tetrahedron Lett.* **1986**, *27* (41), 4969–4970. https://doi.org/10.1016/S0040-4039(00)85109-6.

(62) Becke, A. D. Density-functional Thermochemistry. III. The Role of Exact Exchange. *J. Chem. Phys.* **1993**, *98* (7), 5648–5652. https://doi.org/10.1063/1.464913.

(63) Lee, C.; Yang, W.; Parr, R. G. Development of the Colle-Salvetti Correlation-Energy Formula into a Functional of the Electron Density. *Phys. Rev. B* **1988**, *37* (2), 785–789. https://doi.org/10.1103/PhysRevB.37.785.

(64) Frisch, M. J.; Pople, J. A.; Binkley, J. S. Self-consistent Molecular Orbital Methods 25. Supplementary Functions for Gaussian Basis Sets. *J. Chem. Phys.* **1984**, *80* (7), 3265–3269. https://doi.org/10.1063/1.447079.

(65) Hariharan, P. C.; Pople, J. A. The Influence of Polarization Functions on Molecular Orbital Hydrogenation Energies. *Theor. Chim. Acta* **1973**, *28* (3), 213–222. https://doi.org/10.1007/BF00533485.

(66) *Frisch, M. J.; Trucks, G. W.; Schlegel, H. B.; Scuseria, G. E.; Robb, M. A.; Cheeseman, J. R.; Scalmani, G.; Barone, V.; Mennucci, B.; Petersson, G. A.; Nakatsuji, H.; Caricato, M.; Li, X.; Hratchian, H. P.; Izmaylov, A. F.; Bloino, J.; Zheng, G.; Sonnenberg, J. L.; Hada, M.; Ehara, M.; Toyota, K.; Fukuda, R.; Hasegawa, J.; Ishida, M.; Nakajima, T.; Honda, Y.; Kitao, O.; Nakai, H.; Vreven, T.; Montgomery, J. A., Jr.; Peralta, J. E.; Ogliaro, F.; Bearpark, M.; Heyd, J. J.; Brothers, E.; Kudin, K. N.; Staroverov, V. N.; Kobayashi, R.; Normand, J.; Raghavachari, K.; Rendell, A.; Burant, J. C.; Iyengar, S. S.; Tomasi, J.; Cossi, M.; Rega, N.; Millam, J. M.; Klene, M.; Knox, J. E.; Cross, J. B.; Bakken, V.; Adamo, C.; Jaramillo, J.; Gomperts, R.; Stratmann, R. E.; Yazyev, O.; Austin, A. J.; Cammi, R.; Pomelli, C.; Ochterski, J. W.; Martin, R. L.; Morokuma, K.; Zakrzewski, V. G.; Voth, G. A.; Salvador, P.; Dannenberg, J. J.; Dapprich, S.; Daniels, A. D.; Farkas, Ö.; Foresman, J. B.; Ortiz, J. V.; Cioslowski, J.; Fox, D. J. Gaussian 09, Revision C.01, Gaussian, Inc., Wallingford CT, 2010.*

(67) Cammi, R.; Mennucci, B.; Tomasi, J. An Attempt To Bridge the Gap between Computation and Experiment for Nonlinear Optical Properties: Macroscopic Susceptibilities in Solution. *J. Phys. Chem. A* **2000**, *104* (20), 4690–4698. https://doi.org/10.1021/jp994163p.

(68) Cammi, R.; Mennucci, B.; Tomasi, J. On the Calculation of Local Field Factors for Microscopic Static Hyperpolarizabilities of Molecules in Solution with the Aid of Quantum-Mechanical Methods. *J. Phys. Chem. A* **1998**, *102* (5), 870–875. https://doi.org/10.1021/jp9726807.

(69) Marenich, A. V.; Cramer, C. J.; Truhlar, D. G. Universal Solvation Model Based on Solute Electron Density and on a Continuum Model of the Solvent Defined by the Bulk Dielectric Constant and Atomic Surface Tensions. *J. Phys. Chem. B* **2009**, *113* (18), 6378–6396. https://doi.org/10.1021/jp810292n.

(70) Solis, B. H.; Hammes-Schiffer, S. Substituent Effects on Cobalt Diglyoxime Catalysts for Hydrogen Evolution. *J. Am. Chem. Soc.* **2011**, *133* (47), 19036–19039. https://doi.org/10.1021/ja208091e.

(71) Solis, B. H.; Maher, A. G.; Honda, T.; Powers, D. C.; Nocera, D. G.; Hammes-Schiffer, S. Theoretical Analysis of Cobalt Hangman Porphyrins: Ligand Dearomatization and Mechanistic Implications for Hydrogen Evolution. *ACS Catal.* **2014**, *4* (12), 4516–4526. https://doi.org/10.1021/cs501454y.

(72) Tang, H.; Hall, M. B. Biomimetics of [NiFe]-Hydrogenase: Nickel- or Iron-Centered Proton Reduction Catalysis? *J. Am. Chem. Soc.* **2017**, *139* (49), 18065–18070. https://doi.org/10.1021/jacs.7b10425.

(73) Aidas, K.; Lanevskij, K.; Kubilius, R.; Juška, L.; Petkevičius, D.; Japertas, P. Aqueous Acidities of Primary Benzenesulfonamides: Quantum Chemical Predictions Based on Density Functional Theory and SMD. *J. Comput. Chem.* **2015**, *36* (29), 2158–2167. https://doi.org/10.1002/jcc.23998.

(74) Fernandez, L. E.; Horvath, S.; Hammes-Schiffer, S. Theoretical Analysis of the Sequential Proton-Coupled Electron Transfer Mechanisms for H2 Oxidation and Production Pathways Catalyzed by Nickel Molecular Electrocatalysts. *J. Phys. Chem. C* **2012**, *116* (4), 3171–3180. https://doi.org/10.1021/jp210690q.

(75) Ho, J.; Coote, M. L. A Universal Approach for Continuum Solvent PKa Calculations: Are We There Yet? *Theor. Chem. Acc.* **2009**, *125* (1), 3. https://doi.org/10.1007/s00214-009-0667-0.

(76) Hansch, Corwin.; Leo, A.; Taft, R. W. A Survey of Hammett Substituent Constants and Resonance and Field Parameters. *Chem. Rev.* **1991**, *91* (2), 165–195. https://doi.org/10.1021/cr00002a004.

(77) Roberts, J. A. S.; Bullock, R. M. Direct Determination of Equilibrium Potentials for Hydrogen Oxidation/Production by Open Circuit Potential Measurements in Acetonitrile. *Inorg. Chem.* **2013**, *52* (7), 3823–3835. https://doi.org/10.1021/ic302461q.

(78) Appel, A. M.; Helm, M. L. Determining the Overpotential for a Molecular Electrocatalyst. *ACS Catal.* **2014**, *4* (2), 630–633. https://doi.org/10.1021/cs401013v.

(79) Karaman, R.; Bruice, T. C. Unusual Behavior of 5,10,15,20-Tetraphenylporphine Diacid toward Oxygen Broensted Bases. *Inorg. Chem.* **1992**, *31* (12), 2455–2459. https://doi.org/10.1021/ic00038a028.

(80) De Luca, G.; Romeo, A.; Scolaro, L. M. Counteranion Dependent Protonation and Aggregation of Tetrakis(4-Sulfonatophenyl)Porphyrin in Organic Solvents. *J. Phys. Chem. B* **2006**, *110* (14), 7309–7315. https://doi.org/10.1021/jp0530348.

(81) Cheng, B.; Munro, O. Q.; Marques, H. M.; Scheidt, W. R. An Analysis of Porphyrin Molecular FlexibilityUse of Porphyrin Diacids. *J. Am. Chem. Soc.* **1997**, *119* (44), 10732–10742. https://doi.org/10.1021/ja9716214.

(82) Saegusa, Y.; Ishizuka, T.; Shiota, Y.; Yoshizawa, K.; Kojima, T. Acid–Base Properties of a Freebase Form of a Quadruply Ring-Fused Porphyrin—Stepwise Protonation Induced by Rigid Ring-Fused Structure. *J. Org. Chem.* **2017**, *82* (1), 322–330. https://doi.org/10.1021/acs.joc.6b02419.

(83) Honda, T.; Kojima, T.; Fukuzumi, S. Crystal Structures and Properties of a Monoprotonated Porphyrin. *Chem. Commun.* **2009**, No. 33, 4994–4996. https://doi.org/10.1039/B910077F.

(84) Hambright, P.; Fleisher, E. B. Acid-Base Equilibriums, Kinetics of Copper Ion Incorporation, and Acid-Catalyzed Zinc Ion Displacement from the Water-Soluble Porphyrin .Alpha.,.Beta.,.Gamma.,.Delta.-Tetrakis(1-Methyl-4-Pyridinio)Porphine Tetraiodide. *Inorg. Chem.* **1970**, *9* (7), 1757–1761. https://doi.org/10.1021/ic50089a030.

(85) Pistner, A. J.; Lutterman, D. A.; Ghidiu, M. J.; Ma, Y.-Z.; Rosenthal, J. Synthesis, Electrochemistry, and Photophysics of a Family of Phlorin Macrocycles That Display Cooperative Fluoride Binding. *J. Am. Chem. Soc.* **2013**, *135* (17), 6601–6607. https://doi.org/10.1021/ja401391z.

(86) Vij, V.; Sultan, S.; Harzandi, A. M.; Meena, A.; Tiwari, J. N.; Lee, W.-G.; Yoon, T.; Kim, K. S. Nickel-Based Electrocatalysts for Energy-Related Applications: Oxygen Reduction, Oxygen Evolution, and Hydrogen Evolution Reactions. *ACS Catal.* **2017**, *7* (10), 7196–7225. https://doi.org/10.1021/acscatal.7b01800.

(87) Hu, X.; Brunschwig, B. S.; Peters, J. C. Electrocatalytic Hydrogen Evolution at Low Overpotentials by Cobalt Macrocyclic Glyoxime and Tetraimine Complexes. *J. Am. Chem. Soc.* **2007**, *129* (29), 8988–8998. https://doi.org/10.1021/ja067876b.

(88) Rana, A.; Mondal, B.; Sen, P.; Dey, S.; Dey, A. Activating Fe(I) Porphyrins for the Hydrogen Evolution Reaction Using Second-Sphere Proton Transfer Residues. *Inorg. Chem.* **2017**, *56* (4), 1783–1793. https://doi.org/10.1021/acs.inorgchem.6b01707.

(89) Han, Y.; Fang, H.; Jing, H.; Sun, H.; Lei, H.; Lai, W.; Cao, R. Singly versus Doubly Reduced Nickel Porphyrins for Proton Reduction: Experimental and Theoretical Evidence for a Homolytic Hydrogen-Evolution Reaction. *Angew. Chem. Int. Ed.* **2016**, *55* (18), 5457–5462. https://doi.org/10.1002/anie.201510001.

(90) Lei, H.; Fang, H.; Han, Y.; Lai, W.; Fu, X.; Cao, R. Reactivity and Mechanism Studies of Hydrogen Evolution Catalyzed by Copper Corroles. *ACS Catal.* **2015**, *5* (9), 5145–5153. https://doi.org/10.1021/acscatal.5b00666.

(91) Mondal, B.; Sengupta, K.; Rana, A.; Mahammed, A.; Botoshansky, M.; Dey, S. G.; Gross, Z.; Dey, A. Cobalt Corrole Catalyst for Efficient Hydrogen Evolution Reaction from H2O under Ambient Conditions: Reactivity, Spectroscopy, and Density Functional Theory Calculations. *Inorg. Chem.* **2013**, *52* (6), 3381–3387. https://doi.org/10.1021/ic4000473.

(92) Solis, B. H.; Maher, A. G.; Honda, T.; Powers, D. C.; Nocera, D. G.; Hammes-Schiffer, S. Theoretical Analysis of Cobalt Hangman Porphyrins: Ligand Dearomatization and Mechanistic Implications for Hydrogen Evolution. *ACS Catal.* **2014**, *4* (12), 4516–4526. https://doi.org/10.1021/cs501454y.

(93) Solis, B. H.; Maher, A. G.; Dogutan, D. K.; Nocera, D. G.; Hammes-Schiffer, S. Nickel Phlorin Intermediate Formed by Proton-Coupled Electron Transfer in Hydrogen Evolution Mechanism. *Proc. Natl. Acad. Sci.* **2016**, *113* (3), 485–492. https://doi.org/10.1073/pnas.1521834112.

(94) Lee, C. H.; Dogutan, D. K.; Nocera, D. G. Hydrogen Generation by Hangman Metalloporphyrins. *J. Am. Chem. Soc.* **2011**, *133* (23), 8775–8777. https://doi.org/10.1021/ja202136y.

(95) Bullock, R. M.; Appel, A. M.; Helm, M. L. Production of Hydrogen by Electrocatalysis: Making the H–H Bond by Combining Protons and Hydrides. *Chem. Commun.* **2014**, *50* (24), 3125–3143. https://doi.org/10.1039/C3CC46135A.

(96) Elgrishi, N.; Kurtz, D. A.; Dempsey, J. L. Reaction Parameters Influencing Cobalt Hydride Formation Kinetics: Implications for Benchmarking H2-Evolution Catalysts. *J. Am. Chem. Soc.* **2017**, *139* (1), 239–244. https://doi.org/10.1021/jacs.6b10148.

(97) Zhang, Z.; Zhu, Y.; Chen, X.; Zhang, H.; Wang, J. A Full-Spectrum Metal-Free Porphyrin Supramolecular Photocatalyst for Dual Functions of Highly Efficient Hydrogen and Oxygen Evolution. *Adv. Mater.* **2019**, *31* (7), 1806626. https://doi.org/10.1002/adma.201806626.

(98) Wu, Y.; Rodriguez, N.; Villagran, D. Hydrogen Gas Generation by a Metal-Free Fluorinated Porphyrin. *Chem. Sci.* **2018**. https://doi.org/10.1039/C8SC00093J.

(99) Capar, J.; Conradie, J.; Beavers, C. M.; Ghosh, A. Molecular Structures of Free-Base Corroles: Nonplanarity, Chirality, and Enantiomerization. *J. Phys. Chem. A* **2015**, *119* (14), 3452–3457. https://doi.org/10.1021/jp511188c.

(100) Fang, Y.; Ou, Z.; Kadish, K. M. Electrochemistry of Corroles in Nonaqueous Media. *Chem. Rev.* **2017**, *117* (4), 3377–3419. https://doi.org/10.1021/acs.chemrev.6b00546.

(101) Cramer, C. J.; Truhlar, D. G. Density Functional Theory for Transition Metals and Transition Metal Chemistry. *Phys. Chem. Chem. Phys.* **2009**, *11* (46), 10757–10816. https://doi.org/10.1039/B907148B.

(102) De, S. V.; Stillman, M. J. Challenging Density Functional Theory Calculations with Hemes and Porphyrins., Challenging Density Functional Theory Calculations with Hemes and Porphyrins. *Int. J. Mol. Sci. Int. J. Mol. Sci.* **2016**, *17, 17* (4, 4), 519–519. https://doi.org/10.3390/ijms17040519, 10.3390/ijms17040519.

(103) Fernandez, L. E.; Horvath, S.; Hammes-Schiffer, S. Theoretical Analysis of the Sequential Proton-Coupled Electron Transfer Mechanisms for H2 Oxidation and Production Pathways Catalyzed by Nickel Molecular Electrocatalysts. *J. Phys. Chem. C* **2012**, *116* (4), 3171–3180. https://doi.org/10.1021/jp210690q.

(104) Casasnovas, R.; Ortega-Castro, J.; Frau, J.; Donoso, J.; Muñoz, F. Theoretical PKa Calculations with Continuum Model Solvents, Alternative Protocols to Thermodynamic Cycles. *Int. J. Quantum Chem.* **2014**, *114* (20), 1350–1363. https://doi.org/10.1002/qua.24699.

(105) Namazian, M.; Halvani, S. Calculations of PKa Values of Carboxylic Acids in Aqueous Solution Using Density Functional Theory. *J. Chem. Thermodyn.* **2006**, *38* (12), 1495–1502. https://doi.org/10.1016/j.jct.2006.05.002.

(106) Baik, M.-H.; Friesner, R. A. Computing Redox Potentials in Solution: Density Functional Theory as A Tool for Rational Design of Redox Agents. *J. Phys. Chem. A* **2002**, *106* (32), 7407–7412. https://doi.org/10.1021/jp025853n.

(107) Solis, B. H.; Hammes-Schiffer, S. Computational Study of Anomalous Reduction Potentials for Hydrogen Evolution Catalyzed by Cobalt Dithiolene Complexes. *J. Am. Chem. Soc.* **2012**, *134* (37), 15253–15256. https://doi.org/10.1021/ja306857q.

(108) Lindsey, J. S.; Wagner, R. W. Investigation of the Synthesis of Ortho-Substituted Tetraphenylporphyrins. *J. Org. Chem.* **1989**, *54* (4), 828–836. https://doi.org/10.1021/jo00265a021.

(109) Dogutan, D. K.; Stoian, S. A.; McGuire, R.; Schwalbe, M.; Teets, T. S.; Nocera, D. G. Hangman Corroles: Efficient Synthesis and Oxygen Reaction Chemistry. *J. Am. Chem. Soc.* **2011**, *133* (1), 131–140. https://doi.org/10.1021/ja108904s.

(110) Becke, A. D. Density-functional Thermochemistry. III. The Role of Exact Exchange. *J. Chem. Phys.* **1993**, *98* (7), 5648–5652. https://doi.org/10.1063/1.464913.

(111) Lee, C.; Yang, W.; Parr, R. G. Development of the Colle-Salvetti Correlation-Energy Formula into a Functional of the Electron Density. *Phys. Rev. B* **1988**, *37* (2), 785–789. https://doi.org/10.1103/PhysRevB.37.785.

(112) Frisch, M. J.; Pople, J. A.; Binkley, J. S. Self-consistent Molecular Orbital Methods 25. Supplementary Functions for Gaussian Basis Sets. *J. Chem. Phys.* **1984**, *80* (7), 3265–3269. https://doi.org/10.1063/1.447079.

(113) Hariharan, P. C.; Pople, J. A. The Influence of Polarization Functions on Molecular Orbital Hydrogenation Energies. *Theor. Chim. Acta* **1973**, *28* (3), 213–222. https://doi.org/10.1007/BF00533485.

(114) M. J. Frisch, G. W. Trucks, H. B. Schlegel, G. E. Scuseria, M. A. Robb, J. R. Cheeseman, G. Scalmani, V. Barone, G. A. Petersson, H. Nakatsuji, X. Li, M. Caricato, A. Marenich, J. Bloino, B. G. Janesko, R. Gomperts, B. Mennucci, H. P. Hratchian, J. V. Ortiz, A. F. Izmaylov, J. L. Sonnenberg, D. Williams-Young, F. Ding, F. Lipparini, F. Egidi, J. Goings, B. Peng, A. Petrone, T. Henderson, D. Ranasinghe, V. G. Zakrzewski, J. Gao, N. Rega, G. Zheng, W. Liang, M. Hada, M. Ehara, K. Toyota, R. Fukuda, J. Hasegawa, M. Ishida, T. Nakajima, Y. Honda, O. Kitao, H. Nakai, T. Vreven, K. Throssell, J. A. Montgomery, Jr., J. E. Peralta, F. Ogliaro, M. Bearpark, J. J. Heyd, E. Brothers, K. N. Kudin, V. N. Staroverov, T. Keith, R. Kobayashi, J. Normand, K. Raghavachari, A. Rendell, J. C. Burant, S. S. Iyengar, J. Tomasi, M. Cossi, J. M. Millam, M. Klene, C. Adamo, R. Cammi, J. W. Ochterski, R. L. Martin, K. Morokuma, O. Farkas, J. B. Foresman, and D. J. Fox,. *Gaussian 09, Revision C.01*; Gaussian Inc.: Wallingford CT, 2010.

(115) Marenich, A. V.; Cramer, C. J.; Truhlar, D. G. Universal Solvation Model Based on Solute Electron Density and on a Continuum Model of the Solvent Defined by the Bulk Dielectric Constant and Atomic Surface Tensions. *J. Phys. Chem. B* **2009**, *113* (18), 6378–6396. https://doi.org/10.1021/jp810292n.

(116) Hansch, Corwin.; Leo, A.; Taft, R. W. A Survey of Hammett Substituent Constants and Resonance and Field Parameters. *Chem. Rev.* **1991**, *91* (2), 165–195. https://doi.org/10.1021/cr00002a004.

(117) Perdew, J. P. Density-Functional Approximation for the Correlation Energy of the Inhomogeneous Electron Gas. *Phys. Rev. B* **1986**, *33* (12), 8822–8824. https://doi.org/10.1103/PhysRevB.33.8822.

(118) Zhao, Y.; Truhlar, D. G. The M06 Suite of Density Functionals for Main Group Thermochemistry, Thermochemical Kinetics, Noncovalent Interactions, Excited States, and Transition Elements: Two New Functionals and Systematic Testing of Four M06-Class Functionals and 12 Other Functionals. *Theor. Chem. Acc.* **2008**, *120* (1), 215–241. https://doi.org/10.1007/s00214-007-0310-x.

(119) Hehre, W. J.; Ditchfield, R.; Pople, J. A. Self-Consistent Molecular Orbital Methods. XII. Further Extensions of Gaussian—Type Basis Sets for Use in Molecular Orbital Studies of Organic Molecules. *J. Chem. Phys.* **1972**, *56* (5), 2257–2261. https://doi.org/10.1063/1.1677527.

(120) Hariharan, P. C.; Pople, J. A. Accuracy of AH n Equilibrium Geometries by Single Determinant Molecular Orbital Theory. *Mol. Phys.* **1974**, *27* (1), 209–214. https://doi.org/10.1080/00268977400100171.

(121) Bartmess, J. E. Thermodynamics of the Electron and the Proton. *J. Phys. Chem.* **1994**, *98* (25), 6420–6424. https://doi.org/10.1021/j100076a029.

(122) Solis, B. H.; Hammes-Schiffer, S. Proton-Coupled Electron Transfer in Molecular Electrocatalysis: Theoretical Methods and Design Principles. *Inorg. Chem.* **2014**, *53* (13), 6427–6443. https://doi.org/10.1021/ic5002896.

(123) Arumugam, K.; Becker, U. Computational Redox Potential Predictions: Applications to Inorganic and Organic Aqueous Complexes, and Complexes Adsorbed to Mineral Surfaces. *Minerals* **2014**, *4* (2), 345–387. https://doi.org/10.3390/min4020345.

(124) Ye, S.; Tuttle, T.; Bill, E.; Simkhovich, L.; Gross, Z.; Thiel, W.; Neese, F. The Electronic Structure of Iron Corroles: A Combined Experimental and Quantum Chemical Study. *Chem. – Eur. J.* **2008**, *14* (34), 10839–10851. https://doi.org/10.1002/chem.200801265.

(125) Ghosh, A. Electronic Structure of Corrole Derivatives: Insights from Molecular Structures, Spectroscopy, Electrochemistry, and Quantum Chemical Calculations. *Chem. Rev.* **2017**, *117* (4), 3798–3881. https://doi.org/10.1021/acs.chemrev.6b00590.

(126) Ziegler, C. J.; Sabin, J. R.; Geier, G. R.; Nemykin, V. N. The First TDDFT and MCD Studies of Free Base Triarylcorroles: A Closer Look into Solvent-Dependent UV-Visible Absorption. *Chem. Commun.* **2012**, *48* (39), 4743–4745. https://doi.org/10.1039/C2CC31146A.

(127) Bursa, B.; Barszcz, B.; Bednarski, W.; Lewtak, J. P.; Koszelewski, D.; Vakuliuk, O.; Gryko, D. T.; Wróbel, D. New Meso-Substituted Corroles Possessing Pentafluorophenyl Groups – Synthesis and Spectroscopic Characterization. *Phys. Chem. Chem. Phys.* **2015**, *17* (11), 7411–7423. https://doi.org/10.1039/C4CP05648E.

(128) Gouterman, M. *The Porphyrins*; Academic Press: New York, 1978; Vol. 3.

(129) Gouterman, M.; Wagnière, G. H.; Snyder, L. C. Spectra of Porphyrins: Part II. Four Orbital Model. *J. Mol. Spectrosc.* **1963**, *11* (1), 108–127. https://doi.org/10.1016/0022-2852(63)90011-0.

(130) Salvatori, P.; Amat, A.; Pastore, M.; Vitillaro, G.; Sudhakar, K.; Giribabu, L.; Soujanya, Y.; De Angelis, F. Corrole Dyes for Dye-Sensitized Solar Cells: The Crucial Role of the Dye/Semiconductor Energy Level Alignment. *Comput. Theor. Chem.* **2014**, *1030*, 59–66. https://doi.org/10.1016/j.comptc.2013.12.012.

(131) Beenken, W.; Presselt, M.; Ngo, T. H.; Dehaen, W.; Maes, W.; Kruk, M. Molecular Structures and Absorption Spectra Assignment of Corrole NH Tautomers. *J. Phys. Chem. A* **2014**, *118* (5), 862–871. https://doi.org/10.1021/jp411033h.

(132) Eckert, F.; Leito, I.; Kaljurand, I.; Kütt, A.; Klamt, A.; Diedenhofen, M. Prediction of Acidity in Acetonitrile Solution with COSMO-RS. *J. Comput. Chem.* **2009**, *30* (5), 799–810. https://doi.org/10.1002/jcc.21103.

(133) McCarthy, B. D.; Donley, C. L.; Dempsey, J. L. Electrode Initiated Proton-Coupled Electron Transfer to Promote Degradation of a Nickel(II) Coordination Complex. *Chem. Sci.* **2015**, *6* (5), 2827–2834. https://doi.org/10.1039/C5SC00476D.

(134) Lee, K. J.; McCarthy, B. D.; Dempsey, J. L. On Decomposition, Degradation, and Voltammetric Deviation: The Electrochemist's Field Guide to Identifying Precatalyst Transformation. *Chem. Soc. Rev.* **2019**, *48* (11), 2927–2945. https://doi.org/10.1039/C8CS00851E.

(135) Felton, G. A. N.; Glass, R. S.; Lichtenberger, D. L.; Evans, D. H. Iron-Only Hydrogenase Mimics. Thermodynamic Aspects of the Use of Electrochemistry to Evaluate Catalytic Efficiency for Hydrogen Generation. *Inorg. Chem.* **2006**, *45* (23), 9181–9184. https://doi.org/10.1021/ic060984e.

(136) Capon, J.-F.; Gloaguen, F.; Schollhammer, P.; Talarmin, J. Activation of Proton by the Two-Electron Reduction of a Di-Iron Organometallic Complex. *J. Electroanal. Chem.* **2006**, *595* (1), 47–52. https://doi.org/10.1016/j.jelechem.2006.06.005.

(137) Arafa, W. A. A.; Kärkäs, M. D.; Lee, B.-L.; Åkermark, T.; Liao, R.-Z.; Berends, H.-M.; Messinger, J.; Siegbahn, P. E. M.; Åkermark, B. Dinuclear Manganese Complexes for Water Oxidation: Evaluation of Electronic Effects and Catalytic Activity. *Phys. Chem. Chem. Phys.* **2014**, *16* (24), 11950–11964. https://doi.org/10.1039/C3CP54800G.

(138) Howard, J. B.; Rees, D. C. Structural Basis of Biological Nitrogen Fixation. *Chem. Rev.* **1996**, *96* (7), 2965–2982. https://doi.org/10.1021/cr9500545.

(139) Howard, J. B.; Rees, D. C. How Many Metals Does It Take to Fix N2? A Mechanistic Overview of Biological Nitrogen Fixation. *Proc. Natl. Acad. Sci.* **2006**, *103* (46), 17088–17093. https://doi.org/10.1073/pnas.0603978103.

(140) Einsle, O.; Tezcan, F. A.; Andrade, S. L. A.; Schmid, B.; Yoshida, M.; Howard, J. B.; Rees, D. C. Nitrogenase MoFe-Protein at 1.16 Å Resolution: A Central Ligand in the FeMo-Cofactor. *Science* **2002**, *297* (5587), 1696–1700. https://doi.org/10.1126/science.1073877.

(141) Creutz, C.; Taube, H. Direct Approach to Measuring the Franck-Condon Barrier to Electron Transfer between Metal Ions. *J. Am. Chem. Soc.* **1969**, *91* (14), 3988–3989. https://doi.org/10.1021/ja01042a072.

(142) Fuerholz, U.; Joss, S.; Buergi, H. B.; Ludi, A. The Creutz-Taube Complex Revisited: Crystallographic Study of the Electron-Transfer Series (.Mu.-Pyrazine)Decaamminediruthenium ([(NH3)5Ru(Pyz)Ru(NH3)5]N+ (n = 4-6)). *Inorg. Chem.* **1985**, *24* (6), 943–948. https://doi.org/10.1021/ic00200a028.

(143) Day, P.; Hush, N. S.; Clark, R. J. H. Mixed Valence: Origins and Developments. *Philos. Trans. R. Soc. Math. Phys. Eng. Sci.* **2008**, *366* (1862), 5–14. https://doi.org/10.1098/rsta.2007.2135.

(144) Robin, M. B.; Day, P. Mixed Valence Chemistry-A Survey and Classification. In *Advances in Inorganic Chemistry and Radiochemistry*; Emeléus, H. J., Sharpe, A. G., Eds.; Academic Press, 1968; Vol. 10, pp 247–422. https://doi.org/10.1016/S0065-2792(08)60179-X.

(145) Kaim, W.; Klein, A.; Glöckle, M. Exploration of Mixed-Valence Chemistry: Inventing New Analogues of the Creutz-Taube Ion. *Acc. Chem. Res.* **2000**, *33* (11), 755–763. https://doi.org/10.1021/ar960067k.

(146) Zanello, P. *Inorganic Electrochemistry*; 2003. https://doi.org/10.1039/9781847551146.

(147) Cotton, F. A.; Curtis, N. F.; Harris, C. B.; Johnson, B. F. G.; Lippard, S. J.; Mague, J. T.; Robinson, W. R.; Wood, J. S. Mononuclear and Polynuclear Chemistry of Rhenium (III): Its Pronounced Homophilicity. *Science* **1964**, *145* (3638), 1305–1307. https://doi.org/10.1126/science.145.3638.1305.

(148) Cotton, F. A. Metal-Metal Bonding in [Re2X8]2- Ions and Other Metal Atom Clusters. *Inorg. Chem.* **1965**, *4* (3), 334–336. https://doi.org/10.1021/ic50025a016.

(149) Cotton, F. A.; Harris, C. B. The Crystal and Molecular Structure of Dipotassium Octachlorodirhenate(III) Dihydrate, K2[Re2Cl8]2H2O. *Inorg. Chem.* **1965**, *4* (3), 330–333. https://doi.org/10.1021/ic50025a015.

(150) *Multiple Bonds between Metal Atoms*, 3rd ed.; Cotton, F. A., Murillo, C. A., Walton, R. A., Eds.; Springer-Verlag: New York, 2005.

(151) Cotton, F. A.; Donahue, J. P.; Murillo, C. A. Polyunsaturated Dicarboxylate Tethers Connecting Dimolybdenum Redox and Chromophoric Centers: Syntheses, Structures, and Electrochemistry. *J. Am. Chem. Soc.* **2003**, *125* (18), 5436–5450. https://doi.org/10.1021/ja029101i.

(152) Cotton, F. A.; Liu, C. Y.; Murillo, C. A.; Zhao, Q. Electronic Localization versus Delocalization Determined by the Binding of the Linker in an Isomer Pair. *Inorg. Chem.* **2007**, *46* (7), 2604–2611. https://doi.org/10.1021/ic0622252.

(153) Chisholm, M. H.; Patmore, N. J. Studies of Electronic Coupling and Mixed Valency in Metal−Metal Quadruply Bonded Complexes Linked by Dicarboxylate and Closely

Related Ligands. *Acc. Chem. Res.* **2007**, *40* (1), 19–27. https://doi.org/10.1021/ar068100i.

(154) Xiao, X.; Liu, C. Y.; He, Q.; Han, M. J.; Meng, M.; Lei, H.; Lu, X. Control of the Charge Distribution and Modulation of the Class II–III Transition in Weakly Coupled Mo2–Mo2 Systems. *Inorg. Chem.* **2013**, *52* (21), 12624–12633. https://doi.org/10.1021/ic4017855.

(155) Yu, W. Y.; Meng, M.; Lei, H.; He, X. D.; Liu, C. Y. Optical Determination of Electron Transfer Dynamics and Kinetics for Asymmetrical [Mo2]–Ph–[Mo2] Systems. *J. Phys. Chem. C* **2016**, *120* (23), 12411–12422. https://doi.org/10.1021/acs.jpcc.6b03792.

(156) Bradley, W.; Wright, I. 129. Metal Derivatives of NN′-Diarylamidines. *J. Chem. Soc. Resumed* **1956**, *0* (0), 640–648. https://doi.org/10.1039/JR9560000640.

(157) Cotton, F. A.; Liu, C. Y.; Murillo, C. A.; Villagrán, D.; Wang, X. Modifying Electronic Communication in Dimolybdenum Units by Linkage Isomers of Bridged Oxamidate Dianions. *J. Am. Chem. Soc.* **2003**, *125* (44), 13564–13575. https://doi.org/10.1021/ja036884e.

(158) Cotton, F. A.; Liu, C. Y.; Murillo, C. A. Systematic Preparation of Mo24+ Building Blocks for Supramolecular Assemblies. *Inorg. Chem.* **2004**, *43* (7), 2267–2276. https://doi.org/10.1021/ic035433s.

(159) Manthey, M.; Pyne, S.; Truscott, R. Addition of Aliphatic and Aromatic Amines to Catechol in Aqueous Solution Under Oxidizing Conditions. *Aust. J. Chem.* **1989**, *42* (3), 365–373.

(160) Suarez Vallejo, C. Design and Regioselective Synthesis of Fullerene Derivatives for Metal-Organic Hybrid Architectures. M.S., The University of Texas at El Paso, United States -- Texas, 2017.

(161) Dunning, Thom. H.; Hay, P. J. Gaussian Basis Sets for Molecular Calculations. In *Methods of Electronic Structure Theory*; Schaefer, H. F., Ed.; Modern Theoretical Chemistry; Springer US: Boston, MA, 1977; pp 1–27. https://doi.org/10.1007/978-1-4757-0887-5_1.

(162) Hay, P. J.; Wadt, W. R. Ab Initio Effective Core Potentials for Molecular Calculations. Potentials for the Transition Metal Atoms Sc to Hg. *J. Chem. Phys.* **1985**, *82* (1), 270–283. https://doi.org/10.1063/1.448799.

(163) Wadt, W. R.; Hay, P. J. Ab Initio Effective Core Potentials for Molecular Calculations. Potentials for Main Group Elements Na to Bi. *J. Chem. Phys.* **1985**, *82* (1), 284–298. https://doi.org/10.1063/1.448800.

(164) Hay, P. J.; Wadt, W. R. Ab Initio Effective Core Potentials for Molecular Calculations. Potentials for K to Au Including the Outermost Core Orbitals. *J. Chem. Phys.* **1985**, *82* (1), 299–310. https://doi.org/10.1063/1.448975.

(165) Bauernschmitt, R.; Ahlrichs, R. Treatment of Electronic Excitations within the Adiabatic Approximation of Time Dependent Density Functional Theory. *Chem. Phys. Lett.* **1996**, *256* (4), 454–464. https://doi.org/10.1016/0009-2614(96)00440-X.

(166) Casida, M. E.; Jamorski, C.; Casida, K. C.; Salahub, D. R. Molecular Excitation Energies to High-Lying Bound States from Time-Dependent Density-Functional Response Theory: Characterization and Correction of the Time-Dependent Local Density Approximation Ionization Threshold. *J. Chem. Phys.* **1998**, *108* (11), 4439–4449. https://doi.org/10.1063/1.475855.

(167) Stratmann, R. E.; Scuseria, G. E.; Frisch, M. J. An Efficient Implementation of Time-Dependent Density-Functional Theory for the Calculation of Excitation Energies of

Large Molecules. *J. Chem. Phys.* **1998**, *109* (19), 8218–8224. https://doi.org/10.1063/1.477483.

(168) Van Caillie, C.; Amos, R. D. Geometric Derivatives of Excitation Energies Using SCF and DFT. *Chem. Phys. Lett.* **1999**, *308* (3), 249–255. https://doi.org/10.1016/S0009-2614(99)00646-6.

(169) Van Caillie, C.; Amos, R. D. Geometric Derivatives of Density Functional Theory Excitation Energies Using Gradient-Corrected Functionals. *Chem. Phys. Lett.* **2000**, *317* (1), 159–164. https://doi.org/10.1016/S0009-2614(99)01346-9.

(170) Scalmani, G.; Frisch, M. J.; Mennucci, B.; Tomasi, J.; Cammi, R.; Barone, V. Geometries and Properties of Excited States in the Gas Phase and in Solution: Theory and Application of a Time-Dependent Density Functional Theory Polarizable Continuum Model. *J. Chem. Phys.* **2006**, *124* (9), 094107. https://doi.org/10.1063/1.2173258.

(171) Furche, F.; Ahlrichs, R. Adiabatic Time-Dependent Density Functional Methods for Excited State Properties. *J. Chem. Phys.* **2002**, *117* (16), 7433–7447. https://doi.org/10.1063/1.1508368.

(172) Cheng, T.; Meng, M.; Lei, H.; Liu, C. Y. Perturbation of the Charge Density between Two Bridged Mo2 Centers: The Remote Substituent Effects. *Inorg. Chem.* **2014**, *53* (17), 9213–9221. https://doi.org/10.1021/ic501313q.

(173) Cotton, F. A.; Donahue, J. P.; Lin, C.; Murillo, C. A. The Simplest Supramolecular Complexes Containing Pairs of Mo2(Formamidinate)3 Units Linked with Various Dicarboxylates: Preparative Methods, Structures, and Electrochemistry. *Inorg. Chem.* **2001**, *40* (6), 1234–1244. https://doi.org/10.1021/ic000934o.

(174) Cotton, F. A.; Murillo, C. A.; Villagrán, D.; Yu, R. Uniquely Strong Electronic Communication between [Mo2] Units Linked by Dioxolene Dianions. *J. Am. Chem. Soc.* **2006**, *128* (10), 3281–3290. https://doi.org/10.1021/ja0582962.

(175) Cotton, F. A.; Li, Z.; Liu, C. Y.; Murillo, C. A. Molecular Pairs and A Propeller Containing Quadruply Bonded Dimolybdenum Units Linked by Polyamidate Ligands. *Inorg. Chem.* **2006**, *45* (24), 9765–9770. https://doi.org/10.1021/ic0614723.

(176) Cotton, F. A.; Daniels, L. M.; Donahue, J. P.; Liu, C. Y.; Murillo, C. A. The First Designed Syntheses of Bis-Dimetal Molecules in Which the Bridges Are Diamidate Ligands. *Inorg. Chem.* **2002**, *41* (6), 1354–1356. https://doi.org/10.1021/ic025503f.

(177) Lei, H.; Xiao, X.; Meng, M.; Cheng, T.; Shu, Y.; Tan, Y. N.; Liu, C. Y. Dimolybdenum Dimers Spaced by Phenylene Groups: The Experimental Models for Study of Electronic Coupling. *Inorganica Chim. Acta* **2015**, *424*, 63–74. https://doi.org/10.1016/j.ica.2014.09.039.

(178) Heinze, K.; Huttner, G.; Walter, O. Metal–Metal Interactions in Dinuclear (Triphos)Cobalt Complexes Exhibiting Mixed Valency. *Eur. J. Inorg. Chem.* **1999**, *1999* (4), 593–600. https://doi.org/10.1002/(SICI)1099-0682(199904)1999:4<593::AID-EJIC593>3.0.CO;2-U.

(179) Cotton, F. A.; Jin, J.-Y.; Li, Z.; Murillo, C. A.; Reibenspies, J. H. Exceptionally Strong Electronic Coupling between [Mo2] Units Linked by Substituted Dianionic Quinones. *Chem. Commun.* **2007**, No. 2, 211–213. https://doi.org/10.1039/B710804D.

(180) Mallick, S.; Cheng, T.; Chen, L.; Meng, M.; Zhang, Y. Y.; Liu, C. Y. A Study of Asymmetrical Mixed-Valent Mo2–Mo2 Complexes in the Class III Regime. *Dalton Trans.* **2017**, *46* (17), 5711–5723. https://doi.org/10.1039/C6DT04915J.

(181) Chisholm, M. H.; Feil, F.; Hadad, C. M.; Patmore, N. J. Electronically Coupled MM Quadruply-Bonded Complexes (M = Mo or W) Employing Functionalized Terephthalate Bridges: Toward Molecular Rheostats and Switches. *J. Am. Chem. Soc.* **2005**, *127* (51), 18150–18158. https://doi.org/10.1021/ja0550982.

(182) Cotton, F. A.; Liu, C. Y.; Murillo, C. A.; Villagrán, D.; Wang, X. Strong Electronic Coupling between Dimolybdenum Units Linked by the N,N‘-Dimethyloxamidate Anion in a Molecule Having a Heteronaphthalene-like Structure. *J. Am. Chem. Soc.* **2004**, *126* (45), 14822–14831. https://doi.org/10.1021/ja046775f.

(183) Cotton, F. A.; Donahue, J. P.; Huang, P.; Murillo, C. A.; Villagrán, D. Strong Electronic Coupling between Mo2n+ Units: The Oxidation Products of [Mo2(DAniF)3]2(M−H)2 and Mo2(DAniF)4. *Z. Für Anorg. Allg. Chem.* **2005**, *631* (13–14), 2606–2612. https://doi.org/10.1002/zaac.200500135.

(184) Cotton, F. A.; Li, Z.; Liu, C. Y.; Murillo, C. A. Modulating Electronic Coupling Using O- and S-Donor Linkers. *Inorg. Chem.* **2007**, *46* (19), 7840–7847. https://doi.org/10.1021/ic700932s.

(185) Chen, L.; Mallick, S.; Tan, Y. N.; Meng, M.; Liu, C. Y. Charge Transfer Properties of Triarylamine Integrated Dimolybdenum Dyads. *Inorg. Chem.* **2017**, *56* (13), 7470–7481. https://doi.org/10.1021/acs.inorgchem.7b00913.

(186) Yao, C.-J.; Nie, H.-J.; Yang, W.-W.; Shao, J.-Y.; Yao, J.; Zhong, Y.-W. Strongly Coupled Cyclometalated Ruthenium–Triarylamine Hybrids: Tuning Electrochemical Properties, Intervalence Charge Transfer, and Spin Distribution by Substituent Effects. *Chem. – Eur. J.* **2014**, *20* (52), 17466–17477. https://doi.org/10.1002/chem.201404549.

(187) Nie, H.-J.; Shao, J.-Y.; Yao, C.-J.; Zhong, Y.-W. Organic–Inorganic Mixed-Valence Systems with Strongly-Coupled Triarylamine and Cyclometalated Osmium. *Chem. Commun.* **2014**, *50* (70), 10082–10085. https://doi.org/10.1039/C4CC04268A.

(188) Sukegawa, J.; Schubert, C.; Zhu, X.; Tsuji, H.; Guldi, D. M.; Nakamura, E. Electron Transfer through Rigid Organic Molecular Wires Enhanced by Electronic and Electron–Vibration Coupling. *Nat. Chem.* **2014**, *6* (10), 899–905. https://doi.org/10.1038/nchem.2026.

(189) Li, G.; Zhu, R.; Yang, Y. Polymer Solar Cells. *Nat. Photonics* **2012**, *6* (3), 153–161. https://doi.org/10.1038/nphoton.2012.11.

(190) Buntar, V.; Sauerzopf, F. M.; Weber, H. W.; Halushka, M.; Kuzmany, H. Mixed State Parameters of Single Crystalline ${\mathrm{Rb}}_{3}{\mathrm{C}}_{60}$ Fullerene Superconductors. *Phys. Rev. B* **2005**, *72* (2), 024521. https://doi.org/10.1103/PhysRevB.72.024521.

(191) Torre, G. de la; Giacalone, F.; Segura, J. L.; Martín, N.; Guldi, D. M. Electronic Communication through π-Conjugated Wires in Covalently Linked Porphyrin/C60 Ensembles. *Chem. – Eur. J.* **2005**, *11* (4), 1267–1280. https://doi.org/10.1002/chem.200400604.

(192) Ventra, M.; Evoy, S.; Heflin, J. R. *Introduction to Nanoscale Science and Technology*; Springer Science & Business Media, 2006.

(193) Xie, Q.; Perez-Cordero, E.; Echegoyen, L. Electrochemical Detection of C606- and C706-: Enhanced Stability of Fullerides in Solution. *J. Am. Chem. Soc.* **1992**, *114* (10), 3978–3980. https://doi.org/10.1021/ja00036a056.

(194) Orlandi, G.; Negri, F. Electronic States and Transitions in C60 and C70 Fullerenes. *Photochem. Photobiol. Sci.* **2002**, *1* (5), 289–308. https://doi.org/10.1039/B200178K.

(195) Liu, C. Y.; Xiao, X.; Meng, M.; Zhang, Y.; Han, M. J. Spectroscopic Study of δ Electron Transfer between Two Covalently Bonded Dimolybdenum Units via a Conjugated Bridge: Adequate Complex Models to Test the Existing Theories for Electronic Coupling. *J. Phys. Chem. C* **2013**, *117* (39), 19859–19865. https://doi.org/10.1021/jp406261w.

(196) Xiao, X.; Meng, M.; Lei, H.; Liu, C. Y. Electronic Coupling and Electron Transfer between Two Dimolybdenum Units Spaced by a Biphenylene Group. *J. Phys. Chem. C* **2014**, *118* (16), 8308–8315. https://doi.org/10.1021/jp502163a.

(197) Kang, M. T.; Meng, M.; Tan, Y. N.; Cheng, T.; Liu, C. Y. Tuning the Electronic Coupling and Electron Transfer in Mo2 Donor–Acceptor Systems by Variation of the Bridge Conformation. *Chem. – Eur. J.* **2016**, *22* (9), 3115–3126. https://doi.org/10.1002/chem.201504033.

(198) Barybin, M. V.; Chisholm, M. H.; Patmore, N. J.; Robinson, R. E.; Singh, N. Concerning the Molecular and Electronic Structure of a Tungsten-Tungsten Quadruply Bonded Complex Supported by Two 6-Carboethoxy-2-Carboxylatoazulene Ligands. *Chem. Commun.* **2007**, No. 35, 3652–3654. https://doi.org/10.1039/B708746B.

(199) Alberding, B. G.; Barybin, M. V.; Chisholm, M. H.; Gustafson, T. L.; Reed, C. R.; Robinson, R. E.; Patmore, N. J.; Singh, N.; Turro, C. Molecular, Electronic Structure and Spectroscopic Properties of MM Quadruply Bonded Units Supported by Trans-6-Carboethoxy-2-Carboxylatoazulene Ligands. *Dalton Trans.* **2010**, *39* (8), 1979–1984. https://doi.org/10.1039/B919282D.

(200) Alberding, B. G.; Chisholm, M. H.; Chou, Y.-H.; Ghosh, Y.; Gustafson, T. L.; Liu, Y.; Turro, C. 2-Thienylcarboxylato and 2-Thienylthiocarboxylato Ligands Bonded to MM Quadruple Bonds (M = Mo or W): A Comparison of Ground State, Spectroscopic and Photoexcited State Properties. *Inorg. Chem.* **2009**, *48* (23), 11187–11195. https://doi.org/10.1021/ic901607u.

(201) Alberding, B. G.; Chisholm, M. H.; Gustafson, T. L.; Liu, Y.; Reed, C. R.; Turro, C. Photophysical Studies of Trans-Bis(Phenylethynyldiisopropylamidinato)Bis(Acetato)Dimetal Complexes Involving MM Quadruple Bonds Where M = Mo or W. *J. Phys. Chem. A* **2010**, *114* (48), 12675–12681. https://doi.org/10.1021/jp108544v.

(202) Brown, D. J.; Chisholm, M. H.; Gallucci, J. C. Amidinate–Carboxylate Complexes of Dimolybdenum and Ditungsten: M2(O2CR)2((NiPr)2CR′)2. Preparations, Molecular and Electronic Structures and Reactions. *Dalton Trans.* **2008**, No. 12, 1615–1624. https://doi.org/10.1039/B715258B.

(203) Alberding, B. G.; Chisholm, M. H.; Gallucci, J. C.; Ghosh, Y.; Gustafson, T. L. Electron Delocalization in the S1 and T1 Metal-to-Ligand Charge Transfer States of Trans-Substituted Metal Quadruply Bonded Complexes. *Proc. Natl. Acad. Sci.* **2011**, *108* (20), 8152–8156. https://doi.org/10.1073/pnas.1103082108.

(204) Cotton, F. A.; Daniels, L. M.; Hillard, E. A.; Murillo, C. A. The Lengths of Molybdenum to Molybdenum Quadruple Bonds: Correlations, Explanations, and Corrections. *Inorg. Chem.* **2002**, *41* (9), 2466–2470. https://doi.org/10.1021/ic025508c.

(205) Lawton, D.; Mason, R. The Molecular Structure of Molybdenum(II) Acetate. *J. Am. Chem. Soc.* **1965**, *87* (4), 921–922. https://doi.org/10.1021/ja01082a046.

(206) Brown-Xu, S. E.; Chisholm, M. H.; Durr, C. B.; Lewis, S. A.; Spilker, T. F.; Young, P. J. Molybdenum–Molybdenum Quadruple Bonds Supported by 9,10-Anthraquinone

Carboxylate Ligands. Molecular, Electronic, Ground State and Unusual Photoexcited State Properties. *Chem. Sci.* **2014**, *5* (7), 2657–2666. https://doi.org/10.1039/C4SC00341A.

(207) Cotton, F. A.; Gruhn, N. E.; Gu, J.; Huang, P.; Lichtenberger, D. L.; Murillo, C. A.; Dorn, L. O. V.; Wilkinson, C. C. Closed-Shell Molecules That Ionize More Readily Than Cesium. *Science* **2002**, *298* (5600), 1971–1974. https://doi.org/10.1126/science.1078721.

(208) Lin, C.; Protasiewicz, J. D.; Smith, E. T.; Ren, T. Redox Tuning of the Dimolybdenum Compounds at the Ligand Periphery: A Direct Correlation with the Hammett Constant of the Substituents. *J. Chem. Soc. Chem. Commun.* **1995**, No. 22, 2257–2258. https://doi.org/10.1039/C39950002257.

(209) Cotton, F. A.; Gu, J.; Murillo, C. A.; Timmons, D. J. The First Dinuclear Complex of Palladium(III). *J. Am. Chem. Soc.* **1998**, *120* (50), 13280–13281. https://doi.org/10.1021/ja9832313.

(210) Cotton, F. A.; Murillo, C. A.; Timmons, D. J.; Murillo, C. A. First Paddlewheel Complex with a Doubly-Bonded Ir 2 6+ Core. *Chem. Commun.* **1999**, *0* (15), 1427–1428. https://doi.org/10.1039/A904698D.

(211) Chiarella, G. M.; Cotton, F. A.; Murillo, C. A. An Uncommon Highly Oxidized Multiple Bonded Re28+ Species. *Chem. Commun.* **2011**, *47* (31), 8940–8942. https://doi.org/10.1039/C1CC13193A.

(212) Cotton, F. A.; Matonic, J. H.; Murillo, C. A. A New Type of Divalent Niobium Compound: The First Nb−Nb Triple Bond in a Tetragonal Lantern Environment. *J. Am. Chem. Soc.* **1997**, *119* (33), 7889–7890. https://doi.org/10.1021/ja9715152.

(213) Cotton, F. A.; Daniels, L. M.; Murillo, C. A.; Timmons, D. J.; Wilkinson, C. C. The Extraordinary Ability of Guanidinate Derivatives to Stabilize Higher Oxidation Numbers in Dimetal Units by Modification of Redox Potentials: Structures of Mo25+ and Mo26+ Compounds. *J. Am. Chem. Soc.* **2002**, *124* (31), 9249–9256. https://doi.org/10.1021/ja0266464.

(214) Cotton, F. A.; Donahue, J. P.; Gruhn, N. E.; Lichtenberger, D. L.; Murillo, C. A.; Timmons, D. J.; Van Dorn, L. O.; Villagrán, D.; Wang, X. Facilitating Access to the Most Easily Ionized Molecule: An Improved Synthesis of the Key Intermediate, W2(Hpp)4Cl2, and Related Compounds. *Inorg. Chem.* **2006**, *45* (1), 201–213. https://doi.org/10.1021/ic0515709.

(215) Chiarella, G. M.; Cotton, F. A.; Dalal, N. S.; Murillo, C. A.; Wang, Z.; Young, M. D. Direct Evidence from Electron Paramagnetic Resonance for Additional Configurations in Uncommon Paddlewheel Re27+ Units Surrounded by an Unsymmetrical Bicyclic Guanidinate. *Inorg. Chem.* **2012**, *51* (9), 5257–5263. https://doi.org/10.1021/ic300169f.

(216) Cotton, F. A.; Dalal, N. S.; Huang, P.; Murillo, C. A.; Stowe, A. C.; Wang, X. The First Structurally Confirmed Paddlewheel Compound with an M27+ Core: [Os2(Hpp)4Cl2](PF6). *Inorg. Chem.* **2003**, *42* (3), 670–672. https://doi.org/10.1021/ic026250t.

(217) Bear, J. L.; Li, Y.; Han, B.; Kadish, K. M. Synthesis, Molecular Structure, and Electrochemistry of a Paramagnetic Diruthenium(III) Complex. Characterization of Ru2(Hpp)4Cl2, Where Hpp Is the 1,3,4,6,7,8- Hexahydro-2H-Pyrimido[1,2-a]Pyrimidinate Ion. *Inorg. Chem.* **1996**, *35* (5), 1395–1398. https://doi.org/10.1021/ic950956o.

(218) Novak, I.; Wei, X.; Chin, W. S. Electronic Structures of Very Strong, Neutral Bases. *J. Phys. Chem. A* **2001**, *105* (10), 1783–1788. https://doi.org/10.1021/jp003430k.

(219) Bailey, P. J.; Pace, S. The Coordination Chemistry of Guanidines and Guanidinates. *Coord. Chem. Rev.* **2001**, *214* (1), 91–141. https://doi.org/10.1016/S0010-8545(00)00389-1.

(220) Cotton, F. A.; Donahue, J. P.; Lichtenberger, D. L.; Murillo, C. A.; Villagrán, D. Expeditious Access to the Most Easily Ionized Closed-Shell Molecule, W2(Hpp)4. *J. Am. Chem. Soc.* **2005**, *127* (31), 10808–10809. https://doi.org/10.1021/ja0535458.

(221) Chiarella, G. M.; Cotton, F. A.; Durivage, J. C.; Lichtenberger, D. L.; Murillo, C. A. Solubilizing the Most Easily Ionized Molecules and Generating Powerful Reducing Agents. *J. Am. Chem. Soc.* **2013**, *135* (47), 17889–17896. https://doi.org/10.1021/ja408291k.

(222) Berry, J. F.; Bothe, E.; Cotton, F. A.; Ibragimov, S. A.; Murillo, C. A.; Villagrán, D.; Wang, X. Metal−Metal Bonding in Mixed Valence Ni25+ Complexes and Spectroscopic Evidence for a Ni26+ Species. *Inorg. Chem.* **2006**, *45* (11), 4396–4406. https://doi.org/10.1021/ic060125q.

(223) Albert Cotton, F.; A. Murillo, C.; Wang, X.; C. Wilkinson, C. Increasing the Solubility of Strong Reducing Agents Containing Mo 2 4+ Units and Alkyl-Substituted Guanidinate Ligands. *Dalton Trans.* **2007**, *0* (35), 3943–3951. https://doi.org/10.1039/B707201E.

(224) Cotton, F. A.; Murillo, C. A.; Wang, X.; Wilkinson, C. C. Homologues of the Easily Ionized Compound Mo2(Hpp)4 Containing Smaller Bicyclic Guanidinates. *Inorg. Chem.* **2006**, *45* (14), 5493–5500. https://doi.org/10.1021/ic060449e.

(225) Chiarella, G. M.; Cotton, F. A.; Murillo, C. A.; Young, M. D. Tuning the Electrochemistry of Re26+ Species with Divergent Bicyclic Guanidinate Ligands and by Modification of Axial π Interactions. *Inorg. Chem.* **2011**, *50* (4), 1258–1264. https://doi.org/10.1021/ic101890p.

(226) Chisholm, M. H.; Cotton, F. A.; Daniels, L. M.; Folting, K.; Huffman, J. C.; Iyer, S. S.; Lin, C.; Macintosh, A. M.; Murillo, C. A. Compounds in Which the Mo24+ Unit Is Embraced by One, Two or Three Formamidinate Ligands Together with Acetonitrile Ligands. *J. Chem. Soc. Dalton Trans.* **1999**, *0* (9), 1387–1392. https://doi.org/10.1039/A900389D.

(227) Cotton, F. A.; Daniels, L. M.; Murillo, C. A.; Slaton, J. G. A Pseudo-Jahn−Teller Distortion in an Mo2(M2-O)2 Ring Having the Shortest MoIV−MoIV Double Bond. *J. Am. Chem. Soc.* **2002**, *124* (12), 2878–2879. https://doi.org/10.1021/ja025713r.

(228) Lin, C.; Protasiewicz, J. D.; Smith, E. T.; Ren, T. Linear Free Energy Relationships in Dinuclear Compounds. 2. Inductive Redox Tuning via Remote Substituents in Quadruply Bonded Dimolybdenum Compounds. *Inorg. Chem.* **1996**, *35* (22), 6422–6428. https://doi.org/10.1021/ic960555o.

(229) Dunning, T. H. Gaussian Basis Sets for Use in Correlated Molecular Calculations. I. The Atoms Boron through Neon and Hydrogen. *J. Chem. Phys.* **1989**, *90* (2), 1007–1023. https://doi.org/10.1063/1.456153.

(230) Kendall, R. A.; Dunning, T. H.; Harrison, R. J. Electron Affinities of the First-row Atoms Revisited. Systematic Basis Sets and Wave Functions. *J. Chem. Phys.* **1992**, *96* (9), 6796–6806. https://doi.org/10.1063/1.462569.

(231) Woon, D. E.; Dunning, T. H. Gaussian Basis Sets for Use in Correlated Molecular Calculations. III. The Atoms Aluminum through Argon. *J. Chem. Phys.* **1993**, *98* (2), 1358–1371. https://doi.org/10.1063/1.464303.

(232) Peterson, K. A.; Woon, D. E.; Dunning, T. H. Benchmark Calculations with Correlated Molecular Wave Functions. IV. The Classical Barrier Height of the H+H2→H2+H Reaction. *J. Chem. Phys.* **1994**, *100* (10), 7410–7415. https://doi.org/10.1063/1.466884.

(233) Wilson, A. K.; van Mourik, T.; Dunning, T. H. Gaussian Basis Sets for Use in Correlated Molecular Calculations. VI. Sextuple Zeta Correlation Consistent Basis Sets for Boron through Neon. *J. Mol. Struct. THEOCHEM* **1996**, *388*, 339–349. https://doi.org/10.1016/S0166-1280(96)80048-0.

(234) Tanaka, S.; Mashima, K. Unique Stepwise Substitution Reaction of a Mono(Guanidinate)Tetraplatinum Complex with Amidines , Giving Mono(Amidinate)Tetraplatinum Complexes through Mixed- Ligand Intermediate Complexes. *Dalton Trans.* **2013**, *42* (8), 2831–2840. https://doi.org/10.1039/C2DT32136J.

(235) Chifotides, H. T.; Catalan, K. V.; Dunbar, K. R. Dirhodium Formamidinate Compounds with Bidentate Nitrogen Chelating Ligands. *Inorg. Chem.* **2003**, *42* (26), 8739–8747. https://doi.org/10.1021/ic034737b.

(236) Cotton, F. A.; Mester, Z. C.; Webb, T. R. Dimolybdenum Tetraacetate. *Acta Crystallogr. B* **1974**, *30* (11), 2768–2770. https://doi.org/10.1107/S0567740874008053.

(237) Cotton, F. A.; Lin, C.; Murillo, C. A. Maximum Communication between Coupled Oxidations of Dimetal Units. *J. Am. Chem. Soc.* **2001**, *123* (11), 2670–2671. https://doi.org/10.1021/ja004149m.

(238) Bailey, P. J.; Bone, S. F.; Mitchell, L. A.; Parsons, S.; Taylor, K. J.; Yellowlees, L. J. A New Bridging Ligand for the [Mo2]4+ Dimer: Syntheses and X-Ray Crystal Structures of the Redox Pair [Mo2{μ-H2-(NPh)2CNHPh}4]0/+. *Inorg. Chem.* **1997**, *36* (5), 867–871. https://doi.org/10.1021/ic960712j.

(239) Cai, X.-M.; Zimmermann, T. K.; Pöthig, A.; Kühn, F. E. Synthesis and Electrochemical Properties of Cis- and Trans-[Mo2(O2C-Fc)2(DArF)2] (O2C-Fc = Ferrocenecarboxylate; DArF = N,N′-Diarylformamidinate). *Inorg. Chem.* **2015**, *54* (13), 6631–6640. https://doi.org/10.1021/acs.inorgchem.5b00964.

(240) Cotton, F. A.; Kühn, F. E. Syntheses and Structures of Di(Carboxylato)Hexakis(Acetonitrile)-Dimolybdenum(II) Bis(Tetrafluoroborate) and Trans-[Di(μ-Acetato)-Di(Acetonitrile)Di(μ-Bis(Diphenylphosphino)Amine)Dimolybdenum(II)] Bis(Tetrafluoroborate). *Inorganica Chim. Acta* **1996**, *252* (1), 257–264. https://doi.org/10.1016/S0020-1693(96)05320-0.

(241) Hicks, J.; P. Ring, S.; J. Patmore, N. Tuning the Electronic Structure of Mo–Mo Quadruple Bonds by N for O for S Substitution. *Dalton Trans.* **2012**, *41* (22), 6641–6650. https://doi.org/10.1039/C2DT30234A.

(242) Ketteringham, A. P.; Oldham, C. Raman Spectra of Multiply Bonded Metal Species. *J. Chem. Soc. Dalton Trans.* **1973**, *0* (10), 1067–1070. https://doi.org/10.1039/DT9730001067.

(243) Ventura, K.; Veleta, J. M.; Metta-Magaña, A.; Villagrán, D. Stabilization of a W26+ Bimetallic Complex Supported by Two N,N′,N″-Triphenylguanidinate Ligands. *Inorganica Chim. Acta* **2015**, *424*, 286–292. https://doi.org/10.1016/j.ica.2014.09.019.

(244) Minenkov, Y.; Singstad, Å.; Occhipinti, G.; Jensen, V. R. The Accuracy of DFT-Optimized Geometries of Functional Transition Metal Compounds: A Validation Study of Catalysts for Olefin Metathesis and Other Reactions in the Homogeneous Phase. *Dalton Trans.* **2012**, *41* (18), 5526–5541. https://doi.org/10.1039/C2DT12232D.

(245) Chisholm, M. H.; Gallucci, J.; Hadad, C. M.; Huffman, J. C.; Wilson, P. J. M2(Hpp)4Cl2 and M2(Hpp)4, Where M = Mo and W: Preparations, Structure and Bonding, and Comparisons with C2, C2H2, and C2Cl2 and the Hypothetical Molecules M2(Hpp)4(H)2. *J. Am. Chem. Soc.* **2003**, *125* (51), 16040–16049. https://doi.org/10.1021/ja0301065.

(246) Acho, J. A.; Ren, T.; Yun, J. W.; Lippard, S. J. Dimolybdenum(II) Calixarene Complexes: Synthesis, Structure, Raman Spectroscopy, and Bonding. *Inorg. Chem.* **1995**, *34* (21), 5226–5233. https://doi.org/10.1021/ic00125a023.

(247) Bari, L. D.; Pescitelli, G.; Salvadori, P. Determination of Absolute Configuration of Acyclic 1,2-Diols with [Mo2(OAc)4], Part 2: New Structural Evidence toward a Rationale of the Method: What Remains of [Mo2(OAc)4] in DMSO Solution? *Chem. – Eur. J.* **2004**, *10* (5), 1205–1214. https://doi.org/10.1002/chem.200304883.

(248) Albert Cotton, F.; Timmons, D. J. New Multiply-Bonded Dimetal Compounds Containing Bridging 1,3,4,6,7,8-Hexahydro-2H-Pyrimido[1,2-a]Pyrimidinato Groups—I. The V24+, Cr24+ and Mo24+ Compounds and Some Salts of the Protonated Ligand. *Polyhedron* **1998**, *17* (1), 179–184. https://doi.org/10.1016/S0277-5387(97)00210-6.

(249) Thomas, M. B.; Jindasa, R. G. W.; Hu, Y.; Schmitz, B.; Wang, H.; D'Souza, F. Investigation of the Push–Pull Effects on β-Functionalized Zinc Porphyrin Coordinated to C60 Donor–Acceptor Conjugates. *Can. J. Chem.* **2018**, *96* (9), 881–889. https://doi.org/10.1139/cjc-2017-0416.

(250) Haruta, M.; Kobayashi, T.; Sano, H.; Yamada, N. Novel Gold Catalysts for the Oxidation of Carbon Monoxide at a Temperature Far Below 0 °C. *Chem. Lett.* **1987**, *16* (2), 405–408. https://doi.org/10.1246/cl.1987.405.

(251) Nkosi, B.; Coville, N. J.; Hutchings, G. J. Reactivation of a Supported Gold Catalyst for Acetylene Hydrochlorination. *J. Chem. Soc. Chem. Commun.* **1988**, No. 1, 71–72. https://doi.org/10.1039/C39880000071.

(252) Choudhary, T. V.; Sivadinarayana, C.; Chusuei, C. C.; Datye, A. K.; Fackler, J. P.; Goodman, D. W. CO Oxidation on Supported Nano-Au Catalysts Synthesized from a [Au6(PPh3)6](BF4)2 Complex. *J. Catal.* **2002**, *207* (2), 247–255. https://doi.org/10.1006/jcat.2002.3525.

(253) Grisel, R. J. H.; Kooyman, P. J.; Nieuwenhuys, B. E. Influence of the Preparation of Au/Al2O3 on CH4 Oxidation Activity. *J. Catal.* **2000**, *191* (2), 430–437. https://doi.org/10.1006/jcat.1999.2787.

(254) Salama, T. M.; Ohnishi, R.; Ichikawa, M. Studies of the Selective Reduction of Nitric Oxide by Carbon Monoxide in the Presence and Absence of Hydrogen over Au/NaY Catalysts. *J. Chem. Soc. Faraday Trans.* **1996**, *92* (2), 301–306. https://doi.org/10.1039/FT9969200301.

(255) Fackler, J. P. Forty-Five Years of Chemical Discovery Including a Golden Quarter-Century. *Inorg. Chem.* **2002**, *41* (26), 6959–6972. https://doi.org/10.1021/ic025734m.

(256) Mohamed, A. A.; Abdou, H. E.; Fackler, J. P. Coordination Chemistry of Gold(II) with Amidinate, Thiolate and Ylide Ligands. *Coord. Chem. Rev.* **2010**, *254* (11), 1253–1259. https://doi.org/10.1016/j.ccr.2009.10.017.

(257) Collman, J. *Principles and Applications of Organotransition Metal Chemistry*; Mill Valley, CA, University Science Books, 1987.

(258) Fackler, J. P. Metal-Metal Bond Formation in the Oxidative Addition to Dinuclear Gold(I) Species. Implications from Dinuclear and Trinuclear Gold Chemistry for the Oxidative Addition Process Generally. *Polyhedron* **1997**, *16* (1), 1–17. https://doi.org/10.1016/0277-5387(96)00190-8.

(259) Mohr. *Gold Chemistry: Applications and Future Directions in the Life Sciences*; John Wiley & Sons, 2009.

(260) Low, J. J.; Goddard, W. A. Theoretical Studies of Oxidative Addition and Reductive Elimination: Hydrogen + Diphosphineplatinum .Fwdarw. Dihydridodiphosphineplatinum. *J. Am. Chem. Soc.* **1984**, *106* (23), 6928–6937. https://doi.org/10.1021/ja00335a010.

(261) Pan, Q.-J.; Zhou, X.; Fu, H.-G.; Zhang, H.-X. Isovalent Gold(I), -(II), and -(III) and Mixed-Valent Gold(I)/Gold(III) Phosphorus Ylide Complexes. Combined Ab Initio and Density Functional Study of Electronic Structures and Spectroscopic Properties. *Organometallics* **2008**, *27* (11), 2474–2482. https://doi.org/10.1021/om701114z.

(262) Mohamed, A. A.; Mayer, A. P.; Abdou, H. E.; Irwin, M. D.; Pérez, L. M.; Fackler, J. P. Dinuclear and Tetranuclear Gold−Nitrogen Complexes. Solvent Influences on Oxidation and Nuclearity of Gold Guanidinate Derivatives. *Inorg. Chem.* **2007**, *46* (26), 11165–11172. https://doi.org/10.1021/ic701399s.

(263) Abdou, H. E.; Mohamed, A. A.; Fackler, J. P. Synthesis and X-Ray Structures of Dinuclear and Trinuclear Gold(I) and Dinuclear Gold(II) Amidinate Complexes. *Inorg. Chem.* **2005**, *44* (2), 166–168. https://doi.org/10.1021/ic048855q.

(264) Grubbs, R. H. Homogeneous Catalysis: The Applications and Chemistry of Catalysis by Soluble Transition Metal Complexes. By G. W. Parshall and S. D. Ittel, Wiley, New York, 342 Pp., 1992, $50.00. *AIChE J.* **1993**, *39* (9), 1578–1578. https://doi.org/10.1002/aic.690390919.

(265) Kochi, J. K. Electron Transfer and Charge Transfer: Twin Themes in Unifying the Mechanisms of Organic and Organometallic Reactions. *Angew. Chem. Int. Ed. Engl.* **1988**, *27* (10), 1227–1266. https://doi.org/10.1002/anie.198812273.

(266) Aguirre-Etcheverry, P.; O'Hare, D. Electronic Communication through Unsaturated Hydrocarbon Bridges in Homobimetallic Organometallic Complexes. *Chem. Rev.* **2010**, *110* (8), 4839–4864. https://doi.org/10.1021/cr9003852.

(267) Chen, H. W.; Mallick, S.; Zou, S. F.; Meng, M.; Liu, C. Y. Mapping Bridge Conformational Effects on Electronic Coupling in Mo2–Mo2 Mixed-Valence Systems. *Inorg. Chem.* **2018**, *57* (12), 7455–7467. https://doi.org/10.1021/acs.inorgchem.8b01056.

(268) Shu, Y.; Lei, H.; Tan, Y. N.; Meng, M.; Zhang, X. C.; Liu, C. Y. Tuning the Electronic Coupling in Mo2–Mo2 Systems by Variation of the Coordinating Atoms of the Bridging Ligands. *Dalton Trans.* **2014**, *43* (39), 14756–14765. https://doi.org/10.1039/C4DT00786G.

(269) Demadis, K. D.; Hartshorn, C. M.; Meyer, T. J. The Localized-to-Delocalized Transition in Mixed-Valence Chemistry. *Chem. Rev.* **2001**, *101* (9), 2655–2686. https://doi.org/10.1021/cr990413m.

(270) Chisholm, M. H. Mixed Valency and Metal–Metal Quadruple Bonds. *Coord. Chem. Rev.* **2013**, *257* (9), 1576–1583. https://doi.org/10.1016/j.ccr.2012.10.021.

(271) Ito, T.; Hamaguchi, T.; Nagino, H.; Yamaguchi, T.; Washington, J.; Kubiak, C. P. Effects of Rapid Intramolecular Electron Transfer on Vibrational Spectra. *Science* **1997**, *277* (5326), 660–663. https://doi.org/10.1126/science.277.5326.660.

(272) Lin, C.; Protasiewicz, J. D.; Smith, E. T.; Ren, T. Linear Free Energy Relationships in Dinuclear Compounds. 2. Inductive Redox Tuning via Remote Substituents in Quadruply Bonded Dimolybdenum Compounds. *Inorg. Chem.* **1996**, *35* (22), 6422–6428. https://doi.org/10.1021/ic960555o.

(273) Ren, T. Substituent Effects in Dinuclear Paddlewheel Compounds: Electrochemical and Spectroscopic Investigations. *Coord. Chem. Rev.* **1998**, *175* (1), 43–58. https://doi.org/10.1016/S0010-8545(98)00202-1.

(274) Yeo, C. I.; Ooi, K. K.; Tiekink, E. R. T. Gold-Based Medicine: A Paradigm Shift in Anti-Cancer Therapy? *Mol. J. Synth. Chem. Nat. Prod. Chem.* **2018**, *23* (6). https://doi.org/10.3390/molecules23061410.

(275) Cayton, R. H.; Chisholm, M. H.; Huffman, J. C.; Lobkovsky, E. B. Metal-Metal Multiple Bonds in Ordered Assemblies. 1. Tetranuclear Molybdenum and Tungsten Carboxylates Involving Covalently Linked Metal-Metal Quadruple Bonds. Molecular Models for Subunits of One-Dimensional Stiff-Chain Polymers. *J. Am. Chem. Soc.* **1991**, *113* (23), 8709–8724. https://doi.org/10.1021/ja00023a019.

(276) Das, R. K.; Saha, B.; Rahaman, S. M. W.; Bera, J. K. Bimetallic Catalysis Involving Dipalladium(I) and Diruthenium(I) Complexes. *Chem. – Eur. J.* **2010**, *16* (48), 14459–14468. https://doi.org/10.1002/chem.201001960.

(277) Gray, T. G.; Veige, A. S.; Nocera, D. G. Cooperative Bimetallic Reactivity: Hydrogen Activation in Two-Electron Mixed-Valence Compounds. *J. Am. Chem. Soc.* **2004**, *126* (31), 9760–9768. https://doi.org/10.1021/ja0491432.

(278) Lin, C.; Protasiewicz, J. D.; Ren, T. Electronic Tuning Using Remote Substituents in Tetrakis(μ-N,N‘-Diarylformamidinato)Dinickel. Linear Free Energy Relationships in Dinuclear Compounds. 3. *Inorg. Chem.* **1996**, *35* (25), 7455–7458. https://doi.org/10.1021/ic960842s.

(279) Hariharan, P. C.; Pople, J. A. Accuracy of AH n Equilibrium Geometries by Single Determinant Molecular Orbital Theory. *Mol. Phys.* **1974**, *27* (1), 209–214. https://doi.org/10.1080/00268977400100171.

(280) Hariharan, P. C.; Pople, J. A. The Influence of Polarization Functions on Molecular Orbital Hydrogenation Energies. *Theor. Chim. Acta* **1973**, *28* (3), 213–222. https://doi.org/10.1007/BF00533485.

(281) Ditchfield, R.; Hehre, W. J.; Pople, J. A. Self-Consistent Molecular-Orbital Methods. IX. An Extended Gaussian-Type Basis for Molecular-Orbital Studies of Organic Molecules. *J. Chem. Phys.* **1971**, *54* (2), 724–728. https://doi.org/10.1063/1.1674902.

(282) Fenske, D.; Baum, G.; Zinn, A.; Dehnicke, K. Ag2[Ph – C(NSiMe3)2]2 Und Au2[Ph – C(NSiMe3)2]2: Amidinatokomplexe Mit Kurzen Metall–Metall-Abständen / Ag2[Ph—C(NSiMe3)2]2 and Au2[Ph—C(NSiMe3)2]2: Amidinato Complexes with Short Metal—Metal Distances. *Z. Für Naturforschung B* **2014**, *45* (9), 1273–1278. https://doi.org/10.1515/znb-1990-0909.

(283) Mazany, A. M.; Fackler, J. P. Isomeric Species of the Dinuclear Iodogold Complex [AuCH2P(S)PhI]2. Mixed-Valent Gold(I)/Gold(III) and Isovalent Gold(II)-Gold(II) Complexes with the Same Methylenethiophosphinate Ligand. *J. Am. Chem. Soc.* **1984**, *106* (3), 801–802. https://doi.org/10.1021/ja00315a062.

(284) Abdou, H. E.; Mohamed, A. A.; Fackler, J. P. Oxidative Addition of Small Molecules to a Dinuclear Au(I) Amidinate Complex, Au2[(2,6-Me2Ph)2N2CH]2. Syntheses and Characterization of Au(II) Amidinate Complexes Including One Which Possesses Au(II)−Oxygen Bonds. *Inorg. Chem.* **2007**, *46* (23), 9692–9699. https://doi.org/10.1021/ic700929e.

(285) Sipilä, J.; Nurmi, H.; Kaukonen, A. M.; Hirvonen, J.; Taskinen, J.; Yli-Kauhaluoma, J. A Modification of the Hammett Equation for Predicting Ionisation Constants of P-Vinyl Phenols. *Eur. J. Pharm. Sci.* **2005**, *25* (4), 417–425. https://doi.org/10.1016/j.ejps.2005.04.002.

(286) Lewis, M.; Bagwill, C.; Hardebeck, L. K. E.; Wireduaah, S. The Use of Hammett Constants to Understand the Non-Covalent Binding of Aromatics. *Comput. Struct. Biotechnol. J.* **2012**, *1*. https://doi.org/10.5936/csbj.201204004.

(287) Carlson-Day, K. M.; Eglin, J. L.; Lin, C.; Smith, L. T.; Staples, R. J.; Wipf, D. O. Synthesis of Multiply-Bonded Dichromium Complexes with a Variety of Formamidinate Ligands. *Polyhedron* **1999**, *18* (6), 817–824. https://doi.org/10.1016/S0277-5387(98)00362-3.

(288) Lichtenberger, D. L.; Lynn, M. A.; Chisholm, M. H. Quadruple Metal−Metal Bonds with Strong Donor Ligands. Ultraviolet Photoelectron Spectroscopy of M2(Form)4 (M = Cr, Mo, W; Form = N,N‘-Diphenylformamidinate). *J. Am. Chem. Soc.* **1999**, *121* (51), 12167–12176. https://doi.org/10.1021/ja993065e.

(289) Cotton, F. A.; Ren, T. Formamidinate Complexes of Dirhenium, Re2n+, Cores with n = 4, 5, and 6. *J. Am. Chem. Soc.* **1992**, *114* (7), 2495–2502. https://doi.org/10.1021/ja00033a025.

(290) Ren, T.; Lin, C.; Valente, E. J.; Zubkowski, J. D. The Influence of Remote Substituent in Tetrakis(μ-N,N′-Diarylformamidinato)–Dirhodium(II) Compounds. Part 7. Linear Free Energy Relationships in Dinuclear Compounds. *Inorganica Chim. Acta* **2000**, *297* (1), 283–290. https://doi.org/10.1016/S0020-1693(99)00317-5.

(291) Lin, C.; Ren, T.; Valente, E. J.; Zubkowski, J. D. Probing Diruthenium σ-Alkynyl Bonding Interactions via Substituent Effects. Linear Free Energy Relationships in Dinuclear Compounds VI. *J. Organomet. Chem.* **1999**, *579* (1), 114–121. https://doi.org/10.1016/S0022-328X(98)01211-X.

Appendix

Chapter 2: Hydrogen Gas Generation by a Metal-Free Fluorinated Porphyrin

Cartesian coordinates of the DFT optimized structure [1] in the gas phase

C	-1.13619700	-2.90862300	-0.00003100
C	-0.68764800	-4.27446000	-0.00009500
C	0.68806400	-4.27439300	-0.00009400
C	1.13648100	-2.90851300	-0.00007700
N	0.00010300	-2.11362300	-0.00010300
C	-2.44483100	-2.42335300	0.00002600
C	2.44506800	-2.42311800	-0.00004800
C	2.89692700	-1.10017600	0.00009500
C	4.29711900	-0.68020700	0.00022600
C	4.29701700	0.68070800	0.00016700
C	2.89688100	1.10049500	0.00006900
N	2.05569100	0.00011900	0.00028500
C	2.44476800	2.42353600	0.00000900
C	1.13625400	2.90873400	-0.00010600
C	0.68762700	4.27453100	-0.00020200
C	-0.68804300	4.27446500	-0.00019100
C	-1.13653800	2.90862400	-0.00014100
N	-0.00010300	2.11362500	-0.00032000
C	-2.44500500	2.42330100	-0.00005600
C	-2.89698900	1.10021400	0.00002000
C	-4.29708500	0.68028900	0.00010500
C	-4.29705200	-0.68062500	0.00020600
C	-2.89681900	-1.10045500	0.00011700
N	-2.05569100	-0.00007800	0.00025900
H	-1.33819200	-5.13327300	-0.00009800
H	1.33869200	-5.13314300	-0.00010500
H	0.00005300	-1.09933300	-0.00015900
H	5.15069700	-1.33900700	0.00025300
H	5.15046600	1.33966300	0.00016700
H	1.33795400	5.13351000	-0.00022000
H	-1.33845200	5.13338200	-0.00021100
H	-0.00005400	1.09935300	-0.00047700
H	-5.15060000	1.33915800	0.00007100
H	-5.15056400	-1.33951100	0.00024000
Cl	3.74053100	3.72087200	0.00011900
Cl	-3.74089200	3.72051300	-0.00001200
Cl	-3.74043800	-3.72107700	0.00002900
Cl	3.74079900	-3.72071600	-0.00015300

Cartesian coordinates of the DFT optimized structure $[1]^{\bullet -}$ in the gas phase

C	-1.13915300	2.94027700	-0.00001300
C	-0.69876900	4.28974800	-0.00002600
C	0.69938800	4.28964900	-0.00001800
C	1.13957900	2.94011400	-0.00001100
N	0.00015600	2.14336500	-0.00005500
C	-2.45560200	2.42261600	-0.00000300
C	2.45595300	2.42226300	0.00000100
C	2.89928800	1.10799900	0.00000300
C	4.30274200	0.67934500	0.00000900

C	4.30265600	-0.67992900	0.00000800
C	2.89916600	-1.10842000	0.00000400
N	2.05640900	-0.00012800	0.00001800
C	2.45559000	-2.42256200	-0.00000400
C	1.13915600	-2.94026800	0.00000000
C	0.69877100	-4.28973200	0.00000300
C	-0.69939000	-4.28963200	0.00000000
C	-1.13958200	-2.94010500	0.00000300
N	-0.00015600	-2.14336900	0.00003100
C	-2.45594100	-2.42221000	0.00000200
C	-2.89932700	-1.10800400	0.00001100
C	-4.30275500	-0.67930900	0.00000900
C	-4.30264300	0.67996500	0.00001700
C	-2.89912700	1.10841600	0.00000400
N	-2.05640900	0.00016600	0.00002900
H	-1.34687300	5.15072700	-0.00002700
H	1.34761400	5.15053500	-0.00001300
H	0.00008300	1.12814000	-0.00008500
H	5.15713000	1.33847100	0.00000800
H	5.15696500	-1.33916100	0.00000600
H	1.34688000	-5.15070500	-0.00000200
H	-1.34762100	-5.15051400	-0.00000500
H	-0.00008400	-1.12814200	0.00004900
H	-5.15716000	-1.33841700	0.00000400
H	-5.15693600	1.33921500	0.00001600
Cl	-3.76745000	-3.73385800	-0.00001300
Cl	-3.76687300	3.73435000	0.00000600
Cl	3.76741400	3.73380800	0.00001700
Cl	3.76690900	-3.73440000	-0.00001600

Cartesian coordinates of the DFT optimized structure $[1]^{2-}$ in the gas phase

C	1.12980800	-2.98360400	-0.00000200
C	0.69071800	-4.31902900	0.00000700
C	-0.73053400	-4.31252500	0.00001300
C	-1.15737000	-2.97311400	0.00000700
N	-0.01012200	-2.18058000	-0.00001500
C	2.45450700	-2.43649000	-0.00001000
C	-2.47697400	-2.41383200	0.00000500
C	-2.90472900	-1.10274200	-0.00001300
C	-4.30909400	-0.65969900	-0.00002900
C	-4.30278900	0.69942100	-0.00004500
C	-2.89437600	1.12941400	-0.00001400
N	-2.05529100	0.00942300	-0.00003200
C	-2.45450700	2.43649000	-0.00000400
C	-1.12980800	2.98360400	0.00002000
C	-0.69071800	4.31902900	0.00003000
C	0.73053400	4.31252500	0.00002900
C	1.15737000	2.97311400	0.00003300
N	0.01012200	2.18058000	0.00011200
C	2.47697400	2.41383200	0.00001700
C	2.90472900	1.10274200	-0.00000100
C	4.30909400	0.65969900	-0.00004500
C	4.30278900	-0.69942100	-0.00003000
C	2.89437600	-1.12941400	-0.00001900
N	2.05529100	-0.00942300	-0.00002600

H	1.33385200	-5.18500800	0.00000900
H	-1.38155000	-5.17259900	0.00002000
H	-0.00543400	-1.16387000	-0.00002000
H	-5.16856900	-1.31443600	-0.00003200
H	-5.15614700	1.36211000	-0.00005800
H	-1.33385200	5.18500800	0.00001700
H	1.38155000	5.17260000	0.00001400
H	0.00543400	1.16387000	0.00017800
H	5.16856900	1.31443600	-0.00006000
H	5.15614700	-1.36211000	-0.00003700
Cl	-3.78215000	3.76762500	-0.00002900
Cl	3.81681600	3.73269200	-0.00000500
Cl	3.78215000	-3.76762500	0.00000300
Cl	-3.81681600	-3.73269200	0.00003000

Cartesian coordinates of the DFT optimized structure [1-H] in the gas phase

C	-1.14343900	-2.93229300	0.10314600
C	-0.69813400	-4.18076000	0.57538800
C	0.70640000	-4.17940200	0.57513500
C	1.14914300	-2.93010900	0.10267800
N	0.00206200	-2.16512500	-0.17434600
C	-2.46855900	-2.44420400	-0.05409700
C	2.47329700	-2.43952800	-0.05499100
C	2.92263100	-1.13489100	-0.13702400
C	4.28158900	-0.66788400	-0.32260500
C	4.28682600	0.70186000	-0.28124900
C	2.93454800	1.16058100	-0.08038200
N	2.13505200	0.01529900	-0.01372600
C	2.44125100	2.44610100	0.03609500
C	1.10142900	2.88945200	0.14720000
C	0.68180800	4.26932600	0.24928900
C	-0.69005800	4.26805200	0.24883400
C	-1.10704000	2.88736700	0.14668400
N	-0.00203400	2.04144700	0.10645800
C	-2.44599900	2.44148000	0.03519100
C	-2.93676300	1.15496900	-0.08098300
C	-4.28816100	0.69354900	-0.28154700
C	-4.28030700	-0.67620300	-0.32201000
C	-2.92039500	-1.14046300	-0.13647100
N	-2.13497000	0.01127200	-0.01408200
H	-1.34179700	-4.97852900	0.90866700
H	1.35173100	-4.97591800	0.90819700
H	0.00115800	-1.41200800	-0.84949000
H	5.12885400	-1.31796500	-0.46686300
H	5.14060700	1.35132900	-0.38649100
H	1.15579100	0.09045800	0.22503800
H	1.33568900	5.12482400	0.30283800
H	-1.34557100	5.12232500	0.30193500
H	-5.14320800	1.34130700	-0.38705800
H	-5.12632900	-1.32802200	-0.46573100
H	-1.15588200	0.08865200	0.22484400
Cl	-3.72557800	3.75556800	0.00743000
Cl	3.71834400	3.76271900	0.00937500
Cl	3.76090800	-3.74231200	-0.08158300
Cl	-3.75380500	-3.74942800	-0.07967500

Cartesian coordinates of the DFT optimized structure [1-H]$^-$ in the gas phase

C	-1.14869700	-2.93888700	0.18089800
C	-0.71182200	-4.09399200	0.82900500
C	0.71170000	-4.09401400	0.82900200
C	1.14860700	-2.93892200	0.18089400
N	-0.00003500	-2.23402100	-0.21232500
C	-2.47889100	-2.44234200	-0.06257000
C	2.47881500	-2.44241700	-0.06257700
C	2.92592900	-1.15102000	-0.14937200
C	4.28715100	-0.67158600	-0.37042300
C	4.29242700	0.69425900	-0.31982700
C	2.94350300	1.16463400	-0.08576800
N	2.14223600	0.00561500	-0.00740900
C	2.45294300	2.43550300	0.04150400
C	1.10752900	2.90699200	0.17938700
C	0.69578100	4.26558700	0.32538600
C	-0.69565200	4.26560800	0.32538100
C	-1.10744100	2.90702600	0.17938400
N	0.00003200	2.06111700	0.10823400
C	-2.45286800	2.43557800	0.04149800
C	-2.94346700	1.16472300	-0.08577200
C	-4.29240500	0.69438900	-0.31983100
C	-4.28717100	-0.67145700	-0.37042100
C	-2.92596500	-1.15093200	-0.14936800
N	-2.14223500	0.00567900	-0.00741000
H	-1.35775100	-4.83946100	1.26577300
H	1.35760800	-4.83950200	1.26576900
H	-0.00002500	-1.51173500	-0.91822300
H	5.13135800	-1.32239300	-0.53219800
H	5.14554800	1.34384800	-0.43692500
H	1.16209100	0.07950400	0.22383500
H	1.34697800	5.12271500	0.40239100
H	-1.34682300	5.12275700	0.40238300
H	-5.14550500	1.34400400	-0.43693400
H	-5.13139900	-1.32223800	-0.53219500
H	-1.16209000	0.07953800	0.22383900
Cl	3.76520900	-3.77421100	-0.18564800
Cl	3.74311600	3.76944600	-0.01769500
Cl	-3.74300000	3.76956000	-0.01770700
Cl	-3.76532600	-3.77409800	-0.18563300

Cartesian coordinates of the DFT optimized structure [1-HH] in the gas phase

C	1.14592600	-2.89175600	0.31828900
C	0.70926400	-4.05293300	0.96210100
C	-0.70758500	-4.05322200	0.96210200
C	-1.14472300	-2.89222900	0.31828200
N	0.00045400	-2.17490600	-0.05213800
C	2.47454300	-2.43808800	-0.00426700
C	-2.47352500	-2.43911000	-0.00428000
C	-2.90774100	-1.16326600	-0.21176500
C	-4.20156200	-0.68259800	-0.66773100
C	-4.20184400	0.68085000	-0.66771500
C	-2.90822900	1.16204400	-0.21172500
N	-2.11079700	-0.00044600	0.00543200
C	-2.47454400	2.43807300	-0.00423100

C	-1.14592900	2.89177400	0.31824500
C	-0.70926200	4.05310400	0.96178300
C	0.70758300	4.05339700	0.96177700
C	1.14472600	2.89224700	0.31824000
N	-0.00045400	2.17481300	-0.05198800
C	2.47352700	2.43909500	-0.00424200
C	2.90774300	1.16324600	-0.21173300
C	4.20156300	0.68259000	-0.66770600
C	4.20184200	-0.68085700	-0.66774100
C	2.90822800	-1.16206300	-0.21175700
N	2.11079600	0.00042500	0.00542900
H	1.35365400	-4.80940300	1.38099400
H	-1.35166700	-4.80995600	1.38099400
H	0.00030100	-1.42129900	-0.72412600
H	-5.01010500	-1.33144600	-0.96560500
H	-5.01065900	1.32936700	-0.96557000
H	-1.35364900	4.80966900	1.38050700
H	1.35166100	4.81023000	1.38049400
H	-0.00029900	1.42113700	-0.72390000
H	5.01010900	1.33144500	-0.96555700
H	5.01065300	-1.32936800	-0.96562100
H	1.40101700	0.00026700	0.72633900
H	-1.40101700	-0.00031200	0.72634100
Cl	3.71807000	3.77826200	-0.15477500
Cl	3.71961200	-3.77676100	-0.15487000
Cl	-3.71803700	-3.77830100	-0.15488700
Cl	-3.71964500	3.77672200	-0.15476100

Cartesian coordinates of the DFT optimized structure [1-HH]$^+$ in the gas phase

C	-1.15064300	2.89253900	0.26301600
C	-0.70836500	4.12396800	0.79370700
C	0.69083700	4.12691000	0.79379000
C	1.13833200	2.89737000	0.26309400
N	-0.00454900	2.13368300	-0.02481300
C	-2.47195300	2.44157700	-0.00380600
C	2.46152100	2.45207600	-0.00380900
C	2.90073700	1.15909100	-0.21432700
C	4.19113100	0.69458800	-0.66041100
C	4.19406600	-0.67675900	-0.66038300
C	2.90565600	-1.14676600	-0.21431000
N	2.11447200	0.00448200	0.00963600
C	2.47195300	-2.44161000	-0.00379200
C	1.15065900	-2.89253200	0.26306200
C	0.70836500	-4.12396900	0.79372000
C	-0.69083700	-4.12691600	0.79372800
C	-1.13832000	-2.89738200	0.26300700
N	0.00455300	-2.13371300	-0.02489800
C	-2.46153000	-2.45204000	-0.00382800
C	-2.90071900	-1.15907100	-0.21433500
C	-4.19117300	-0.69456800	-0.66038400
C	-4.19408500	0.67674900	-0.66041400
C	-2.90563000	1.14675000	-0.21432200
N	-2.11452000	-0.00448100	0.00961600
H	-1.35418800	4.91088900	1.14913100
H	1.33331200	4.91653900	1.14928100

H	-0.00285100	1.38354200	-0.70252700
H	4.99798700	1.34363900	-0.96188100
H	5.00370100	-1.32234900	-0.96182500
H	1.35417000	-4.91087500	1.14920900
H	-1.33332900	-4.91654600	1.14918100
H	0.00306500	-1.38360200	-0.70264800
H	-4.99802200	-1.34363500	-0.96184100
H	-5.00369600	1.32235800	-0.96188100
H	-1.37238100	-0.00291400	0.69698000
H	1.37263200	0.00291500	0.69735700
Cl	3.73265700	-3.74415300	-0.07057900
Cl	3.71663600	3.75999400	-0.07072400
Cl	-3.73265000	3.74411900	-0.07057500
Cl	-3.71664800	-3.75994800	-0.07067100

Cartesian coordinates of the DFT optimized structure $[1\text{-HH}]^{2+}$ in the gas phase

C	1.15715600	2.88728300	-0.23505800
C	0.70942800	4.15468000	-0.72322200
C	-0.67288500	4.16071900	-0.72329500
C	-1.13171100	2.89735700	-0.23495200
N	0.00932500	2.11744700	0.02125700
C	2.46851600	2.44682900	-0.00010600
C	-2.44688600	2.46854600	0.00012500
C	-2.88728900	1.15717300	0.23513800
C	-4.15470300	0.70945400	0.72324300
C	-4.16079800	-0.67287000	0.72319500
C	-2.89736800	-1.13171300	0.23508500
N	-2.11744700	0.00932300	-0.02111000
C	-2.46852900	-2.44690300	0.00003000
C	-1.15717200	-2.88727700	-0.23501100
C	-0.70946900	-4.15462200	-0.72335000
C	0.67284400	-4.16077500	-0.72317600
C	1.13169500	-2.89736200	-0.23500600
N	-0.00932200	-2.11744600	0.02125000
C	2.44687300	-2.46847100	-0.00001200
C	2.88729100	-1.15715200	0.23501000
C	4.15471200	-0.70943800	0.72317500
C	4.16081000	0.67285300	0.72312100
C	2.89737100	1.13169100	0.23495400
N	2.11743200	-0.00932300	-0.02115300
H	1.35793900	4.94972400	-1.05750800
H	-1.31437900	4.96139400	-1.05768500
H	0.00604100	1.37387600	0.70766900
H	-4.94976400	1.35793700	1.05754100
H	-4.96155000	-1.31433600	1.05744900
H	-1.35797800	-4.94960600	-1.05778500
H	1.31433800	-4.96151000	-1.05741500
H	-0.00607700	-1.37387100	0.70765900
H	4.94976200	-1.35795000	1.05745200
H	4.96155200	1.31434800	1.05735100
H	1.37362400	-0.00605800	-0.70729100
H	-1.37380600	0.00605800	-0.70744300
Cl	3.71191400	-3.74472000	0.00012000
Cl	-3.74471400	-3.71190300	-0.00014700
Cl	-3.71188300	3.74473400	0.00002400

Cl	3.74474600	3.71188800	-0.00005900

Cartesian coordinates of the DFT optimized structure of p-toluenesulfonic acid (TsOH) in the gas phase

C	-2.70639100	0.00323200	0.01153100
C	-1.98945400	1.21451900	-0.01436600
C	-0.59055900	1.22731600	-0.06625800
C	0.06356100	0.00104800	-0.08928500
C	-0.59327000	-1.22559600	-0.06585800
C	-1.99039300	-1.21080700	-0.01450300
H	-2.52700300	2.15740900	0.00561000
H	-0.03167000	2.15588800	-0.09389400
H	-0.03504600	-2.15457100	-0.09319800
H	-2.52953400	-2.15317200	0.00517100
C	-4.21766700	-0.00153700	0.04661300
H	-4.61491800	0.98190600	0.31519000
H	-4.63149400	-0.27061900	-0.93432300
H	-4.59733000	-0.73077500	0.77115400
S	1.92056700	-0.00065400	-0.14691400
O	2.49143300	1.40635000	-0.72948000
O	2.48835300	-1.40934400	-0.72839600
O	2.17480600	-0.00007200	1.66747600
H	3.14622500	-0.00013000	1.85086500

Cartesian coordinates of the DFT optimized structure of tosylate (TsO^{-}) in the gas phase

C	-2.68689900	-0.00053100	-0.00000200
C	-1.96233400	-1.21002400	-0.00000300
C	-0.56315200	-1.21004900	0.00000900
C	0.11218400	0.00904500	-0.00000800
C	-0.56754900	1.22035200	-0.00001500
C	-1.97172600	1.20918700	0.00001300
H	-2.49915400	-2.15672900	0.00001100
H	0.00065100	-2.13690300	0.00002500
H	0.00748700	2.14082400	-0.00000400
H	-2.51521200	2.15177400	0.00002000
C	-4.20256300	-0.01183700	-0.00000500
H	-4.60078100	-0.52821000	-0.88413600
H	-4.60079200	-0.52840700	0.88400500
H	-4.60518800	1.00743700	0.00011100
S	2.00583100	0.00433500	-0.00001100
O	2.41758300	-0.81555100	-1.39042200
O	2.41756900	-0.81561400	1.39039900
O	2.38633900	1.62416400	0.00004900

Cartesian coordinates of the DFT optimized structure of acetic acid (AcOH) in the gas phase

C	-0.07469800	0.13141800	-0.00007000
O	-0.61797500	1.23976300	0.00001000
C	1.39726400	-0.14320700	-0.00001000
H	1.66955000	-0.73161100	0.88256100
H	1.66944800	-0.73284900	-0.88174500
H	1.94500000	0.79925600	-0.00055300
O	-0.81248000	-1.04153700	-0.00000400
H	-1.77575100	-0.84987200	0.00016800

Cartesian coordinates of the DFT optimized structure of acetate (AcO^{-}) in the gas phase

C	0.19443700	0.00071300	-0.00002400
O	0.80637500	-1.13131900	-0.00000800
C	-1.35903900	-0.04379300	0.00003300
H	-1.74257600	0.48128500	0.88575800
H	-1.74272700	0.48243400	-0.88493600
H	-1.72137600	-1.07753900	-0.00057200
O	0.71791200	1.17785700	-0.00003000

Cartesian coordinates of the solvated DFT optimized structure [1] in THF

C	-1.13633000	2.91143200	-0.00019300
C	-0.68783000	4.27783000	-0.00038400
C	0.68781100	4.27783300	-0.00035100
C	1.13631700	2.91143700	-0.00019000
N	-0.00000500	2.11601900	-0.00031100
C	-2.44407200	2.42444700	-0.00008400
C	2.44406100	2.42445800	-0.00008300
C	2.89675000	1.10114800	0.00017400
C	4.29631900	0.68093900	0.00048600
C	4.29632100	-0.68092900	0.00043100
C	2.89673900	-1.10112800	0.00020700
N	2.05481800	0.00000500	0.00074800
C	2.44406900	-2.42443600	-0.00002200
C	1.13632300	-2.91142700	-0.00012300
C	0.68782900	-4.27783800	-0.00031500
C	-0.68781000	-4.27784100	-0.00026100
C	-1.13631000	-2.91143200	-0.00009700
N	0.00000500	-2.11602700	-0.00030300
C	-2.44405800	-2.42444700	0.00002600
C	-2.89673400	-1.10114100	0.00023200
C	-4.29631800	-0.68094800	0.00046700
C	-4.29632300	0.68092000	0.00046900
C	-2.89675500	1.10113600	0.00017600
N	-2.05481800	-0.00000400	0.00071100
H	-1.33498700	5.13925500	-0.00046100
H	1.33496400	5.13926100	-0.00040400
H	-0.00000200	1.10188000	-0.00040900
H	5.15215800	1.33697500	0.00050300
H	5.15216300	-1.33696200	0.00041300
H	1.33500800	-5.13924500	-0.00039400
H	-1.33498500	-5.13925100	-0.00029900
H	0.00000200	-1.10188700	-0.00045000
H	-5.15215700	-1.33698500	0.00047900
H	-5.15216500	1.33695200	0.00047300
Cl	3.74161100	-3.72156600	-0.00014000
Cl	-3.74159400	-3.72158300	-0.00002600
Cl	-3.74161000	3.72156500	-0.00018900
Cl	3.74159400	3.72158100	-0.00015900

Cartesian coordinates of the solvated DFT optimized structure [1]$^{\cdot -}$ in THF

C	-1.13944200	-2.94259700	0.00002800
C	-0.69833900	-4.29179500	0.00005900
C	0.70005400	-4.29151900	0.00004300
C	1.14062300	-2.94214500	0.00002800

N	0.00043200	-2.14443400	0.00013500
C	-2.45636100	-2.42474700	-0.00000100
C	2.45733500	-2.42377000	-0.00000100
C	2.89912200	-1.10898500	-0.00000900
C	4.30163500	-0.67888200	-0.00004700
C	4.30136500	0.68059200	-0.00003100
C	2.89868600	1.11014200	-0.00001200
N	2.05324700	0.00040500	-0.00004200
C	2.45636100	2.42474100	0.00000900
C	1.13944300	2.94260000	0.00000500
C	0.69834000	4.29179400	0.00000400
C	-0.70005500	4.29151800	0.00002000
C	-1.14062400	2.94214800	0.00000400
N	-0.00043200	2.14443700	-0.00005100
C	-2.45733400	2.42376500	0.00000700
C	-2.89913200	1.10898800	-0.00002200
C	-4.30163800	0.67887300	-0.00002700
C	-4.30136200	-0.68060100	-0.00007200
C	-2.89867600	-1.11013900	-0.00001700
N	-2.05324800	-0.00040900	-0.00006800
H	-1.34244300	-5.15592100	0.00005700
H	1.34450000	-5.15539000	0.00002900
H	0.00023100	-1.12974000	0.00021500
H	5.15885300	-1.33424300	-0.00006100
H	5.15832100	1.33629500	-0.00003300
H	1.34244300	5.15592000	0.00001200
H	-1.34450000	5.15538900	0.00003800
H	-0.00023100	1.12974300	-0.00009200
H	-5.15885800	1.33423100	-0.00001400
H	-5.15831500	-1.33630700	-0.00009200
Cl	-3.76665700	3.73222600	0.00005500
Cl	-3.76516200	-3.73371800	-0.00003200
Cl	3.76665500	-3.73222100	-0.00004200
Cl	3.76516400	3.73372100	0.00003700

Cartesian coordinates of the solvated DFT optimized structure $[1]^{2-}$ in THF

C	1.19229600	-2.95723900	0.00002200
C	0.78042500	-4.30035300	0.00001700
C	-0.64066900	-4.32326600	0.00002100
C	-1.09563600	-2.99421400	0.00002700
N	0.03540000	-2.17599000	0.00005800
C	2.50755400	-2.38651600	0.00000500
C	-2.42863900	-2.46624400	0.00001300
C	-2.87992900	-1.16455700	0.00000200
C	-4.29160000	-0.74891400	-0.00002400
C	-4.31378300	0.60940200	-0.00005600
C	-2.91639100	1.07087000	0.00000800
N	-2.04856000	-0.03302300	0.00000200
C	-2.50755400	2.38651600	0.00001100
C	-1.19229600	2.95723900	0.00005400
C	-0.78042500	4.30035300	0.00006200
C	0.64066900	4.32326600	0.00004500
C	1.09563600	2.99421400	0.00005700
N	-0.03540000	2.17599000	0.00020900
C	2.42863900	2.46624400	0.00001900

C	2.87992900	1.16455700	0.00002100
C	4.29160000	0.74891400	-0.00005500
C	4.31378300	-0.60940200	-0.00001000
C	2.91639100	-1.07087000	0.00000600
N	2.04856000	0.03302300	0.00002100
H	1.43690200	-5.15607800	0.00000100
H	-1.26921700	-5.19966300	0.00000800
H	0.01909500	-1.16024900	0.00008600
H	-5.13977000	-1.41748200	-0.00003600
H	-5.18340000	1.24979900	-0.00009100
H	-1.43690200	5.15607800	0.00003200
H	1.26921700	5.19966300	0.00000300
H	-0.01909500	1.16024900	0.00033100
H	5.13977000	1.41748200	-0.00009800
H	5.18340000	-1.24979900	-0.00002400
Cl	-3.85181300	3.68494100	-0.00008400
Cl	3.73079900	3.80686600	-0.00009300
Cl	3.85181300	-3.68494100	-0.00003500
Cl	-3.73079900	-3.80686600	-0.00000800

Cartesian coordinates of the solvated DFT optimized structure [1-H] in THF

C	-1.14242700	-2.93112800	0.10564600
C	-0.69930200	-4.16214900	0.62716400
C	0.70501200	-4.16124000	0.62693800
C	1.14636700	-2.92959200	0.10543500
N	0.00142200	-2.17810300	-0.20441300
C	-2.46676900	-2.44313600	-0.06194800
C	2.47003800	-2.43981900	-0.06248800
C	2.92176800	-1.13676000	-0.14909600
C	4.28189300	-0.67028500	-0.33630800
C	4.28810700	0.69876700	-0.28977700
C	2.93419400	1.15737200	-0.08438300
N	2.13591600	0.01280500	-0.01952100
C	2.44202000	2.44281300	0.03631800
C	1.10329300	2.89283900	0.14960900
C	0.68437600	4.27128700	0.26439300
C	-0.69014700	4.27039900	0.26409100
C	-1.10722700	2.89140600	0.14921800
N	-0.00141300	2.04691600	0.10015300
C	-2.44528100	2.43960800	0.03560000
C	-2.93570700	1.15346700	-0.08489900
C	-4.28903600	0.69299800	-0.28988200
C	-4.28101500	-0.67607400	-0.33571400
C	-2.92021900	-1.14066300	-0.14888800
N	-2.13585200	0.01000700	-0.01999000
H	-1.34117400	-4.94532600	0.99719800
H	1.34802000	-4.94360100	0.99674000
H	0.00088800	-1.46136100	-0.91893800
H	5.13064500	-1.31748600	-0.48537400
H	5.14410000	1.34539100	-0.39490100
H	1.15359900	0.08014400	0.20759100
H	1.33604900	5.12828500	0.32718000
H	-1.34296700	5.12654100	0.32661000
H	-5.14594700	1.33842700	-0.39489300
H	-5.12897000	-1.32445200	-0.48414900

H	-1.15344600	0.07890200	0.20633800
Cl	-3.72816400	3.75608600	0.01204800
Cl	3.72314700	3.76100100	0.01336600
Cl	3.75835300	-3.74627900	-0.08698400
Cl	-3.75339300	-3.75124900	-0.08567500

Cartesian coordinates of the solvated DFT optimized structure $[1\text{-H}]^{-}$ in THF

C	-1.14897800	-2.92242200	0.20970200
C	-0.71454900	-4.01568900	0.96128300
C	0.70852200	-4.01681000	0.96116500
C	1.14455000	-2.92412300	0.20966300
N	-0.00173200	-2.25953300	-0.24750400
C	-2.47943700	-2.44125800	-0.07005300
C	2.47572200	-2.44494600	-0.07012800
C	2.92727700	-1.15752500	-0.17094500
C	4.28612000	-0.67802300	-0.41184900
C	4.29348500	0.68662800	-0.35445600
C	2.94515200	1.15731700	-0.09740400
N	2.14621700	-0.00113000	-0.01115900
C	2.45805200	2.42774700	0.04178900
C	1.11176500	2.90106500	0.19580300
C	0.70098700	4.25387700	0.37925300
C	-0.69460300	4.25488400	0.37934400
C	-1.10736000	2.90270700	0.19566400
N	0.00158500	2.05863500	0.10074700
C	-2.45434300	2.43139500	0.04154900
C	-2.94334600	1.16170600	-0.09773700
C	-4.29240300	0.69305700	-0.35472100
C	-4.28713500	-0.67161000	-0.41194000
C	-2.92901200	-1.15316000	-0.17107400
N	-2.14611700	0.00206300	-0.01178800
H	-1.35840000	-4.71697800	1.46959400
H	1.35134800	-4.71909800	1.46939200
H	-0.00128000	-1.60737500	-1.01927700
H	5.13054000	-1.32471300	-0.58938800
H	5.14819800	1.33243600	-0.48094500
H	1.16229200	0.06281800	0.20432300
H	1.34959200	5.11091400	0.48101500
H	-1.34195700	5.11286000	0.48116500
H	-5.14615100	1.34015400	-0.48114500
H	-5.13256400	-1.31703300	-0.58928700
H	-1.16200100	0.06454600	0.20325300
Cl	3.74855200	-3.78761500	-0.21510500
Cl	3.74430300	3.76415200	-0.02484900
Cl	-3.73862000	3.76970900	-0.02486900
Cl	-3.75435600	-3.78199100	-0.21460200

Cartesian coordinates of the solvated DFT optimized structure [1-HH] in THF

C	1.05567700	-2.91327900	0.31949700
C	0.59419200	-3.99217500	1.08148300
C	-0.82282300	-3.94759500	1.09761900
C	-1.23199700	-2.84109600	0.34555400
N	-0.07227500	-2.21044600	-0.11634700
C	2.39473800	-2.51024200	-0.03330000

C	-2.54803400	-2.35668600	0.01111100
C	-2.94976600	-1.07055600	-0.20203700
C	-4.22599400	-0.55615200	-0.68092500
C	-4.18254600	0.80627100	-0.69745200
C	-2.87650600	1.24911400	-0.22754900
N	-2.13588300	0.06758400	0.02224200
C	-2.39474900	2.51011500	-0.03242400
C	-1.05568800	2.91327100	0.32007200
C	-0.59413200	3.99331500	1.08041600
C	0.82285700	3.94871600	1.09659600
C	1.23201300	2.84106600	0.34619100
N	0.07224400	2.20964300	-0.11459500
C	2.54804900	2.35654300	0.01206400
C	2.94981200	1.07045400	-0.20139600
C	4.22600500	0.55625400	-0.68058100
C	4.18252300	-0.80615900	-0.69780300
C	2.87651000	-1.24920200	-0.22798600
N	2.13594700	-0.06776300	0.02247100
H	1.22059000	-4.71814200	1.57627700
H	-1.48204900	-4.63396700	1.60599800
H	-0.06298000	-1.53025500	-0.86307700
H	-5.05180600	-1.18079300	-0.98329100
H	-4.96748500	1.47454800	-1.01493800
H	-1.22048200	4.72011600	1.57403400
H	1.48210300	4.63590900	1.60382700
H	0.06291000	1.52826100	-0.86022000
H	5.05180300	1.18102200	-0.98272300
H	4.96741100	-1.47430200	-1.01569500
H	1.36544300	-0.05435800	0.67470200
H	-1.36530100	0.05384700	0.67437300
Cl	3.82947200	3.67114000	-0.14825300
Cl	3.58676800	-3.90166000	-0.23008500
Cl	-3.82936700	-3.67134000	-0.14972500
Cl	-3.58694600	3.90145600	-0.22844100

Cartesian coordinates of the solvated DFT optimized structure [1-HH]$^+$ in THF

C	-1.38202500	2.78763000	0.26507300
C	-1.03866000	4.04566900	0.81125900
C	0.35406600	4.16484000	0.79444300
C	0.89339600	2.98209700	0.23822700
N	-0.18405000	2.13915400	-0.05834700
C	-2.66257200	2.22517800	0.01892100
C	2.24691400	2.64202300	-0.02707900
C	2.79797500	1.39010000	-0.21437200
C	4.12237700	1.03212700	-0.66558600
C	4.24017700	-0.33284100	-0.64802800
C	2.99496100	-0.90097000	-0.18740900
N	2.12132900	0.18073200	0.03915000
C	2.66257200	-2.22517800	0.01892800
C	1.38202400	-2.78763100	0.26507300
C	1.03865600	-4.04567100	0.81125400
C	-0.35407100	-4.16484100	0.79442800
C	-0.89339700	-2.98209800	0.23821000
N	0.18405000	-2.13915400	-0.05835400
C	-2.24691400	-2.64202300	-0.02710300

C	-2.79797400	-1.39009900	-0.21439400
C	-4.12237300	-1.03212400	-0.66561400
C	-4.24017400	0.33284300	-0.64805000
C	-2.99495900	0.90097100	-0.18742200
N	-2.12133100	-0.18073300	0.03913800
H	-1.74237600	4.76770700	1.19282400
H	0.93387900	4.99634400	1.16128200
H	-0.13021200	1.38725200	-0.73308100
H	4.86788700	1.74164600	-0.98678100
H	5.09660700	-0.91234800	-0.95314100
H	1.74236800	-4.76770900	1.19282300
H	-0.93388600	-4.99634600	1.16126300
H	0.13022000	-1.38725500	-0.73309300
H	-4.86788100	-1.74164300	-0.98681700
H	-5.09660200	0.91235200	-0.95316500
H	-1.36614400	-0.12571100	0.70995900
H	1.36615200	0.12570900	0.70998400
Cl	4.03377300	-3.42410700	-0.03178400
Cl	3.39220900	4.05629000	-0.11930400
Cl	-4.03377300	3.42410600	-0.03179200
Cl	-3.39220800	-4.05629000	-0.11933900

Cartesian coordinates of the solvated DFT optimized structure [1-HH]$^{2+}$ in THF

C	-0.81453200	-2.99612000	-0.23096500
C	-0.22667200	-4.19820700	-0.74162100
C	1.14418200	-4.04753000	-0.73525600
C	1.45173400	-2.74649800	-0.22122400
N	0.23416000	-2.11592000	0.05447900
C	-2.16570200	-2.70460400	-0.00915600
C	2.70465700	-2.16576300	0.00959500
C	2.99603600	-0.81458900	0.23164600
C	4.19859800	-0.22661400	0.74110500
C	4.04787300	1.14421200	0.73467300
C	2.74634300	1.45165600	0.22176400
N	2.11550200	0.23403300	-0.05294100
C	2.16572000	2.70460000	-0.00929900
C	0.81455300	2.99613900	-0.23106800
C	0.22663300	4.19829400	-0.74149300
C	-1.14422200	4.04761000	-0.73499300
C	-1.45172000	2.74650700	-0.22109400
N	-0.23410800	2.11589100	0.05437200
C	-2.70463400	2.16574400	0.00975800
C	-2.99601400	0.81457400	0.23177900
C	-4.19871100	0.22658300	0.74094900
C	-4.04800200	-1.14423900	0.73452500
C	-2.74634200	-1.45167500	0.22193000
N	-2.11543400	-0.23404900	-0.05256100
H	-0.78257500	-5.04980400	-1.09885600
H	1.87481300	-4.75797600	-1.08664900
H	0.14920900	-1.37241900	0.73618900
H	5.05060500	-0.78244600	1.09746600
H	4.75867800	1.87493500	1.08513800
H	0.78249000	5.04995500	-1.09864300
H	-1.87489500	4.75811000	-1.08618800
H	-0.14901600	1.37236400	0.73604500

H	-5.05082100	0.78241000	1.09706600
H	-4.75891700	-1.87497200	1.08474600
H	-1.37010100	-0.14897200	-0.73221200
H	1.37057500	0.14890500	-0.73306500
Cl	-4.11379600	3.29528900	0.02052200
Cl	3.29554100	4.11352600	-0.02140200
Cl	4.11381300	-3.29530900	0.02033600
Cl	-3.29553200	-4.11352000	-0.02144600

Cartesian coordinates of the solvated DFT optimized structure of p-toluenesulfonic acid (TsOH) in THF

C	-2.71175200	0.00000200	-0.01491500
C	-1.99502100	-1.21358300	0.00809400
C	-0.59717200	-1.22893300	0.05809300
C	0.05631800	0.00001200	0.08211600
C	-0.59717600	1.22894900	0.05808200
C	-1.99502900	1.21358700	0.00808400
H	-2.53181500	-2.15637900	-0.01249900
H	-0.04590200	-2.16153600	0.08129600
H	-0.04590800	2.16155300	0.08127600
H	-2.53182600	2.15638100	-0.01251700
C	-4.22166100	-0.00001200	-0.03747800
H	-4.61351900	-0.88776400	-0.54331300
H	-4.62281300	-0.00021900	0.98502900
H	-4.61354500	0.88792300	-0.54297100
S	1.91247200	-0.00001000	0.14078600
O	2.49950100	-1.39848900	0.74115100
O	2.49949500	1.39837400	0.74138100
O	2.20107400	0.00009200	-1.65993000
H	3.17418600	0.00023600	-1.84215400

Cartesian coordinates of the solvated DFT optimized structure of tosylate (TsO^{-}) in THF

C	-2.69346900	0.00223700	0.01069000
C	-1.97195900	-1.20857800	0.00066600
C	-0.57244500	-1.21562400	-0.02082300
C	0.09836800	0.00554500	-0.03773600
C	-0.57342200	1.22375300	-0.02103000
C	-1.97538500	1.21257200	0.00113700
H	-2.50797100	-2.15345100	0.01046600
H	-0.01795500	-2.14698600	-0.03550900
H	-0.02088100	2.15625800	-0.03475800
H	-2.51359100	2.15590000	0.01158600
C	-4.20623400	-0.00522100	0.01432900
H	-4.60076700	-0.28292500	-0.97224900
H	-4.59955900	-0.73014900	0.73624400
H	-4.60905500	0.98044500	0.26712800
S	1.97633500	0.00020700	-0.00058300
O	2.44518600	-1.34834000	-0.86105700
O	2.43240300	-0.09602100	1.60551300
O	2.44937100	1.43554700	-0.70157700

Cartesian coordinates of the DFT optimized structure of acetic acid (AcOH) in THF

C	-0.07469800	0.13141800	-0.00007000
O	-0.61797500	1.23976300	0.00001000
C	1.39726400	-0.14320700	-0.00001000
H	1.66955000	-0.73161100	0.88256100
H	1.66944800	-0.73284900	-0.88174500
H	1.94500000	0.79925600	-0.00055300
O	-0.81248000	-1.04153700	-0.00000400
H	-1.77575100	-0.84987200	0.00016800

Cartesian coordinates of the DFT optimized structure of acetate (AcO^-) in THF

C	0.19443700	0.00071300	-0.00002400
O	0.80637500	-1.13131900	-0.00000800
C	-1.35903900	-0.04379300	0.00003300
H	-1.74257600	0.48128500	0.88575800
H	-1.74272700	0.48243400	-0.88493600
H	-1.72137600	-1.07753900	-0.00057200
O	0.71791200	1.17785700	-0.00003000

Chapter 3: Hydrogen Evolution Catalyzed by a Metal-Free Corrole: Experimental and Theoretical Mechanistic Study

Cartesian coordinates of the DFT optimized structure [C-3H] in the gas phase

C	2.95972800	-3.15766500	0.35083100
C	1.75009100	-3.86811300	0.29325600
C	0.72629800	-2.96761500	-0.11275100
N	1.35320300	-1.76218300	-0.33720000
C	2.69961100	-1.80427700	-0.02092200
C	2.51429300	2.93516000	-0.25269800
C	3.49107200	1.95618900	-0.27216000
C	2.88299800	0.68413700	-0.03014900
N	1.49678900	0.94651500	0.13753500
C	1.24228400	2.32319100	0.00475000
C	3.43150900	-0.60024800	-0.00249500
C	-3.57312900	1.94079300	0.14067100
C	-2.59830300	2.92425600	0.18948400
C	-1.30635600	2.29831300	0.08891400
N	-1.55117200	0.93816800	-0.01232700
C	-2.92153000	0.67425200	0.01265800
C	-0.03007400	2.89780800	0.06243200
C	-1.75058500	-3.90117600	-0.04918800
C	-2.94626900	-3.20685600	-0.05494300
C	-2.61393200	-1.79568100	-0.13967400
N	-1.23749100	-1.66003600	-0.21540800
C	-0.69718900	-2.91508500	-0.14527900
C	-3.40672100	-0.64183300	-0.05699900
Cl	5.24731900	-0.73568500	0.06674700
Cl	-0.04296500	4.73503800	0.05213400
Cl	-5.21381200	-0.85187000	0.01917500
H	3.91671800	-3.53968100	0.67134500
H	1.60577200	-4.90184800	0.56912300
H	0.87345300	-0.99431000	-0.77662200
H	2.65575900	3.98758600	-0.43843200
H	4.54036400	2.09829200	-0.47895400
H	0.91600900	0.34585300	0.70776900
H	-4.64085500	2.08530200	0.19348800
H	-2.75698100	3.98560800	0.28886400
H	-0.93747800	0.12684900	-0.14890900
H	-1.62173700	-4.97256900	0.01143700
H	-3.94233000	-3.61880700	0.01130400

Cartesian coordinates of the DFT optimized structure [C-3H]$^{\bullet-}$ in the gas phase

C	2.97542300	-3.14618600	0.42697500
C	1.74844000	-3.87301100	0.37350900
C	0.74025500	-2.99706500	-0.06711100
N	1.36886800	-1.79266300	-0.32017900
C	2.71512600	-1.81909900	0.01427800
C	2.50447100	2.94992700	-0.27138000
C	3.49725900	1.96545800	-0.30983100
C	2.89971300	0.69634300	-0.04881100
N	1.51695000	0.95874300	0.14519900
C	1.25360900	2.34217500	0.01088500

C	3.44226400	-0.59461300	-0.01125800
C	-3.58238900	1.94530800	0.13052000
C	-2.60917800	2.92526900	0.19080900
C	-1.30723200	2.30456400	0.09728800
N	-1.55721700	0.93508800	-0.00751200
C	-2.93404400	0.66719500	0.00714300
C	-0.04246500	2.89736900	0.08169500
C	-1.74578300	-3.91866200	-0.06014300
C	-2.96004400	-3.21027800	-0.07024600
C	-2.62412100	-1.81928500	-0.13544500
N	-1.24363100	-1.68327800	-0.18474800
C	-0.70440900	-2.94724900	-0.12517100
C	-3.41249400	-0.63586900	-0.07067800
Cl	5.28057400	-0.72670700	-0.01585700
Cl	-0.05629900	4.75524900	0.10289400
Cl	-5.24271300	-0.84766400	-0.03480100
H	3.93047800	-3.51735000	0.76724700
H	1.60316800	-4.89703500	0.68576600
H	0.88014800	-1.02745100	-0.75401800
H	2.64036600	4.00233900	-0.46516400
H	4.54192400	2.11157100	-0.53620700
H	0.93940300	0.35030800	0.70871600
H	-4.65110100	2.09025300	0.17329700
H	-2.76831900	3.98733800	0.29008400
H	-0.94228100	0.12326700	-0.12900400
H	-1.62410900	-4.99301900	-0.01438400
H	-3.95742200	-3.62411500	-0.02185600

Cartesian coordinates of the DFT optimized structure [C-3H]$^{2-}$ in the gas phase

C	2.95470700	-3.12644800	0.63618500
C	1.71974900	-3.87073600	0.53669900
C	0.74805100	-3.02532700	-0.00644600
N	1.39897900	-1.83697300	-0.29263900
C	2.72339900	-1.83402500	0.13776300
C	2.49750100	2.94290800	-0.33232600
C	3.50110000	1.95988100	-0.35934600
C	2.91863900	0.69301000	-0.01594900
N	1.54016600	0.96693500	0.21090600
C	1.26279400	2.35728000	0.02519700
C	3.45281900	-0.59128900	0.07607700
C	-3.58642500	1.95186300	0.14984100
C	-2.60927200	2.92796700	0.24715100
C	-1.30678400	2.31929900	0.11870800
N	-1.56099200	0.94232700	-0.04086200
C	-2.94133400	0.66749900	-0.02113700
C	-0.04102100	2.89650200	0.10415000
C	-1.74554100	-3.93822700	-0.11090500
C	-2.97656900	-3.21567900	-0.14477800
C	-2.63441500	-1.83843900	-0.17772800
N	-1.24964900	-1.70503800	-0.18129200
C	-0.71130400	-2.97726100	-0.12610000
C	-3.41460600	-0.62635700	-0.12251700
Cl	5.31030800	-0.73211800	-0.21857300
Cl	-0.05673000	4.78922900	0.15921600
Cl	-5.27070700	-0.83516800	-0.09444900

H	3.88895500	-3.47942600	1.05061800
H	1.55170800	-4.87511300	0.90231100
H	0.91760000	-1.06292200	-0.72075800
H	2.62290600	3.98680000	-0.58154200
H	4.53894900	2.10060600	-0.61953800
H	0.97113900	0.37466100	0.79840300
H	-4.65566400	2.09725400	0.20040500
H	-2.76930100	3.98714600	0.38373500
H	-0.93603700	0.13926900	-0.14740700
H	-1.63094200	-5.01617300	-0.08073500
H	-3.97657400	-3.63041500	-0.13081800

Cartesian coordinates of the DFT optimized structure $[C\text{-}4H]^-$ in the gas phase

C	3.09935800	-3.12689000	0.10948800
C	1.89173400	-3.90072200	-0.02061100
C	0.82406300	-3.01540700	-0.16552800
N	1.37720400	-1.74015200	-0.15005900
C	2.75165500	-1.77194200	0.03000800
C	2.44908600	3.00255100	-0.14893600
C	3.45858400	2.04868800	-0.18372100
C	2.89399200	0.75498900	0.08986900
N	1.47587800	0.97660800	0.34469400
C	1.20161700	2.39388500	0.15302600
C	3.44852100	-0.50832700	0.06480700
C	-3.60848000	1.87466400	-0.08602000
C	-2.66648800	2.88571100	0.05806900
C	-1.35840900	2.31832400	0.10792700
N	-1.56294400	0.91817800	-0.00115300
C	-2.92855500	0.60129900	-0.10973400
C	-0.09471300	2.91805400	0.14385300
C	-1.57610000	-3.85823000	0.49661800
C	-2.82893300	-3.15069600	0.52646000
C	-2.64155300	-1.90826700	-0.08620700
N	-1.30761700	-1.88914400	-0.53053900
C	-0.63433900	-3.06721700	-0.14669500
C	-3.41500400	-0.69984000	-0.18447900
Cl	5.28390700	-0.61527600	-0.10949900
Cl	-0.14575800	4.78183200	0.10876900
Cl	-5.25368100	-0.91201100	-0.15639600
H	4.09998800	-3.51333800	0.22817900
H	1.82161300	-4.97853300	0.00789200
H	0.88272000	-0.86776100	-0.25807000
H	2.56571800	4.05056300	-0.38272700
H	4.49280300	2.21567800	-0.44179700
H	1.14450900	0.58693500	1.22637700
H	-4.67823300	1.99128300	-0.15843400
H	-2.86951900	3.94464700	0.10397900
H	-0.84250700	0.23179700	0.12512100
H	-1.36998200	-4.79593600	0.99343000
H	-3.73710700	-3.47686400	1.01020500
H	-1.01984000	-1.31794300	-1.31277400

Cartesian coordinates of the DFT optimized structure [C-4H] in the gas phase

C	3.04226200	-3.13859700	0.16717400
C	1.83825200	-3.88700200	0.05762400
C	0.78522900	-2.98811700	-0.18458000
N	1.36142400	-1.72942400	-0.24450800
C	2.72624700	-1.77642500	-0.00747700
C	2.48123100	2.97703700	-0.15917500
C	3.47242600	2.01212100	-0.19478600
C	2.89341900	0.72815400	0.06939100
N	1.48288600	0.96160700	0.29950000
C	1.22252800	2.36458100	0.12998800
C	3.44646800	-0.54108100	0.03837300
C	-3.58038800	1.90033700	-0.09184600
C	-2.62687400	2.90307200	0.02964200
C	-1.33020000	2.30923900	0.10639900
N	-1.54770900	0.92481400	0.03559800
C	-2.91686000	0.63029100	-0.08323500
C	-0.05812400	2.91652000	0.14035600
C	-1.62445900	-3.85940100	0.37124200
C	-2.86361300	-3.15734300	0.40890300
C	-2.65744600	-1.87199100	-0.11936300
N	-1.31104000	-1.82252600	-0.52584900
C	-0.65758300	-3.02560400	-0.19358100
C	-3.42609700	-0.67316400	-0.13316700
Cl	5.26490200	-0.66769500	-0.03467100
Cl	-0.09677900	4.75537400	0.09872800
Cl	-5.23886000	-0.86729900	-0.05438400
H	4.02718600	-3.53269600	0.36283500
H	1.74398600	-4.95745500	0.16000500
H	0.88903800	-0.86011100	-0.43275900
H	2.60782200	4.02578500	-0.37789000
H	4.51004900	2.16817400	-0.44606100
H	1.09529300	0.51998500	1.13062700
H	-4.64691900	2.03094000	-0.18235700
H	-2.81293700	3.96479300	0.04514500
H	-0.85019200	0.21809700	0.18000900
H	-1.43882000	-4.83218000	0.80217800
H	-3.78321600	-3.50811100	0.85110700
H	-1.03618800	-1.26073100	-1.32174300

Cartesian coordinates of the DFT optimized structure [C-4H]$^+$ in the gas phase

C	-2.99729200	-3.14196900	-0.20895800
C	-1.80393100	-3.86330000	-0.11205000
C	-0.75613600	-2.95321000	0.21361100
N	-1.35505700	-1.71151300	0.32949000
C	-2.70977000	-1.76494700	0.03902800
C	-2.48634000	2.95737200	0.23316000
C	-3.47481200	1.98454100	0.26038400
C	-2.89160600	0.71969400	-0.03268000
N	-1.49527000	0.96254400	-0.25518400
C	-1.23582800	2.34561200	-0.08418500
C	-3.44622200	-0.56579800	-0.03309200
C	3.56497800	1.90987300	0.06874600
C	2.61185300	2.90403300	-0.03505000
C	1.30911900	2.29686200	-0.09885800

N	1.53140900	0.92345500	-0.03090100
C	2.90442300	0.63723600	0.07010800
C	0.04594800	2.91505600	-0.12804500
C	1.64960300	-3.85408400	-0.27298700
C	2.87158200	-3.16391400	-0.31603900
C	2.66131200	-1.84493700	0.16201800
N	1.31131100	-1.77748500	0.55577500
C	0.66156000	-2.98626000	0.24642100
C	3.42520100	-0.66291500	0.10462600
Cl	-5.24475400	-0.70255900	-0.09058700
Cl	0.07632600	4.73607500	-0.11338300
Cl	5.21432700	-0.85080100	-0.05413300
H	-3.96787400	-3.53653200	-0.46657800
H	-1.68593700	-4.92418300	-0.27226700
H	-0.90852500	-0.85645400	0.61546200
H	-2.61295400	4.00205600	0.46864400
H	-4.51075200	2.13302800	0.52425800
H	-1.05310000	0.47004800	-1.02598100
H	4.63199300	2.04600300	0.14956800
H	2.79085300	3.96671200	-0.05264500
H	0.84641500	0.20431700	-0.17613600
H	1.47113700	-4.84615500	-0.66025800
H	3.79625700	-3.53043600	-0.73507800
H	1.05359400	-1.22724200	1.36755000

Cartesian coordinates of the DFT optimized structure $[C\text{-}2H]^-$ in the gas phase

C	2.97556600	-3.20886700	-0.00005400
C	1.77307800	-3.90818100	0.00011900
C	0.71878200	-2.92117400	0.00013000
N	1.26383800	-1.66881900	0.00023600
C	2.63590800	-1.79968000	-0.00005900
C	2.57587300	2.95145000	0.00011100
C	3.55133900	1.96866000	-0.00008300
C	2.90239800	0.68741800	-0.00017100
N	1.53163100	0.95418800	-0.00047400
C	1.27984600	2.31452700	-0.00001600
C	3.40331500	-0.61967400	-0.00014900
C	-3.53618900	1.96440000	-0.00021100
C	-2.57285400	2.94210200	0.00005500
C	-1.27609900	2.27091800	0.00001300
N	-1.46404300	0.90445200	0.00026900
C	-2.84834500	0.68374000	-0.00004200
C	-0.00346900	2.87749600	0.00003900
C	-1.76815700	-3.91293300	0.00029700
C	-2.98802300	-3.21432000	0.00012900
C	-2.68789300	-1.81447300	0.00012500
N	-1.31545600	-1.72740800	0.00005900
C	-0.70904200	-2.95463500	0.00025800
C	-3.40569700	-0.60417300	-0.00006900
Cl	5.23740500	-0.79962000	-0.00011200
Cl	-0.01096700	4.73886000	0.00025300
Cl	-5.24195600	-0.75270600	-0.00028100
H	3.97356500	-3.62438200	-0.00015200
H	1.65065900	-4.98356400	0.00017700
H	2.73233900	4.01836600	0.00028300

H	4.62049200	2.11686000	-0.00003900
H	0.86371000	0.18395600	-0.00088500
H	-4.60792600	2.10071200	-0.00037900
H	-2.72598700	4.01066300	0.00006800
H	-1.64767000	-4.98686900	0.00036800
H	-3.97934500	-3.64227800	0.00007800
H	-0.84984500	-0.81701900	-0.00030900

Cartesian coordinates of the DFT optimized structure of *p*-toluenesulfonic acid (TsOH) in the gas phase

C	0.06356100	0.00104800	-0.08928500
C	-0.59055900	1.22731600	-0.06625800
C	-0.59327000	-1.22559600	-0.06585800
C	-1.98945400	1.21451900	-0.01436600
H	-0.03167000	2.15588800	-0.09389400
S	1.92056700	-0.00065400	-0.14691400
C	-1.99039300	-1.21080700	-0.01450300
H	-0.03504600	-2.15457100	-0.09319800
C	-2.70639100	0.00323200	0.01153100
H	-2.52700300	2.15740900	0.00561000
O	2.49143300	1.40635000	-0.72948000
O	2.48835300	-1.40934400	-0.72839600
H	-2.52953400	-2.15317200	0.00517100
C	-4.21766700	-0.00153700	0.04661300
H	-4.59733000	-0.73077500	0.77115400
H	-4.63149400	-0.27061900	-0.93432300
H	-4.61491800	0.98190600	0.31519000
O	2.17480600	-0.00007200	1.66747600
H	3.14622500	-0.00013000	1.85086500

Cartesian coordinates of the DFT optimized structure of tosylate (TsO^{-}) in the gas phase

C	-2.68689900	-0.00053100	-0.00000200
C	-1.96233400	-1.21002400	-0.00000300
C	-0.56315200	-1.21004900	0.00000900
C	0.11218400	0.00904500	-0.00000800
C	-0.56754900	1.22035200	-0.00001500
C	-1.97172600	1.20918700	0.00001300
H	-2.49915400	-2.15672900	0.00001100
H	0.00065100	-2.13690300	0.00002500
H	0.00748700	2.14082400	-0.00000400
H	-2.51521200	2.15177400	0.00002000
C	-4.20256300	-0.01183700	-0.00000500
H	-4.60078100	-0.52821000	-0.88413600
H	-4.60079200	-0.52840700	0.88400500
H	-4.60518800	1.00743700	0.00011100
S	2.00583100	0.00433500	-0.00001100
O	2.41758300	-0.81555100	-1.39042200
O	2.41756900	-0.81561400	1.39039900
O	2.38633900	1.62416400	0.00004900

Cartesian coordinates of the DFT optimized structure of benzoic acid (HBza) in the gas phase

C	1.91840800	1.18571100	0.00020900
C	0.52221900	1.23209600	0.00020100
C	0.44264400	-1.20375800	-0.00013000

C	1.84045100	-1.24395100	-0.00022300
C	2.57929500	-0.05196300	-0.00003200
H	2.48996600	2.10824400	0.00040700
H	-0.00720900	2.17850400	0.00030300
H	-0.13806200	-2.11804000	-0.00019400
H	2.35229500	-2.20099600	-0.00043900
H	3.66450800	-0.08699200	-0.00008600
C	-0.22101000	0.03713500	0.00003600
H	-3.29482600	-0.98931700	0.00021700
C	-1.69364200	0.12962600	-0.00003000
O	-2.35336200	1.17948000	-0.00047500
O	-2.32124600	-1.10457800	0.00042600

Cartesian coordinates of the DFT optimized structure of benzoate (Bza$^-$) in the gas phase

C	1.21256700	-1.83910900	0.00000000
C	1.20966500	-0.43706400	0.00000000
C	-1.20967000	-0.43704300	0.00000000
C	-1.21259600	-1.83909300	0.00000000
C	-0.00002200	-2.54719600	0.00000000
H	2.15679400	-2.38073800	0.00000000
H	2.13042200	0.13740100	0.00000000
H	-2.13042500	0.13742600	0.00000000
H	-2.15683600	-2.38070000	0.00000000
H	-0.00002600	-3.63537900	0.00000000
C	0.00000000	0.27882500	0.00000000
C	0.00001400	1.81723200	0.00000000
O	1.15396700	2.38390700	0.00000000
O	-1.15392600	2.38392800	0.00000000

Cartesian coordinates of the DFT optimized structure [C-3H] in MeCN

C	2.95972800	-3.15766500	0.35083100
C	1.75009100	-3.86811300	0.29325600
C	0.72629800	-2.96761500	-0.11275100
N	1.35320300	-1.76218300	-0.33720000
C	2.69961100	-1.80427700	-0.02092200
C	2.51429300	2.93516000	-0.25269800
C	3.49107200	1.95618900	-0.27216000
C	2.88299800	0.68413700	-0.03014900
N	1.49678900	0.94651500	0.13753500
C	1.24228400	2.32319100	0.00475000
C	3.43150900	-0.60024800	-0.00249500
C	-3.57312900	1.94079300	0.14067100
C	-2.59830300	2.92425600	0.18948400
C	-1.30635600	2.29831300	0.08891400
N	-1.55117200	0.93816800	-0.01232700
C	-2.92153000	0.67425200	0.01265800
C	-0.03007400	2.89780800	0.06243200
C	-1.75058500	-3.90117600	-0.04918800
C	-2.94626900	-3.20685600	-0.05494300
C	-2.61393200	-1.79568100	-0.13967400
N	-1.23749100	-1.66003600	-0.21540800
C	-0.69718900	-2.91508500	-0.14527900
C	-3.40672100	-0.64183300	-0.05699900
Cl	5.24731900	-0.73568500	0.06674700

Cl	-0.04296500	4.73503800	0.05213400
Cl	-5.21381200	-0.85187000	0.01917500
H	3.91671800	-3.53968100	0.67134500
H	1.60577200	-4.90184800	0.56912300
H	0.87345300	-0.99431000	-0.77662200
H	2.65575900	3.98758600	-0.43843200
H	4.54036400	2.09829200	-0.47895400
H	0.91600900	0.34585300	0.70776900
H	-4.64085500	2.08530200	0.19348800
H	-2.75698100	3.98560800	0.28886400
H	-0.93747800	0.12684900	-0.14890900
H	-1.62173700	-4.97256900	0.01143700
H	-3.94233000	-3.61880700	0.01130400

Cartesian coordinates of the DFT optimized structure [C-3H]$^{\bullet-}$ in MeCN

C	2.97542300	-3.14618600	0.42697500
C	1.74844000	-3.87301100	0.37350900
C	0.74025500	-2.99706500	-0.06711100
N	1.36886800	-1.79266300	-0.32017900
C	2.71512600	-1.81909900	0.01427800
C	2.50447100	2.94992700	-0.27138000
C	3.49725900	1.96545800	-0.30983100
C	2.89971300	0.69634300	-0.04881100
N	1.51695000	0.95874300	0.14519900
C	1.25360900	2.34217500	0.01088500
C	3.44226400	-0.59461300	-0.01125800
C	-3.58238900	1.94530800	0.13052000
C	-2.60917800	2.92526900	0.19080900
C	-1.30723200	2.30456400	0.09728800
N	-1.55721700	0.93508800	-0.00751200
C	-2.93404400	0.66719500	0.00714300
C	-0.04246500	2.89736900	0.08169500
C	-1.74578300	-3.91866200	-0.06014300
C	-2.96004400	-3.21027800	-0.07024600
C	-2.62412100	-1.81928500	-0.13544500
N	-1.24363100	-1.68327800	-0.18474800
C	-0.70440900	-2.94724900	-0.12517100
C	-3.41249400	-0.63586900	-0.07067800
Cl	5.28057400	-0.72670700	-0.01585700
Cl	-0.05629900	4.75524900	0.10289400
Cl	-5.24271300	-0.84766400	-0.03480100
H	3.93047800	-3.51735000	0.76724700
H	1.60316800	-4.89703500	0.68576600
H	0.88014800	-1.02745100	-0.75401800
H	2.64036600	4.00233900	-0.46516400
H	4.54192400	2.11157100	-0.53620700
H	0.93940300	0.35030800	0.70871600
H	-4.65110100	2.09025300	0.17329700
H	-2.76831900	3.98733800	0.29008400
H	-0.94228100	0.12326700	-0.12900400
H	-1.62410900	-4.99301900	-0.01438400
H	-3.95742200	-3.62411500	-0.02185600

Cartesian coordinates of the DFT optimized structure [C-3H]$^{2-}$ in MeCN

C	2.96872300	-3.12719900	0.53734900
C	1.73053500	-3.86490000	0.47165800
C	0.74428200	-3.00790900	-0.01074500
N	1.38084200	-1.81327000	-0.28236300
C	2.71665700	-1.82607400	0.08401900
C	2.49677000	2.94633600	-0.27845400
C	3.49844400	1.96650300	-0.32478400
C	2.90808300	0.69379800	-0.04238400
N	1.53164700	0.95738700	0.16796400
C	1.26021600	2.34550100	0.02847500
C	3.44282700	-0.58866800	0.01124700
C	-3.57709600	1.95121400	0.13044600
C	-2.59704100	2.92189300	0.20870100
C	-1.30264300	2.30199900	0.11029000
N	-1.55979600	0.92897000	-0.01148200
C	-2.93600800	0.66650100	-0.00305400
C	-0.04105600	2.88371900	0.09752400
C	-1.74019000	-3.91871000	-0.09737500
C	-2.96914400	-3.19987800	-0.12024600
C	-2.62911800	-1.82703900	-0.14512800
N	-1.24931600	-1.68998500	-0.15051200
C	-0.71131200	-2.95869600	-0.10865000
C	-3.41356700	-0.62325400	-0.09416000
Cl	5.28203800	-0.72313700	-0.15011200
Cl	-0.05799600	4.74627700	0.13499000
Cl	-5.24739900	-0.83085600	-0.08450100
H	3.91877200	-3.48934900	0.90367200
H	1.57544900	-4.87849800	0.81513400
H	0.89112300	-1.04212600	-0.70697800
H	2.62384500	3.99885000	-0.48613300
H	4.54106800	2.11397500	-0.56106000
H	0.96420700	0.35292800	0.74478300
H	-4.64611900	2.10104000	0.16764800
H	-2.74961000	3.98540300	0.31671700
H	-0.95007400	0.10633400	-0.10938700
H	-1.62224800	-4.99588500	-0.07724100
H	-3.96914100	-3.61402800	-0.10718500

Cartesian coordinates of the DFT optimized structure [C-4H]$^{-}$ in MeCN

C	3.09935800	-3.12689000	0.10948800
C	1.89173400	-3.90072200	-0.02061100
C	0.82406300	-3.01540700	-0.16552800
N	1.37720400	-1.74015200	-0.15005900
C	2.75165500	-1.77194200	0.03000800
C	2.44908600	3.00255100	-0.14893600
C	3.45858400	2.04868800	-0.18372100
C	2.89399200	0.75498900	0.08986900
N	1.47587800	0.97660800	0.34469400
C	1.20161700	2.39388500	0.15302600
C	3.44852100	-0.50832700	0.06480700
C	-3.60848000	1.87466400	-0.08602000
C	-2.66648800	2.88571100	0.05806900
C	-1.35840900	2.31832400	0.10792700
N	-1.56294400	0.91817800	-0.00115300

C	-2.92855500	0.60129900	-0.10973400
C	-0.09471300	2.91805400	0.14385300
C	-1.57610000	-3.85823000	0.49661800
C	-2.82893300	-3.15069600	0.52646000
C	-2.64155300	-1.90826700	-0.08620700
N	-1.30761700	-1.88914400	-0.53053900
C	-0.63433900	-3.06721700	-0.14669500
C	-3.41500400	-0.69984000	-0.18447900
Cl	5.28390700	-0.61527600	-0.10949900
Cl	-0.14575800	4.78183200	0.10876900
Cl	-5.25368100	-0.91201100	-0.15639600
H	4.09998800	-3.51333800	0.22817900
H	1.82161300	-4.97853300	0.00789200
H	0.88272000	-0.86776100	-0.25807000
H	2.56571800	4.05056300	-0.38272700
H	4.49280300	2.21567800	-0.44179700
H	1.14450900	0.58693500	1.22637700
H	-4.67823300	1.99128300	-0.15843400
H	-2.86951900	3.94464700	0.10397900
H	-0.84250700	0.23179700	0.12512100
H	-1.36998200	-4.79593600	0.99343000
H	-3.73710700	-3.47686400	1.01020500
H	-1.01984000	-1.31794300	-1.31277400

Cartesian coordinates of the DFT optimized structure [C-4H] in MeCN

C	3.04226200	-3.13859700	0.16717400
C	1.83825200	-3.88700200	0.05762400
C	0.78522900	-2.98811700	-0.18458000
N	1.36142400	-1.72942400	-0.24450800
C	2.72624700	-1.77642500	-0.00747700
C	2.48123100	2.97703700	-0.15917500
C	3.47242600	2.01212100	-0.19478600
C	2.89341900	0.72815400	0.06939100
N	1.48288600	0.96160700	0.29950000
C	1.22252800	2.36458100	0.12998800
C	3.44646800	-0.54108100	0.03837300
C	-3.58038800	1.90033700	-0.09184600
C	-2.62687400	2.90307200	0.02964200
C	-1.33020000	2.30923900	0.10639900
N	-1.54770900	0.92481400	0.03559800
C	-2.91686000	0.63029100	-0.08323500
C	-0.05812400	2.91652000	0.14035600
C	-1.62445900	-3.85940100	0.37124200
C	-2.86361300	-3.15734300	0.40890300
C	-2.65744600	-1.87199100	-0.11936300
N	-1.31104000	-1.82252600	-0.52584900
C	-0.65758300	-3.02560400	-0.19358100
C	-3.42609700	-0.67316400	-0.13316700
Cl	5.26490200	-0.66769500	-0.03467100
Cl	-0.09677900	4.75537400	0.09872800
Cl	-5.23886000	-0.86729900	-0.05438400
H	4.02718600	-3.53269600	0.36283500
H	1.74398600	-4.95745500	0.16000500
H	0.88903800	-0.86011100	-0.43275900
H	2.60782200	4.02578500	-0.37789000

H	4.51004900	2.16817400	-0.44606100
H	1.09529300	0.51998500	1.13062700
H	-4.64691900	2.03094000	-0.18235700
H	-2.81293700	3.96479300	0.04514500
H	-0.85019200	0.21809700	0.18000900
H	-1.43882000	-4.83218000	0.80217800
H	-3.78321600	-3.50811100	0.85110700
H	-1.03618800	-1.26073100	-1.32174300

Cartesian coordinates of the DFT optimized structure [C-4H]$^+$ in MeCN

C	-2.99729200	-3.14196900	-0.20895800
C	-1.80393100	-3.86330000	-0.11205000
C	-0.75613600	-2.95321000	0.21361100
N	-1.35505700	-1.71151300	0.32949000
C	-2.70977000	-1.76494700	0.03902800
C	-2.48634000	2.95737200	0.23316000
C	-3.47481200	1.98454100	0.26038400
C	-2.89160600	0.71969400	-0.03268000
N	-1.49527000	0.96254400	-0.25518400
C	-1.23582800	2.34561200	-0.08418500
C	-3.44622200	-0.56579800	-0.03309200
C	3.56497800	1.90987300	0.06874600
C	2.61185300	2.90403300	-0.03505000
C	1.30911900	2.29686200	-0.09885800
N	1.53140900	0.92345500	-0.03090100
C	2.90442300	0.63723600	0.07010800
C	0.04594800	2.91505600	-0.12804500
C	1.64960300	-3.85408400	-0.27298700
C	2.87158200	-3.16391400	-0.31603900
C	2.66131200	-1.84493700	0.16201800
N	1.31131100	-1.77748500	0.55577500
C	0.66156000	-2.98626000	0.24642100
C	3.42520100	-0.66291500	0.10462600
Cl	-5.24475400	-0.70255900	-0.09058700
Cl	0.07632600	4.73607500	-0.11338300
Cl	5.21432700	-0.85080100	-0.05413300
H	-3.96787400	-3.53653200	-0.46657800
H	-1.68593700	-4.92418300	-0.27226700
H	-0.90852500	-0.85645400	0.61546200
H	-2.61295400	4.00205600	0.46864400
H	-4.51075200	2.13302800	0.52425800
H	-1.05310000	0.47004800	-1.02598100
H	4.63199300	2.04600300	0.14956800
H	2.79085300	3.96671200	-0.05264500
H	0.84641500	0.20431700	-0.17613600
H	1.47113700	-4.84615500	-0.66025800
H	3.79625700	-3.53043600	-0.73507800
H	1.05359400	-1.22724200	1.36755000

Cartesian coordinates of the DFT optimized structure [C-2H]$^-$ in MeCN

C	2.97556600	-3.20886700	-0.00005400
C	1.77307800	-3.90818100	0.00011900
C	0.71878200	-2.92117400	0.00013000
N	1.26383800	-1.66881900	0.00023600

C	2.63590800	-1.79968000	-0.00005900
C	2.57587300	2.95145000	0.00011100
C	3.55133900	1.96866000	-0.00008300
C	2.90239800	0.68741800	-0.00017100
N	1.53163100	0.95418800	-0.00047400
C	1.27984600	2.31452700	-0.00001600
C	3.40331500	-0.61967400	-0.00014900
C	-3.53618900	1.96440000	-0.00021100
C	-2.57285400	2.94210200	0.00005500
C	-1.27609900	2.27091800	0.00001300
N	-1.46404300	0.90445200	0.00026900
C	-2.84834500	0.68374000	-0.00004200
C	-0.00346900	2.87749600	0.00003900
C	-1.76815700	-3.91293300	0.00029700
C	-2.98802300	-3.21432000	0.00012900
C	-2.68789300	-1.81447300	0.00012500
N	-1.31545600	-1.72740800	0.00005900
C	-0.70904200	-2.95463500	0.00025800
C	-3.40569700	-0.60417300	-0.00006900
Cl	5.23740500	-0.79962000	-0.00011200
Cl	-0.01096700	4.73886000	0.00025300
Cl	-5.24195600	-0.75270600	-0.00028100
H	3.97356500	-3.62438200	-0.00015200
H	1.65065900	-4.98356400	0.00017700
H	2.73233900	4.01836600	0.00028300
H	4.62049200	2.11686000	-0.00003900
H	0.86371000	0.18395600	-0.00088500
H	-4.60792600	2.10071200	-0.00037900
H	-2.72598700	4.01066300	0.00006800
H	-1.64767000	-4.98686900	0.00036800
H	-3.97934500	-3.64227800	0.00007800
H	-0.84984500	-0.81701900	-0.00030900

Cartesian coordinates of the DFT optimized structure of *p*-toluenesulfonic acid (TsOH) in MeCN

C	-2.70639100	0.00323200	0.01153100
C	-1.98945400	1.21451900	-0.01436600
C	-0.59055900	1.22731600	-0.06625800
C	0.06356100	0.00104800	-0.08928500
C	-0.59327000	-1.22559600	-0.06585800
C	-1.99039300	-1.21080700	-0.01450300
H	-2.52700300	2.15740900	0.00561000
H	-0.03167000	2.15588800	-0.09389400
H	-0.03504600	-2.15457100	-0.09319800
H	-2.52953400	-2.15317200	0.00517100
C	-4.21766700	-0.00153700	0.04661300
H	-4.61491800	0.98190600	0.31519000
H	-4.63149400	-0.27061900	-0.93432300
H	-4.59733000	-0.73077500	0.77115400
S	1.92056700	-0.00065400	-0.14691400
O	2.49143300	1.40635000	-0.72948000
O	2.48835300	-1.40934400	-0.72839600
O	2.17480600	-0.00007200	1.66747600
H	3.14622500	-0.00013000	1.85086500

Cartesian coordinates of the DFT optimized structure of tosylate (TsO^{-}) in MeCN

C	-2.68689900	-0.00053100	-0.00000200
C	-1.96233400	-1.21002400	-0.00000300
C	-0.56315200	-1.21004900	0.00000900
C	0.11218400	0.00904500	-0.00000800
C	-0.56754900	1.22035200	-0.00001500
C	-1.97172600	1.20918700	0.00001300
H	-2.49915400	-2.15672900	0.00001100
H	0.00065100	-2.13690300	0.00002500
H	0.00748700	2.14082400	-0.00000400
H	-2.51521200	2.15177400	0.00002000
C	-4.20256300	-0.01183700	-0.00000500
H	-4.60078100	-0.52821000	-0.88413600
H	-4.60079200	-0.52840700	0.88400500
H	-4.60518800	1.00743700	0.00011100
S	2.00583100	0.00433500	-0.00001100
O	2.41758300	-0.81555100	-1.39042200
O	2.41756900	-0.81561400	1.39039900
O	2.38633900	1.62416400	0.00004900

Cartesian coordinates of the DFT optimized structure of benzoic acid (HBza) in MeCN

C	1.91840800	1.18571100	0.00020900
C	0.52221900	1.23209600	0.00020100
C	0.44264400	-1.20375800	-0.00013000
C	1.84045100	-1.24395100	-0.00022300
C	2.57929500	-0.05196300	-0.00003200
H	2.48996600	2.10824400	0.00040700
H	-0.00720900	2.17850400	0.00030300
H	-0.13806200	-2.11804000	-0.00019400
H	2.35229500	-2.20099600	-0.00043900
H	3.66450800	-0.08699200	-0.00008600
C	-0.22101000	0.03713500	0.00003600
H	-3.29482600	-0.98931700	0.00021700
C	-1.69364200	0.12962600	-0.00003000
O	-2.35336200	1.17948000	-0.00047500
O	-2.32124600	-1.10457800	0.00042600

Cartesian coordinates of the DFT optimized structure of benzoate (Bza^{-}) in MeCN

C	1.21256700	-1.83910900	0.00000000
C	1.20966500	-0.43706400	0.00000000
C	-1.20967000	-0.43704300	0.00000000
C	-1.21259600	-1.83909300	0.00000000
C	-0.00002200	-2.54719600	0.00000000
H	2.15679400	-2.38073800	0.00000000
H	2.13042200	0.13740100	0.00000000
H	-2.13042500	0.13742600	0.00000000
H	-2.15683600	-2.38070000	0.00000000
H	-0.00002600	-3.63537900	0.00000000
C	0.00000000	0.27882500	0.00000000
C	0.00001400	1.81723200	0.00000000
O	1.15396700	2.38390700	0.00000000
O	-1.15392600	2.38392800	0.00000000

Chapter 4: Study of Multielectron Redox Chemistry through Quadruply Bonded Non–Symmetric Dimolybdenum Systems

Cartesian coordinates of the DFT optimized of model structure for 1

N	-4.55000300	0.97209400	2.15758200
C	-4.52553300	-0.17620700	2.82058500
Mo	-4.72523600	-1.23375300	-0.00121500
Mo	-4.63290900	0.90319100	0.00133800
N	-4.64616400	-1.31170300	-2.15773800
N	-4.54952500	0.97722300	-2.15478000
C	-4.52519300	-0.16951400	-2.82047600
N	-6.86652400	-1.21742800	-0.00151200
N	-6.76832400	1.07032100	0.00101800
C	-7.48788100	-0.04489300	-0.00041500
N	-4.64624000	-1.31682800	2.15511000
Mo	4.29713700	0.38720100	0.00120700
Mo	4.04496400	-1.73713700	-0.00178800
N	6.16925100	-2.06191600	-0.00272900
N	6.44749900	0.21292500	0.00054900
C	6.97138600	-1.00480000	-0.00166100
N	4.29262700	0.46254500	-2.16464900
N	3.99409000	-1.80817900	-2.15955200
N	3.99464400	-1.81456600	2.15584200
N	4.29318100	0.45613600	2.16739300
C	4.11609700	-0.67918500	2.82899500
C	4.11514000	-0.67081900	-2.82947400
H	-4.39881900	-0.18275200	3.90928500
H	-4.39817800	-0.17350400	-3.90915200
H	-8.58226500	0.00200600	-0.00048100
H	8.05894500	-1.13916000	-0.00233400
H	4.06428600	-0.67827300	3.92381900
H	4.06280200	-0.66669500	-3.92426600
C	-1.47737000	0.45132700	0.00109400
C	-1.54205400	-1.03714800	-0.00041900
C	-0.33308400	-1.74586000	-0.00098300
C	0.92609200	-1.13400700	-0.00035500
C	1.00053800	0.35637400	0.00119500
C	-0.22238900	1.06460700	0.00204000
H	-0.37017900	-2.83049900	-0.00213500
H	-0.21695800	2.14768600	0.00366300
N	2.20192500	0.96316700	0.00196100
O	1.98413300	-1.87353100	-0.00138400
O	-2.55428300	1.16716500	0.00205400
O	-2.66755700	-1.66317100	-0.00137600
C	2.22547200	2.39252400	0.00160400
C	2.27296100	3.10423900	1.21156700
C	2.37376100	4.49629800	1.20772500
C	2.42444700	5.19749800	0.00040300
C	2.36541900	4.49580300	-1.20633300
C	2.26462500	3.10382000	-1.20897500
H	2.22231900	2.54951500	2.14329500
H	2.40758400	5.03484300	2.15156900
H	2.50277900	6.28125100	-0.00007500
H	2.39279500	5.03401000	-2.15058000
H	2.20780900	2.54871300	-2.14013400

H	-4.41408300	1.78998400	2.74272700
H	-4.58083700	-2.14440000	2.73876700
H	-7.49195300	-2.01685000	-0.00242000
H	-7.32317500	1.92024100	0.00203600
H	-4.41321200	1.79644200	-2.73797600
H	-4.58092400	-2.13784400	-2.74345000
H	4.38427700	1.28083100	-2.75740100
H	3.82194300	-2.61860400	-2.74543600
H	6.65745300	-2.95155000	-0.00424100
H	7.13546200	0.95893900	0.00169000
H	4.38541200	1.27261600	2.76253900
H	3.82254500	-2.62664400	2.73944100

Cartesian coordinates of the DFT optimized of model structure for 2

Mo	-4.05693900	1.06930500	-0.00002300
Mo	-4.05700200	-1.06934900	-0.00051300
N	-4.08370700	1.14423100	2.16665600
N	-4.08391400	-1.14511400	2.16613500
N	-1.94443400	-1.43955700	-0.00041600
N	-6.22181800	-1.14685800	-0.00042500
N	-4.08409200	-1.14409700	-2.16721800
N	-4.08377200	1.14523400	-2.16655500
N	-1.94440000	1.43956600	0.00000100
N	-6.22173200	1.14696400	0.00003900
C	-4.10177400	-0.00060000	2.83401900
C	-0.78812900	-0.74495200	-0.00022300
C	-1.86369700	-2.86856200	0.00015200
C	-6.88675100	0.00007600	-0.00014100
C	-4.10192900	0.00076400	-2.83453700
C	-0.78812000	0.74494400	-0.00014900
C	-1.86364500	2.86856300	0.00042100
H	-4.12679000	-0.00084200	3.92992400
C	0.46579300	-1.39536100	-0.00016900
C	-1.85340300	-3.58115700	1.21077300
C	-1.85592200	-3.58228300	-1.20980100
H	-7.98317400	0.00011900	-0.00007000
H	-4.12695500	0.00109300	-3.93043700
C	0.46579900	1.39535700	-0.00023200
C	-1.85377200	3.58130200	1.21095500
C	-1.85543500	3.58211800	-1.20961400
C	1.70021400	-0.74168100	-0.00017500
H	0.50254200	-2.47725700	-0.00022500
C	-1.85342400	-4.97678100	1.20824900
H	-1.83665300	-3.02329700	2.14183700
C	-1.85594800	-4.97793100	-1.20596400
H	-1.84103100	-3.02531500	-2.14142700
C	1.70021900	0.74167600	-0.00031000
H	0.50254600	2.47725400	-0.00032600
C	-1.85375200	4.97693100	1.20826400
H	-1.83737200	3.02354300	2.14208800
C	-1.85541500	4.97776400	-1.20595300
H	-1.84028400	3.02503000	-2.14116800
O	2.79860900	-1.42139400	-0.00014100
C	-1.85894200	-5.68089800	0.00146700
H	-1.84322700	-5.51560100	2.15249200

H	-1.84769100	-5.51763100	-2.14972400
O	2.79862000	1.42137900	-0.00056600
C	-1.85881000	5.68089200	0.00139000
H	-1.84387800	5.51585600	2.15245000
H	-1.84681600	5.51733900	-2.14978200
Mo	4.87239600	-1.06910800	0.00001400
H	-1.85830700	-6.76748600	0.00198000
Mo	4.87242800	1.06908500	-0.00030800
H	-1.85812800	6.76748000	0.00174800
N	4.78820300	-1.14516400	2.15660400
N	4.78866700	-1.14573000	-2.15659300
N	7.01279200	-1.14474900	0.00022900
N	7.01283000	1.14467400	-0.00011300
N	4.78869800	1.14513900	-2.15692900
N	4.78823600	1.14571300	2.15628400
C	4.71446800	0.00037400	2.82071300
C	4.71509400	-0.00039800	-2.82104700
C	7.68448500	-0.00005000	0.00010600
H	4.58598800	0.00052400	3.90940300
H	4.58692800	-0.00055500	-3.90977300
H	8.77995700	-0.00006900	0.00018600
H	4.68579600	-1.96845300	2.74101000
H	4.68603000	1.96918100	2.74047300
H	7.60348600	1.97015600	-0.00025300
H	7.60341300	-1.97025500	0.00044400
H	4.68653900	-1.96920800	-2.74078000
H	4.68654000	1.96842900	-2.74137600
H	-4.10615400	1.97068100	-2.75593700
H	-6.81607100	1.96929700	0.00026400
H	-6.81622200	-1.96914600	-0.00054100
H	-4.10642800	1.96929600	2.75655700
H	-4.10659300	-1.97048700	2.75560300
H	-4.10708900	-1.96913300	-2.75714900

Cartesian coordinates of the DFT optimized 3

N	4.21660100	1.21170300	-1.97293000
C	3.94686500	0.08590100	-2.62614700
C	3.79415100	-2.27021100	-2.76505700
C	4.04062800	2.44883300	-2.64599500
C	4.57735300	2.68361500	-3.92520700
C	3.34156700	3.48832000	-2.01996700
C	3.17485200	4.72799200	-2.64325000
C	4.40625500	3.90898200	-4.55616500
C	3.70540800	4.94363900	-3.92012700
C	3.03782200	-3.28343700	-2.16000700
C	2.74253700	-4.47055700	-2.83594300
C	3.19834900	-4.66093900	-4.14548600
C	4.25622800	-2.48148000	-4.07863700
O	3.59849300	6.11176300	-4.62435100
O	2.96665200	-5.77829400	-4.90005200
Mo	4.78490800	-1.08941700	0.03676100
Mo	4.84227200	1.03524200	0.10042400
N	5.25245500	-1.27323400	2.15271000
N	5.29307900	1.03896100	2.23278100
C	5.37116400	-0.14186800	2.84154600

C	5.15032900	-2.49312600	2.87387300
C	5.49116300	2.21039200	3.00716700
C	6.58176600	2.35098300	3.88662700
C	4.60165100	3.28564900	2.87960000
C	6.76218200	3.51849700	4.61806200
C	4.78255300	4.46697700	3.60405000
C	5.86539800	4.58816900	4.48274500
C	4.30958100	-2.62252500	3.99615300
C	5.86630500	-3.61973300	2.45098000
C	5.76415900	-4.83877600	3.12654500
C	4.93781700	-4.94803800	4.25061300
C	4.21127400	-3.82797900	4.67927400
O	4.76745000	-6.08770000	4.98831700
O	6.13694500	5.69359100	5.24153900
N	6.86397600	-1.21439400	-0.55338000
N	6.91686500	1.09926300	-0.47816900
C	7.52106400	-0.06507000	-0.69841600
C	7.60540100	-2.42034900	-0.67111900
C	7.62217600	2.29138900	-0.79857900
C	7.59876900	3.37855500	0.08306900
C	8.33274800	2.42994700	-2.00589100
C	9.01051500	3.60489800	-2.30449700
C	8.98430000	4.68584500	-1.41198800
C	8.26851000	4.56793000	-0.21537800
O	9.67966800	5.79769100	-1.80104300
C	5.47556000	-7.24882300	4.59334600
C	2.19556900	-6.82033200	-4.32884900
C	2.91350600	7.19377300	-4.02031100
C	5.25650700	6.79916100	5.14848700
C	9.67019000	6.92365600	-0.94210600
C	7.08818400	-3.49485100	-1.40574900
C	7.78594000	-4.70053600	-1.51721200
C	9.02946200	-4.84964400	-0.89261700
C	9.55496900	-3.78281500	-0.14948300
O	9.79778900	-5.98033300	-0.93929100
C	8.85054900	-2.59077600	-0.03450400
C	9.31519400	-7.08367900	-1.68530300
C	3.95695900	-3.65436600	-4.76063200
N	4.10611600	-1.09585000	-2.03470400
H	3.54503000	0.13372700	-3.64278800
H	5.15330600	1.90267700	-4.41352300
H	2.89529000	3.30967100	-1.04563700
H	2.62023300	5.50547900	-2.12990200
H	4.82378600	4.09480000	-5.54097300
H	2.65130500	-3.12342500	-1.15743800
H	2.14764500	-5.22622800	-2.33534000
H	4.87496500	-1.72651100	-4.55535500
H	5.51902600	-0.18192600	3.92511300
H	7.30314500	1.54362900	3.97484600
H	3.73995900	3.17919800	2.22653100
H	7.60424600	3.63016100	5.29428600
H	4.06707900	5.27279300	3.48427100
H	3.71169000	-1.77411800	4.31631400
H	6.53173700	-3.53712300	1.59756900
H	6.34338600	-5.68405400	2.77247500
H	3.56159900	-3.93000100	5.54321400

H	8.57040400	-0.07851400	-1.00511400
H	7.07237700	3.28706800	1.02796600
H	8.33101800	1.61463400	-2.72357200
H	9.55594000	3.71474400	-3.23679800
H	8.23297300	5.38262100	0.49898400
H	5.19650700	-8.02856200	5.30497700
H	6.56258100	-7.09498800	4.63380100
H	5.19781600	-7.56836500	3.57944200
H	2.13167300	-7.59994900	-5.09056800
H	1.18252300	-6.48161900	-4.07252500
H	2.67276100	-7.23230000	-3.42892500
H	2.95405200	8.01498100	-4.73878400
H	3.39617700	7.50776100	-3.08452300
H	1.86302200	6.94577000	-3.81478600
H	5.65238700	7.55741700	5.82702100
H	4.23694100	6.53320200	5.45926000
H	5.22412200	7.20784900	4.12902400
H	10.26916100	7.68819200	-1.44107900
H	10.11865400	6.69367700	0.03412300
H	8.65211100	7.30615400	-0.78629100
H	6.13825700	-3.38100700	-1.91830300
H	7.35342100	-5.50325800	-2.10365700
H	10.51325200	-3.91548500	0.34337300
H	9.25290700	-1.78696400	0.57518600
H	10.07327800	-7.86403600	-1.59325800
H	9.18419800	-6.83006600	-2.74602700
H	8.36160000	-7.45709800	-1.28722300
H	4.31500300	-3.81984500	-5.77221500
O	2.74910900	1.13790800	0.64978600
O	2.70140400	-1.09962500	0.62198700
C	2.12697400	0.02897700	0.79412600
C	-1.33854000	1.29743300	1.64925100
C	0.00905500	1.27137400	1.31018700
C	0.69093800	0.05318500	1.17142800
C	-0.00857700	-1.14310400	1.39042300
C	-1.35575200	-1.12643000	1.73298400
C	-2.03048500	0.09603600	1.85912800
H	-1.85958100	2.24406100	1.75575500
H	0.54893000	2.19702500	1.14372300
H	0.51862800	-2.08533000	1.28863100
H	-1.88877800	-2.05631000	1.90611200
N	-3.37688400	0.12376300	2.29885000
C	-10.73558500	-0.71674500	-1.62413100
C	-10.89481200	-1.38146400	-0.34128200
C	-11.03286600	-0.62469400	0.82421900
C	-11.02297800	0.82842800	0.75302700
C	-10.87538900	1.46582600	-0.48073900
C	-10.72616000	0.67698500	-1.69245900
C	-9.79424800	-1.49050100	-2.41675800
C	-9.37420700	-2.63405100	-1.62562100
C	-10.05476300	-2.56654100	-0.34205700
C	-9.38727000	-2.94863200	0.82343200
C	-10.33494500	-1.01956200	2.03409600
C	-10.31906400	1.33009700	1.91905400
C	-9.49758700	2.45263000	1.81040500
C	-9.34607300	3.11859700	0.52628100

C	-10.01946700	2.63368900	-0.59674600
C	-9.33890500	2.56631600	-1.88035600
C	-9.77498500	1.35677400	-2.55640800
C	-8.86707300	0.61470900	-3.31476900
C	-8.87696600	-0.83848300	-3.24354100
C	-8.05278600	-3.08054900	-1.69298500
C	-7.09705000	-2.39967800	-2.55199600
C	-7.50256200	-1.30051100	-3.30991300
C	-6.64091000	-0.13379200	-3.41603000
C	-7.48659000	1.04934500	-3.42515600
C	-7.06570800	2.21159000	-2.77773500
C	-8.01155400	2.98609100	-1.99008800
C	-7.31246700	3.48844500	-0.82052600
C	-7.96540100	3.55352000	0.40986300
C	-9.88675900	0.18810100	2.70880800
C	-5.50060300	1.60385200	2.38094600
C	-6.40960600	0.92741400	3.18155900
C	-6.41948000	-0.54852500	3.25378100
C	-5.52007700	-1.31215100	2.52375200
C	-4.41660900	-0.69497100	1.72846600
C	-4.39179700	1.48465800	0.27662200
C	-5.27141100	2.62819000	0.27429200
C	-5.95230500	2.69703000	1.55686400
C	-7.27050600	3.15412400	1.62238900
C	-8.21079300	2.47754100	2.48498900
C	-7.78803900	1.37682400	3.23847700
C	-7.80385100	-0.97145000	3.35350400
C	-8.24197700	-2.13457600	2.71073700
C	-7.31151400	-2.90491400	1.91908800
C	-5.98717300	-2.47448500	1.81021100
C	-5.30651900	-2.54033600	0.52733000
C	-4.41163000	-1.41406600	0.41837600
C	-4.27753900	-0.75963700	-0.79719600
C	-4.26750300	0.71288300	-0.86919500
C	-5.93761900	3.02050200	-0.88958400
C	-5.78414000	2.23652200	-2.09331000
C	-4.97181600	1.09786300	-2.07706300
C	-5.41334200	-0.10958800	-2.75316200
C	-4.98778100	-1.25115200	-1.96210900
C	-5.81555900	-2.37479200	-1.86749000
C	-5.97883100	-3.03526800	-0.59304600
C	-7.35980100	-3.47571300	-0.47948700
C	-8.01267200	-3.41141600	0.75097200
C	-8.64699300	0.21106100	3.34898900
C	-9.52890200	-2.15842100	2.03626700
C	-4.40633800	0.89700800	1.65070300

Cartesian coordinates of the DFT optimized of model structure for 4

N	3.95637773	-1.25448639	-0.07369877
N	3.93364567	1.30577568	0.12511266
C	2.71287631	-0.71112654	-0.02905731
C	4.39691481	-2.58558828	-0.07546806
C	2.72611372	0.78741425	0.08032214
C	4.21064694	2.67063435	0.09212064
C	1.51619626	-1.39121118	-0.12827901

C	3.69572363	-3.63464863	0.54236440
C	5.63740059	-2.85845055	-0.67986856
C	1.46812009	1.44297014	0.16900109
C	5.25618970	3.14634727	0.91052075
C	3.58464987	3.58495760	-0.78272070
C	0.27141742	-0.71202715	-0.07248888
H	1.47842906	-2.46222737	-0.27880558
C	4.21879452	-4.92767259	0.52421715
H	2.76871569	-3.43461223	1.06555503
C	6.15323961	-4.15094628	-0.68318754
H	6.18436698	-2.04774258	-1.15468808
C	0.25618735	0.76959736	0.11188608
H	1.43786905	2.51707769	0.30683242
C	5.63135633	4.48635332	0.88758071
H	5.75471987	2.43887521	1.56698776
C	3.98086931	4.92093254	-0.81491726
H	2.80958576	3.23141443	-1.45514601
O	-0.80833954	-1.38563035	-0.17721371
C	5.44312650	-5.19775993	-0.08893995
H	3.66520593	-5.72762743	1.00895558
H	7.11186414	-4.34140572	-1.15834608
O	-0.87337114	1.40072668	0.21573908
C	4.99638972	5.38498352	0.02473905
H	6.43064676	4.83047456	1.53960605
H	3.49182817	5.60469564	-1.50491293
Mo	-2.89426838	-1.10004097	-0.15637133
H	5.84263807	-6.20769724	-0.09796669
Mo	-2.91548140	1.01824308	0.15705407
H	5.29646724	6.42901292	-0.00045409
N	-2.80105339	-0.86363278	-2.30058062
N	-2.82958849	-1.49235021	1.96728129
N	-5.03006720	-1.19415556	-0.18329031
N	-5.05597403	1.07092083	0.15289904
N	-2.85612444	0.77470912	2.29761587
N	-2.83588395	1.40238142	-1.96371062
C	-2.74807437	0.36811465	-2.78904911
C	-2.78005761	-0.45417763	2.79067024
C	-5.71312358	-0.06900966	-0.02031694
H	-2.62485046	0.52993788	-3.86558772
H	-2.66918041	-0.60991310	3.86944041
H	-6.80804242	-0.08078856	-0.02858298
H	-2.70134885	-1.59072701	-3.00146112
H	-2.74870568	2.30482476	-2.41974918
H	-5.65533134	1.88158569	0.26990507
H	-5.61037074	-2.01725201	-0.30949282
H	-2.74075833	-2.39111459	2.43007257
H	-2.77186015	1.50701427	2.99520283
H	4.66222177	-0.51131905	-0.08041576

Cartesian coordinates of the DFT optimized of model structure for 4^{-}

N	3.94569988	-1.25514925	-0.30608139
N	3.93778398	1.28336645	0.18844607
C	2.67938082	-0.69323413	-0.15889583
C	4.41167121	-2.54741468	-0.18305350
C	2.70447207	0.74849753	0.09153758

C	4.22872403	2.62336336	0.14017979
C	1.47034293	-1.35303877	-0.31668460
C	3.64722230	-3.64143844	0.28262387
C	5.76582159	-2.79225108	-0.52127375
C	1.44776320	1.38069309	0.26763494
C	5.42846575	3.05502628	0.76986777
C	3.49647336	3.61776335	-0.56674086
C	0.22210660	-0.70095715	-0.16542873
H	1.43035945	-2.39793413	-0.60031478
C	4.21607886	-4.91053889	0.37958682
H	2.62521577	-3.48560732	0.60163016
C	6.31795126	-4.06199068	-0.41397899
H	6.37132128	-1.96135558	-0.87718107
C	0.21828931	0.72060763	0.16934560
H	1.41212741	2.43277198	0.52785155
C	5.84902190	4.37836390	0.72396715
H	6.01015108	2.30398780	1.29877232
C	3.93407664	4.93918696	-0.61699666
H	2.59805961	3.32921607	-1.10160014
O	-0.87003886	-1.40916295	-0.33631005
C	5.54808547	-5.14372325	0.03080239
H	3.60110399	-5.73030946	0.74666329
H	7.36164755	-4.21034943	-0.68504828
O	-0.89514998	1.39444418	0.38379531
C	5.10538903	5.34308152	0.03184397
H	6.77026250	4.66385554	1.23069926
H	3.34877542	5.66728915	-1.17775491
Mo	-2.92546838	-1.07481259	-0.26134534
H	5.97792176	-6.13919339	0.10590677
Mo	-2.94059600	0.99801738	0.27805082
H	5.43426706	6.37911235	-0.00590907
N	-2.82683025	-0.60278415	-2.37752464
N	-2.84710713	-1.69388566	1.81819566
N	-5.08479576	-1.16081163	-0.29308470
N	-5.10465115	1.05872010	0.28521869
N	-2.85287451	0.52554424	2.39540604
N	-2.83876872	1.61670100	-1.80135902
C	-2.72730588	0.67339276	-2.72477220
C	-2.74980143	-0.74857558	2.74338844
C	-5.76357258	-0.05507674	-0.00820491
H	-2.54448979	0.94596276	-3.77248627
H	-2.57614115	-1.02127910	3.79266085
H	-6.86139153	-0.06330710	-0.01583024
H	-2.66452499	-1.24910989	-3.14272587
H	-2.67219654	2.55473233	-2.15055838
H	-5.70892948	1.84887163	0.48795043
H	-5.67573054	-1.95888592	-0.50406763
H	-2.69279906	-2.63169992	2.17360649
H	-2.68891699	1.17406399	3.15837946
H	4.63698906	-0.50001274	-0.26516302

Cartesian coordinates of the DFT optimized of model structure for 5

N	7.07492127	-1.04728920	0.05630894
N	6.87039517	1.51961497	0.08831159
C	5.80007703	-0.58693595	0.07815831

C	7.59795922	-2.34883108	0.12043798
C	5.70680028	0.91030692	0.10323638
C	7.04101694	2.89555971	-0.04926579
C	4.65127528	-1.35446172	0.01756642
C	6.97459922	-3.39496741	0.82010898
C	8.83766520	-2.58316092	-0.49946461
C	4.40341517	1.47804774	0.18670312
C	8.07293052	3.50460574	0.69420050
C	6.31944206	3.69288979	-0.96412199
C	3.36701183	-0.76128950	0.03565118
H	4.69066727	-2.43114563	-0.08470592
C	7.57348641	-4.65371801	0.86680949
H	6.04909371	-3.21619841	1.35401721
C	9.43014062	-3.84118795	-0.43747289
H	9.32342324	-1.77303405	-1.03752020
C	3.24866352	0.71537370	0.17447352
H	4.29712321	2.55172528	0.28406709
C	8.34210626	4.86362995	0.56310263
H	8.64512363	2.88617225	1.37967137
C	6.61105667	5.04825240	-1.10588530
H	5.55577479	3.23350222	-1.58343129
O	2.33383452	-1.51513236	-0.06158508
C	8.79774327	-4.88795470	0.23848372
H	7.08111688	-5.45318790	1.41398927
H	10.38716116	-4.00485545	-0.92539500
O	2.07423364	1.27297015	0.28947560
C	7.61323477	5.64612524	-0.33791489
H	9.13233988	5.31367281	1.15892158
H	6.05140924	5.64104636	-1.82548162
Mo	0.26040717	-1.34674041	-0.17696231
H	9.25729857	-5.87109452	0.28075928
Mo	0.10023735	0.77374410	0.12357140
H	7.83190123	6.70463812	-0.44843599
N	0.42535502	-1.10222510	-2.30369255
N	0.14352450	-1.72491506	1.93585179
N	-0.04458049	0.53280651	2.25339442
N	0.20955495	1.15361437	-1.99117244
C	0.35908264	0.12171572	-2.80935662
C	0.01215262	-0.69242918	2.75685294
H	0.42605347	0.27756923	-3.89106474
H	-0.04912416	-0.84939223	3.83876356
H	0.52460277	-1.83803653	-2.99561301
H	0.17936287	2.05614579	-2.45424293
H	0.16882547	-2.62856174	2.39709240
H	-0.13465089	1.26790271	2.94733439
H	7.73276210	-0.26435398	-0.00396238
C	-4.03904507	-2.00719728	-0.47866522
C	-2.88024565	-1.27991782	-0.32320505
C	-2.99961109	0.17891769	-0.09378717
C	-4.28934540	0.76606332	-0.04198254
C	-5.45032717	0.02903038	-0.17467331
C	-5.36154578	-1.46205422	-0.37653675
H	-3.96972586	-3.07636388	-0.64462611
H	-4.32030982	1.84399621	0.05206467
O	-1.97505721	0.93732620	0.03394247
O	-1.70187505	-1.84944879	-0.38159683

N	-6.69305099	0.59366571	-0.20584938
H	-7.44561221	-0.02734110	-0.47762228
N	-6.36353099	-2.29037865	-0.50918703
C	-7.09791350	1.91543908	0.07820188
C	-8.18824549	2.43276898	-0.64012090
C	-6.51193838	2.69233003	1.09008759
C	-8.67174289	3.70901707	-0.36306293
H	-8.64715244	1.82874640	-1.41861020
C	-6.99710311	3.97346999	1.35043614
H	-5.70489455	2.28558428	1.68817039
C	-8.07325088	4.49144323	0.62729683
H	-9.51541758	4.09423759	-0.92905474
H	-6.53577840	4.56412883	2.13731251
H	-8.44537388	5.48981406	0.83774834
C	-7.71592733	-2.10419610	-0.25653135
C	-8.65019098	-2.26511393	-1.30409407
C	-8.21379284	-1.90092271	1.05249919
C	-10.01999751	-2.19385847	-1.05412377
H	-8.27619723	-2.44997321	-2.30683870
C	-9.58517309	-1.84896287	1.29027153
H	-7.50710330	-1.80421157	1.87184218
C	-10.49940818	-1.98779883	0.24187735
H	-10.71756621	-2.31245943	-1.87973406
H	-9.94217178	-1.69858554	2.30629951
H	-11.56756780	-1.94438685	0.43391385

Cartesian coordinates of the DFT optimized of model structure for 5^-

N	7.04924327	-1.09724740	0.06985820
N	6.87997666	1.47087674	0.23365715
C	5.75929212	-0.60879533	0.08460738
C	7.57418604	-2.36913062	0.24914389
C	5.69166930	0.86279146	0.16326050
C	7.08437804	2.82753109	0.08012889
C	4.60009604	-1.35584925	-0.04622049
C	6.86986726	-3.44912273	0.81916177
C	8.92043259	-2.57703246	-0.12484903
C	4.39627271	1.43827684	0.21384095
C	8.17548258	3.40741511	0.77367813
C	6.35884566	3.67264996	-0.79782274
C	3.32006706	-0.75385026	-0.03995734
H	4.62924514	-2.42702484	-0.20083521
C	7.49178674	-4.68691372	0.98071955
H	5.85552174	-3.30858675	1.16943622
C	9.52914084	-3.81436046	0.04914437
H	9.47537506	-1.75053664	-0.56289475
C	3.22395514	0.69064529	0.12996992
H	4.29068652	2.50907500	0.34409346
C	8.50004466	4.75151245	0.62778197
H	8.75121441	2.76339090	1.43314843
C	6.70089218	5.01478309	-0.94900621
H	5.54634019	3.25478993	-1.38292033
O	2.26950411	-1.51914604	-0.19104214
C	8.81859439	-4.88790494	0.59654093
H	6.92646801	-5.50227729	1.42659229
H	10.56653929	-3.94295517	-0.25162456

O	2.05249591	1.29709458	0.20491791
C	7.76443246	5.57303443	-0.23415698
H	9.33827566	5.16334331	1.18698542
H	6.12865673	5.63242198	-1.63904948
Mo	0.24067195	-1.30999947	-0.33444354
H	9.29173526	-5.85766326	0.72416259
Mo	0.09369251	0.81708190	-0.01009403
H	8.02036866	6.62303999	-0.35219827
N	0.43956959	-1.03689006	-2.46410750
N	0.06291439	-1.71105803	1.77941997
N	-0.09512606	0.54676636	2.12163887
N	0.26024769	1.21971109	-2.12525654
C	0.40654783	0.19470483	-2.95000761
C	-0.07436499	-0.68559905	2.60571211
H	0.49978460	0.36382562	-4.02912769
H	-0.17048993	-0.85564786	3.68444773
H	0.54258016	-1.76413252	-3.16355181
H	0.25269000	2.12772894	-2.57703810
H	0.05557759	-2.61993766	2.22952898
H	-0.19777017	1.27342013	2.82176414
H	7.70314172	-0.30917213	0.05292733
C	-4.05275821	-1.90019377	-0.69356409
C	-2.88109245	-1.17746282	-0.52600493
C	-2.98251249	0.25451513	-0.29198551
C	-4.26653839	0.84276800	-0.27044104
C	-5.43522413	0.10438616	-0.40166912
C	-5.36214714	-1.34977077	-0.58981310
H	-3.98137199	-2.97002649	-0.86068678
H	-4.29912520	1.92371147	-0.20090446
O	-1.93790954	1.03100571	-0.13580512
O	-1.70739779	-1.79510576	-0.57790967
N	-6.68892833	0.70399335	-0.50229979
H	-7.40162843	0.10163044	-0.89148971
N	-6.39983758	-2.17747119	-0.77685624
C	-7.16535423	1.90488041	0.01406659
C	-8.39297379	2.39428456	-0.48160237
C	-6.52061975	2.63532384	1.03221345
C	-8.94452090	3.57126597	0.01160823
H	-8.90611401	1.83545280	-1.26101845
C	-7.08170485	3.81859484	1.51043489
H	-5.60105341	2.26141686	1.46521958
C	-8.29061186	4.30338731	1.00756479
H	-9.89251622	3.92161891	-0.39037377
H	-6.56473805	4.36155113	2.29855129
H	-8.71728870	5.22841239	1.38546333
C	-7.65477063	-2.08015323	-0.23280390
C	-8.75395973	-2.60243609	-0.96703905
C	-7.93165088	-1.60479520	1.08039908
C	-10.04014456	-2.61841451	-0.43794883
H	-8.55465041	-2.99205704	-1.96178339
C	-9.22075904	-1.63846076	1.60209271
H	-7.10859139	-1.23120010	1.68310190
C	-10.29200388	-2.13687006	0.85195587
H	-10.85685291	-3.01862120	-1.03648840
H	-9.39221940	-1.27071285	2.61231356
H	-11.29668811	-2.15710280	1.26635856

Chapter 5: Redox Potential Tuning of Dimolybdenum Systems through Systematic Substitution by Guanidinate Ligands

Cartesian coordinates of the DFT optimized structure III

Mo	1.05396100	0.04099000	0.08067800
Mo	-1.06502200	0.16863800	-0.10435800
C	2.00711800	-2.24434300	2.14587200
C	-2.66192200	-1.90143200	1.80684500
C	2.25185000	1.98787900	2.37994500
O	-6.08730100	3.85991800	3.21054700
O	6.34874500	3.95709500	-2.70271400
O	-5.06781000	3.96810800	-4.69152600
N	1.16204700	-1.53358600	-1.46047600
N	-1.16206300	-1.49358900	-1.53982100
C	2.01978600	-3.64849300	2.17022600
N	0.90907600	-1.51074700	1.62034300
N	-1.40245300	-1.34322600	1.44548100
N	1.10863400	1.59664200	1.62864800
N	-1.19828400	1.76299000	1.39778000
N	1.41898100	1.55813900	-1.45983500
N	-0.88872200	1.64947200	-1.73287600
C	0.00837700	-1.98194400	-1.95036500
C	3.11907700	-4.36308600	2.66138200
C	4.24798300	-3.67640900	3.12606500
C	3.15208800	-1.56952300	2.61512400
C	4.25328000	-2.27251900	3.09224700
O	5.37954200	-4.26699900	3.61790700
C	5.41871600	-5.68140200	3.68316100
C	-2.34300400	-2.19669500	-1.89315300
C	-2.37040400	-3.57779800	-2.15431300
C	-3.57293600	-1.50842200	-1.94130500
C	-4.76183900	-3.52980700	-2.56195100
C	-4.75691700	-2.15704600	-2.26866600
C	-3.55635800	-4.23805600	-2.49741500
C	-0.31575600	-1.90030400	1.97503100
C	-2.87441000	-3.29563100	1.82831600
C	-3.74435900	-1.07031300	2.12326400
C	-4.10983300	-3.82884400	2.17791300
C	-5.18455100	-2.98547700	2.49984200
C	-4.99506500	-1.59838400	2.46358000
O	-6.35824900	-3.61051800	2.82318700
C	-7.48092400	-2.80092800	3.12320000
C	2.35144800	-2.00489900	-2.07904000
C	2.49193300	-2.06360000	-3.47455600
C	3.67487500	-2.51544400	-4.07258100
C	4.75710000	-2.90487100	-3.27371000
C	4.63360800	-2.83465300	-1.87593500
C	3.45145700	-2.39606400	-1.28907300

O	5.96028100	-3.35401000	-3.74588100
C	6.12676800	-3.46034700	-5.14853400
C	-0.05682800	2.13973900	1.97436700
C	-2.40416100	2.31654400	1.90208000
C	-3.45575800	2.63085000	1.01758600
C	-4.66397200	3.13691800	1.48451500
C	-4.86605300	3.35454200	2.85692100
C	-3.83555200	3.04017800	3.75210900
C	-2.62738300	2.51869300	3.27472600
C	-6.33428200	4.10340900	4.58405900
C	2.22017500	2.06880500	3.78898500
C	3.35025800	2.43073800	4.51433200
C	4.56012400	2.70877000	3.85836600
C	4.61338800	2.61151200	2.46190200
C	3.46847800	2.25797900	1.73818100
O	5.61129100	3.05135600	4.66319700
C	6.85697200	3.33070600	4.04846000
C	0.33606600	2.05660500	-2.05421800
C	-1.94833100	2.26587600	-2.47112000
C	-2.67585400	1.53691400	-3.42977800
C	-2.28189300	3.61174400	-2.27040300
C	-3.31518200	4.22336000	-2.99215800
C	-4.03920100	3.48145000	-3.93475300
C	-3.70804100	2.13281000	-4.14749400
C	-5.43869800	5.32522200	-4.52152400
C	2.66788900	2.14830600	-1.79832000
C	3.79364200	1.34745900	-2.03703600
C	5.04014900	1.90964300	-2.33736300
C	5.18309100	3.30120200	-2.41360200
C	4.06485400	4.11489300	-2.17202500
C	2.83284000	3.54877200	-1.86144400
C	7.50405300	3.17835400	-2.95817400
O	-5.97783300	-4.07088000	-2.87978900
C	-6.03600800	-5.45852200	-3.15482200
H	1.16735200	-4.20077700	1.77028400
H	0.02938700	-2.78048700	-2.70663800
H	3.08492100	-5.45240700	2.65532700
H	3.16656200	-0.47936500	2.62194200
H	5.13508800	-1.74626300	3.46203300
H	6.39592300	-5.93925800	4.11292100
H	5.33184300	-6.14243100	2.68218200
H	4.62035500	-6.08498900	4.33243500
H	-1.45906800	-4.16994500	-2.05940600
H	-3.59893900	-0.43910000	-1.72550600
H	-5.70221200	-1.61278200	-2.30501100
H	-3.52319400	-5.31076000	-2.68752800
H	-0.42926600	-2.68280300	2.74043300
H	-2.06546600	-3.96794000	1.53694400
H	-3.60744900	0.01072100	2.12376100

H	-4.27494400	-4.90786300	2.18778900
H	-5.80523000	-0.91109400	2.70602800
H	-7.30432500	-2.16478900	4.00991300
H	-8.30684200	-3.49264800	3.33708800
H	-7.76089400	-2.15470100	2.27139200
H	1.67449100	-1.72014500	-4.11141400
H	3.73980700	-2.53768800	-5.16030100
H	5.48122700	-3.14495100	-1.26215600
H	3.36662900	-2.37175800	-0.20169400
H	7.14110800	-3.85072700	-5.30615900
H	5.39657900	-4.15847200	-5.59715300
H	6.03554000	-2.47917400	-5.64967300
H	-0.07290500	2.93744300	2.73157200
H	-3.31173100	2.49276900	-0.05458900
H	-5.47154500	3.38447400	0.79309900
H	-3.96225000	3.17418500	4.82626300
H	-1.85907500	2.23315300	3.99522800
H	-7.35244900	4.51074400	4.64290000
H	-5.62519900	4.83956000	5.00486400
H	-6.28126700	3.17531800	5.18229800
H	1.30286600	1.81290500	4.32255500
H	3.32520800	2.48677300	5.60424500
H	5.53292000	2.81930100	1.91557500
H	3.52361500	2.21136100	0.65078800
H	7.55014100	3.57629800	4.86407300
H	7.24606400	2.45758200	3.49349700
H	6.79081200	4.19143800	3.35831600
H	0.45567700	2.80660200	-2.85141400
H	-2.40920400	0.49682700	-3.61872800
H	-1.72927700	4.19039300	-1.52742300
H	-3.54352300	5.27213800	-2.80347200
H	-4.27203300	1.57111800	-4.89444700
H	-6.26957800	5.50244300	-5.21728200
H	-4.60822600	6.01184800	-4.76729800
H	-5.77983700	5.53176500	-3.49072900
H	3.69595800	0.26235200	-2.00713400
H	5.88324000	1.24403600	-2.52112200
H	4.19103100	5.19839400	-2.21540200
H	1.98712500	4.20073500	-1.63476200
H	8.31246900	3.89214500	-3.16593500
H	7.36985300	2.51894800	-3.83500800
H	7.78384200	2.55828500	-2.08677000
H	-7.08717900	-5.68044600	-3.38289900
H	-5.71961700	-6.06343800	-2.28533200
H	-5.41201700	-5.73217700	-4.02555000

Cartesian coordinates of the DFT optimized structure IV

Mo	-0.02906371	-0.03723467	1.04910133

Mo	0.02900991	0.03768154	-1.04912307
N	-3.28554943	-2.75194901	-0.19068106
C	-3.62734833	-3.38138938	-1.45533712
C	2.05207749	1.83994357	2.56443289
C	3.48209307	2.37169425	2.58409806
N	1.40453235	-1.68230619	1.13481973
N	1.44761728	-1.62277714	-1.16629376
N	2.81368319	-3.21821078	-0.03052719
N	-1.67740253	-1.46901241	1.04470766
N	-1.61974306	-1.38475877	-1.24804901
N	-1.44780690	1.62306283	1.16637628
N	-1.40473536	1.68264092	-1.13473935
N	1.61970899	1.38508168	1.24795729
N	1.67733263	1.46935552	-1.04481031
C	1.88580780	-2.17171526	-0.02096348
C	1.89676130	-2.21971345	-2.41494517
C	3.37917205	-2.58152263	-2.34416003
C	3.56786131	-3.58989250	-1.21850196
C	3.12412458	-4.00786872	1.15169589
C	2.16913405	-3.70644420	2.29914345
C	1.97295281	-2.19319126	2.37218884
C	-2.17550879	-1.88532367	-0.13197884
C	-3.48161463	-2.37245756	-2.58420101
C	-2.05201684	-1.83957551	-2.56457347
C	-3.58050669	-2.57723274	2.21700404
C	-3.67601689	-3.48637000	1.00129004
C	3.62861957	3.38057680	1.45527362
N	3.28594025	2.75167569	0.19060605
C	2.15524901	2.03930326	-2.29784153
C	3.58121763	2.57602750	-2.21705329
C	-2.15517466	-2.03879873	2.29787037
C	3.67781840	3.48518887	-1.00143510
C	-1.88617368	2.17188664	0.02104186
C	2.17564021	1.88548184	0.13188669
C	-1.89716603	2.21975852	2.41507850
C	-1.97344250	2.19327322	-2.37207689
C	-3.37961411	2.58138787	2.34424822
C	-2.16992345	3.70649941	-2.29910511
C	-3.12485774	4.00784215	-1.15157838
C	-3.56837146	3.58979787	1.21865108
N	-2.81454954	3.21792876	0.03052413
H	-2.99117664	-4.27216656	-1.65892894
H	-4.66643609	-3.74478508	-1.38069508
H	1.37109360	2.63428660	2.93678232
H	1.95716805	1.00078769	3.27671359
H	3.70883682	2.84238591	3.55490508
H	4.19741257	1.54658760	2.42745932
H	1.71593276	-1.50437490	-3.23443081
H	1.31362128	-3.13321966	-2.66415711

H	3.96153758	-1.66697403	-2.14185549
H	3.74044760	-3.01315017	-3.29208955
H	3.25167624	-4.59817654	-1.56043662
H	4.63908178	-3.67796171	-0.94905977
H	4.16906278	-3.80616300	1.46964532
H	3.08630455	-5.08279211	0.88484558
H	2.58005679	-4.11155448	3.23853747
H	1.19166750	-4.18538563	2.12087958
H	1.29712903	-1.93531939	3.20469219
H	2.94907707	-1.71139985	2.60073065
H	-3.70797314	-2.84334446	-3.55500304
H	-4.19760768	-1.54793085	-2.42758619
H	-1.37044405	-2.63324759	-2.93726663
H	-1.95791058	-1.00013713	-3.27663664
H	-3.84057770	-3.13047510	3.13451397
H	-4.29586006	-1.74509654	2.10385017
H	-4.70965971	-3.84290931	0.85384824
H	-3.04498600	-4.39081603	1.15425938
H	4.66806712	3.74292131	1.38048958
H	2.99342291	4.27199094	1.65909414
H	1.48231355	2.86102087	-2.62524154
H	2.09330633	1.26578707	-3.08452431
H	3.84197565	3.12891106	-3.13458488
H	4.29552566	1.74299775	-2.10386146
H	-1.48136611	-2.85952984	2.62593814
H	-2.09440336	-1.26478332	3.08416459
H	3.04826084	4.39060081	-1.15474676
H	4.71198538	3.84017176	-0.85384410
H	-1.31416135	3.13329728	2.66447597
H	-1.71630022	1.50433778	3.23448973
H	-1.29768505	1.93548768	-3.20465848
H	-2.94950013	1.71125622	-2.60042195
H	-3.96187850	1.66679483	2.14185192
H	-3.74097386	3.01291375	3.29219224
H	-1.19251773	4.18561116	-2.12097344
H	-2.58100336	4.11149900	-3.23847818
H	-3.08687123	5.08272832	-0.88457391
H	-4.16983314	3.80633349	-1.46949890
H	-4.63961986	3.67808255	0.94941771
H	-3.25191438	4.59801838	1.56054391

Cartesian coordinates of the DFT optimized structure 1

Mo	1.08191736	0.04935317	-0.34792880
Mo	-1.03803214	-0.06570934	-0.37783849
O	6.28204034	-4.65160340	-0.95572567
O	-5.45766786	-5.54355958	0.80409149
O	5.76659228	-0.15098970	5.03519261
O	-5.91107466	0.97345879	4.71493210

O	5.48411344	5.66084669	0.08769733
O	-6.10102045	4.55129667	-2.05600209
N	1.20547620	-0.09945965	-2.50561392
N	-1.09262865	-0.18881017	-2.54135981
N	0.09801096	-0.29753689	-4.60770822
N	1.31399516	-2.12620546	-0.24985795
N	-1.00365251	-2.27217794	-0.22184513
N	1.14518670	0.17320896	1.85252230
N	-1.17822256	0.09074024	1.81452388
N	1.04547614	2.25859048	-0.47794785
N	-1.26937255	2.10104440	-0.56517620
C	0.06936088	-0.19665970	-3.21957313
C	-2.33001848	-0.32059423	-3.30375606
H	-3.16166802	0.06563309	-2.69344629
H	-2.55458083	-1.38752396	-3.51558104
C	-2.24922304	0.43975800	-4.62468115
H	-2.08713971	1.50987309	-4.41655192
H	-3.18505850	0.34529324	-5.19832789
C	-1.09231851	-0.13130547	-5.43078608
H	-1.38270671	-1.10798898	-5.87138118
H	-0.84190203	0.53138363	-6.28128066
C	1.30888975	-0.63088389	-5.34774071
H	1.62208469	0.24100447	-5.95838765
H	1.07355194	-1.44302595	-6.06260197
C	2.43728092	-1.04714923	-4.41496191
H	3.39311920	-1.04311489	-4.96297640
H	2.27094090	-2.06785895	-4.03362389
C	2.46686592	-0.07580413	-3.23825016
H	3.28088565	-0.34405256	-2.54644601
H	2.68881111	0.94468472	-3.61621426
C	0.19774835	-2.84947361	-0.20343631
H	0.26975906	-3.94698497	-0.14851434
C	-2.12584982	-3.10507303	0.01699138
C	-2.12704936	-4.09435339	1.02470404
H	-1.24519493	-4.21859087	1.65583307
C	-3.24554901	-4.88911121	1.25274098
H	-3.24393851	-5.65008608	2.03553895
C	-4.41389036	-4.71382896	0.49482945
C	-4.43843130	-3.72289627	-0.49547859
H	-5.32683085	-3.55762930	-1.10479370
C	-3.30382906	-2.93569819	-0.72590427
H	-3.32967378	-2.18228719	-1.51374169
C	-6.65615485	-5.41115509	0.06206636
H	-7.34850290	-6.16265319	0.46463420
H	-6.49726276	-5.60624295	-1.01435671
H	-7.10484418	-4.40743071	0.17922407
C	2.54184644	-2.80691495	-0.44856305
C	3.69802966	-2.38450534	0.24015502
H	3.62365803	-1.56661515	0.95856027

C	4.92072234	-3.01619434	0.04447521
H	5.81033270	-2.69394422	0.58877271
C	5.03455358	-4.09923762	-0.84302219
C	3.89874807	-4.52849271	-1.53972826
H	3.95112231	-5.35581140	-2.24747576
C	2.67243600	-3.87831793	-1.34763627
H	1.80628717	-4.20220816	-1.92818540
C	6.44259325	-5.75950385	-1.82250136
H	7.49922850	-6.05085773	-1.75269343
H	6.20860525	-5.49921558	-2.87133014
H	5.81088780	-6.61433201	-1.51870911
C	-0.02848857	0.17916828	2.48281049
H	-0.04956822	0.26221768	3.58053181
C	-2.37365488	0.29106115	2.55548710
C	-2.50907833	1.34895031	3.47994482
H	-1.67932008	2.04322505	3.62527306
C	-3.69347098	1.54218572	4.18354942
H	-3.79756611	2.36343490	4.89529909
C	-4.79268944	0.69424338	3.97618354
C	-4.68110728	-0.34945066	3.04814437
H	-5.51042805	-1.03196001	2.86392641
C	-3.48185815	-0.54436762	2.35226599
H	-3.40199692	-1.37750345	1.65309844
C	-7.04285514	0.13913859	4.54911296
H	-7.81223764	0.53067153	5.22814336
H	-6.82366972	-0.91044791	4.81781947
H	-7.42760294	0.16743531	3.51281031
C	2.31258349	0.10888258	2.65988026
C	3.42040460	0.91655124	2.36416224
H	3.36075153	1.62241666	1.53510278
C	4.59261261	0.85812664	3.12697025
H	5.42220616	1.51367458	2.86293107
C	4.67669465	-0.01631518	4.21846419
C	3.57785563	-0.83582143	4.52059662
H	3.66093924	-1.52634249	5.36209888
C	2.42052912	-0.78034212	3.75051295
H	1.59223329	-1.45367452	3.97942057
C	6.89786730	0.65949152	4.77270538
H	7.64307777	0.39866846	5.53615268
H	6.66009108	1.73604050	4.85236662
H	7.32249309	0.46198887	3.77124305
C	-0.15501026	2.82834795	-0.58500567
H	-0.22701512	3.92138625	-0.69819745
C	-2.48809006	2.73449430	-0.91844543
C	-2.57596340	3.64891697	-1.99030389
H	-1.68289931	3.87982197	-2.57441083
C	-3.78840565	4.23934297	-2.33448378
H	-3.85495860	4.94497417	-3.16496786
C	-4.96123946	3.92244127	-1.63200104

C	-4.89401204	3.00334221	-0.57617121
H	-5.78140760	2.73761688	-0.00218747
C	-3.66917704	2.42327700	-0.22754606
H	-3.62772797	1.73312662	0.61646056
C	-7.31055766	4.26323159	-1.37809835
H	-8.08680486	4.86321631	-1.87179449
H	-7.26092882	4.54441199	-0.31031973
H	-7.57903590	3.19326841	-1.45210820
C	2.16373078	3.12063833	-0.34968107
C	3.36191976	2.82304401	-1.01592017
H	3.40585716	1.94262324	-1.65740822
C	4.49357773	3.63786670	-0.89586599
H	5.39819437	3.36592995	-1.43950838
C	4.44553743	4.78929770	-0.09892273
C	3.25697001	5.09510431	0.58236965
H	3.23681602	5.98249348	1.21798016
C	2.14123012	4.27243533	0.46695763
H	1.24275908	4.50812872	1.04020356
C	6.70310282	5.39673792	-0.58282848
H	7.38758862	6.20825552	-0.30173638
H	6.57662782	5.39501354	-1.68104716
H	7.14232136	4.43032212	-0.27386081

Cartesian coordinates of the DFT optimized structure 2

Mo	-1.07408857	0.07064748	-0.03879188
Mo	1.03995792	-0.02438682	-0.00624189
O	-6.21818267	-4.69825781	0.56358315
O	5.59871699	-5.33937802	-1.20677866
O	-5.60407322	5.46963388	-0.99148304
O	6.05242393	4.75430969	1.37472084
N	-1.19986055	0.00938205	2.13203227
N	1.10025358	-0.07362290	2.16933570
N	-0.08860701	-0.10229546	4.24015756
N	-1.26602779	-2.12217556	-0.06747090
N	1.05113368	-2.22908866	-0.09345342
N	-1.13202829	0.18622154	-2.21352139
N	1.16333842	-0.01297048	-2.17793396
N	-1.08125827	2.27859185	-0.01254714
N	1.23291776	2.16522406	0.09054877
C	-0.06206480	-0.05617932	2.84689098
C	2.33363543	-0.19116044	2.93880152
C	2.26112941	0.62927294	4.22427096
C	1.09951557	0.10592139	5.05577166
C	-1.29939659	-0.39586233	4.99518005
C	-2.43248406	-0.84429324	4.08337228
C	-2.45800606	0.07625911	2.86599334
C	-0.13778019	-2.82937071	-0.09947843
C	2.19407632	-3.02138940	-0.35652627

C	2.19769309	-4.04756929	-1.32734017
C	3.34085772	-4.80006237	-1.57715555
C	4.53215227	-4.54437833	-0.88084569
C	4.55417682	-3.51612964	0.07066458
C	3.39592365	-2.77237356	0.32419611
C	6.82233444	-5.12040598	-0.52957839
C	-2.48366623	-2.81696010	0.11831128
C	-3.63802144	-2.40042778	-0.57763143
C	-4.85886299	-3.04197798	-0.40459977
C	-4.97364301	-4.13458496	0.47072954
C	-3.84170417	-4.55977623	1.17623278
C	-2.61818632	-3.89865722	1.00539379
C	-6.38117683	-5.80980124	1.42522136
C	0.02942892	0.12136827	-2.88959060
C	0.10653083	2.87589934	0.06622746
C	2.44117024	2.83405371	0.39358997
C	2.52487929	3.85253826	1.36902016
C	3.73570096	4.47315331	1.66102719
C	4.91487267	4.08713987	1.00531825
C	4.85510248	3.06615487	0.04732040
C	3.63076090	2.45689836	-0.24956876
C	7.26942910	4.38760005	0.75138154
C	-2.21778540	3.08896178	-0.24618163
C	-3.44324931	2.77007525	0.35927554
C	-4.59613765	3.53130219	0.13665445
C	-4.54535961	4.64915783	-0.70648644
C	-3.33077828	4.97474803	-1.32950973
C	-2.19257602	4.20468568	-1.11216129
C	-6.85077211	5.17979559	-0.38630205
C	-2.33195314	0.49856089	-2.98112330
C	2.39225337	-0.24288002	-2.92741897
C	-2.36054159	-0.29753822	-4.28360862
C	2.47279381	0.70158276	-4.12427566
C	1.28739596	0.41134287	-5.03616292
C	-1.13906103	0.09531657	-5.10374536
N	0.06027198	0.18723545	-4.28115825
H	3.17200768	0.15726464	2.31463480
H	2.54535616	-1.25102416	3.19649780
H	2.10663720	1.68964088	3.96555341
H	3.19602367	0.55457396	4.80272831
H	1.38624850	-0.84660150	5.54903270
H	0.85013670	0.81383837	5.86988059
H	-1.60723196	0.50345810	5.56830761
H	-1.06893439	-1.17766518	5.74508207
H	-3.38688389	-0.81235312	4.63332220
H	-2.27121455	-1.88098902	3.74473641
H	-3.27605586	-0.21713238	2.18879411
H	-2.67392517	1.11414758	3.19817310
H	-0.19090390	-3.92894464	-0.13658484

H	1.29562634	-4.23689477	-1.91221624
H	3.33966870	-5.59084103	-2.33003996
H	5.46003678	-3.28816473	0.63225592
H	3.41980721	-1.99180119	1.08579597
H	7.53089643	-5.85555110	-0.93435358
H	6.72317483	-5.27672677	0.56037850
H	7.21633019	-4.10291070	-0.70846438
H	-3.55755710	-1.57109004	-1.28201468
H	-5.74666283	-2.72060582	-0.95271363
H	-3.89589994	-5.39330885	1.87658079
H	-1.75741631	-4.22023111	1.59492769
H	-7.43490976	-6.10818625	1.34220874
H	-6.16116155	-5.55092366	2.47736806
H	-5.74008934	-6.65946565	1.12645678
H	0.15978861	3.97501083	0.11249760
H	1.62948977	4.14095830	1.92292937
H	3.79654970	5.25761994	2.41805530
H	5.74874763	2.74045791	-0.48501108
H	3.59235219	1.68042481	-1.01540804
H	8.04313461	5.03225756	1.18962914
H	7.23871174	4.55251325	-0.34134701
H	7.52843110	3.33009967	0.94413898
H	-3.49106510	1.91745212	1.03790941
H	-5.52099128	3.24497267	0.63724643
H	-3.30674819	5.83530547	-2.00108894
H	-1.27160200	4.45385585	-1.64251369
H	-7.54833753	5.95060293	-0.74061072
H	-6.79291510	5.22468183	0.71682212
H	-7.23136771	4.18480334	-0.68217414
H	-2.39001616	1.58304837	-3.20847970
H	-3.21768400	0.27212868	-2.36659187
H	3.25277357	-0.09595186	-2.25552185
H	2.45626100	-1.29349367	-3.27856521
H	-2.33912050	-1.37482073	-4.04882771
H	-3.27503292	-0.09491514	-4.86432389
H	2.43690955	1.74245986	-3.76193554
H	3.41142919	0.56968360	-4.68665629
H	1.12381764	1.24787254	-5.74377728
H	1.50077596	-0.48286463	-5.65714006
H	-0.95868930	-0.63615789	-5.91547159
H	-1.31887178	1.07149656	-5.60028119

Cartesian coordinates of the DFT optimized structure 3

Mo	-0.31117946	-1.17336038	0.02167841
Mo	1.12117988	0.36941779	-0.07264297
O	-7.26591934	-1.37628744	1.24395306
O	0.66170495	7.43744150	0.48263922
N	3.31531315	-3.18912797	-1.46185022

C	2.90150508	-4.51482798	-1.89406112
N	-0.97420998	-0.81309910	-2.02636413
N	0.57542563	0.88811911	-2.11868409
N	-0.77504723	0.45149311	-4.03946395
N	-1.90115978	0.20402262	0.69907680
N	-0.32522934	1.90451599	0.59183878
N	0.26341050	-1.71810428	2.05230298
N	1.82543688	-0.03602102	1.95318638
N	1.09831044	-2.65578291	-0.72072529
N	2.65479119	-0.97321319	-0.82799635
C	-0.39090359	0.17686045	-2.72563419
C	1.13896236	2.02547794	-2.83466918
C	1.33268130	1.69852644	-4.31361597
C	-0.02588553	1.35033380	-4.90571459
C	-1.98978711	-0.08873840	-4.63536403
C	-2.85657128	-0.80272666	-3.60636013
C	-1.94700078	-1.64792455	-2.71755523
C	-1.57740290	1.49343477	0.79011377
C	-0.08400445	3.29935239	0.59509369
C	-0.90934571	4.20690520	-0.10500372
C	-0.63780111	5.57120776	-0.11459717
C	0.48022809	6.08172654	0.56325489
C	1.31755957	5.19656800	1.25430857
C	1.02857042	3.82653816	1.26780061
C	1.78347299	7.99687086	1.13952881
C	-3.26783798	-0.14118278	0.82457592
C	-3.64913340	-1.23656304	1.62650832
C	-4.98060432	-1.62106859	1.74104273
C	-5.98794025	-0.91770532	1.06088227
C	-5.63123149	0.17385341	0.25975549
C	-4.28564819	0.54542676	0.14125350
C	-8.31638301	-0.69588660	0.58302307
C	1.25957051	-1.03880556	2.64947024
C	2.34817411	-2.26771035	-1.02474887
C	1.79622569	-5.03327170	-0.98665614
C	0.65673486	-4.01926572	-0.99564545
C	4.56559672	-2.70843407	-2.02855472
C	5.05194099	-1.49013018	-1.25846433
C	3.94082146	-0.44522882	-1.26801661
C	-0.24237230	-2.93729117	2.67153688
C	3.03151313	0.60277967	2.46552110
C	-0.22637954	-2.87701180	4.19464909
C	3.06756782	0.66858433	3.98820553
C	2.85858229	-0.73922512	4.52361876
C	1.18652402	-2.52902373	4.63519635
N	1.64230488	-1.31611800	3.97308666
H	3.78626683	-5.17271401	-1.85444432
H	2.55403897	-4.51103979	-2.95124873
H	2.10292984	2.29083384	-2.37044232

H	0.49256596	2.92293320	-2.73920230
H	2.02165224	0.84193432	-4.40769804
H	1.76948038	2.54818476	-4.86333180
H	-0.61023061	2.27909983	-5.07683790
H	0.09022863	0.87114540	-5.89746321
H	-1.71984690	-0.78927219	-5.45317176
H	-2.55192653	0.73885974	-5.11133875
H	-3.60923763	-1.42135971	-4.12181809
H	-3.39236035	-0.07348004	-2.97670421
H	-2.54245314	-2.19049698	-1.96578206
H	-1.44616371	-2.41922130	-3.34236016
H	-2.35100390	2.22655199	1.06895353
H	-1.76195499	3.82562414	-0.67038565
H	-1.27585896	6.26872910	-0.66108493
H	2.19084235	5.55722563	1.79813552
H	1.66789076	3.14910244	1.83540694
H	1.74449731	9.07706276	0.94418472
H	2.73471569	7.59273524	0.74649820
H	1.74935859	7.82654178	2.23142547
H	-2.87881624	-1.77003270	2.18457670
H	-5.27187788	-2.46463448	2.37011087
H	-6.38444630	0.73718070	-0.29134098
H	-4.02030645	1.37670365	-0.51502079
H	-9.24188745	-1.21606434	0.86467053
H	-8.20269414	-0.73135850	-0.51624696
H	-8.38589906	0.36134402	0.89899800
H	1.44324786	-6.01767260	-1.33492020
H	2.19106867	-5.15367274	0.03637410
H	0.14559902	-4.06426135	-1.97999433
H	-0.10258033	-4.30234336	-0.24581976
H	5.29913234	-3.53052218	-1.97060718
H	4.45555527	-2.45568654	-3.10674954
H	5.28808772	-1.78317397	-0.22148866
H	5.96957970	-1.08752786	-1.71777535
H	3.85173924	-0.02669459	-2.29322796
H	4.21692392	0.40244434	-0.61663987
H	0.35686120	-3.81215186	2.33993692
H	-1.26816537	-3.12130734	2.30987035
H	3.93271507	0.05996271	2.10788975
H	3.10416315	1.61807411	2.03975763
H	-0.92719674	-2.10208067	4.54801815
H	-0.53310736	-3.84196291	4.63036233
H	4.03126248	1.07058905	4.34172409
H	2.26391476	1.32828908	4.35632979
H	3.74650912	-1.36798198	4.28969455
H	2.75979199	-0.73189410	5.62273820
H	1.22766536	-2.35386425	5.72413279
H	1.86801182	-3.38365959	4.42620803

Chapter 6: Electronic Tuning of Digold Compounds via Remote Substituent Effect

Cartesian coordinates of the DFT optimized 2

Au	0.00009691	1.41450940	0.00027047
N	2.07970730	1.19731186	0.02930224
C	2.93601560	-2.34932741	-0.14287821
N	2.07950758	-1.19762929	-0.02928139
C	2.65555919	-0.00020979	0.00002465
C	2.93641711	2.34885846	0.14292859
C	4.31113425	-3.82596034	-1.47583448
C	3.16936296	3.15281931	-0.99858514
C	3.49486095	2.68952486	1.39781100
C	3.98129020	4.28449401	-0.86144120
C	3.49461253	-2.69000092	-1.39769187
C	4.55624551	-4.62056610	-0.36084330
C	4.55706148	4.61978141	0.36097356
C	3.16858037	-3.15345423	0.99859484
C	3.98030106	-4.28528331	0.86149031
Au	-0.00015616	-1.41451294	-0.00032015
N	-2.07956689	1.19763990	-0.02881974
C	-2.65562268	0.00020895	-0.00002848
C	-2.93646119	-2.34894321	0.14181580
C	-3.98021992	4.28493451	0.86350538
C	-3.16939339	-3.15234718	-1.00008599
C	-3.49483535	-2.69028579	1.39655033
C	-3.98122103	-4.28416048	-0.86347763
C	-4.31145753	-3.82620384	1.47420460
C	-4.55601608	4.62095131	-0.35869444
C	-4.55690058	-4.62012157	0.35879258
C	-3.49452964	2.69082097	-1.39649663
C	-4.31090757	3.82691952	-1.47409643
H	-4.75633317	4.09582799	-2.42826352
H	-4.16856739	-4.91073875	-1.73127110
H	-5.19081564	-5.49909361	0.44165029
H	-4.16727823	4.91161793	1.73128437
H	-5.18974525	5.50006147	-0.44150781
H	4.16737640	-4.91239971	1.72895273
H	5.19008434	-5.49955690	-0.44408481
H	4.75666925	-4.09430547	-2.43010885
H	-3.75006637	0.00030116	-0.00001265
H	3.75000394	-0.00029928	0.00004491
H	4.16865985	4.91149203	-1.72892548
H	5.19106640	5.49865010	0.44424398
N	-2.07977013	-1.19732480	0.02875018
C	-3.16862333	3.15294808	1.00006158
C	-2.93604947	2.34941837	-0.14182624
C	4.31159432	3.82532918	1.47599659
H	4.75703441	4.09366134	2.43031801

H	-4.75681977	-4.09506053	2.42841544
C	2.54347674	2.83981110	-2.35455059
C	3.59066960	2.75760328	-3.48129124
C	1.44473633	3.86506101	-2.70019138
H	2.06346417	1.85971838	-2.28246608
H	4.37063199	2.02417921	-3.24986929
H	3.11163819	2.45956928	-4.42181354
H	4.08100321	3.72252249	-3.65562195
H	0.66652384	3.88344330	-1.92812609
H	1.85813490	4.87741794	-2.78521133
H	0.97043104	3.61384194	-3.65685369
C	3.23262019	1.87517486	2.66239705
C	2.61704512	2.73594698	3.78298059
C	4.51319514	1.17255501	3.15535237
H	2.49937059	1.10129792	2.41830812
H	1.69277280	3.21877373	3.44818745
H	2.37994494	2.11168725	4.65305206
H	3.30343134	3.52232030	4.11862211
H	4.93375793	0.51623374	2.38464665
H	5.28739609	1.90082207	3.42522889
H	4.30310230	0.56332014	4.04244074
C	3.23268153	-1.87557158	-2.66229112
C	2.61713421	-2.73625385	-3.78296149
C	4.51342011	-1.17313402	-3.15507202
H	2.49951065	-1.10158881	-2.41830074
H	1.69275097	-3.21895399	-3.44829039
H	2.38024226	-2.11196533	-4.65306852
H	3.30346395	-3.52272310	-4.11849497
H	4.93394634	-0.51683455	-2.38432706
H	5.28757416	-1.90150439	-3.42480476
H	4.30353931	-0.56391062	-4.04221828
C	2.54251657	-2.84048081	2.35448773
C	3.58954346	-2.75854813	3.48140365
C	1.44356291	-3.86560120	2.69983979
H	2.06266681	-1.86030433	2.28243704
H	4.36964504	-2.02520830	3.25018608
H	3.11040519	-2.46054749	4.42188268
H	4.07971401	-3.72355575	3.65570123
H	0.66547100	-3.88376931	1.92764432
H	1.85679347	-4.87803056	2.78480163
H	0.96914882	-3.61442944	3.65645947
C	-3.23259178	-1.87657635	2.66154684
C	-2.61685245	-2.73788370	3.78162531
C	-4.51321462	-1.17436400	3.15495918
H	-2.49944245	-1.10248929	2.41781796
H	-1.69256217	-3.22044814	3.44650133
H	-2.37974233	-2.11406179	4.65200775
H	-3.30314394	-3.52449431	4.11690453
H	-4.93391128	-0.51769528	2.38462356

H	-5.28730928	-1.90286434	3.42451252
H	-4.30313311	-0.56556126	4.04234689
C	-2.54361749	-2.83862074	-2.35593251
C	-3.59088222	-2.75611331	-3.48257980
C	-1.44471797	-3.86353273	-2.70206947
H	-2.06377292	-1.85847250	-2.28343464
H	-4.37094596	-2.02291211	-3.25079869
H	-3.11194534	-2.45759774	-4.42299710
H	-4.08107514	-3.72103500	-3.65730012
H	-0.66645523	-3.88208739	-1.93005979
H	-1.85794495	-4.87592707	-2.78747369
H	-0.97051891	-3.61184308	-3.65866113
C	-3.23260790	1.87702927	-2.66150512
C	-2.61676279	2.73818530	-3.78164260
C	-4.51344257	1.17512661	-3.15479980
H	-2.49961850	1.10276801	-2.41784749
H	-1.69230025	3.22048769	-3.44661514
H	-2.37992561	2.11431626	-4.65206572
H	-3.30287653	3.52499267	-4.11682382
H	-4.93422217	0.51854372	-2.38443662
H	-5.28739010	1.90381572	-3.42426751
H	-4.30359147	0.56629285	-4.04222055
C	-2.54266412	2.83921512	2.35582671
C	-3.58975588	2.75689675	3.48265331
C	-1.44356495	3.86399725	2.70171267
H	-2.06295711	1.85900159	2.28331350
H	-4.36996552	2.02380319	3.25102124
H	-3.11071718	2.45834043	4.42300597
H	-4.07977903	3.72189608	3.65741248
H	-0.66543320	3.88238778	1.92956260
H	-1.85663387	4.87645501	2.78712143
H	-0.96924450	3.61230394	3.65824153

Cartesian coordinates of the DFT optimized 3

Au	-0.00000128	-1.29852635	0.00001183
N	2.06570057	-1.15495032	0.25226666
C	2.89084227	2.25880388	-0.66847984
N	2.06572771	1.15498353	-0.25201300
C	2.66080093	0.00000977	0.00013963
C	2.89078830	-2.25885661	0.66855273
C	4.41268039	4.05390993	-0.14925785
C	2.98972586	-2.54983004	2.04876868
C	3.58146705	-3.02136209	-0.30084172
C	3.82426857	-3.60173201	2.44082599
C	3.58155920	3.02143954	0.30078842
C	4.53697285	4.34472753	-1.50424693
C	4.53682443	-4.34500238	1.50396969

C	2.98979392	2.54953986	-2.04876300
C	3.82439964	3.60132491	-2.44098221
Au	0.00003318	1.29855161	0.00024771
N	-2.06569112	-1.15497483	-0.25220149
C	-2.66075957	0.00000092	-0.00000223
C	-2.89087020	2.25883751	0.66848120
C	-3.82434340	-3.60135248	-2.44113709
C	-2.99011366	2.54978151	2.04868265
C	-3.58130877	3.02139636	-0.30103701
C	-3.82473541	3.60167915	2.44058877
C	-4.41244902	4.05399603	0.14867680
C	-4.53679975	-4.34485101	-1.50439374
C	-4.53704200	4.34501281	1.50359822
C	-3.58139064	-3.02155238	0.30064138
C	-4.41245209	-4.05406757	-0.14939893
H	-4.96281495	-4.64699116	0.57574659
H	-3.91795555	3.84289632	3.49580106
H	-5.18344725	5.15585110	1.82903433
H	-3.91738742	-3.84240114	-3.49640478
H	-5.18314392	-5.15563820	-1.83008021
H	3.91741099	3.84242957	-3.49624257
H	5.18338470	5.15545529	-1.82994889
H	4.96317261	4.64672679	0.57587464
H	-3.75361417	0.00003807	-0.00014405
H	3.75365474	-0.00000941	0.00014600
H	3.91723808	-3.84300976	3.49604744
H	5.18318653	-5.15582600	1.82952862
N	-2.06568263	1.15494155	0.25235665
C	-2.98979685	-2.54951768	-2.04890718
C	-2.89080136	-2.25881383	-0.66863501
C	4.41255201	-4.05393755	0.14903028
H	4.96299287	-4.64666907	-0.57621307
H	-4.96268185	4.64678893	-0.57667316
Cl	0.00005657	3.76731884	0.00058994
Cl	-0.00006252	-3.76728711	-0.00008695
C	2.20670174	-1.77939406	3.10745041
C	3.13160959	-1.12486869	4.15142418
C	1.15809814	-2.68303219	3.78717468
H	1.66331887	-0.97314836	2.60482971
H	3.86685602	-0.46409057	3.67926752
H	2.54343641	-0.52892622	4.85951257
H	3.68198812	-1.87570626	4.73044874
H	0.48740330	-3.13263825	3.04812411
H	1.63633520	-3.49748759	4.34434075
H	0.55742332	-2.10158857	4.49775394
C	3.45706603	-2.76135787	-1.79857942
C	2.98327358	-4.01602432	-2.55790498
C	4.77760214	-2.22695580	-2.38880563
H	2.69189216	-1.99321538	-1.94462572

H	2.04286504	-4.38861831	-2.14147715
H	2.82605312	-3.77773156	-3.61690645
H	3.72359759	-4.82323841	-2.50874544
H	5.10140677	-1.30435744	-1.89227663
H	5.58630604	-2.95952274	-2.28062026
H	4.66186097	-2.01405072	-3.45811723
C	3.45716972	2.76163288	1.79855643
C	2.98366757	4.01644985	2.55779293
C	4.77766512	2.22708903	2.38875360
H	2.69185390	1.99364825	1.94470185
H	2.04323792	4.38911730	2.14147398
H	2.82656824	3.77829609	3.61684329
H	3.72408221	4.82357040	2.50845596
H	5.10139497	1.30447663	1.89220606
H	5.58641859	2.95960093	2.28053965
H	4.66192535	2.01418502	3.45806195
C	2.20677975	1.77891063	-3.10731281
C	3.13167108	1.12430827	-4.15123928
C	1.15812066	2.68241030	-3.78713665
H	1.66347226	0.97270706	-2.60455670
H	3.86669315	0.46326352	-3.67910079
H	2.54346654	0.52863076	-4.85952407
H	3.68234348	1.87509478	-4.73005305
H	0.48751277	3.13221750	-3.04813211
H	1.63633085	3.49670977	-4.34455969
H	0.55736229	2.10081063	-4.49751595
C	-3.45653015	2.76149467	-1.79876136
C	-2.98212044	4.01610050	-2.55781187
C	-4.77703366	2.22756502	-2.38946820
H	-2.69153752	1.99313379	-1.94463868
H	-2.04176012	4.38841536	-2.14102328
H	-2.82459605	3.77786711	-3.61677894
H	-3.72225156	4.82350107	-2.50882176
H	-5.10128386	1.30500847	-1.89315502
H	-5.58555111	2.96036555	-2.28146469
H	-4.66100235	2.01475425	-3.45876623
C	-2.20739660	1.77926720	3.10754611
C	-3.13261328	1.12454970	4.15112428
C	-1.15910578	2.68290620	3.78772818
H	-1.66382391	0.97309762	2.60500774
H	-3.86750071	0.46360410	3.67864397
H	-2.54458953	0.52874449	4.85945376
H	-3.68342182	1.87524494	4.72992674
H	-0.48819720	3.13265950	3.04896319
H	-1.63762763	3.49726067	4.34480263
H	-0.55863633	2.10145805	4.49847195
C	-3.45691640	-2.76186458	1.79841705
C	-2.98318363	-4.01669213	2.55749844
C	-4.77743160	-2.22754227	2.38877067

H	-2.69168857	-1.99380050	1.94459415
H	-2.04276276	-4.38923502	2.14104422
H	-2.82600178	-3.77860640	3.61655244
H	-3.72352182	-4.82388189	2.50815253
H	-5.10129566	-1.30489568	1.89236898
H	-5.58611236	-2.96012577	2.28051854
H	-4.66166113	-2.01476497	3.45810318
C	-2.20692867	-1.77875870	-3.10747626
C	-3.13203226	-1.12408416	-4.15118978
C	-1.15832014	-2.68209948	-3.78754852
H	-1.66359129	-0.97258813	-2.60469052
H	-3.86706444	-0.46320183	-3.67884041
H	-2.54398106	-0.52822668	-4.85945170
H	-3.68268109	-1.87485017	-4.73005038
H	-0.48751862	-3.13187508	-3.04869887
H	-1.63653210	-3.49642148	-4.34493665
H	-0.55776087	-2.10039007	-4.49800654

Cartesian coordinates of the DFT optimized 4

Au	1.40529193	0.14223245	0.07956652
N	0.95726249	2.17882602	0.02859378
C	-2.62730182	2.67107573	-0.34060748
N	-1.41741921	1.94736350	-0.15475558
C	-0.28204796	2.63871576	-0.06680352
C	2.01132906	3.15246523	0.15566997
C	-4.98998148	2.92952997	0.16947257
C	2.41239849	3.57972315	1.44169903
C	2.65007194	3.63286407	-1.01037187
C	3.44927514	4.51662104	1.53393784
C	-3.77780092	2.24759870	0.32884071
C	-5.06244091	4.05254168	-0.66532852
C	4.07809080	5.01388852	0.39586589
C	-2.70190714	3.78635288	-1.19719390
C	-3.90984881	4.46271234	-1.34012228
Au	-1.40528699	-0.14224825	-0.07947208
N	1.41742875	-1.94737301	0.15477780
C	0.28206004	-2.63872941	0.06678679
C	-2.01131398	-3.15248041	-0.15572590
C	4.98997557	-2.92958493	-0.16950469
C	-2.65015872	-3.63283079	1.01028266
C	-2.41231107	-3.57974474	-1.44177371
C	-3.67985664	-4.57025782	0.86220746
C	-3.44921304	-4.51661014	-1.53406470
C	5.06243642	-4.05257977	0.66531775
C	-4.07811231	-5.01384716	-0.39602618
C	2.70192033	-3.78635076	1.19723172
C	3.90985607	-4.46272210	1.34014999
H	3.96465289	-5.31945354	2.00680093

H	-4.17747902	-4.95911237	1.74696338
H	-4.87871763	-5.74307242	-0.48934026
H	5.99119696	-4.59262873	0.80583361
H	-3.96463584	5.31945994	-2.00675327
H	-5.99120717	4.59257653	-0.80585903
H	0.38342503	-3.72689269	0.05644794
H	-0.38340166	3.72688084	-0.05653355
H	3.76762131	4.86164258	2.51432431
H	4.87868533	5.74313100	0.48913696
N	-0.95725391	-2.17884409	-0.02858671
C	3.77779888	-2.24764042	-0.32886200
C	2.62731215	-2.67109629	0.34061457
C	3.67975980	4.57031192	-0.86234705
H	4.17733077	4.95917486	-1.74712871
H	-3.76752197	-4.86162803	-2.51446473
H	-3.74236540	1.38578908	0.98770229
H	-1.83399029	4.09309006	-1.77217240
H	3.74236232	-1.38583900	-0.98773437
H	1.83400835	-4.09305066	1.77223635
O	-6.04114082	2.42232662	0.87786062
O	6.04112113	-2.42241916	-0.87793832
C	2.24997591	3.16032436	-2.40501165
C	3.43067196	2.50501299	-3.14672934
C	1.64085695	4.30504426	-3.23848407
H	1.47904947	2.39363128	-2.28780429
H	3.84180727	1.66844973	-2.57075289
H	3.10246079	2.11971843	-4.11957598
H	4.24337866	3.21808900	-3.32914930
H	0.77182036	4.74664767	-2.73644366
H	2.36693369	5.10939334	-3.40765721
H	1.31567100	3.93664514	-4.21886845
C	1.76442953	3.04394702	2.71522196
C	1.08027130	4.16312338	3.52396371
C	2.78204302	2.27573522	3.58120933
H	0.98940514	2.33016343	2.42322573
H	0.32465503	4.68402596	2.92483265
H	0.58368207	3.74732330	4.40884552
H	1.80405845	4.91138651	3.86884636
H	3.24107359	1.45714247	3.01539373
H	3.58651998	2.93059254	3.93722655
H	2.28774830	1.84615114	4.46091783
C	-2.25012273	-3.16028439	2.40493886
C	-1.64109045	-4.30501215	3.23846065
C	-3.43081954	-2.50490259	3.14659547
H	-1.47915581	-2.39362769	2.28775645
H	-0.77204978	-4.74666337	2.73646943
H	-1.31593582	-3.93660846	4.21885407
H	-2.36721094	-5.10932697	3.40761362
H	-3.84190770	-1.66834192	2.57058212

H	-4.24356180	-3.21793486	3.32902695
H	-3.10261977	-2.11958676	4.11943813
C	-1.76427779	-3.04395742	-2.71525786
C	-2.78181848	-2.27561746	-3.58121869
C	-1.08017221	-4.16312715	-3.52404911
H	-0.98920622	-2.33024722	-2.42320724
H	-3.24079231	-1.45702028	-3.01536452
H	-2.28747684	-1.84602323	-4.46089607
H	-3.58633798	-2.93039510	-3.93728432
H	-0.32462471	-4.68413267	-2.92492053
H	-1.80399156	-4.91131203	-3.86903484
H	-0.58350637	-3.74729602	-4.40887436
C	7.29624056	-3.07332950	-0.77571693
H	7.24164931	-4.11423340	-1.12185798
H	7.67874659	-3.05655498	0.25362460
C	-7.29622532	3.07332169	0.77575105
H	-7.67881131	3.05660073	-0.25356215
H	-7.24153755	4.11421259	1.12191527
H	7.97671868	-2.51457521	-1.42104831
H	-7.97669196	2.51459404	1.42111760

Cartesian coordinates of the DFT optimized 5

Au	-0.85536500	-1.12572000	-0.01610800
N	0.93864500	-2.18626200	-0.06801300
C	3.74686300	0.09824800	0.23622100
N	2.39349800	-0.29057000	0.05936000
C	2.12144300	-1.59486100	-0.01066400
C	0.92332500	-3.61975600	-0.22088600
C	5.94746100	-0.20228500	1.23536800
C	0.76840200	-4.42954100	0.92736900
C	1.01993600	-4.18494300	-1.51276900
C	0.72961100	-5.81843000	0.75640800
C	4.61842800	-0.59962100	1.08918700
C	6.41066600	0.91351600	0.54197500
C	0.83703200	-6.39460900	-0.50659600
C	4.23446700	1.22886500	-0.43889600
C	5.55657800	1.63809200	-0.29069800
Au	0.85537600	1.12571900	-0.01611600
N	-2.39348700	0.29056900	0.05937300
C	-2.12143000	1.59485900	-0.01068100
C	-0.92331500	3.61975700	-0.22088400
C	-5.55657000	-1.63810500	-0.29058700
C	-0.76833400	4.42954500	0.92736300
C	-1.01998100	4.18493900	-1.51276100
C	-0.72954500	5.81843300	0.75639200
C	-0.97924400	5.58057000	-1.62663700
C	-6.41065000	-0.91350900	0.54207600
C	-0.83704100	6.39460900	-0.50660800

C	-4.61840700	0.59964700	1.08922500
C	-5.94743800	0.20231300	1.23543200
H	-6.61129700	0.74517800	1.89993600
H	-0.61510200	6.45814300	1.62761700
H	-0.80803700	7.47535000	-0.61767900
H	-5.92405000	-2.50974000	-0.82165500
H	5.92405400	2.50971300	-0.82179200
H	6.61132700	-0.74513500	1.89987800
H	-2.98526300	2.26412000	-0.04110300
H	2.98527700	-2.26412200	-0.04104400
H	0.61522700	-6.45813600	1.62764300
H	0.80801700	-7.47535100	-0.61766300
N	-0.93863200	2.18626200	-0.06802300
C	-4.23446100	-1.22888000	-0.43881200
C	-3.74685000	-0.09824300	0.23626600
C	0.97917600	-5.58057400	-1.62663600
H	1.05759600	-6.03563200	-2.61045000
H	-1.05773300	6.03562500	-2.61044700
C	0.63737800	-3.83665500	2.32723200
C	1.78627200	-4.28839100	3.24976600
C	-0.73487600	-4.16120500	2.94940500
H	0.70004300	-2.74860500	2.23692800
H	2.76391100	-4.02774600	2.82723800
H	1.70119500	-3.80698300	4.23126000
H	1.77473100	-5.37311300	3.40947200
H	-1.55039400	-3.79711500	2.31410500
H	-0.87210100	-5.24055500	3.08554300
H	-0.83167900	-3.68537800	3.93263100
C	1.14709000	-3.33133400	-2.77209200
C	-0.05856000	-3.53223700	-3.71133700
C	2.47361500	-3.59432500	-3.51123300
H	1.14360900	-2.28043500	-2.47032400
H	-0.99930500	-3.30298100	-3.19802900
H	0.02315600	-2.87245000	-4.58338200
H	-0.11966500	-4.56373400	-4.07805300
H	3.33717600	-3.41143200	-2.86154800
H	2.53914600	-4.62993300	-3.86553900
H	2.56157500	-2.93748800	-4.38482600
C	-1.14725200	3.33130800	-2.77205600
C	0.05821900	3.53229700	-3.71151200
C	-2.47392600	3.59417400	-3.51097700
H	-1.14363200	2.28041500	-2.47026400
H	0.99907700	3.30316800	-3.19835500
H	-0.02357500	2.87245900	-4.58351100
H	0.11915400	4.56378100	-4.07829400
H	-3.33736300	3.41120200	-2.86114800
H	-2.53960600	4.62978000	-3.86526400
H	-2.56197500	2.93733100	-4.38455600
C	-0.63720500	3.83667500	2.32722300

C	-1.78606000	4.28838000	3.24982100
C	0.73507400	4.16127700	2.94931200
H	-0.69983700	2.74862200	2.23693600
H	-2.76371500	4.02770300	2.82734800
H	-1.70091100	3.80697800	4.23131200
H	-1.77454500	5.37310300	3.40952200
H	1.55056600	3.79721000	2.31396400
H	0.87227200	5.24063200	3.08543700
H	0.83195100	3.68545800	3.93253400
H	-4.25120300	1.44085700	1.66934400
H	-3.56539900	-1.78288300	-1.09120900
H	3.56539500	1.78285200	-1.09129500
H	4.25122800	-1.44081800	1.66932900
Cl	-8.08196100	-1.42594800	0.73271400
Cl	8.08198200	1.42595800	0.73257700

Cartesian coordinates of the DFT optimized 6

Au	-1.18380961	-0.56002759	-0.20395305
N	-1.96985006	1.36366181	-0.13648492
C	0.78479594	3.61242546	0.51720087
N	0.14811685	2.36575888	0.20320522
C	-1.17120036	2.38837123	0.11616070
C	-3.37318199	1.63865027	-0.17985918
C	2.06650369	5.53559588	-0.19000977
C	-4.06259492	1.58775013	-1.40079530
C	-4.06493440	1.98759091	0.98092946
C	-5.41121965	1.89968115	-1.45544464
C	1.47487909	4.29879979	-0.47718326
C	1.95751337	6.08179115	1.09607144
C	-6.10373444	2.26120825	-0.28708057
C	0.67485632	4.14625985	1.80889576
C	1.26136449	5.37836362	2.08272517
Au	1.17419803	0.56245155	0.05385963
N	-0.16124463	-2.36984704	-0.26200365
C	1.16044108	-2.38667019	-0.26377617
C	3.37456828	-1.61402637	-0.18245105
C	-1.98094168	-5.50090778	0.61795588
C	4.13807972	-1.34547433	-1.32803258
C	3.99386946	-2.17228112	0.93615812
C	5.49074795	-1.64577574	-1.35336385
C	5.35548607	-2.48290137	0.91909063
C	-2.02019036	-6.15084984	-0.62288908
C	6.11086495	-2.21703909	-0.22924516
C	-0.85408577	-4.27818316	-1.64023176
C	-1.45434248	-5.52989341	-1.73990275
H	-1.49101861	-6.03399645	-2.70170480
H	6.09547991	-1.44296479	-2.23131390
H	-2.48788678	-7.12248939	-0.73003611
H	1.18404235	5.80158545	3.08046529

H	2.41050565	7.03611057	1.33805376
H	1.63693476	-3.36557172	-0.35026893
H	-1.65167755	3.36191692	0.23395755
H	-5.95852704	1.86510929	-2.39182403
N	1.96875023	-1.34364434	-0.17265922
C	-1.37238732	-4.24409278	0.73023577
C	-0.81512201	-3.64072787	-0.39273669
C	-5.42423376	2.30631834	0.93592139
H	-5.93613316	2.57516317	1.85248083
H	5.81041324	-2.91772323	1.80135655
H	1.57681577	3.87977919	-1.47175924
H	0.15209407	3.58897388	2.57979319
H	-1.36115147	-3.74325964	1.69185470
H	-0.43211547	-3.78525799	-2.51020855
O	2.71685000	6.12896043	-1.23090098
O	-2.49574741	-6.00728236	1.77480078
C	-3.15494723	-7.26168131	1.72532273
H	-2.47522658	-8.06441150	1.40862951
H	-4.02132523	-7.23587445	1.05139116
C	3.36485660	7.36899687	-1.00029092
H	4.14210682	7.28073513	-0.22991589
H	2.65115789	8.15014875	-0.70517463
H	-3.49609082	-7.46044447	2.74297119
H	3.82789981	7.64524888	-1.94932272
H	3.40873441	-2.35708499	1.83237717
H	3.66085393	-0.89224272	-2.19133901
H	-3.53011735	1.29460601	-2.29977438
H	-3.53959358	1.99933553	1.93179065
O	-7.42573219	2.54681870	-0.45072547
O	7.44292463	-2.47320012	-0.35800316
C	-8.19098239	2.87676173	0.69739837
H	-7.82102145	3.79125872	1.18005854
H	-8.19285023	2.05794875	1.42869289
C	8.13722391	-3.00727208	0.75789232
H	7.74611139	-3.99313996	1.04309260
H	8.08563670	-2.33422177	1.62365709
H	-9.20870116	3.04475334	0.34055795
H	9.17688951	-3.11053141	0.44199046

Vita

Nancy Rodriguez Lopez was born and raised in Veracruz, México. In 2008 she attended Instituto Tecnológico y de Estudios Superiores de Monterrey (ITESM) in Monterrey, México to pursue her Bachelor of Science. While pursuing her bachelor's degree, Nancy was offered several undergraduate research opportunities. During summer of 2012 and 2013, Nancy had the opportunity to visit the University of Texas at El Paso (UTEP) for an undergraduate summer research program at Dr. Dino Villagrán's group, where she worked on the study of multielectron redox chemistry through dimolybdenum complexes. She graduated in December 2013 with a Bachelor of Science in Chemistry after defending her undergraduate thesis. In January 2014 Nancy came back to UTEP to pursue her Doctoral degree with a major in Chemistry.

Contact Information: rdzl.nancy@gmail.com

This dissertation was typed by Nancy Rodríguez López.